Titre: Title:	Anisotropic Artificial Substrates for Microwave Applications
Auteur: Author:	Attieh Shahvarpour
Date:	2013
Type:	Mémoire ou thèse / Dissertation or Thesis
Référence: Citation:	Shahvarpour, A. (2013). Anisotropic Artificial Substrates for Microwave Applications [Thèse de doctorat, École Polytechnique de Montréal]. PolyPublie. https://publications.polymtl.ca/1125/

UNIVERSITÉ DE MONTRÉAL

ANISOTROPIC ARTIFICIAL SUBSTRATES FOR MICROWAVE APPLICATIONS

ATTIEH SHAHVARPOUR
DÉPARTEMENT DE GÉNIE ÉLECTRIQUE
ÉCOLE POLYTECHNIQUE DE MONTRÉAL

THÈSE PRÉSENTÉE EN VUE DE L'OBTENTION
DU DIPLÔME DE PHILOSOPHIÆ DOCTOR
(GÉNIE ÉLECTRIQUE)
AVRIL 2013

UNIVERSITÉ DE MONTRÉAL

ÉCOLE POLYTECHNIQUE DE MONTRÉAL

Cette thèse intitulée :

ANISOTROPIC ARTIFICIAL SUBSTRATES FOR MICROWAVE APPLICATIONS

présentée par : SHAHVARPOUR Attieh
en vue de l'obtention du diplôme de : Philosophiæ Doctor
a été dûment acceptée par le jury d'examen constitué de :

M. AKYEL Cevdet, Ph.D., président
M. CALOZ Christophe, Ph.D., membre et directeur de recherche
M. ALVAREZ-MELCÓN Alejandro, Ph.D., membre et codirecteur de recherche
M. WU Ke, Ph.D., membre
M. SEBAK Abdel Razik, Ph.D., membre

To my family.

ACKNOWLEDGMENTS

Foremost, I would like to express my gratitude to my supervisor Prof. Christophe Caloz for his leadership, inspiring guidance, and continuous support throughout this work.

My special thanks go to my co-supervisor Prof. Alejandro Alvarez Melcón for his support during and after my unforgettable stay in Spain. This PhD project could not be accomplished without his consistent encouragement and his patience in guiding me on my endless questions.

I would also like to thank the members of my thesis jury, Prof. Ke Wu and Prof. Cevdet Akyel from École Polytechnique de Montréal and Prof. Abdel Razik Sebak from Concordia University, for dedicating time to my thesis and for their valuable comments.

I would like to acknowledge all technical staffs of Poly-Grames Research Center, Mr. Jules Gauthier, Mr. Traian Antonescu, Mr. Steve Dubé and Mr. Maxime Thibault, for patiently assisting me in the fabrication and realization of my components. In addition, I would like to express my gratitude to Mrs. Ginette Desparois, Mrs. Louise Clément, and Mrs. Nathalie Lévesque for their assistance with all the administrative works, and to Mr. Jean-Sébastien Décarie for his technical support for solving the problems related to my computer system.

I am deeply grateful to my colleagues at the Electromagnetics Theory and Applications (ETA) research group for educating me on different aspects of science and beyond. In particular, Dr. Toshiro Kodera, Dr. Armin Parsa, Dr. Ning Yang, Dr. Hoang Nguyen, Dr. Louis-Philippe Carignan and Dr. Dimitrios Sounas have definitely taught me a great deal. Many thanks to Shulabh for bringing the spirit of joy to our group and for arranging for several memorable group activities. Special appreciations to Juan Sebastián and his kind family for their precious unconditional support during my stay in Spain and for their continuous kindness towards me.

I would like to take this opportunity to thank my former professors at K. N. Toosi University of Technology, Tehran, Iran, Mr. Mohsen Aboutorab, Dr. Sadegh Abrishamian, Dr. Nosrat Granpayeh and Dr. Manouchehr Kamyab who have introduced to me the beautiful aspects of electromagnetic science and microwave engineering in the first place, and by their great support and encouragement they have motivated me to find my path towards learning more and being creative in these fields and even beyond.

I owe my deepest gratitude to my family in Iran, my parents to whom I dedicate this thesis for their unconditional love, support and patience, to my loveliest sisters Azadeh, Shideh, Fahimeh and Shaghayegh, to my kindest brothers Ali, Mohammad and Saman, to my sweetest angels Rashno, Ahura and Radin and to my dearest aunt Nargues. I extend my sincere gratitude to my lovely new family in Canada, Mr. and Mrs. Couture, Philippe,

Anabel and Alexandre, for their kind hearts and endless support.

For last but not least, I would like to dedicate my most profound feeling of gratitude and appreciation to my husband Simon for all the moments that he has made my heart warm and my steps determined in my journey towards living my dreams.

RÉSUMÉ

Les matériaux anisotropes possèdent des propriétés électromagnétiques qui sont différentes dans différentes directions, ce qui résulte en des degrés de liberté supplémentaires pour la conception de dispositifs électromagnétique et mène à des applications. Certains matériaux anisotropes peuvent être trouvés dans la nature, comme les matériaux ferrimagnétiques, alors que d'autres peuvent être conçus artificiellement pour des applications spécifiques. Ces matériaux artificiels sont des structures composites qui sont faites d'implants métalliques insérés dans un médium hôte. Ces structures peuvent être considérées comme des matériaux effectifs nouveaux et peuvent posséder des propriétés que l'on ne retrouve pas dans la nature comme un indice de réfraction négatif, une chiralité ou une bi-anisotropie ; ils sont donc appelés méta-matériaux. Dû à la grande diversité d'implants qu'il est possible de concevoir, ces matériaux sont prometteurs pour la conception de dispositifs uniques et novateurs comme de nouvelles antennes, des antennes miniaturisées, des dispositifs non-réciproques, des analyseurs de signaux analogiques et des dispositifs de génie biomédical. Puisque dans les matériaux artificiels l'effet des implants dans le médium hôte n'est pas le même dans toutes les directions, ces matériaux ont la plupart du temps des caractéristiques anisotropes qui peuvent être contrôlées par les propriétés des implants. Cette propriété amène des degrés de liberté supplémentaires dans la conception de dispositifs nouveaux. L'effet d'anisotropie dans les structures artificielles est plus évident dans la plupart des substrats artificiels anisotropes à cause de leur structure planaire 2D.

Une analyse électromagnétique rigoureuse des substrats artificiels anisotropes est requise afin de mieux comprendre leurs propriétés, ce qui est essentiel pour proposer des applications. L'insuffisance de l'analyse disponible dans la littérature a servi de motivation pour cette thèse dont l'objectif est d'effectuer l'analyse électromagnétique rigoureuse de substrats artificiels anisotropes dans le but d'explorer des applications.

Afin de mieux comprendre les propriétés de l'anisotropie des substrats artificiels, leur méthode d'analyse et leurs applications, il peut être utile de d'abord mieux comprendre l'anisotropie de substrats naturels existant comme les matériaux ferrimagnétiques. Cette approche peut aussi mener à de nouvelles applications de ces matériaux anisotropes naturels. De plus, afin d'étudier certaines propriétés et applications des substrats anisotropes, certains aspects mal compris des matériaux isotropes doivent tout d'abord être éclaircis.

Basée sur les objectifs et la méthodologie décrits ci-haut, la présente thèse contribue les réalisations et avancements suivants au domaine du génie micro-ondes.

Le conducteur électromagnétique parfait (PEMC) comme condition frontière est un concept

électromagnétique nouveau et fondamental. C'est une description généralisée des conditions aux frontières électromagnétiques incluant le conducteur électrique parfait (PEC) et le conducteur magnétique parfait (PMC). De par ses propriétés fondamentales, le PEMC a le potentiel de rendre possible plusieurs applications électromagnétiques. Cependant, jusqu'à maintenant le concept de condition frontière PEMC était demeuré un concept théorique et n'avait jamais été réalisé en pratique. Ainsi, motivée par l'importance de ce concept fondamental en électromagnétisme et de ses applications potentielles, la première contribution de cette thèse se concentre sur l'implémentation pratique de la condition frontière PEMC en exploitant le principe de la rotation de Faraday et de la réflexion par un plan de masse dans les matériaux ferrimagnétiques qui sont intrinsèquement anisotropes. Conséquemment, la présente thèse rapporte la première approche pratique permettant la réalisation des conditions frontière PEMC. Une matrice de dispersion généralisée (GSM) est utilisée pour l'analyse de la structure PEMC constituée d'une ferrite posée sur un plan de masse. Comme application de la condition frontière PEMC, la démonstration expérimentale d'un guide d'onde transverse-électromagnétique (TEM) est effectuée en utilisant la ferrite posée sur un plan de masse comme murs de côté PMC (ce qui est un cas spécial de la frontière PEMC). Les conditions frontières conducteur électromagnétique parfait pourraient trouver des applications dans divers types de senseurs, réflecteurs, convertisseurs de polarisation et identificateurs radiofréquences basés sur la polarisation.

Les antennes à onde de fuite sont des antennes à haute directivité et à faisceau balayé en fréquence, et par conséquent rendent possible des applications dans les systèmes radar, en communication point-à-point et dans les systèmes MIMO. La seconde contribution de cette thèse est l'introduction et l'analyse d'une nouvelle antenne à onde de fuite bidimensionnelle à large bande et ayant une directivité élevée. Cette antenne fonctionne différemment dans les basses et hautes fréquences. Vers les basses fréquences, elle permet un balayage de l'espace complet de son faisceau conique alors qu'à hautes fréquences, elle rayonne avec un faisceau fixe dont l'angle est ajustable par conception et dont la variation en fréquence est très faible, ce qui la rend particulièrement adaptée pour des applications en communication point-à-point à large bande et dans les systèmes radar. Cette antenne est constituée d'un substrat artificiel de type champignon ayant une anisotropie électrique et magnétique posé sur un plan de masse et caractérisé par des tenseurs de permittivité et de perméabilité anisotropes et uniaxiaux. Un modèle de ligne de transmission spectral basé sur l'approche des fonctions de Green est choisi pour l'analyse de la structure. Une comparaison rigoureuse entre les antennes à onde de fuite isotropes et anisotropes est effectuée et révèle que contrairement au substrat anisotrope, le substrat isotrope démontre de piètres performances en tant qu'antenne à onde de fuite.

Les propriétés particulières aux antennes planaires telles qu'un bas profil, un faible coût,

la compatibilité avec les circuits intégrés et leur nature " conformal " en font des antennes appropriées pour les systèmes de communication. Parallèlement, les restrictions en termes de bande passante et de miniaturisation ont fait augmenter la demande pour les systèmes sans-fil à ondes millimétriques tels que les radars, les senseurs à distance et les réseaux locaux à haute vitesse. Cependant, lorsque la fréquence augmente vers le régime des ondes millimétriques, l'efficacité de rayonnement des antennes planaires devient un problème important. Ceci est dû à l'augmentation de l'épaisseur électrique du substrat et donc à l'augmentation du nombre de modes de surface qui sont excités et qui transportent une partie de l'énergie du système sans contribuer de manière efficace au rayonnement. Ainsi, ces antennes souffrent d'une faible efficacité de rayonnement. Ce problème a motivé la troisième contribution de cette thèse qui est l'interprétation et l'analyse du comportement de l'efficacité de rayonnement des antennes planaires sur des substrats électriquement épais. Une nouvelle approche basée sur un dipôle de substrat est introduite pour expliquer le comportement de l'efficacité. Ce dipôle modélise le substrat et réduit le problème d'une source électrique horizontale sur le substrat au problème équivalent d'un dipôle rayonnant dans l'espace libre. De plus, dans ce travail quelques solutions pour l'amélioration de l'efficacité de rayonnement aux épaisseurs électriques où l'efficacité est minimale sont données. Utilisant la meilleure compréhension du comportement de l'efficacité de rayonnement acquise pour le cas des antennes planaires imprimées sur un substrat isotrope (substrat conventionnel), l'effet d'un substrat anisotrope sur l'efficacité de rayonnement des antennes planaires est étudié.

ABSTRACT

Anisotropic materials exhibit different electromagnetic properties in different directions and therefore they provide some degrees of freedom in the design of electromagnetic devices and enable many applications. Some kinds of anisotropic materials are available in the nature such as ferrimagnetic materials, while many others can be artificially designed for specific applications. The artificial materials are composite structures made of sub-wavelength metallic implants in a host medium, which constitute novel effective materials. These materials may exhibit properties not readily available in the nature, such as negative refractive index, chirality or bi-anisotropy, and therefore are called metamaterials. Due to the diversity of their possible implants, they have a great potential in unique and novel components, such as specific antennas, miniaturized antennas, non-reciprocal devices, analog signal processors, and biomedical engineering devices. Since in most of the artificial materials, the effect of the implants in the host medium is not the same in all the directions, these materials exhibit anisotropic characteristics which can be controlled by the properties of the implant. This characteristic provides some additional degrees of freedom in the design of novel devices. The anisotropy effect in the artificial structures is more evident in most of the anisotropic artificial substrates due to their 2D planar structure.

Rigorous electromagnetic analysis of the anisotropic artificial substrates is required for gaining a better understanding of their properties which is essential for proposing novel applications. Insufficient available analysis in the literature has motivated this thesis whose objective is to perform rigorous electromagnetic analysis of the anisotropic artificial substrates towards exploring their applications.

To acquire more insight into the anisotropic properties of artificial substrates, their analysis method, and their applications, it is useful to first better understand anisotropy of existing natural substrates such as ferrimagnetic materials. This approach may also lead to novel applications of the natural anisotropic materials. In addition, to investigating some of properties and applications of the anisotropic substrates, foremost we may need to clarify some unclear aspects regarding the isotropic materials.

Based on the objectives and methodology of the thesis which were explained above, this thesis contributes to the following achievements and advances in microwave engineering.

The perfect electromagnetic conductor (PEMC) boundary is a novel fundamental electromagnetic concept. It is a generalized description of the electromagnetic boundary conditions including the perfect electric conductor (PEC) and the perfect magnetic conductor (PMC) and due to its fundamental properties, it has the potential of enabling several electromag-

netic applications. However, the PEMC boundaries concept had remained at the theoretical level and has not been practically realized. Therefore, motivated by the importance of this electromagnetic fundamental concept and its potential applications, the first contribution of this thesis is focused on the practical implementation of the PEMC boundaries by exploiting Faraday rotation principle and ground reflection in the ferrite materials which are intrinsically anisotropic. As a result, this thesis reports the first practical approach for the realization of PEMC boundaries. A generalized scattering matrix (GSM) is used for the analysis of the grounded-ferrite PEMC boundaries structure. As an application of the PEMC boundaries, a transverse electromagnetic (TEM) waveguide is experimentally demonstrated using grounded ferrite PMC (as particular case of the PEMC boundaries) side walls. Perfect electromagnetic conductor boundaries may find applications in various types of sensors, reflectors, polarization convertors and polarization-based radio frequency identifiers.

Leaky-wave antennas perform as high directivity and frequency beam scanning antennas and as a result they enable applications in radar, point-to-point communications and MIMO systems. The second contribution of this thesis is introducing and analysing a novel broadband and highly directive two-dimensional leaky-wave antenna. This antenna operates differently in the lower and higher frequency ranges. Toward its lower frequencies, it allows full-space conical-beam scanning while at higher frequencies, it provides fixed-beam radiation (at a designable angle) with very low-beam squint, which makes it particularly appropriate for applications in wide band point-to-point communication and radar systems. The antenna is constituted of a mushroom type anisotropic magneto-dielectric artificial grounded slab with uniaxially anisotropic permittivity and permeability tensors. A spectral transmission-line model based on Green functions approach is chosen for the analysis of the structure. A rigorous comparison between the isotropic and anisotropic leaky-wave antennas is performed which reveals that as opposed to anisotropic slabs, isotropic slabs show weak performance in leaky-wave antennas.

The properties of planar antennas such as low profile, low cost, compatibility with integrated circuits and their conformal nature have made them appropriate antennas for communications systems. In parallel, bandwidth and miniaturization requirements have increased the demand for millimeter-wave wireless systems, such as radar, remote sensors and high-speed local area networks. However, as frequency increases towards millimeter-wave regime, the radiation efficiency of planar antennas becomes an important issue. This is due to the increased electrical thickness of the substrate and therefore increased number of the excited surface modes which carry part of the energy of the system in the substrate without any efficient contribution to radiation. Therefore, these antennas suffer from low radiation efficiency. This has motivated the third contribution of the thesis which is the interpretation and

analysis of the radiation efficiency behavior of the planar antennas on electrically thick substrates. A novel substrate dipole approach is introduced for the explanation of the efficiency behavior. This dipole models the substrate and reduces the problem of the horizontal electric source on the substrate to an equivalent dipole radiating in the free-space. In addition, in this work, some efficiency enhancement solutions at the electrical thicknesses where the radiation efficiency is minimal are provided. Following the obtained knowledge about the radiation efficiency behavior of the planar antennas printed on the isotropic (conventional) substrates, finally, the effect of the anisotropy of the substrate on the planar antenna radiation efficiency is studied.

TABLE OF CONTENTS

DEDICATION iii

ACKNOWLEDGMENTS iv

RÉSUMÉ vi

ABSTRACT ix

TABLE OF CONTENTS xii

LIST OF TABLES xvi

LIST OF FIGURES xvii

LIST OF APPENDICES xxvi

LIST OF ABREVIATIONS AND NOTATIONS xxvii

CHAPTER 1 INTRODUCTION 1
1.1 Definitions and Basic Concepts 1
1.1.1 Natural Anisotropic Materials 1
1.1.2 Artificial Anisotropic Materials 4
1.2 Motivations, Objectives, Contributions and Organization of the Thesis 18
1.2.1 Motivations, Objectives and Contributions 18
1.2.2 Organization 23

CHAPTER 2 ARTICLE 1: ARBITRARY ELECTROMAGNETIC CONDUCTOR BOUNDARIES USING FARADAY ROTATION IN A GROUNDED FERRITE SLAB . . . 25
2.1 Abstract 25
2.2 Introduction 25
2.3 Principle of Electromagnetic Boundaries in a Grounded Ferrite Slab Using Faraday Rotation 27
2.3.1 Grounded Ferrite Slab Structure and Initial Assumptions 27
2.3.2 Perfect Electromagnetic Conductor Boundary Realization 29
2.4 Theory 31

2.4.1 Faraday Rotation and Effective Permeability for Propagation Parallel to the Bias Field in an Unbounded Ferrite . . . 31
2.4.2 Effect of Oblique Incidence at the Air-Ferrite Interface . . . 33
2.4.3 Exact Analysis for Normal Incidence by the Generalized Scattering Matrix Method . . . 35
2.4.4 PMC and Free-Space Perfect Electromagnetic Conductor Realizations . 40
2.4.5 Effect of Multiple Reflections . . . 42
2.4.6 General Perfect Electromagnetic Conductor Admittance . . . 43
2.5 PMC-Walls TEM Waveguide . . . 47
2.5.1 Principle . . . 47
2.5.2 Full-wave and Experimental Demonstration . . . 49
2.5.3 Tunability . . . 51
2.6 Conclusion . . . 53

CHAPTER 3 ARTICLE 2: BROADBAND AND LOW-BEAM SQUINT LEAKY WAVE RADIATION FROM A UNIAXIALLY ANISOTROPIC GROUNDED SLAB . . . 55
3.1 Abstract . . . 55
3.2 Introduction . . . 56
3.3 Definition of the Medium . . . 57
3.4 Dispersion Relation of the Uniaxially Anisotropic Grounded Slab . . . 59
3.5 Dispersion Analysis . . . 61
3.5.1 Effect of Uniaxial Anisotropy (Non-dispersive Medium) . . . 61
3.5.2 Effect of Drude/Lorentz Dispersion in Addition to Anisotropy . . . 62
3.6 Far-Field Radiation Analysis . . . 66
3.6.1 Green Functions for Vertical Point Source . . . 66
3.6.2 Asymptotic Far-Field Expressions . . . 70
3.7 Leaky-Wave Properties Discussion . . . 70
3.7.1 Inappropriateness of the Isotropic Structure . . . 70
3.7.2 Appropriateness and Performance of the Double Anisotropic Structure 75
3.7.3 Importance of the Dispersion Associated with Magnetic Anisotropy . . 79
3.8 Conclusion . . . 80

CHAPTER 4 ARTICLE 3: RADIATION EFFICIENCY ISSUES IN PLANAR ANTENNAS ON ELECTRICALLY THICK SUBSTRATES AND SOLUTIONS . . . 81
4.1 Abstract . . . 81
4.2 Introduction . . . 81
4.3 Radiation Efficiency . . . 82

4.3.1 Definition . . . 82
4.3.2 Dependence on the Electrical Thickness . . . 84
4.4 Explanation of the Radiation Efficiency Response versus the Substrate Thickness 87
4.4.1 Radiated Power . . . 87
4.4.2 Surface-Wave Power . . . 97
4.4.3 Radiation Efficiency . . . 98
4.5 Half-wavelength Dipole Antenna Extension . . . 100
4.6 Solutions to the Low Radiation Efficiency Issue . . . 100
4.6.1 Enhancement Principle . . . 102
4.6.2 Enhancement Solutions . . . 102
4.7 Conclusions . . . 105

CHAPTER 5 EFFECT OF SUBSTRATE ANISOTROPY ON RADIATION EFFICIENCY . . . 108
5.1 Abstract . . . 108
5.2 Introduction . . . 108
5.2.1 Radiation Efficiency Computation . . . 109
5.3 Non-Dispersive Uniaxially Anisotropic Substrates . . . 111
5.3.1 Definition of Various Cases of Study . . . 111
5.3.2 Results and Discussion . . . 112
5.4 Dispersive Anisotropic Substrate . . . 121
5.4.1 Dispersive Material Definition . . . 121
5.4.2 Results . . . 122
5.5 Conclusions . . . 123

CHAPTER 6 GENERAL DISCUSSION . . . 125

CHAPTER 7 CONCLUSIONS AND FUTURE WORKS . . . 129
7.1 Conclusions . . . 129
7.2 Future Works . . . 130
7.2.1 Rotating Field-Polarization Waveguide Application of the Grounded-Ferrite Perfect Electromagnetic Conductor (PEMC) Boundaries . . . 130
7.2.2 Grounded-Ferrite PMC Application for Gain Enhancement of a Low-Profile Patch Antenna . . . 132
7.2.3 Practical Demonstration of the Oscillatory Variations of the Radiation Efficiency versus Frequency for a Horizontal Electric Dipole on an Electrically Thick Substrate . . . 134

7.2.4 Bandwidth Enhancement of a Patch Antenna Using a Wire-Ferrite Substrate . . . 136

REFERENCES . . . 141

APPENDICES . . . 150
A.1 Physical Interpretation of the Signs of the Wave Numbers . . . 150
A.2 Definition of the Proper and Improper Modes . . . 150
B.1 Source-less Problem . . . 155
B.1.1 TM_z Modes . . . 157
B.1.2 TE_z Modes . . . 159
B.2 Horizontal Infinitesimal Electric Dipole Source . . . 161
B.2.1 TM_z Modes . . . 162
B.2.2 TE_z Modes . . . 164
B.3 Vertical Infinitesimal Electric Dipole Source . . . 165
C.1 Spectral Domain Green Functions . . . 169
C.1.1 Field Green Functions . . . 170
C.1.2 Vector Potential Green Functions . . . 170
C.2 Powers Computation . . . 171
C.2.1 Radiated Power . . . 171
C.2.2 Surface-Wave Power . . . 172
E.1 Spectral Domain Green Functions . . . 174
E.1.1 Vector Potentials Green Functions . . . 175
E.2 Power Computation . . . 176
E.3 Radiated Power . . . 176
E.4 Surface-wave Power . . . 176
F.1 Peer-Reviewed Journal Publications . . . 178
F.2 Conference Publications . . . 178
F.3 Non-Refereed Publications . . . 179
F.4 Awards and Honors . . . 180
F.4.1 Awards . . . 180
F.4.2 Travel Grants . . . 180

LIST OF TABLES

Table 2.1 Exact perfect electromagnetic conductor (PEMC) boundary conditions with the Faraday grounded ferrite slab. 45

Table 4.1 Values of ϕ_0, ϕ_{-d}, $k_{\mathrm{zd}}d$, Z_{in} and $d/\lambda_{\mathrm{eff}}^{\mathrm{cutoff}}$ at the TE and TM surface-wave mode cutoffs for the grounded and ungrounded substrates. 95

Table 5.1 Various uniaxially anisotropic substrate cases ($\mu_\rho\varepsilon_z = \mu_z\varepsilon_\rho = n\mu_0\varepsilon_0$), with $d = 2.5$ mm and $n = 6.15$. 112

Table A.1 Physical interpretation of the signs of the transverse and longitudinal wave numbers. 150

Table A.2 Typical modes in a dielectric slab ($k_{\mathrm{d}} = \omega\sqrt{\mu_{\mathrm{d}}\varepsilon_{\mathrm{d}}}$ represents the wave number in the medium with effective permeability μ_{d} and permittivity ε_{d}). 151

Table A.3 Characteristics of the different TM_z modes shown in the dispersion curves of Fig. A.2. SW, LW and IN stand for surface-wave, leaky-wave and non-physical modes, respectively. 153

LIST OF FIGURES

Figure 1.1 Concave metallic Kock lens. Taken from "Metal-lens antennas," *Proc. of IRE*, 1946, by W. E. Kock. ©1946 IEEE. 6

Figure 1.2 Three dimensional array of conducting disks, studied by Estrin. Adapted from "The effective permeability of an array of thin conducting disks," *J. Appl. Phys.* 1950, by G. Estrin. 7

Figure 1.3 Rodded media. (a) One dimensional, (b) two dimensional and (c) three dimensional structures. Adapted from "Plasma simulation by artificial dielectrics and parallel-plate media," IRE Trans. Antennas Propagat., 1962, by W. Rotman. 8

Figure 1.4 Plasma effective permittivity of the rodded medium of Rotman. 9

Figure 1.5 Artificial dielectric with plasma electric response in the gigahertz range, consisting of a 3D cubic lattice of very thin infinitely long metallic wires proposed by Pendry. Reprinted figure with permission from J.B. Pendry, A.J. Holden, W.J. Stewart and I. Youngs, Extremely low frequency plasmons in metallic mesostructures, *Phys. Rev. Lett.* 76 4773-6 and 1996. Copyright 1996 by the American Physical Society. . . 10

Figure 1.6 Artificial magnetic materials proposed by Pendry. (a) Arrays of non-magnetic conducting cylinders. (b) Modified cylinders with two concentric metallic cylinders in the form of split rings. (c) Printed split-ring unit-cell, its two dimensional array and its stacked configuration. Taken from "Magnetism from conductors and enhanced nonlinear phenomena," *IEEE Trans. Microwave Theory Tech.*, 1999, by J. B. Pendry *et al.*. ©1999 IEEE 11

Figure 1.7 Resonant effective Lorentz permeability of the artificial magnetic material of Pendry. 12

Figure 1.8 Wire medium constituted of two dimensional array of metallic wires. Adapted from *Analytical Modeling in Applied Electromagnetics*, *Artech House*, 2003, by S. A. Tretyakov. 13

Figure 1.9 Wire medium in the form of embedding metallic wires or drilling vias in a dielectric substrate. 15

Figure 1.10 A stack of two-dimensional arrays of split ring resonators (SRRs) embedded in a substrate. (a) SRRs in the xy plane. (b) SRRs in the yz plane. 16

Figure 1.11 Mushroom-type magneto-dielectric anisotropic substrate. 17
Figure 2.1 Perspective view of the grounded ferrite slab, with perpendicular magnetic bias field $\mathbf{H}_0$ and Faraday-rotating RF electromagnetic fields. $\mathbf{k}_0$ and $\mathbf{k}_f$ are the propagation vectors in free space and the ferrite, respectively. 28
Figure 2.2 Principle of the proposed grounded ferrite perfect electromagnetic conductor boundary (Fig. 2.1), ignoring phase shifts and multiple reflections for simplicity. The structure uses arbitrary Faraday rotation with single-trip angle θ and perfect electric conductor (PEC) reflection on the ground plane. The different panels show the evolution of the vectorial $\mathbf{E}$ and $\mathbf{H}$ fields, for a matched and lossless ferrite slab. 30
Figure 2.3 Particular cases of PMC and free space perfect electromagnetic conductor boundaries, corresponding to $\theta = 90°$ and $\theta = 45°$ Faraday rotation angles, respectively. (a) PMC. (b) Free-space perfect electromagnetic conductor. 32
Figure 2.4 Permeability and Faraday rotation angle versus frequency for an unbounded ferrite medium (YIG) with parameters: $\mu_0 M_s = 0.188$ T, $\Delta H = 10$ Oe, $\varepsilon_r = 15$, and $\mu_0 \mathbf{H}_0 = 0.2$ T (internal bias field). The parameters M_s, ΔH and ε_r correspond to the specifications of the ferrite which will be used in the experiment (Sec. 2.5) while the parameter $\mu_0 \mathbf{H}_0$ will be determined in Sec. 2.4.4 to provide an exact PMC at $\theta = 90°$. (a) Real and imaginary parts of $\mu_{e\pm}$ computed by (2.5). (b) Real and imaginary parts of μ_e computed by (2.9), and Faraday rotation angle calculated by (2.3). The $\tan\delta_m$ at 5.19 GHz (PMC) and at 4.7 GHz (free-space perfect electromagnetic conductor (PEMC)) are of 0.0129 and 0.0045, respectively. 34
Figure 2.5 Reflection and refraction at the interface between air and a ferrite medium for plane wave oblique incidence. 36
Figure 2.6 Approximate Faraday rotation angle variation due to oblique incidence with the parameters of Fig. 2.4 after refraction through an interface with air (Fig. 2.5) for different incidence angles ψ_i, computed by (2.3) with (2.10), using (2.11). 36
Figure 2.7 Definition of the incident and scattered RHCP (+) and LHCP (−) waves in the grounded ferrite slab for application of the generalized scattering matrix analysis under normal incidence. 38

Figure 2.8 Components z and y of the electric field scattered (or reflected) by the grounded ferrite slab computed by the generalized scattering matrix (GSM) method [(2.23)] and compared with HFSS (FEM) results, for a slab of thickness of $h = 3$ mm (sample used in the experiment, Sec. 2.5, and for a Faraday rotation angle of $\theta = 90°$). The ferrite parameters are given in the caption Fig. 2.4, and the bias field $\mathbf{H}_0 = 0.2$ T was obtained from (2.23) as a solution providing the PMC boundary at 5.19 GHz. The incident wave is linearly polarized along the z direction, so the z and y reflected field components correspond to the co- and cross-polarized fields with respect to the incident field. (a) Amplitude. (b) Phase. 41

Figure 2.9 Components z (co-polarized) and y (cross-polarized) of the scattered electric field as a function of the number of propagation round trips inside the ferrite slab, computed by (2.25), to show the effect of multiple reflections and related phase shifts caused by mismatch (lossless case). 44

Figure 2.10 Normalized admittance $Y\eta_0$ versus frequency computed by (2.29) from generalized scattering matrix results for the grounded ferrite perfect electromagnetic conductor, assuming a lossless ferrite. (a) Magnitude. (b) Phase. 46

Figure 2.11 Normalized admittance $Y\eta_0$ versus frequency computed by (2.29) from generalized scattering matrix results for the grounded ferrite perfect electromagnetic conductor, for a lossy ferrite of $\triangle H = 10$ Oe. (a) Magnitude. (b) Phase. 48

Figure 2.12 Transverse electromagnetic (TEM) rectangular waveguide realized by inserting ferrite slabs against the lateral walls of a rectangular waveguide according to the grounded ferrite PMC (GF-PMC) principle depicted in Fig. 2.3a. (a) Perspective view. (b) Top view with ray-optic illustration of the TEM waveguide phenomenology. (c) Zoom on the ferrite region of (b) to illustrate the phase coherence condition between the TEM wave in the air region and the surface wave in the ferrite slab. 50

Figure 2.13 Comparison between a G-band rectangular waveguide (3.95−5.85 GHz) and a grounded ferrite PMC waveguide (Fig. 2.12) with the parameters of Fig. 2.8 operating in the same frequency range, specifically at $f =$ 5.2 GHz, but with a much smaller width (around 3× smaller). The dimensions are in millimeters. The waveguide is excited by a coaxial probe located a quarter-wavelength away from a short-circuiting wall (here removed for visualization). 51

Figure 2.14 Comparative full-wave (CST Microwave Studio) and experimental results for the grounded ferrite PMC TEM rectangular waveguide of Figs. 2.12 and 2.13. (a) Scattering parameters for an empty waveguide of same width, which is a waveguide with cutoff of $f_c = c/(2a) = 10$ GHz. (b) Scattering parameters for the grounded ferrite PMC TEM waveguide. The inset shows grounded ferrite PMC waveguide sandwiched between two biasing magnets. 52

Figure 2.15 Full-wave (CST Microwave Studio) electric field distribution at the half-height of the grounded ferrite PMC (GF-PMC) waveguide of Fig. 2.14b, compared with an ideal PMC waveguide and a PEC waveguide. The inset shows the vectorial field distribution in the entire cross section. . 53

Figure 2.16 Experimental demonstration of the tunability of the grounded ferrite PMC TEM waveguide of Fig. 2.14b with the bias field $\mu_0\mathbf{H}_0$. (a) S_{11}. (b) S_{21}. 54

Figure 3.1 Effective uniaxial anisotropic medium (unbounded), characterized by the permittivity and permeability tensors of (3.1) along with the TM_z and TE_z field configurations. 58

Figure 3.2 Uniaxially anisotropic grounded slab and its transmission line model, where $i \equiv TM_z, TE_z$. (a) TM_z and TE_z waves incident onto the slab. (b) Transmission line model (source-less case). 60

Figure 3.3 TM_z dispersion curves for the uniaxial anisotropic grounded slab with $\varepsilon_\rho = 2\varepsilon_0$ and $\mu_z = \mu_0$, for a fixed μ_ρ/μ_z and various $\varepsilon_\rho/\varepsilon_z$. (a) $\mathrm{Re}(k_\rho^{TM_z}/k_0^{TM_z})$. (b) $\mathrm{Im}(k_\rho^{TM_z}/k_0^{TM_z})$. (c) $\mathrm{Re}(k_{z0}^{TM_z}/k_0^{TM_z})$. (d) $\mathrm{Im}(k_{z0}^{TM_z}/k_0^{TM_z})$. The surface-wave (SW), leaky-wave (LW) and improper non-physical (IN) modes are indicated on the curves for the isotropic case. These indications also apply to Figs. 3.4 and 3.5. 63

Figure 3.4 TM_z dispersion curves for the uniaxial anisotropic grounded slab with $\varepsilon_\rho = 2\varepsilon_0$ and $\mu_z = \mu_0$, for a fixed $\varepsilon_\rho/\varepsilon_z$ and various μ_ρ/μ_z. (a) $\mathrm{Re}(k_\rho^{TM_z}/k_0^{TM_z})$. (b) $\mathrm{Im}(k_\rho^{TM_z}/k_0^{TM_z})$. (c) $\mathrm{Re}(k_{z0}^{TM_z}/k_0^{TM_z})$. (d) $\mathrm{Im}(k_{z0}^{TM_z}/k_0^{TM_z})$. 64

Figure 3.5 TE_z dispersion curves for the uniaxial anisotropic grounded slab with $\varepsilon_\rho = 2\varepsilon_0$ and $\mu_z = \mu_0$, for a fixed $\varepsilon_\rho/\varepsilon_z = 1$ and various μ_ρ/μ_z. (a) $\mathrm{Re}(k_\rho^{\mathrm{TE}_z}/k_0^{\mathrm{TE}_z})$. (b) $\mathrm{Im}(k_\rho^{\mathrm{TE}_z}/k_0^{\mathrm{TE}_z})$. (c) $\mathrm{Re}(k_z^{\mathrm{TE}_z}/k_0^{\mathrm{TE}_z})$. (d) $\mathrm{Im}(k_z^{\mathrm{TE}_z}/k_0^{\mathrm{TE}_z})$. 65

Figure 3.6 Dispersive response for the permittivity $\varepsilon_z/\varepsilon_0$ (Drude model) [Eq. (3.2)] and permeability μ_ρ/μ_0 (Lorentz model) [Eq. (3.3)] for equal electric and magnetic plasma frequencies ($\omega_{\mathrm{pe}} = \omega_{\mathrm{pm}}$). The parameters are: $F = 0.56$, $\omega_{\mathrm{m0}} = 2\pi \times 7.3 \times 10^9$ rad/s, fixing $\omega_{\mathrm{pm}} = \omega_{\mathrm{m0}}/\sqrt{1-F} = 2\pi \times 11 \times 10^9$ rad/s, $\varepsilon_r = 2$, $\omega_{\mathrm{pe}} = \omega_{\mathrm{pm}}$, $\zeta_{\mathrm{e}} = 0$ and $\zeta_{\mathrm{m}} = 0$. The substrate thickness is $d = 3$ mm. 66

Figure 3.7 Comparison of the dispersions of the first TM_z leaky modes for different grounded slabs: non-dispersive (slab medium) isotropic ($\varepsilon_z = \varepsilon_\rho = 2\varepsilon_0, \mu_\rho = \mu_z = \mu_0$), non-dispersive (slab medium) anisotropic ($\varepsilon_\rho/\varepsilon_z = 2.5$, $\varepsilon_\rho = 2\varepsilon_0$, $\mu_\rho/\mu_z = 0.5$, $\mu_z = \mu_0$), and dispersive anisotropic ($\varepsilon_z = \varepsilon_r(1-\omega_{\mathrm{pe}}{}^2/\omega^2)\varepsilon_0$ with $\varepsilon_r = 2$, $\varepsilon_\rho = 2\varepsilon_0$, $\mu_\rho = [1 - F\omega^2/(\omega^2 - \omega_{\mathrm{m0}}{}^2)]\mu_0$, $\mu_z = \mu_0$). (a) $\mathrm{Re}(k_\rho^{\mathrm{TM}_z}/k_0^{\mathrm{TM}_z})$. (b) $\mathrm{Im}(k_\rho^{\mathrm{TM}_z}/k_0^{\mathrm{TM}_z})$. The non specified parameters are equal to those of Fig. 3.6. 67

Figure 3.8 Uniaxially anisotropic grounded slab excited by an embedded vertical point source. (a) Physical structure. (b) Transmission line model. . . . 68

Figure 3.9 Radiation pattern for a vertical point source located at $h = 1.5$ mm from the ground plane in the anisotropic grounded slab [Fig. 3.8a] at $f = 51$ GHz where $k_\rho/k_0 = 0.78 - j0.07$ (Fig. 3.7) for the parameters of Fig. 3.6. (a) Comparison between theory [Eq. (3.16)] and full-wave (FIT-CST) simulation results. (b) 3D conical pattern. 71

Figure 3.10 Pointing angle of the leaky mode and its variation over frequency calculated from $\theta_{\mathrm{p}} = \sin^{-1}(\beta_\rho/k_0)$ (*Leaky-Wave Antennas*, by A. Oliner and D. Jackson, 2007) for the slab with the dispersion curves of Fig. 3.7 and $d = 3$ mm. (a) Isotropic slab with $\varepsilon_z = \varepsilon_\rho = 2\varepsilon_0$, $\mu_\rho = \mu_z = \mu_0$. (b) Anisotropic slab with $\varepsilon_z = \varepsilon_r(1 - \omega_{\mathrm{pe}}{}^2/\omega^2)\varepsilon_0$, $\varepsilon_\rho = 2\varepsilon_0$, $\mu_\rho = [1 - F\omega^2/(\omega^2 - \omega_{\mathrm{m0}}{}^2)]\mu_0$, $\mu_z = \mu_0$. (c) Comparison of the variations of the pointing angle with respect to frequency for the isotropic and anisotropic substrates. 73

Figure 3.11 Comparison of the leaky-wave behavior of the isotropic grounded slab for different permittivities ($\varepsilon_r = 2, 3, 4$), with $\mu_r = 1$ and $d = 3$ mm. . . 74

Figure 3.12 The radiation from an isotropic grounded slab for various frequencies from Fig. 3.10a and for the frequency of $f = 27$ GHz, which lies in the improper non-physical (IN) region of the dispersion curve of Fig. 3.7. . 75

Figure 3.13 Comparison of the leaky-wave bandwidth versus the host medium permittivity ε_r between the isotropic, double anisotropic and permittivity-only anisotropic grounded slabs. 76
Figure 3.14 Minimum pointing angle $\theta_{\mathrm{p}},_{min}$ for the isotropic substrate versus the permittivity ε_r and corresponding leakage factor $\alpha(\theta_{\mathrm{pmin}})/k_0$. 76
Figure 3.15 Maximum pointing angle of the leaky mode radiation from the double anisotropic grounded slab. 77
Figure 3.16 The scanning behavior of the double anisotropic substrate in a wide band frequency range. 78
Figure 3.17 Beam squinting of the leaky mode radiation of the anisotropic slab of Fig. 3.10b in the bandwidth of $\Delta f = 5$ GHz for $f = 30 - 35$ GHz. . . . 79
Figure 4.1 *Grounded* (PEC) dielectric substrate excited by an infinitesimal horizontal electric dipole. (a) Structure. (b) Transmission-line model. (c) Equivalent free-space dipole pair $J_{\mathrm{eq}} = J_{\mathrm{s}} + J'_{\mathrm{sub}}$ formed by the source dipole J_{s} and the auxiliary substrate dipole J'_{sub}. (d) Equivalent transmission-line model of the equivalent free-space dipole pair radiating into free-space. 85
Figure 4.2 *Ungrounded* dielectric substrate excited by an infinitesimal horizontal electric dipole. (a) Structure. (b) Transmission-line model. (c) Equivalent free-space dipole pair $J_{\mathrm{eq}} = J_{\mathrm{s}} + J'_{\mathrm{sub}}$ formed by the source dipole J_{s} and the auxiliary substrate dipole J'_{sub}. (d) Equivalent transmission-line model of the equivalent free-space dipole pair radiating into free-space. 86
Figure 4.3 Response to an infinitesimal horizontal dipole on a *grounded* substrate (Fig. 4.1a) versus the electrical thickness of the substrate. (a) Radiation efficiency [Eq. (4.2)]. (b) TM_z and TE_z surface modes [poles of (C.11)]. (c) Radiated power [Eq. (4.3a)]. (d) Surface-modes powers [Eq. (4.3b)]. 88
Figure 4.4 Response to an infinitesimal horizontal dipole on an *ungrounded* substrate (Fig. 4.2a) versus the electrical thickness of the substrate. (a) Radiation efficiency [Eq. (4.2)]. (b) TM_z and TE_z surface modes [poles of (C.11)]. (c) Radiated power [Eq. (4.3a)]. (d) Surface-modes powers [Eq. (4.3b)]. 89
Figure 4.5 Ray-optics representation of wave propagation in the air and in the dielectric (only one leaky-wave ($\theta < 90°$) or surface-wave ($\theta = 90°$) is shown) in the grounded substrate and ungrounded substrate cases. (a) Grounded case. (b) Ungrounded case. 90

Figure 4.6 Vectorial field configurations at the TE and TM cutoffs. 93
Figure 4.7 Magnitude of the total equivalent dipole current $\tilde{I}_{\rm eq}^{\rm tot} = \tilde{I}_{\rm eq}^{\rm TE} + \tilde{I}_{\rm eq}^{\rm TM}$ [Eq. (4.9)] versus the electrical thickness of the substrate and the angle of radiation. (a) Grounded case. (b) Ungrounded case. 94
Figure 4.8 Comparison of the radiation efficiency behaviors of the infinitesimal dipole and the half-wavelength dipole on the grounded and ungrounded substrates, computed from the Green function analysis and from full-wave simulation, respectively. (a) Grounded substrate. (b) Ungrounded substrate. 101
Figure 4.9 Quarter-wavelength grounded dielectric PMC boundary configuration for the enhancement of the radiation efficiency at the minima of the radiation efficiency of the original grounded substrate (Fig. 4.3a). (a) Original grounded substrate. (b) Quarter-wavelength dielectric PMC boundary structure. (c) Substituting the PEC ground plane of the grounded substrate by the quarter-wavelength PMC structure. 104
Figure 4.10 Comparison between the efficiency of the original and the PMC grounded substrates. 104
Figure 4.11 Full-wave HFSS simulation results for the differential unwrapped phase between the reflected fields from a PEC plane and the EBG structure. . 105
Figure 4.12 EBG-PMC boundary configuration for the enhancement of the radiation efficiency at the minima of the radiation efficiency of the original grounded substrate (Fig. 4.3a). (a) Original grounded substrate. (b) EBG-PMC boundary structure. (b) Substituting the PEC ground plane of the original grounded substrate by the EBG-PMC structure. . 106
Figure 4.13 Comparison between the efficiency of the PEC and the EBG-PMC grounded substrate. 106
Figure 5.1 Uniaxially anisotropic grounded substrate excited by an infinitesimal horizontal electric dipole. (a) Structure. (b) Transmission-line model. . 111
Figure 5.2 Response to an infinitesimal horizontal dipole on the isotropic grounded substrate (Fig. 5.1a) of *case 1* versus the electrical thickness of the substrate. (a) Radiation efficiency [Eq. (5.2)]. (b) TM_z and TE_z surface modes. 113
Figure 5.3 Response to an infinitesimal horizontal dipole on the uniaxially anisotropic grounded substrate (Fig. 5.1a) of *case 2* versus the electrical thickness of the substrate. (a) Radiation efficiency [Eq. (5.2)]. (b) TM_z and TE_z surface modes. 114

Figure 5.4 Response to an infinitesimal horizontal dipole on the uniaxially anisotropic grounded substrate (Fig. 5.1a) of *case 3* versus the electrical thickness of the substrate. (a) Radiation efficiency [Eq. (5.2)]. (b) TM_z and TE_z surface modes. 115

Figure 5.5 Response to an infinitesimal horizontal dipole on the uniaxially anisotropic grounded substrate (Fig. 5.1a) of *case 4* versus the electrical thickness of the substrate. (a) Radiation efficiency [Eq. (5.2)]. (b) TM_z and TE_z surface modes. 116

Figure 5.6 Response to an infinitesimal horizontal dipole on the uniaxially anisotropic grounded substrate (Fig. 5.1a) of *case 5* versus the electrical thickness of the substrate. (a) Radiation efficiency [Eq. (5.2)]. (b) TM_z and TE_z surface modes. 117

Figure 5.7 Comparison between the radiation efficiency behaviors and radiated powers for the grounded substrates of cases 1-5. (a) Radiation efficiency η. (b) Radiated power P_{rad}. 118

Figure 5.8 Spectral domain Green functions $\tilde{G}_{\mathrm{A}}^{xx}$ and $\tilde{G}_{\mathrm{A}}^{zx}$ for the isotropic substrate of case 1, limited in the range of $-21 < \log\left(\left|\tilde{G}_{\mathrm{A}}^{xx,zx}\right|\right) < 0$. (a) $\tilde{G}_{\mathrm{A}}^{xx}$. (b) $\tilde{G}_{\mathrm{A}}^{xx}$. 119

Figure 5.9 Spectral domain Green functions $\tilde{G}_{\mathrm{A}}^{xx}$ and $\tilde{G}_{\mathrm{A}}^{zx}$ for the anisotropic substrate of case 5, limited in the range of $-21 < \log\left(\left|\tilde{G}_{\mathrm{A}}^{xx,zx}\right|\right) < 0$. (a) $\tilde{G}_{\mathrm{A}}^{xx}$. (b) $\tilde{G}_{\mathrm{A}}^{xx}$. 120

Figure 5.10 $\tilde{G}_{\mathrm{A}}^{zx}/(\mu_\rho/\mu_0)$, limited in the range of $-21 < \log\left(\left|\tilde{G}_{\mathrm{A}}^{xx,zx}\right|\right) < 0$. 120

Figure 5.11 Drude permittivity along the z axis, ε_z, and Lorentz permeability in the ρ plane μ_ρ of the dispersive uniaxially anisotropic substrate with $\varepsilon_r = 6.15$, $\zeta_{\mathrm{e}} = 0$, $F = 0.56$, $\zeta_{\mathrm{m}} = 0$, and $\omega_{\mathrm{pe}} = \omega_{\mathrm{pm}} = 1$ GHz. 122

Figure 5.12 Response to an infinitesimal horizontal dipole on the dispersive uniaxially anisotropic grounded substrate (Fig. 5.1a) versus the electrical thickness of the substrate. (a) Radiation efficiency [Eq. (5.2)]. (b) TM_z and TE_z surface modes. 123

Figure 5.13 Comparison between the radiation efficiency behaviors of the isotropic grounded (case 1) and the dispersive anisotropic substrates. 124

Figure 7.1 PEMC waveguide. (a) $Y = \infty$ (PEC). (b) $Y = 1.5$ (PEMC). Taken from "Possible applications of perfect electromagnetic conductor (PEMC) media," in Proc. EuCap, 2006, by A. Sihvola and I. V. Lindell. ©2006 IEEE 131

Figure 7.2 A horizontal antenna above the ground plane. (a) The antenna is very close to the ground plane. (a) The antenna is placed at a quarter-wavelength distance from the ground plane. (b) The antenna above and close to the grounded-ferrite PMC boundary (proposed antenna gain-enhancement solution). 133

Figure 7.3 10 prototypes of printed half-wavelength dipole on a grounded substrate of RT/Duroid 6006 with $\varepsilon_{\rm rd} = 6.15$ and $d = 2.5$ mm. 134

Figure 7.4 Wire-ferrite medium substrate. 137

Figure 7.5 Effective constitutive parameters of the wired-ferrite substrate supporting the patch antenna (Fig. 7.4) with $r_1 = 0.35$ mm, $r_2 = 0.11$ mm, $p = 4.1$ mm, $\mathbf{H}_0 = 1382$ G and a ferrite host medium with the saturation magnetization of $4\pi \mathrm{M_s} = 1600$ G, line width of $\triangle H = 5$ Oe, $\varepsilon_{\rm f} = 14.6$ and $t = 1$ mm. (a) Theoretical (Dewar, 2005) effective permeability and permittivity (f_p^{ε} as the plasma frequency of the Drude permittivity). (b) Full-wave simulated and theoretical effective refractive index. 138

Figure 7.6 Comparison between the bandwidth of a patch antenna on the 1) wire-ferrite structure (Fig. 7.4), 2) its effective medium (Fig. 7.5a) and 3) a conventional dielectric substrate with the same refractive index (Fig. 7.5b), achieved by the full-wave simulation. 139

Figure A.1 Ray-optics representation of surface-wave and leaky-wave modes propagation in a dielectric slab. (a) Surface-wave modes. (b) Leaky-wave Modes. 152

Figure A.2 TM_z dispersion curves for an isotropic grounded slab with $\varepsilon_{\rm d} = 2\varepsilon_0$, $\mu_{\rm d} = \mu_0$. (a) $\mathrm{Re}(k_\rho^{\mathrm{TM}_z}/k_0^{\mathrm{TM}_z})$. (b) $\mathrm{Im}(k_\rho^{\mathrm{TM}_z}/k_0^{\mathrm{TM}_z})$. (c) $\mathrm{Re}(k_{z0}^{\mathrm{TM}_z}/k_0^{\mathrm{TM}_z})$. (d) $\mathrm{Im}(k_{z0}^{\mathrm{TM}_z}/k_0^{\mathrm{TM}_z})$. 153

Figure A.3 TE_z dispersion curves for an isotropic grounded slab with $\varepsilon_{\rm d} = 2\varepsilon_0$, $\mu_{\rm d} = \mu_0$. (a) $\mathrm{Re}(k_\rho^{\mathrm{TE}_z}/k_0^{\mathrm{TE}_z})$. (b) $\mathrm{Im}(k_\rho^{\mathrm{TE}_z}/k_0^{\mathrm{TE}_z})$. (c) $\mathrm{Re}(k_{z0}^{\mathrm{TE}_z}/k_0^{\mathrm{TE}_z})$. (d) $\mathrm{Im}(k_{z0}^{\mathrm{TE}_z}/k_0^{\mathrm{TE}_z})$. 154

LIST OF APENDICES

Appendix A Definition of Proper and Improper Modes in a Dielectric Slab 150

Appendix B Spectral Domain Transmission-Line Modeling of a Uniaxially Anisotropic Medium 155

Appendix C Computation of the Radiation Efficiency of a Horizontal Infinitesimal Dipole on an Isotropic Substrate 169

Appendix D Relation between $\tilde{I}'_{\text{sub}}$ and $\tilde{I}_{\text{sub}}$ 173

Appendix E Computation of the Radiation Efficiency of a Horizontal Infinitesimal Dipole on a Uniaxially Anisotropic Substrate 174

Appendix F List of Publications and Awards 178

LIST OF ABREVIATIONS AND NOTATIONS

Abbreviations

AMC	Artificial Magnetic Conductor
CRLH	Composite Right/Left-Handed
EBG	Electromagnetic Band-Gap
GSM	Generalized Scattering Matrix
LHCP	Left-Handed Circularly Polarized
PEC	Perfect Electric Conductor
PEMC	Perfect Electromagnetic Conductor
PMC	Perfect Electric Conductor
RHCP	Right-Handed Circularly Polarized
SRR	Split Ring Resonator
TEM	Transverse Electric Magnetic
TE	Transverse Electric
TM	Transverse Magnetic

Symbols

c	Speed of light in the vacuum
λ_0	Free-space wavelength
$\lambda_{\text{eff}}^{\text{cutoff}}$	Effective wavelength at the TM_z and TE_z cutoffs
ε_0	Free-space permittivity
ε_{r}	Dielectric constant
ε	Permittivity
$\bar{\bar{\varepsilon}}_{\text{r}}$	Dielectric constant tensor
$\bar{\bar{\varepsilon}}$	Permittivity tensor
ε_z	Permittivity along the z axis
ε_ρ	Permittivity in the ρ plane
ε_{h}	Host medium permittivity
ε_{eff}	Effective permittivity
$\bar{\bar{\varepsilon}}_{\text{eff}}$	Effective permittivity tensor
ε_{p}	Plasma permittivity
μ_0	Free-space permeability
μ_{r}	Magnetic constant
μ	Permeability
$\bar{\bar{\mu}}_{\text{r}}$	Magnetic constant tensor
$\bar{\bar{\mu}}$	Permeability tensor
μ_z	Permeability along the z axis
μ_ρ	Permeability in the ρ plane
μ_{h}	Host medium permeability
μ_{eff}	Effective permeability
$\bar{\bar{\mu}}_{\text{eff}}$	Effective permeability tensor
μ_e	Ferrite isotropic-effective permeability
$\mu_{e\pm}$	RHCP/LHCP effective relative permeabilities
χ_{e}	Electric susceptibility
$\mathbf{P}_{\text{e}}$	Electric polarization density
$\bar{\bar{\chi}}_{\text{e}}$	Electric susceptibility tensor
χ_{m}	Magnetic susceptibility
$\mathbf{P}_{\text{m}}$	Magnetic polarization density
$\bar{\bar{\chi}}_{\text{m}}$	Magnetic susceptibility tensor
ω	Angular Frequency
ω_{pe}	Electric plasma frequency

ω_{pm}	Magnetic plasma frequency
ω_0	Ferromagnetic resonance
F	Unit-cell fractional volume
Y	PEMC admittance
$\mathbf{H}_0$	Magnetic bias field
ΔH	Line width
γ	Gyromagnetic ratio
M_s	Saturation magnetization
Γ_+	RHCP reflection coefficient
Γ_-	LHCP reflection coefficient
$S_\pm$	RHCP/LHCP total scattering matrix
$T_\pm$	RHCP/LHCP transmission matrix
$T_{f\pm}$	RHCP/LHCP ferrite transmission matrix
$\mathbf{k}_f$	Propagation vector in the ferrite
$k_\rho^{\mathrm{TM}_z,\mathrm{TE}_z}$	$\mathrm{TM}_z/\mathrm{TE}_z$ transverse wave number
$k_z^{\mathrm{TM}_z,\mathrm{TE}_z}$	$\mathrm{TM}_z/\mathrm{TE}_z$ longitudinal wave number
k_x	Wave number along the x axis
k_y	Wave number along the y axis
$\beta_z^{\mathrm{TM}_z}$	TM_z phase constants along the z axis
$\beta_z^{\mathrm{TE}_z}$	TE_z phase constants along the z axis
$k_{z0}^{\mathrm{TM}_z}$	TM_z free-space longitudinal wave number
$k_{z0}^{\mathrm{TE}_z}$	TE_z free-space longitudinal wave number
$Z_c^{\mathrm{TM}_z}$	TM_z dielectric characteristic impedance
$Z_c^{\mathrm{TE}_z}$	TM_z dielectric characteristic impedance
$Z_{c0}^{\mathrm{TM}_z}$	TM_z free-space characteristic impedance
$Z_{c0}^{\mathrm{TE}_z}$	TE_z free-space characteristic impedance
Z_L^{TE}	TE_z load impedance
Z_L^{TM}	TM_z load impedance
J_z	Electric point source along z
J_x	Electric point source along x
J_{s}	Source dipole
J'_{sub}	Substrate dipole
$\tilde{V}$	Spectral domain voltage of the equivalent transmission line
$\tilde{I}$	Spectral domain current along the equivalent transmission line
$\tilde{I}_{\mathrm{eq}}$	Equivalent current
$\tilde{I}_{\mathrm{sub}}$	Transmission-line equivalent substrate current

$\mathbf{E}$	Electric field
$\mathbf{H}$	Magnetic field
$\mathbf{D}$	Electric flux density
$\mathbf{B}$	Magnetic flux density
$\bar{\bar{G}}_{\mathrm{A}}$	Spectral-domain magnetic vector potential dyadic Green function
$\tilde{G}_{\mathrm{A}}^{zz}$	Spectral-domain magnetic vector potential long the z axis due to J_z
$\tilde{G}_{\mathrm{A}}^{xx}$	Spectral-domain magnetic vector potential long the x axis due to J_x
$\tilde{G}_{\mathrm{A}}^{zx}$	Spectral-domain magnetic vector potential long the z axis due to J_x
$\tilde{G}_{\mathrm{EJ}}^{xz,\mathrm{TM}_z}$	TM_z electric field Green function along the x axis due to J_z
$\tilde{G}_{\mathrm{EJ}}^{zz,\mathrm{TM}_z}$	TM_z electric field Green function along the z axis due to J_z
$\tilde{G}_{\mathrm{HJ}}^{xz,\mathrm{TM}_z}$	TM_z magnetic field Green function along the x axis due to J_z
$\tilde{G}_{\mathrm{HJ}}^{\mathrm{zz},\mathrm{TM}_z}$	TM_z magnetic field Green function along the z axis due to J_z
$\tilde{G}_{\mathrm{EJ}}^{xx,\mathrm{TM}_z,\mathrm{TE}_z}$	$\mathrm{TM}_z/\mathrm{TE}_z$ electric field Green function along the x axis due to J_x
$\tilde{G}_{\mathrm{EJ}}^{zx,\mathrm{TM}_z,\mathrm{TE}_z}$	$\mathrm{TM}_z/\mathrm{TE}_z$ electric field Green function along the z axis due to J_x
$\tilde{G}_{\mathrm{HJ}}^{xx,\mathrm{TM}_z,\mathrm{TE}_z}$	$\mathrm{TM}_z/\mathrm{TE}_z$ magnetic field Green function along the x axis due to J_x
$\tilde{G}_{\mathrm{HJ}}^{\mathrm{zx},\mathrm{TM}_z,\mathrm{TE}_z}$	$\mathrm{TM}_z/\mathrm{TE}_z$ magnetic field Green function along the z axis due to J_x
P_{tot}	Total power
P_{loss}	Loss power
P_{ref}	Reflected power due to mismatch
P_{diel}	Dissipated power due to dielectric loss
P_{metal}	Dissipated power due to metallic loss
P_{mat}	Dissipated power due to material loss
P_{rad}	Radiated power
P_{sw}	Surface-wave power
η	Radiation efficiency
$\mathbf{S}_{\mathrm{rad,av}}$	Radiated time-averaged Poynting vector
$\mathbf{S}_{\mathrm{sw,av}}$	Surface-wave time-averaged Poynting vector

CHAPTER 1

INTRODUCTION

1.1 Definitions and Basic Concepts

Anisotropic materials are structures which exhibit different properties in different directions. Anisotropic materials may be natural with intrinsic anisotropic properties or they may be artificially designed with specific anisotropic characteristics for specific applications. In the following, the anisotropy in the natural and artificial materials and substrates, along with some of their applications, are explained.

1.1.1 Natural Anisotropic Materials

Electric Anisotropy

When an external electric field $\mathbf{E}$ propagates through a dielectric material it induces electric dipole moments, $\mathbf{p}_{\mathrm{e}} = \alpha_{\mathrm{e}}\mathbf{E}$, in the material, where α_{e} is the electric polarizability of the atom or molecule and defines the response of the charge distribution of the atom or molecule to the applied field. The average of the dipole moments in the material defines the material electric polarization $\mathbf{P}_{\mathrm{e}}$. In a homogeneous, linear and isotropic material, the polarization is aligned with and proportional to the electric field $\mathbf{E}$,

$$\mathbf{P}_{\mathrm{e}} = \varepsilon_0 \chi_{\mathrm{e}} \mathbf{E}, \tag{1.1}$$

where ε_0 is the free-space permittivity, and χ_{e} is the electric susceptibility of the medium related to the average of the polarizabilities in the medium volume. However, in an electrically anisotropic material, the electric field and the induced polarization are not in the same direction and therefore

$$\mathbf{P}_{\mathrm{e}} = \varepsilon_0 \bar{\bar{\chi}}_{\mathrm{e}} \cdot \mathbf{E}, \tag{1.2}$$

where $\bar{\bar{\chi}}_{\mathrm{e}}$ is the electric susceptibility tensor of the medium. In this case, the electric polarization in the $i-$direction $P_{\mathrm{e,i}}$ is induced by the $j-$direction electric field E_{j}, as expressed in the following relation

$$P_{\mathrm{e},i} = \sum_j \varepsilon_0 \chi_{\mathrm{e},ij} E_j, \tag{1.3}$$

where $\chi_{e,ij}$ is the ij component of the electric susceptibility tensor $\bar{\bar{\chi}}_e$ of the medium [1]. This equation demonstrates that in anisotropic materials, the induced polarization and the electric field are not necessarily aligned.

The electric polarization and the electric field define the electric flux density $\mathbf{D}$ as follows

$$\mathbf{D} = \varepsilon_0 \mathbf{E} + \mathbf{P}_e. \tag{1.4}$$

By substituting the polarization $\mathbf{P}_e$ of isotropic materials from (1.1) into (1.4), this equation reduces to

$$\begin{aligned} \mathbf{D} &= \varepsilon_0 \varepsilon_r \mathbf{E} \\ &= \varepsilon \mathbf{E}, \end{aligned} \tag{1.5}$$

where $\varepsilon_r = 1 + \chi_e$ and ε are the dielectric constant and the permittivity of the isotropic material, respectively. For anisotropic materials, substituting (1.2) into (1.4), results in

$$\begin{aligned} \mathbf{D} &= \varepsilon_0 \bar{\bar{\varepsilon}}_r \cdot \mathbf{E} \\ &= \bar{\bar{\varepsilon}} \cdot \mathbf{E}, \end{aligned} \tag{1.6}$$

where $\bar{\bar{\varepsilon}}_r = 1 + \bar{\bar{\chi}}_e$ and $\bar{\bar{\varepsilon}}$ are the dielectric constant and the permittivity tensors of the anisotropic material, respectively, with

$$\bar{\bar{\varepsilon}} = \begin{pmatrix} \varepsilon_{xx} & \varepsilon_{xy} & \varepsilon_{xz} \\ \varepsilon_{yx} & \varepsilon_{yy} & \varepsilon_{yz} \\ \varepsilon_{zx} & \varepsilon_{zy} & \varepsilon_{zz} \end{pmatrix}, \tag{1.7}$$

where ε_{ij} ($i, j = x, y$ or z) is the ij component of the permittivity tensor. The tensor $\bar{\bar{\varepsilon}}$ shows that in an electrically anisotropic material, the electric response of the medium to the applied electric field is different in the different x, y and z directions.

Crystals and ionized gases are examples of materials which exhibit electrical anisotropic characteristics [2, 3, 4]. Specially, ferroelectric materials which are inherently anisotropic due to their crystalline structure [5, 6, 7, 8] have several applications at microwave frequencies [9].

Magnetic Anisotropy

A magnetic field $\mathbf{H}$ applied to a magnetic material may align the magnetic dipoles in the material which are oriented in random directions and therefore produce a magnetic polarization $\mathbf{P}_{\mathrm{m}}$ which for linear isotropic materials reads

$$\mathbf{P}_{\mathrm{m}} = \mu_0 \chi_{\mathrm{m}} \mathbf{H}, \tag{1.8}$$

while for the anisotropic materials it yields

$$\mathbf{P}_{\mathrm{m}} = \mu_0 \bar{\bar{\chi}}_{\mathrm{m}} \cdot \mathbf{H}, \tag{1.9}$$

where μ_0, χ_{m} and $\bar{\bar{\chi}}_{\mathrm{m}}$ are the free-space permeability, the magnetic susceptibility of the isotropic material, and the magnetic susceptibility tensor of the anisotropic material, respectively. Equation (1.9) shows that as opposed to isotropic magnetic materials, in the anisotropic materials the magnetic polarization is not aligned with the magnetic field and an $i-$direction magnetic polarization $P_{\mathrm{m},i}$ is related to a $j-$direction magnetic field H_{j} through the following relation

$$P_{\mathrm{m},i} = \sum_j \mu_0 \chi_{\mathrm{m},ij} H_j, \tag{1.10}$$

where $\chi_{\mathrm{m},ij}$ is the ij component of the magnetic susceptibility tensor $\bar{\bar{\chi}}_{\mathrm{m}}$ of the medium.

The magnetic flux density $\mathbf{B}$ is related to the magnetic polarization and the magnetic field by the following expression

$$\mathbf{B} = \mu_0 \mathbf{H} + \mathbf{P}_{\mathrm{m}}. \tag{1.11}$$

By substituting $\mathbf{P}_{\mathrm{m}}$ of the isotropic materials from (1.8) into the above equation, this expression reduces to

$$\begin{aligned} \mathbf{B} &= \mu_0 \mu_{\mathrm{r}} \mathbf{H} \\ &= \mu \mathbf{H}, \end{aligned} \tag{1.12}$$

where $\mu_{\mathrm{r}} = 1 + \chi_{\mathrm{m}}$ and μ are the magnetic constant and the permeability of the isotropic

material, respectively. For the anisotropic materials, substituting (1.9) into (1.11) results in

$$\begin{aligned} \mathbf{B} &= \mu_0 \bar{\bar{\mu}}_{\mathrm{r}} \cdot \mathbf{H} \\ &= \bar{\bar{\mu}} \cdot \mathbf{H}, \end{aligned} \tag{1.13}$$

where $\bar{\bar{\mu}}_{\mathrm{r}}$ and $\bar{\bar{\mu}}$ are the magnetic constant and permeability tensors of the anisotropic material, respectively, and

$$\bar{\bar{\mu}} = \begin{pmatrix} \mu_{xx} & \mu_{xy} & \mu_{xz} \\ \mu_{yx} & \mu_{yy} & \mu_{yz} \\ \mu_{zx} & \mu_{zy} & \mu_{zz} \end{pmatrix}, \tag{1.14}$$

where $\mu_{ij}(i, j = x, y \text{ or } z)$ is the ij component of the permeability tensor. $\bar{\bar{\mu}}$ shows that in a magnetically anisotropic material, the magnetic response of the medium to the applied magnetic field is different in the different directions.

Ferrimagnetic materials, such as ferrites are the most practical natural anisotropic magnetic materials used in microwave engineering. Their magnetic anisotropy is induced by an applied DC magnetic bias field which aligns the magnetic dipole moments in the material, causing them to precess at a frequency which is controlled by the strength of the bias field. A microwave field which is circularly polarized in the direction of the precession of the dipole moments interacts strongly with them, while a field that is oppositely polarized interacts less strongly. Since the right-handed and left-handed circularly polarizations are defined as functions of the direction of propagation, fields propagating in opposite directions will have opposite polarizations. Therefore, when they propagate through a ferrimagnetic material in opposite directions they have different behaviors which is called non-reciprocity. This effect can be used in the design of nonreciprocal devices such as isolators, circulators and gyrators. Another characteristic of ferrimagnetic materials is their tunability by changing the applied DC bias field, since the ferrite interaction with the microwave field can be controlled by adjusting the strength of the bias field. This behavior leads to tunable devices such as phase shifters, switches, resonators and filters [2, 10].

1.1.2 Artificial Anisotropic Materials

Artificial Materials

Artificial materials are composite structures constituted of various types of sub-wavelength metallic, dielectric or magnetic implants in a host medium. An external applied field illumi-

nating the artificial materials induces electric or magnetic current dipoles on the implants. Each dipole emulates the behavior of an atom or a molecule in natural materials in that it exhibits a dipole moment as explained in Sec. 1.1.1. Since the implants are sub-wavelength the combined effect of the implants produces a net average electric or magnetic dipole polarization $\mathbf{P}_{\mathrm{e,m}}$ per unit volume. This results in effectively altering the macroscopic properties of the medium leading to an effective permittivity and permeability [11, 12, 13]. Due to the diversity of possible implants, synthesis of a wide variety of macroscopic effective material properties is possible. Specially, the properties not readily available in nature such as negative refractive index [14], bi-isotropy, bi-anisotropy and chirality [1] [15], may be achieved by special design of artificial materials, which in this case, are also known *metamaterials* [16, 17]. These properties expand the range of available material characteristics, which opens up a new horizon for microwave engineers to design novel microwave devices.

In the literature, if artificial structures exhibit effective electric properties due to their implants, they are called *artificial dielectrics*, while if it shows effective magnetic characteristics it is called *artificial magnetic material*. An artificial material may have both effective electric and magnetic properties in which case it is called *magneto-dielectric*. In this document, we follow the same terminology to designate artificial dielectric, magnetic or magneto-dielectric structures.

One of the first artificial dielectric was suggested by Kock, in 1946. This structure was designed to be used as a lens for overcoming the excessive weight of the convectional lenses [18, 19]. As shown in Fig. 1.1, this structure consists of metallic parallel plates acting as waveguides. The operation principle is based on the fact that the electromagnetic wave propagating between the plates experiences a higher phase velocity as compared to the propagation in free-space,

$$v = \frac{v_0}{1 - \sqrt{1 - (\frac{\lambda_0}{2a})^2}}, \tag{1.15}$$

where, v and v_0 are the phase velocities in the waveguides and in the air, respectively, and λ_0 and a are the free-space wavelength and the distance between the two metallic plates,

1. In bi-isotropic materials the electric and magnetic fields are coupled and an applied electric or magnetic field both polarizes and magnetizes the material. The constitutive relations for bi-isotropic materials reads $\mathbf{D} = \varepsilon_{\mathrm{r}}\varepsilon_0\mathbf{E} + \xi\mathbf{H}$ and $\mathbf{B} = \varsigma\mathbf{E} + \mu_{\mathrm{r}}\mu_0\mathbf{H}$ where ξ and ς are the coupling constants of the material. For a bi-anisotropic material ε_{r}, μ_{r}, ξ and ς are dependent on the direction and are tensorial. In the special case, where in a bi-isotropic material $\xi = -\varsigma = j\kappa\sqrt{\varepsilon_0\mu_0}$, the bi-isotropic material reduces to a chiral material and κ represents the chirality of the material [15].

respectively. This leads to an effective refractive index as follows

$$n = \frac{v_0}{v} = 1 - \sqrt{1 - (\frac{\lambda_0}{2a})^2}, \tag{1.16}$$

which is less than unity, and for a concave structure results in a focusing lens effect.

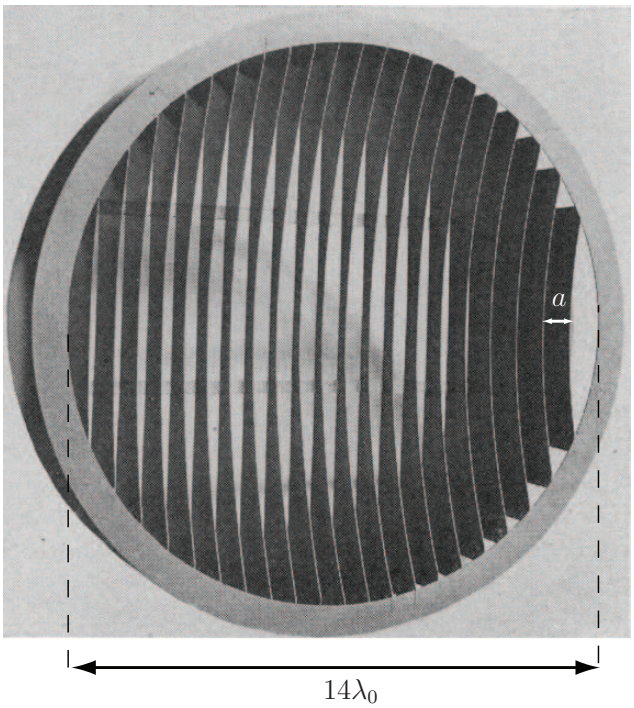

Figure 1.1 Concave metallic Kock lens. Taken from "Metal-lens antennas," *Proc. of IRE*, 1946, by W. E. Kock. ©1946 IEEE.

In 1949, Cohn presented an analytical study on metal-strip lens using a transmission line approach [20] and in 1950 he performed an experimental measurement to calculate the refractive index of the metallic lens media of Kock [21]. During the same period, Estrin calculated the effective permittivity and permeability of a three dimensional array of conducting disks [22], as illustrated in Fig. 1.2, and for this purpose, he calculated the induced electric and magnetic dipole moments of each disk for certain directions of applied electric and magnetic fields, using Maxwell equations. Moreover, he analyzed the anisotropic properties of this structure.

In 1960, Brown published a review on the previous works that had been done on artificial dielectrics [23]. He presented two types of classifications the artificial dielectrics. One category was according to the value of the refractive index of the artificial dielectrics: if the refractive index was greater than unity the structure was called *delay dielectric* and if the refractive index was less than unity it was named *path-advance dielectric*. The second category was

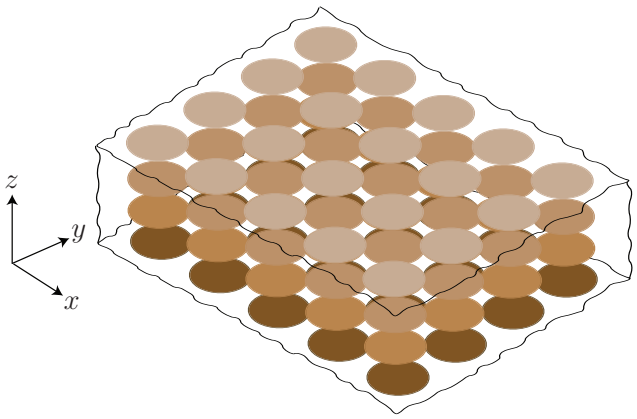

Figure 1.2 Three dimensional array of conducting disks, studied by Estrin. Adapted from "The effective permeability of an array of thin conducting disks," *J. Appl. Phys.* 1950, by G. Estrin.

according to the form of the structures constituting lattices of conducting elements. He also discussed several calculation methods for the refractive index of the artificial materials such as classical Lorentz theory and transmission-line method. Some applications of the artificial materials such as microwave lenses and polarization filters where considered in his paper.

In 1962, Rotman demonstrated that a special type of artificial dielectric called *rodded medium* exhibits electric plasma properties in the absence of DC magnetic fields [24]. The rodded medium attracted much attention due to its plasma permittivity and was extensively cited in many articles related to artificial materials. As illustrated in Fig. 1.3, this structure was composed of periodically spaced lattices of metallic rods, where an applied electric field parallel to the wires could interact with the wires leading to a plasma permittivity, also named Drude permittivity, along the axis of the wires as demonstrated in Fig. 1.4 and given by

$$\varepsilon_{\mathrm{p}} = \varepsilon_0 \left(1 - \frac{\omega_{\mathrm{pe}}^2}{\zeta_{\mathrm{pe}}^2 + \omega^2} + j\frac{\omega_{\mathrm{pe}}^2 \zeta_{\mathrm{pe}}/\omega}{\zeta_{\mathrm{pe}}^2 + \omega^2}\right), \tag{1.17}$$

where, ω_{pe} and ζ_{pe} are the plasma frequency and the collision frequency of the effective plasma artificial dielectric.

He analyzed the dispersion of the structure and calculated the propagation constant $\gamma_{\mathrm{p}} = \alpha_{\mathrm{p}} + j\beta_{\mathrm{p}} = j\omega\sqrt{\mu_0 \varepsilon_{\mathrm{p}}}$ of a lossy rodded medium with

$$\beta_{\mathrm{p}} = \frac{\omega}{c}\left[1 - (\frac{\omega_{\mathrm{pe}}}{\omega})^2\right]^{1/2}, \tag{1.18a}$$

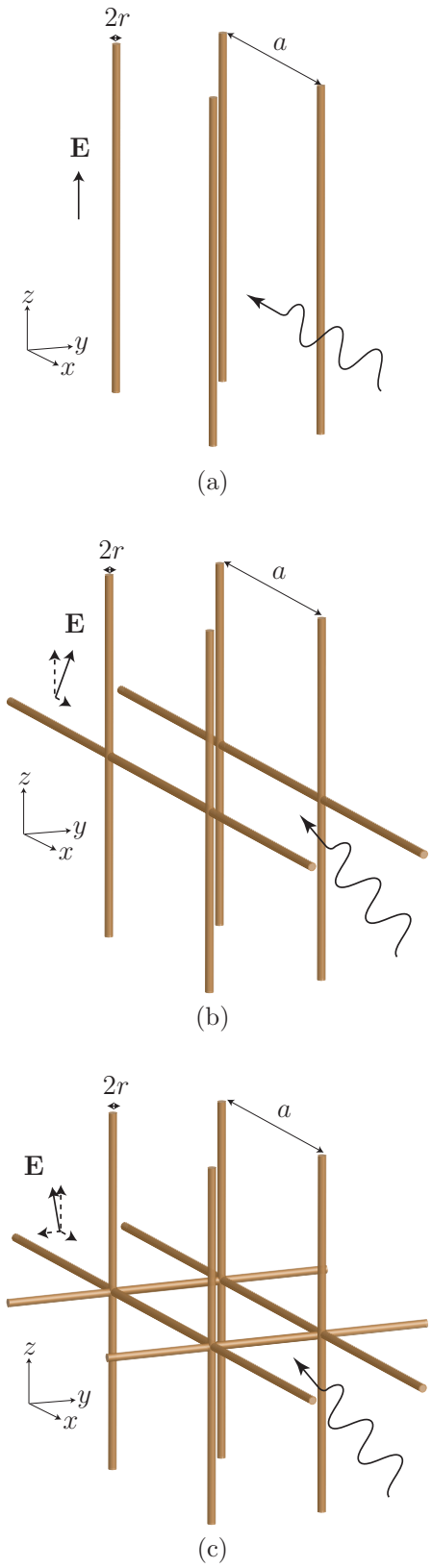

Figure 1.3 Rodded media. (a) One dimensional, (b) two dimensional and (c) three dimensional structures. Adapted from "Plasma simulation by artificial dielectrics and parallel-plate media," IRE Trans. Antennas Propagat., 1962, by W. Rotman.

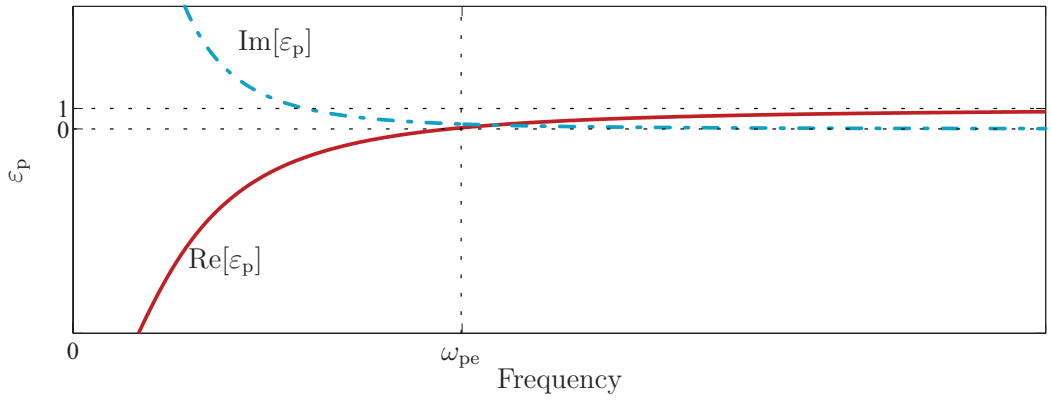

Figure 1.4 Plasma effective permittivity of the rodded medium of Rotman.

$$\alpha_p = \frac{\omega}{2c}\left\{\frac{\left(\frac{\omega_{pe}}{\omega}\right)^2\left(\frac{\zeta_{pe}}{\omega}\right)}{\left[1-\left(\frac{\omega_{pe}}{\omega}\right)^2\right]^{1/2}}\right\}, \tag{1.18b}$$

where, α_p and β_p are the attenuation constant and the phase constant of the effective material, respectively, and c is the speed of light in the vacuum. Moreover, he presented some of the applications of the rodded media such as gain enhancement of the radiation from an electric field aperture by a plasma slab cover.

During this period, several studies on the effect of artificial substrates on antenna patterns and beam shaping were carried out. For example, in 1965, Golden studied a horn aperture in an infinite ground plane covered with a plasma layer for beam shaping application [25] and in 1975, Bahl and Gupta studied the application of artificial dielectrics as a beam shaping element in a leaky-wave lens antenna [26, 27].

In 1990, Collin presented various analysis methods of the artificial dielectrics in his book [11]. He classified the analysis methods in three basic categories: the simplest approach is Lorentz theory, which considers only the dipole interaction between the electric and magnetic dipoles induced on the implants by the applied field, the second approach is a rigorous static field solution, and finally, the third method is rigorously solving the Maxwell equations.

In 1996, Pendry *et al.* showed a structure consisting of very thin infinitely long metallic wires arranged in a 3D cubic lattice that modelled the plasma response in the form of (1.17), with a negative effective permittivity below the plasma frequency in the gigahertz range [28]. Later, in 1998, he published a paper on the experimental validation of the theoretical analysis of this structure [29].

In 1999, Pendry *et al.* reported another study which was performed on artificial magnetic

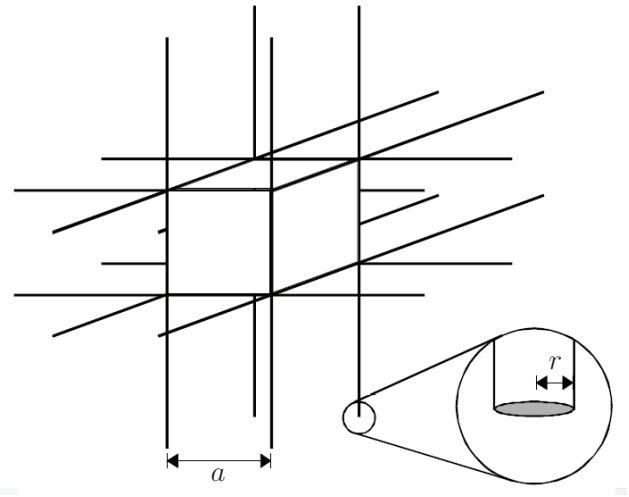

Figure 1.5 Artificial dielectric with plasma electric response in the gigahertz range, consisting of a 3D cubic lattice of very thin infinitely long metallic wires proposed by Pendry. Reprinted figure with permission from J.B. Pendry, A.J. Holden, W.J. Stewart and I. Youngs, Extremely low frequency plasmons in metallic mesostructures, *Phys. Rev. Lett.* 76 4773-6 and 1996. Copyright 1996 by the American Physical Society.

materials. This structure was constituted of non-magnetic conducting sheets which could provide effective magnetic permeability [30]. As demonstrated in Fig.1.6a, the basic structure was a square array of metallic cylinders. An applied magnetic field along the cylinders could result in an effective dispersive magnetic permeability along the axis of the cylinders in the form of

$$\mu_{\text{eff}} = 1 - \frac{\pi r^2}{a^2}\left[1 + j\frac{2\sigma}{\omega r \mu_0}\right]^{-1}, \tag{1.19}$$

where r, a and σ are the radius of the cylinders, the lattice constant and the resistance of the cylinder surface per unit area, respectively [30]. This structure showed a limited magnetic response. To extend the range of the magnetic properties, a capacitative element was added to the structure. The modified model was composed of arrays of two concentric metallic cylinders in the form of *split rings* which were separated from each other by a distance d as illustrated in Fig. 1.6b. In this configuration, the capacitance between the two cylinders, balances the inductance of the cylinders leading to a resonant structure and therefore a resonant effective permeability, known as a Lorentz-model permeability, as shown in Fig.1.7 and as expressed in

$$\mu_{\text{eff}} = 1 - \frac{F}{1 + \frac{j2\sigma}{\omega r \mu_0} - \frac{3}{\pi^2 \mu_0}\omega^2 C r^3}, \tag{1.20}$$

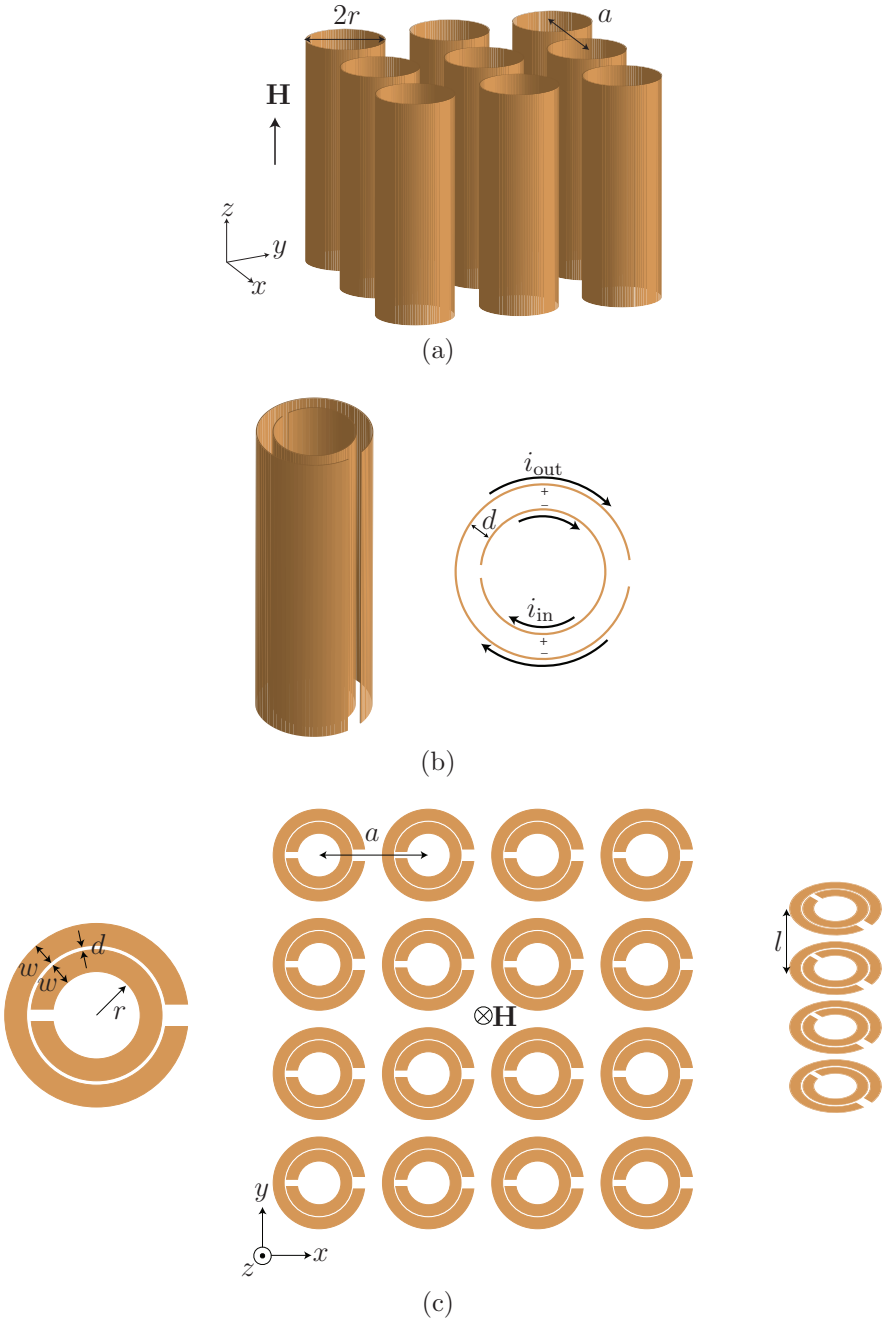

Figure 1.6 Artificial magnetic materials proposed by Pendry. (a) Arrays of non-magnetic conducting cylinders. (b) Modified cylinders with two concentric metallic cylinders in the form of split rings. (c) Printed split-ring unit-cell, its two dimensional array and its stacked configuration. Taken from "Magnetism from conductors and enhanced nonlinear phenomena," *IEEE Trans. Microwave Theory Tech.*, 1999, by J. B. Pendry *et al.*. ©1999 IEEE

where $F = \pi r^2/a^2$ is the fractional volume of the unit-cell occupied by the interior of the cylinder, and C is the capacitance per unit area between the two cylinders [30]. Next, in

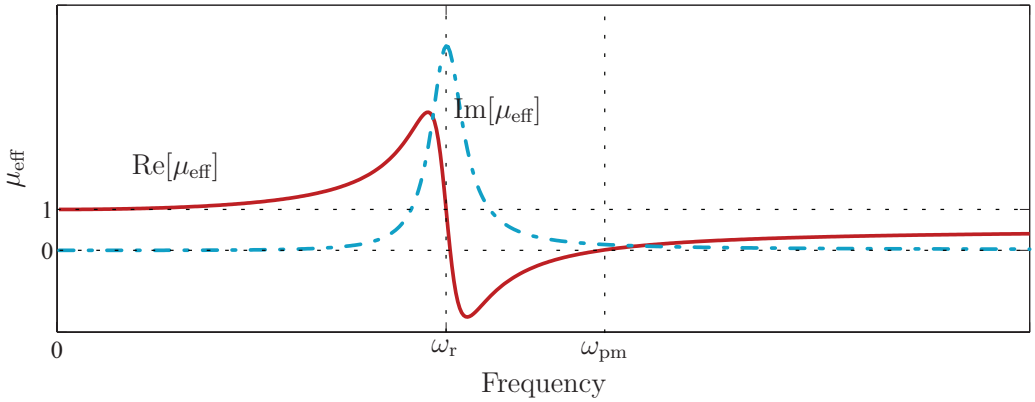

Figure 1.7 Resonant effective Lorentz permeability of the artificial magnetic material of Pendry.

order to make the structure more compact, the split-ring cylinder array was replaced by stacked arrays of printed split-ring configurations, but in a slightly modified form. The unit cell and its array are shown in Fig.1.6c. The split rings have an internal radius r, a width w, a separating gap d and are placed in arrays of period a. The arrays are placed in the xy plane while they are stacked along the z axis with the distance l. The magnetic field $\mathbf{H}$ is perpendicular to the plane of the rings. The effective permittivity of this structure reads [30]

$$\mu_{\text{eff}} = 1 - \frac{F}{1 + \frac{j2l\sigma_1}{\omega r \mu_0} - \frac{3l}{\pi^2 \mu_0}\omega^2 C_1 r^3}, \tag{1.21}$$

where, σ_1 is the resistance of unit length of the sheets measured around the circumference and C_1 is the capacitance between the unit length of two parallel sections of the metallic strips. As seen in the above equation, similar to the split-ring cylinders, the permeability of the stacked printed split-ring arrays exhibits a resonant behavior. Because of this property, this structure was later named *split ring resonators* (*SRR*) and it became the building block of several future magnetic and magneto-dielectric artificial materials [31, 32, 33].

Beside the reported studies on the analysis methods of artificial materials, in 1997, Ziolkowski published a paper on synthesis methods of various artificial dielectrics with different dispersion models of effective permittivity. In his approach, he assumed that the implants of the artificial dielectrics are electrically small dipole antennas loaded with passive electrical circuit elements and he showed how the different passive loads of the small antennas lead to different effective permittivity models [34].

In 2003, Tretyakov discussed various artificial electric and magnetic structures, their electromagnetic analysis methods and their applications in his book [12]. He proposed a modified model for a two dimensional array of infinite metallic wires named *wire medium* which was basically similar to the plasma medium of Pendry [28], and in his model he considered the anisotropy and the non-locality [35] of the structure. The structure is shown in Fig. 1.8 which is constituted of metallic wires with the radius r and period a. The wires are oriented along the z axis and the electric field $\mathbf{E}$ of the incident plane wave is along the axis of the wires z.

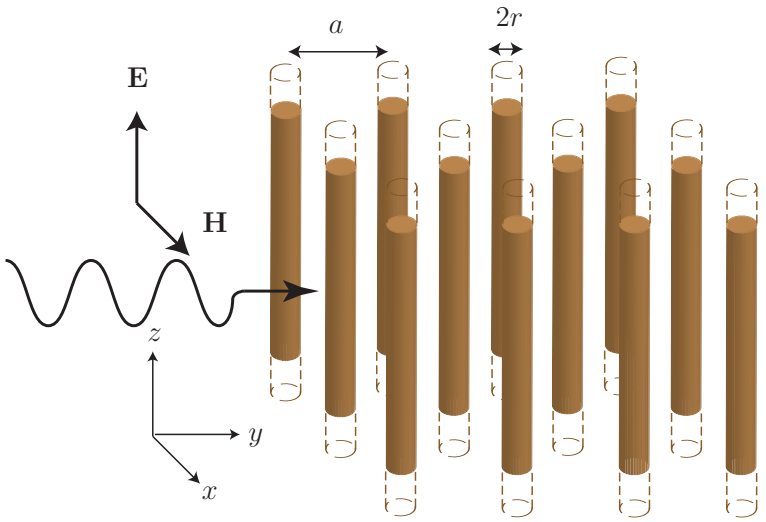

Figure 1.8 Wire medium constituted of two dimensional array of metallic wires. Adapted from *Analytical Modeling in Applied Electromagnetics*, *Artech House*, 2003, by S. A. Tretyakov.

In Tretyakov's work, it is demonstrated that the plasma permittivity model of Rotman and Pendry [Eq. (1.17)], for the two dimensional array of Fig. 1.8, is only accurate for the TEM plane-wave incidence, perpendicular to the axis of wires ($k_z = 0$). In this case, the electric field is perfectly parallel to the wires (E_z) and therefore there is no interaction between the wires. For a TM mode or an oblique plane-wave incidence, the electric field component in the plane perpendicular to the wires (E_x or E_y) causes the wires to interact and as a result the local permittivity model of (1.17) is not accurate anymore. Therefore, (1.17) was modified to a non-local model which considers the *spatial dispersion* in the structure as follows

$$\varepsilon_{\text{eff},z} = \varepsilon_0 \left(1 - \frac{k_{\text{p}}^2}{k^2 - q_z^2}\right), \tag{1.22}$$

where ε_z is the permittivity along the axis of wires z, $k = \omega^2 \mu_0 \varepsilon_{\text{h}}$ is the wave number of the host medium with ε_{h} as the permittivity of the host medium, q_z is the propagation constant

along the z axis and k_{p} represents the plasma frequency which reads [12]

$$k_{\mathrm{p}}^2 = \frac{2\pi}{a^2\left(\log\frac{a}{2\pi r} + 0.5275\right)}. \tag{1.23}$$

Following such basic researches and reports on artificial materials, their analysis and synthesis methods and their applications, there have been several studies on artificial materials by many research groups, where they analyzed various building blocks of artificial materials resulting in various novel applications in microwave [36].

Artificial Substrates

Whereas bulk artificial materials have been extensively studied in the past, as seen above, artificial materials in the form of substrates (also known as *meta-substrates*) are more recent. Due to the diversity of the implants that can be used for the realization of artificial substrates, they have a great potential for unique and novel microwave components, such as miniaturized antennas and microwave components, non-reciprocal devices or analog signal processors.

For example, in 2000, Hansen and Bruke demonstrated that magneto-dielectric substrates with effective permeability higher than one can contribute in the enhancement of the bandwidth of patch antennas [37]. This report inspired several groups to study the application of various magneto-dielectric substrates in the enhancement of antenna properties [32, 33, 38, 39, 40]. In parallel, many other types of artificial substrates such as negative refractive index substrates [41, 42, 43] and their various applications such as full-space scanning leaky-wave antennas [41, 42], microwave device miniaturization [44, 45, 46] and delay lines for analog signal processing [47] were proposed.

Anisotropic Artificial Substrates

In most artificial materials, the electromagnetic effect of the implants in the host medium and its interaction with the applied field is not the same in all directions, and therefore, the composite materials usually exhibit anisotropic behavior [12, 22, 30]. This effect is even more pronounced in the artificial substrates since due to their planar structure, the implants are usually arranged in a two-dimensional configuration which prevents the structure from an isotropic response to the applied electric field as opposed to the three-dimensional configurations (e.g. the 3D thin wire array proposed by Pendry and shown in Fig. 1.5 [28]). The anisotropy of artificial materials can be controlled by the properties of the implants and provides some additional degrees of freedom in the design of microwave components, leading to novel applications and devices.

As mentioned in Sec. 1.1.2, the wire medium is an example of artificial materials which exhibit electrically anisotropic properties [12]. The electric field along the axis of the wires z (Fig. 1.8) interacts with the wires leading to an effective permittivity in the form of (1.22), while the permittivity along the x and y axes remains as the permittivity of the host medium ε_{h}. Therefore, the permittivity of the medium exhibits a uniaxial tensorial behavior as

$$\bar{\bar{\varepsilon}}_{\mathrm{eff}} = \begin{pmatrix} \varepsilon_{\mathrm{h}} & 0 & 0 \\ 0 & \varepsilon_{\mathrm{h}} & 0 \\ 0 & 0 & \varepsilon_{\mathrm{eff},z} \end{pmatrix}, \tag{1.24}$$

where $\bar{\bar{\varepsilon}}_{\mathrm{eff}}$ is the permittivity tensor of the anisotropic artificial dielectric and $\varepsilon_{\mathrm{eff},z}$ is the effective permittivity in the form of (1.22) along the z axis.

Embedding metallic wires or drilling vias in a dielectric substrate, as shown in Fig. 1.9, resembles the same effective electrical behavior as the wire medium (Fig. 1.8) [48].

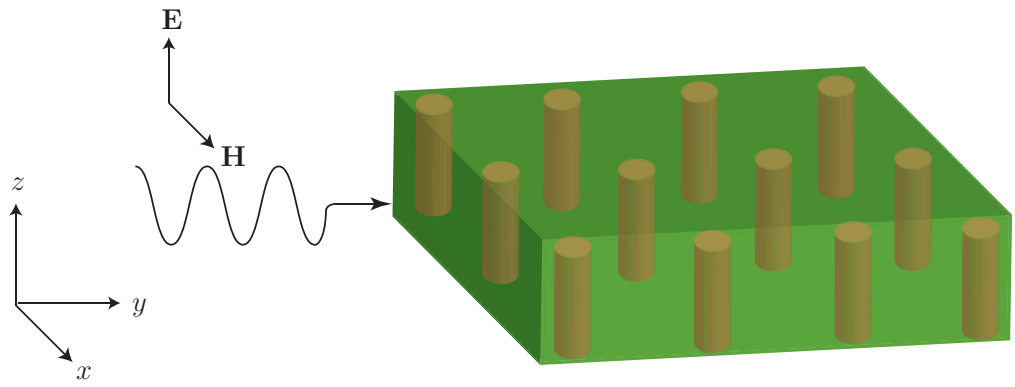

Figure 1.9 Wire medium in the form of embedding metallic wires or drilling vias in a dielectric substrate.

This substrate has found many applications in microwave, such as miniaturization of microwave components [44, 45, 46] and delay lines for analog signal processing [47]. However, in most of these structures, the anisotropy of the structure was not taken into account [44, 45, 47]

A stack of two-dimensional arrays of split ring resonators (SRRs) [30] embedded in a substrate exhibits a magnetically anisotropic response.

As shown in Fig. 1.10a, a magnetic field along the z axis, which is perpendicular to the plane of the rings, xy, interacts with the rings and therefore alters the permeability of the medium along the perpendicular axis to the rings z. However the permeability along the other axes remain the same as the permeability of the host medium μ_{h}. Therefore, the effective

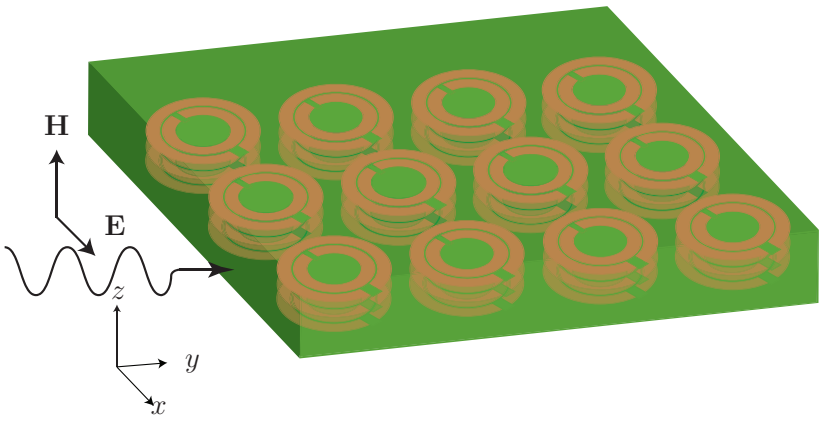

(a)

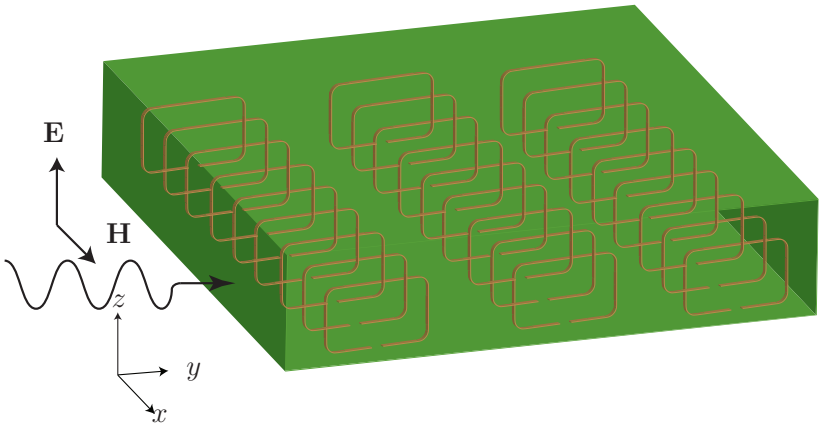

(b)

Figure 1.10 A stack of two-dimensional arrays of split ring resonators (SRRs) embedded in a substrate. (a) SRRs in the xy plane. (b) SRRs in the yz plane.

permeability tensor $\bar{\bar{\mu}}_{\text{eff}}$ of the artificial magnetic structure becomes uniaxially anisotropic, expressed as follows

$$\bar{\bar{\mu}}_{\text{eff}} = \begin{pmatrix} \mu_{\text{h}} & 0 & 0 \\ 0 & \mu_{\text{h}} & 0 \\ 0 & 0 & \mu_{\text{eff},z} \end{pmatrix}, \tag{1.25}$$

where $\mu_{\text{eff},z}$ is the effective magnetic permeability induced by the applied magnetic field along the axis z in the form of (1.21). For a non-magnetic host medium $\mu_{\text{h}} = \mu_0$.

By changing the configuration of the embedded rings in the substrate, the substrate exhibits different anisotropic behaviors. For example, if the rings are embedded in the substrate with their plane in the yz plane as shown in Fig. 1.10b, the effective permeability of

the anisotropic magnetic material will change to

$$\bar{\bar{\mu}}_{\text{eff}} = \begin{pmatrix} \mu_{\text{eff},x} & 0 & 0 \\ 0 & \mu_{\text{h}} & 0 \\ 0 & 0 & \mu_{\text{h}} \end{pmatrix}, \tag{1.26}$$

where $\mu_{\text{eff},x}$ is the effective magnetic permeability induced by the applied magnetic field along the axis x in the form of (1.21). This structure has been studied by several groups for the enhancement of the properties of planar antennas [32, 39], however in some of these studies such as [39], the anisotropy of the structure was not taken into account in the analysis.

The mushroom structure is an example of magneto-dielectric materials which exhibit both electric and magnetic anisotropic properties [49]. As shown in Fig. 1.11, the structure is composed of a two-dimensional array of metallic wires in the form of drilled vias with patches on top [50]. A propagating wave, with the electric field along the axis of the wires z, interacts with the wires, and by inducing currents on the wires, it changes the effective permittivity along the axis of the wires in the form of (1.22). A propagating wave, with the magnetic field in the plane of the substrate xy (ρ plane) induces currents in the form of a loop between each two adjacent mushrooms, which results in altering the permeability of the material along the perpendicular axis to the wires, x and y, in the form of (1.21). Therefore the mushroom structure exhibits a tensorial permittivity similar to (1.24) and a tensorial permeability as follows

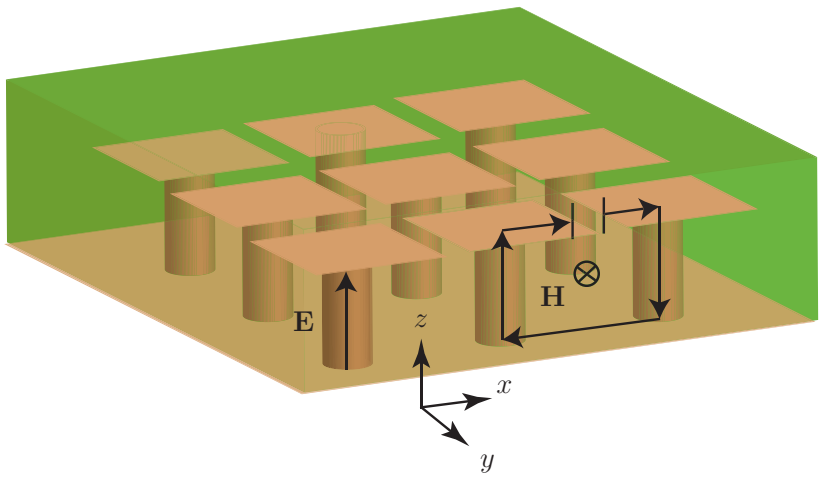

Figure 1.11 Mushroom-type magneto-dielectric anisotropic substrate.

$$\bar{\bar{\mu}}_{\text{eff}} = \begin{pmatrix} \mu_{\text{eff},\rho} & 0 & 0 \\ 0 & \mu_{\text{eff},\rho} & 0 \\ 0 & 0 & \mu_0 \end{pmatrix}, \tag{1.27}$$

where, $\mu_{\text{eff},\rho}$ is the effective permeability along the ρ axis due to the presence of the current loops on the adjacent mushrooms.

An application of the anisotropic mushroom structure is the realization of composite right/left-handed (CRLH) substrates. In this case, a uniform microstrip line printed on the mushroom-type substrate demonstrates full-space scanning leaky-wave properties [49] similar to the conventional printed CRLH circuits on dielectric substrates [16].

1.2 Motivations, Objectives, Contributions and Organization of the Thesis

1.2.1 Motivations, Objectives and Contributions

Intense research in the past years has led to several unique artificial materials and their innovative applications in the field of microwaves. The basic properties that have made artificial materials and substrates pioneering in the design of novel microwave devices are as follows: First, as demonstrated in Sec.1.1, artificial materials have the potential of providing the electromagnetic properties that are not available in the nature. For example, the permittivity of the wire-medium substrate [Eq. (1.22)] becomes less than one right above the plasma frequency [12] while it is negative below the plasma frequency, in the microwave region. In addition, the mushroom-type substrate demonstrates negative refractive index in the frequency band where both the wire-medium effective permittivity [Eq. (1.22)] and the current loops effective permeability [Eq. (1.21)] become negative [41, 42, 49]. This characteristic could only be achieved by an artificial material. Second, since the effective permittivity and permeability of the artificial structures are functions of the dimensions of the implants, their periodicity, and their orientation, the effective properties of the artificial substrates can be controlled by the properties of the implants and their arrangements in the substrates. This is evident in the effective permittivity expressions of (1.22) and (1.23), for the wire-medium substrate of Fig. 1.9, and in the effective permeability equation of (1.21) for the split ring resonator substrate of Fig. 1.10. As a result of these unique properties, artificial substrates enable specific properties for specific applications which leads to novel microwave components and applications.

Additionally, the anisotropy of anisotropic artificial substrates may provide additional degrees of freedom in the design of microwave components. This is because the property of

the substrate is different in the different directions and therefore, the electromagnetic wave interacts differently with the material in the different directions which may lead to several unique applications. As an example, let us consider the wire-medium substrate of Fig. 1.9. The TM_z modes of the structure, with an electric field along the axis of the wires E_z, interact with the wires and provide the effective Drude permittivity of (1.22) along this axis. However, since the TE_z modes do not have any electric field along the z axis, they do not interact with the wires, and therefore they don't experience the presence of the wire-inclusions in the structure. Consequently, the behavior of the TM_z modes of the structure can be controlled independently of the TE_z modes, by changing the properties of the wires.

Despite the extensive research on artificial substrates and their applications, in many studies the inherent anisotropy of the artificial substrates that comes from the special arrangement of the implants in the substrate is not taken into account, and they have been considered to have effective isotropic properties [41, 42, 39, 44, 45, 47]. However, the anisotropy properties cannot be neglected in many cases. On the other hand, in some other cases, where the anisotropy of the medium is considered, an in-depth electromagnetic analysis on the structure is not provided [32, 49].

Lack of sufficient in-depth analysis on the anisotropy of artificial substrates in the literature, and knowing that exploiting the anisotropy properties of artificial substrates, with all their unique properties and benefits as mentioned above, may lead to novel microwave applications and devices, motivated this project whose objectives are to provide rigorous electromagnetic analysis of anisotropic artificial substrates and exploring their novel applications.

For better understanding of the anisotropy in the artificial substrates and their applications, it is useful to first better understand the anisotropy in the existing natural substrates such as ferrimagnetic materials. This approach not only provides a deeper insight about anisotropic materials and their analysis methods but also may lead to novel applications of these materials. Moreover, in order to study some of the applications of the anisotropic substrates, first we need to unveil the dark zones in the literature about the explanation and analysis of some specific phenomena in isotropic materials.

Based on the objectives and methodology of the thesis which were mentioned above, in this thesis, three basic problems in microwave engineering are chosen to be studied. The next three sections discuss in greater details the problematic and the contribution of the thesis to address the problems.

Practical Implementation of Perfect Electromagnetic Conductor Boundaries

A perfect magnetic conductor (PMC) is a fundamental electromagnetic concept, dual to the that of a perfect electric conductor (PEC), but unfortunately no PMC is available in the nature due to the non-existence of magnetic charges [51]. To overcome this deficiency of nature, many attempts to design artificial PMCs have been made. For instance, electromagnetic band-gap (EBG) structures, and their subsequent applications, including gain-enhanced low-profile antennas and transverse electromagnetic (TEM) waveguides, have been reported [50, 52]. These EBGs are resonant-type periodic structures, and their period is therefore necessarily in the order of half a wavelength. This constraint is acceptable when the structure is illuminated by a plane wave as a far-field reflector. However, it becomes problematic when circuit elements are placed in the near-field for a twofold reason. First, the EBG is highly inhomogeneous, and therefore dramatically different from an ideal PMC surface. Secondly, the EBG period is typically in the order of the circuit element, and can therefore not be designed independently from the circuit. For instance, a patch antenna on an EBG *PMC* ground plane has roughly the same size as the EBG period. Therefore, the EBG acts as a diffracting periodic structure, rather than an electromagnetic surface, and the EBG elements must be regarded as parasitic radiators of the patch as opposed to microscopic *molecules* of an actual PMC ground medium. Another method for the realization of the PMC boundaries was suggested by Kildal *et. al.* [53]. In this report it is shown that a quarter-wavelength grounded dielectric slab exhibits PMC characteristics at its air-dielectric interface. This method provides a uniform PMC boundary, however, as compared to the EBG-PMC, and specially at low frequencies, a relatively thick dielectric slab is required for the realization of the PMC.

On the other hand, in 2005, Lindell and Sihvola theoretically introduced the concept of a perfect electromagnetic conductor (PEMC) [54] and discussed a tentative, but unsuccessful, implementation of a PEMC boundary based on an array of magnetic and electric wires [55]. A PEMC is a generalization of the well-known perfect electric conductor (PEC) and the perfect magnetic conductor (PMC) [54, 56] with several potential applications such as rotating-field waveguides [57], sensors, reflectors and polarization converters. A PEMC is requested by Maxwell equations to exhibit gyrotropy, and is therefore non-reciprocal [54, 55].

Motivated by the fundamental properties of the PEMC boundaries explained above and its potential applications, in this project, for the first time, we propose a practical solution for the realization of the PEMC boundaries, including the PMC, which is perfectly homogeneous and efficient both in the far-field and in the near-field. This structure is simply a grounded ferrite slab with perpendicular bias field providing an effective PEMC boundary condition at its surface by exploiting Faraday rotation [10] and ground reflection. Since the ferrite properties

are tunable by adjusting the DC magnetic bias field, this structure provides tunable PEMC and PMC boundaries and therefore leads to tunable devices. The structure is rigorously analyzed by generalized scattering matrix (GSM) [58, 59, 60, 61]. An application of the grounded ferrite PMC as a tunable TEM waveguide, along with its experimental validation, is presented.

Analysis of Anisotropic Magneto-dielectric Substrates with Application to Leaky-wave Antenna

Leaky-wave antennas feature high directivity and frequency beam scanning capabilities. They find many applications in radar, point-to-point communications and MIMO systems. Leaky-wave antennas may be one-dimensional (1D) or two-dimensional (2D) [62]. In 1D leaky-wave antennas, the wave propagates in one direction outward from the source and generally produces a fan beam, while in the 2D leaky-wave antennas, the wave propagates radially outward from the source and produces a conical beam. Trentini proposed the first 2D high-directivity leaky-wave antenna which was a periodic partially reflective screen over a ground plane [63]. Later, a uniform 2D leaky-wave antenna consisting of dielectric superstrate layers was proposed by Jackson and Oliner [64]. Following these works, several studies on the properties of the 2D leaky-wave antennas based on artificial substrates were performed and reported by several groups [41, 42, 65, 66, 67].

Recently, it was experimentally shown that an artificial substrate constituted of a mushroom structure [50], shown in Fig. 1.11, could exhibit two-dimensional leaky-wave radiation properties [41, 42]. However, in this work the anisotropy of the structure was not taken into account. Later in [49] it was shown that the same structure, with enhanced capacitive coupling and a dielectric cover supporting microstrip line printed on top of it could exhibit the same full-space scanning leaky-wave capability as composite left/right handed (CRLH) structured-line [16] leaky-wave antennas. Although in this study the anisotropy of the substrate was properly considered, a rigorous analysis on the structure has not been provided.

Several works related to anisotropic substrates have been reported in the literature. Different planar transmission lines printed on non-dispersive anisotropic substrates were studied using quasi-static, dynamic and empirical methods in [68]. Bi-anisotropic multilayered structures were analyzed using Green functions and the integral equation technique [69, 70, 71, 72]. While most reports included homogenous anisotropic structures, inhomogeneous anisotropic substrates were also analyzed in [73, 74] using quasi-TEM and integral equations approach, respectively. However, none of these works addresses the problem of the mushroom-type anisotropic magneto-dielectric substrate for the leaky-wave antenna application.

The interesting properties of the two-dimensional leaky-wave antennas reported in [41, 42,

49] and lack of adequate in-depth analysis study on the structure have motivated this part of the thesis. Consequently, this project presents a novel broadband and low beam squint two-dimensional leaky-wave antenna constituted of an anisotropic magneto-dielectric artificial substrate similar to [41, 42, 49], excited by a vertical source. The structure is rigourously analyzed by the spectral transmission-line model based on dyadic Green functions [75, 76] of the uniaxially anisotropic grounded slab, and the two-dimensional leaky-wave antenna properties of this structure are investigated in great details.

Analysis of the Radiation Efficiency Behavior of Planar Antennas on Electrically Thick Substrates and Efficiency Enhancement Solutions

Planar antennas have found countless applications in communication systems thanks to their low profile, low cost, compatibility with integrated circuits and conformal nature. In parallel, bandwidth requirements and miniaturization constraints have attracted much attention to millimeter-wave wireless systems, such as radar, remote sensors and high-speed local area networks.

Toward millimeter-wave regime, the radiation efficiency of planar antennas is an important issue, since the substrates become electrically thick, which leads to an increase in surface mode excitation and henceforth degrade the efficiency of the antennas. Therefore, an exact characterization of the radiation efficiency of planar antennas with electrically thick substrates is of paramount importance.

There have been a few studies on the radiation efficiency of electric and magnetic sources on electrically thick substrates showing that the radiation efficiency does not decay monotonically with the electrical thickness [77, 78, 79]. However, no detailed explanation of this behavior has been reported to date.

Since this behavior has a critical impact on the efficiency of electrically thick antennas, particularly millimeter-wave antennas, it is a topic of great practical importance, and we address it thoroughly in this part of the thesis. We specifically analyze a radiating horizontal electric dipole on conventional grounded and ungrounded substrate, using a spectral transmission line model based on dyadic Green functions [75, 76], since these problems represent the basis of planar antennas. Moreover, solutions for enhancing the efficiency at frequencies where the efficiency is close to zero (no radiation) are presented. After acquiring the required knowledge about the efficiency behavior of the planar antennas on the isotropic (conventional) substrates, the more complicated case of anisotropic substrates are analyzed and discussed.

1.2.2 Organization

This thesis is written in the format of articles. Chapters 2- 4 present one of the three problems mentioned in Sec. 1.2 by an article while Chapter 5 discusses the extensions of Chapter 4. The details of the content of each chapter is as follows

Chapter 2 Article 1: Arbitrary Electromagnetic Conductor Boundaries Using Faraday Rotation in a Grounded Ferrite Slab

In this chapter, the first practical realization of a perfect electromagnetic conductor (PEMC) boundary, to the authors' knowledge, using the Faraday rotation principle in a grounded ferrite slab is proposed. A description of the operation phenomenology of the structure and its exact electromagnetic analysis based on the generalized scattering matrix (GSM) method is presented. A tunable perfect magnetic conductor (PMC) as a special case of the PEMC is experimentally examined through the implementation of a tunable transverse electromagnetic (TEM) waveguide with grounded ferrite PMC lateral walls.

Chapter 3 Article 2: Broadband and Low Beam Squint Leaky-Wave Radiation from a Uniaxially Anisotropic Grounded Slab

In this chapter, a novel broadband and low beam squint 2D leaky-wave antenna, constituted of an anisotropic magneto-dielectric artificial substrate similar to the mushroom-type structure, and excited by a vertical source is reported. The antenna is analyzed using spectral domain transmission-line model. The performance of the novel leaky-wave antenna is compared with an isotropic leaky-wave antenna.

This chapter is associated with Appendix A where the proper and improper modes in the dielectric slab are explained and Appendix B for the spectral domain transmission-line modeling of the uniaxially anisotropic medium. Particularly, Sec. B.3 is dedicated to the vertical dipole excitation of the uniaxially anisotropic substrate.

Chapter 4 Article 3: Radiation Efficiency Issues in Planar Antennas on Electrically Thick Substrates and Solutions

In this chapter, the radiation efficiency of a horizontal infinitesimal electric dipole on grounded and ungrounded substrates as a function of its electrical thickness is investigated thoroughly. The efficiency behavior is analyzed using a spectral transmission-line analysis in conjunction with a newly introduced substrate dipole collocated with the source which models the substrate (and the ground plane if present). From this substrate dipole, the efficiency maxima and minima are essentially explained in terms of equivalent PMC and PEC walls

at the position of the source. Finally, two solutions for enhancing the efficiency at electrical thicknesses where the efficiency is minimal (no radiation) are provided.

This chapter includes two appendices: Appendix C presents the computation of the radiation efficiency of a horizontal infinitesimal dipole on a substrate while Appendix D presents the transmission-line modeling of the substrate dipole.

Chapter 5 The Effect of Substrate Anisotropy on Radiation Efficiency Behavior

This chapter is dedicated to an extension to Chapter 4 and presents the efficiency behavior of various types of uniaxial anisotropic artificial substrates. It studies the effect of the anisotropy on the efficiency behavior providing guidelines on how the anisotropy can be beneficial in efficiency enhancement.

This chapter is related to Appendix B for the spectral domain transmission-line modeling of the uniaxially anisotropic medium. Specially, Sec. B.2 presents the horizontal dipole excitation of uniaxially anisotropic substrates.

Chapter 6 General Discussion

This section provides a general overview on the thesis, including its background, motivations, objectives and contributions. A general discussion on the assessment of the thesis's contributions are discussed in this chapter.

Chapter 7 Conclusions and Future Works

This chapter concludes the thesis with a summary of the projects performed in this thesis and provides some possible future extensions of this thesis.

CHAPTER 2

ARTICLE 1: ARBITRARY ELECTROMAGNETIC CONDUCTOR BOUNDARIES USING FARADAY ROTATION IN A GROUNDED FERRITE SLAB

Attieh Shahvarpour, Toshiro Kodera, Armin Parsa, and Christophe Caloz
Poly-Grames Research Center, Department of Electrical Engineering,
École Polytechnique de Montréal, Centre de Recherche en Électronique Radiofréquence (CREER),
Montréal, QC, H3T 1J4, Canada.

2.1 Abstract

The realization of arbitrary perfect electromagnetic conductor boundaries by a grounded ferrite slab using Faraday rotation is proposed. This is the first practical realization of a perfect electromagnetic conductor boundary to the authors' knowledge. The key principle of the grounded ferrite perfect electromagnetic conductor boundary is the combination of Faraday rotation and reflection from the perfect electric conductor of the ground plane. From this combined effect, arbitrary angles between the incident and reflected fields can be obtained at the surface of the slab, so as to achieve arbitrary perfect electromagnetic conductor conditions by superposition with the incident field. An exact electromagnetic analysis of the structure is performed based on the generalized scattering matrix method and an in-depth description of its operation phenomenology is provided. As an illustration, a tunable transverse electromagnetic (TEM) waveguide with grounded ferrite PMC lateral walls is demonstrated experimentally. Due to its flexibility in the control of the polarization of the reflected field, the proposed grounded ferrite perfect electromagnetic conductor may find applications in various types of reflectors and polarization-based radio frequency identifiers.

2.2 Introduction

The exciting and promising fundamental concept of a perfect electromagnetic conductor was recently introduced by Lindell and Sihvola [54]. A perfect magnetic conductor is a generalization of the perfect electric conductor (PEC) and of the perfect magnetic conductor

(PMC) [56, 51]. According to [55], a perfect electromagnetic conductor must exhibit gyrotropy following Maxwell's equations. By definition, the electric and magnetic fields at the boundary of a perfect electromagnetic conductor are related by [54]

$$\mathbf{n} \times (\mathbf{H} + Y\mathbf{E}) = 0, \tag{2.1a}$$

$$\mathbf{n} \cdot (\mathbf{D} - Y\mathbf{B}) = 0, \tag{2.1b}$$

where $\mathbf{n}$ is the unit vector normal to the surface of the perfect electromagnetic conductor and Y represents the admittance of the perfect electromagnetic conductor. In the limiting cases where $Y \to \pm\infty$ and $Y \to 0$, the perfect electromagnetic conductor boundary corresponds to a PEC boundary ($\mathbf{n} \times \mathbf{E} = 0$ and $\mathbf{n} \cdot \mathbf{H} = 0$) and a PMC boundary ($\mathbf{n} \times \mathbf{H} = 0$ and $\mathbf{n} \cdot \mathbf{E} = 0$), respectively. In the case of a plane wave normally incident on a perfect electromagnetic conductor surface, which is of primary interest in this work, (2.1) reduces to

$$\mathbf{H} + Y\mathbf{E} = 0. \tag{2.2}$$

This relation states that $\mathbf{E}$ and $\mathbf{H}$ are collinear and simply related by the admittance value $Y = -|\mathbf{H}|/|\mathbf{E}|$ at the boundary. Thus, the net power flow vanishes, i.e. $\mathbf{S} = \mathrm{Re}\left[\mathbf{E} \times \mathbf{H}^*\right]/2 = 0$, where $\mathbf{S}$ is the time average Poynting vector, and as a result no energy can penetrate into the material (ideal perfect electromagnetic conductor).

The perfect electromagnetic conductor was initially described from a purely conceptual viewpoint [54]. Later, a structure, constituted of conducting metal wires and high-permeability magnetic cylinders embedded in a dielectric medium, was presented in [55] as an implementation of a perfect electromagnetic conductor boundary. To operate as a perfect electromagnetic conductor boundary, this structure would have to satisfy the conditions $\varepsilon_{xx} \to \infty$ and $\mu_{xx} \to \infty$, respectively, where x is the coordinate parallel to the axes of the wires and cylinders, and where the static bias field $\mathbf{H}_0$ is parallel to this axis. In this manner, we would have $E_x \to 0$ and $H_x \to 0$, from which it may be shown that the perfect electromagnetic conductor conditions of (2.1) would then be met [55]. However, in this configuration, we have from the Polder tensor of a magnetic material $\mu_{xx} = \mu_0$ and not $\mu_{xx} \to \infty$, since $\mathbf{H}_0 \| \mathbf{x}$ [10]. Thus, this structure, in fact, does *not* operate as a perfect electromagnetic conductor boundary.

In this work, we demonstrate a practical realization of a general perfect electromagnetic conductor boundary, which consists of a grounded ferrite slab using Faraday rotation. This is the first practical realization of a perfect electromagnetic conductor to the authors' knowledge.

The principle is the same as the one presented for the particular case of a PMC boundary in [80] and for the particular case of a free-space perfect electromagnetic conductor boundary in [81]. Essentially, it is based on the Faraday rotation and ground plane reflection of a plane wave incident on the grounded ferrite slab. However, this paper presents the grounded ferrite perfect electromagnetic conductor in a generalized and unified manner, with an exact solution based on the generalized scattering matrix method, and an in-depth analysis of the phenomenology of the structure. In addition, it demonstrates as an illustration, a tunable transverse electromagnetic (TEM) waveguide with grounded ferrite PMC lateral walls.

The reminder of the paper is organized as follows. Sec. 2.3 presents the PEMC structure in the simplified problem of perfect matching and zero phase shifts across the slab to provide direct insight into its principle of operation. Sec. 2.4 provides an exact analysis of the problem, covering Faraday rotation in an unbounded medium, the effect of oblique incidence at the air-ferrite interface, and finally the resolution of the complete PEMC structure by the generalized scattering matrix method with a discussion on the different types of achievable PEMC boundaries, the effect of multiple reflection, and the description of the general possible admittances. Sec. 2.5 experimentally demonstrates the proposed PEMC structure for the particular case of a grounded ferrite perfect magnetic conductor and its application to a miniaturized and tunable grounded ferrite perfect electromagnetic conductor transverse electromagnetic rectangular waveguide. Finally, conclusions are given in Sec. 2.6.

2.3 Principle of Electromagnetic Boundaries in a Grounded Ferrite Slab Using Faraday Rotation

2.3.1 Grounded Ferrite Slab Structure and Initial Assumptions

The proposed structure used to generate the arbitrary perfect electromagnetic conductor boundary discussed in Sec. 2.2 is shown in Fig. 2.1. It consists of a grounded ferrite slab with a magnetic bias field $\mathbf{H}_0$ applied perpendicularly to its surface. In this configuration, a plane wave normally incident on the structure experiences Faraday rotation in the ferrite medium [10]. If the incidence is normal, as represented in the figure, the wave undergoes a pure Faraday rotation effect, since the propagation vector in the ferrite, $\mathbf{k}_f$, is parallel to the bias field $\mathbf{H}_0$. If the incidence is oblique, it undergoes a mixed Faraday-birefringence effect, which may be analyzed by superposing the solutions of the Faraday and the birefringence problems using projections of $\mathbf{H}_0$ onto the directions parallel and perpendicular to $\mathbf{k}_f$, respectively, with corresponding rotated Polder tensors.

For simplicity, this section considers only the case of normal incidence and ignores the effects of mismatch, phase shifts and multiple reflections. This is appropriate to show the

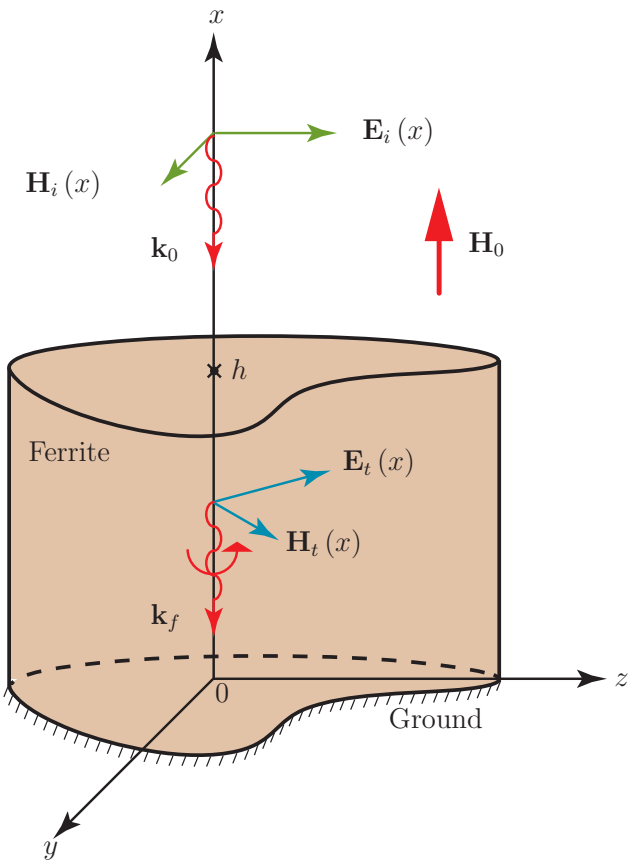

Figure 2.1 Perspective view of the grounded ferrite slab, with perpendicular magnetic bias field $\mathbf{H}_0$ and Faraday-rotating RF electromagnetic fields. $\mathbf{k}_0$ and $\mathbf{k}_f$ are the propagation vectors in free space and the ferrite, respectively.

principle of operation of the structure, but insufficient for accurate design. The general case of oblique incidence is treated in Sec. 2.4.2, and the complete problem including exact phase shifts and multiple reflections is analyzed rigorously by the generalized scattering matrix method in Sec. 2.4.3. Since the PEC boundary is naturally achieved by conventional good conductors, it will not be specifically discussed. Instead, the emphasis will be set on the PMC boundary and on a special perfect electromagnetic conductor boundary called the "free-space perfect electromagnetic conductor" because its impedance is equal to that of the free space, η_0. The design of the Faraday PEC boundary and other perfect electromagnetic conductor boundaries with different impedances may be easily inferred from the description of these two boundaries.

The key operation principle of the structure is the combination of Faraday rotation and PEC (ground plane) reflection. The PEC boundary discriminates the **E** and **H** fields, which are purely tangential under plane wave normal incidence, since it reverses the phase of **E** while

it does not affect $\mathbf{H}$. Using this fact and designing the structure to the proper Faraday rotation angle, an arbitrary angle between the incident and reflected fields can be obtained at the surface of the slab, and thus, by superposition of these fields, arbitrary perfect electromagnetic conductor conditions can be achieved.

2.3.2 Perfect Electromagnetic Conductor Boundary Realization

The principle of the perfect electromagnetic conductor grounded ferrite slab is depicted in Fig. 2.2 in connection with Fig. 2.1. An incident plane wave $(\mathbf{E}_i, \mathbf{H}_i)$, with propagation vector $\mathbf{k}_0$, normally hits the ferrite's interface at $x = h$ with $\mathbf{E}_i$ polarized along z, as shown in Fig. 2.2a, and experiences pure Faraday rotation after penetrating into the ferrite, since the direction of propagation, dictated by the propagation vector $\mathbf{k}_f$, is parallel to $\mathbf{H}_0$. Assuming that the slab is designed so as to provide a given Faraday rotation angle of θ across it, the transmitted fields $\mathbf{E}_t$ and $\mathbf{H}_t$ reaching the ground plane at $x = 0$, are polarized along the $-\mathbf{y}\sin\theta + \mathbf{z}\cos\theta$ and $\mathbf{y}\cos\theta + \mathbf{z}\sin\theta$ directions, respectively, as shown in Fig. 2.2b. At $x = 0$, the electric field is reversed due to the PEC ground plane condition $\mathbf{n} \times \mathbf{E} = 0$, as shown in Fig. 2.2c, polarizing the reflected field $\mathbf{E}_g$ along the $\mathbf{y}\sin\theta - \mathbf{z}\cos\theta$ direction, while maintaining $\mathbf{H}_g = \mathbf{H}_t$. The reflected fields propagating backward through the slab experience in turn θ Faraday rotation (of course, still in the same direction, dictated by $\mathbf{H_0}$), so that the overall reflected fields $\mathbf{E}_r$ and $\mathbf{H}_r$ emerge at the interface $x = h$ polarized along the $\mathbf{y}\sin 2\theta - \mathbf{z}\cos 2\theta$ and $\mathbf{y}\cos 2\theta + \mathbf{z}\sin 2\theta$ directions, respectively, as shown in Fig. 2.2d.

In the continuous wave regime, if we neglect mismatch (and hence also multiple reflections), phase shifts and losses, which ensures $|\mathbf{E}_r|{=}|\mathbf{E}_i|$ and $|\mathbf{H}_r|{=}|\mathbf{H}_i|$, the total electric and magnetic fields at $x = h$, $\mathbf{E}(h) = \mathbf{E}_i(h) + \mathbf{E}_r(h)$ and $\mathbf{H}(h) = \mathbf{H}_i(h) + \mathbf{H}_r(h)$, are collinear. Although the actual operation of the grounded ferrite perfect electromagnetic conductor will be shown in Sec. 2.4.5 to greatly depart from this simplistic configuration, the present approximation will be useful to define the different grounded ferrite perfect electromagnetic conductors, where the actual grounded ferrite perfect electromagnetic conductors will be characterized in terms of perturbations of these simplified grounded ferrite perfect electromagnetic conductors. The collinearity between the total electric and magnetic fields can be seen, with the help of Fig. 2.2d, by noting that $\angle\mathbf{H} = \pi/2 - \theta$ and $\angle\mathbf{E} = (\pi - 2\theta)/2 = \pi/2 - \theta = \angle\mathbf{H}$. Therefore, the perfect electromagnetic conductor boundary condition of (2.1a), or (2.2), is achieved at $x = h$, while the perfect electromagnetic conductor boundary condition of (2.1b) is automatically satisfied since the fields are purely transverse. Thus, a general perfect electromagnetic conductor boundary condition is achieved at $x = h$.

The PMC and free-space perfect electromagnetic conductor boundaries are obtained as particular cases of the perfect electromagnetic conductor boundary described above by de-

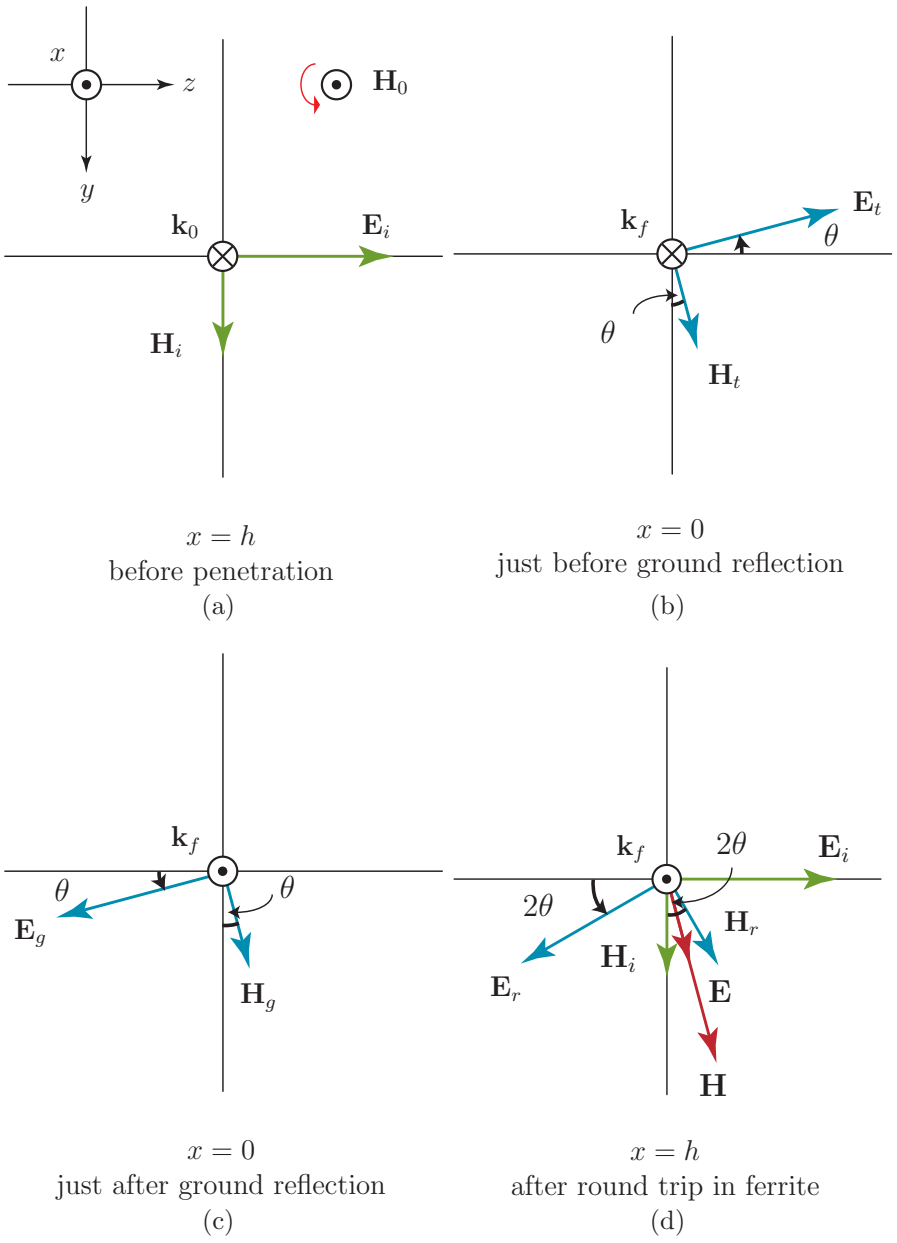

Figure 2.2 Principle of the proposed grounded ferrite perfect electromagnetic conductor boundary (Fig. 2.1), ignoring phase shifts and multiple reflections for simplicity. The structure uses arbitrary Faraday rotation with single-trip angle θ and perfect electric conductor (PEC) reflection on the ground plane. The different panels show the evolution of the vectorial $\mathbf{E}$ and $\mathbf{H}$ fields, for a matched and lossless ferrite slab.

signing the ferrite slab for Faraday rotations of $\theta = 90°$ and $\theta = 45°$, respectively. The corresponding fields for a PMC and free-space perfect electromagnetic conductor boundaries exhibit the configurations shown in Figs. 2.3a and 2.3b, respectively.

It should be noted that the particular case of a PMC boundary can also be realized by a simple quarter-wavelength grounded dielectric slab. However, the proposed grounded ferrite PMC is based on a different operation principle, inherently exhibits higher power handling from the superior thermal properties of the ferrite, and also provides frequency tunability via the bias magnetic field. It may therefore be considered as an interesting and useful alternative for PMC. More generally, the arbitrariness in the achievable angles between the incident and reflected angles, which is *specific* to this Faraday-rotation based grounded ferrite perfect electromagnetic conductor implementation, may find interesting applications in various types of polarizing reflectors.

2.4 Theory

2.4.1 Faraday Rotation and Effective Permeability for Propagation Parallel to the Bias Field in an Unbounded Ferrite

The Faraday rotation angle θ experienced by a wave travelling a distance x along the direction of the bias field $\mathbf{H}_0$ in a ferrite is given by [10, 2]

$$\theta(\omega, x) = -\left[\frac{\beta_+(\omega) - \beta_-(\omega)}{2}\right] x. \tag{2.3}$$

In this expression, $\beta_+(\omega)$ and $\beta_-(\omega)$ represent the right-handed circularly polarized (RHCP) and left-handed circularly polarized (LHCP) propagation constants, respectively,

$$\begin{aligned}\beta_\pm(\omega) &= \omega\sqrt{\varepsilon\mu_0[\mu(\omega) \pm \kappa(\omega)]} \\ &= \omega\sqrt{\varepsilon\mu_0}\sqrt{[\mu'(\omega) - j\mu''(\omega)] \pm [\kappa'(\omega) - j\kappa''(\omega)]} \\ &= \omega\sqrt{\varepsilon\mu_0\mu_{e\pm}(\omega)},\end{aligned} \tag{2.4}$$

where ε is the permittivity of the ferrite, μ_0 is the free space permeability and $\mu_{e\pm}(\omega)$ are the RHCP/LHCP effective relative permeabilities

$$\begin{aligned}\mu_{e\pm}(\omega) &= \mu'_{e\pm}(\omega) - j\mu''_{e\pm}(\omega) \\ &= [\mu'(\omega) \pm \kappa'(\omega)] - j[\mu''(\omega) \pm \kappa''(\omega)] \\ &= \mathrm{Re}[\mu(\omega) \pm \kappa(\omega)] - j\mathrm{Im}[\mu(\omega) \pm \kappa(\omega)].\end{aligned} \tag{2.5}$$

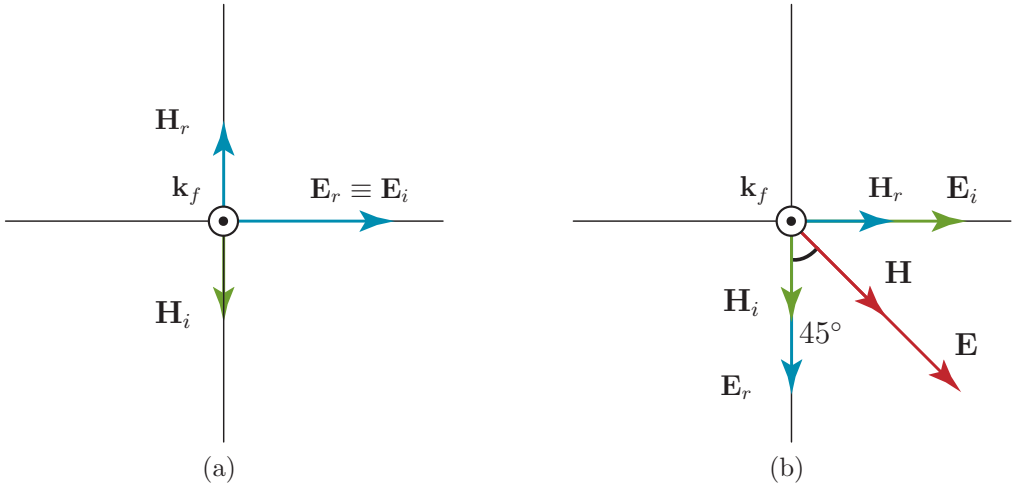

Figure 2.3 Particular cases of PMC and free space perfect electromagnetic conductor boundaries, corresponding to $\theta = 90°$ and $\theta = 45°$ Faraday rotation angles, respectively. (a) PMC. (b) Free-space perfect electromagnetic conductor.

In this expression, $\mu(\omega)$ and $\kappa(\omega)$ are the usual elements of the Polder tensor (here for x-directed bias)

$$\overline{\overline{\mu}} = \mu_0 \begin{pmatrix} 1 & 0 & 0 \\ 0 & \mu & j\kappa \\ 0 & -j\kappa & \mu \end{pmatrix}, \tag{2.6}$$

which read $\mu = (1 + \chi_{zz})$ and $\kappa = -j\chi_{zy}$, where $\chi_{zz} = \chi'_{zz} - j\chi''_{zz}$ and $\chi_{zy} = \chi''_{zy} + j\chi'_{zy}$, with

$$\chi'_{zz} = \left[\omega_0\omega_m\left(\omega_0^2 - \omega^2\right) + \omega_0\omega_m\omega^2\alpha^2\right]/T, \tag{2.7a}$$

$$\chi''_{zz} = \left\{\alpha\omega\omega_m\left[\omega_0^2 + \omega^2\left(1 + \alpha^2\right)\right]\right\}/T, \tag{2.7b}$$

$$\chi'_{zy} = \left\{\omega\omega_m\left[\omega_0^2 - \omega^2\left(1 + \alpha^2\right)\right]\right\}/T, \tag{2.7c}$$

$$\chi''_{zy} = 2\omega_0\omega_m\omega^2\alpha/T, \tag{2.7d}$$

where $T = \left[\omega_0^2 - \omega^2\left(1 + \alpha^2\right)\right]^2 + 4\omega_0^2\omega^2\alpha^2$, and α is related to the line width ΔH by $\alpha = \gamma\Delta H\mu_0/(2\omega)$, γ being the gyromagnetic ratio which is equal to 1.76×10^{11} rad/T.s for a ferrite. In addition, $\omega_0 = \mu_0\gamma\mathbf{H}_0$ is the ferromagnetic resonance and $\omega_m = \gamma(\mu_0 M_s)$, where M_s is the saturation

magnetization. The *isotropic-effective* permeability μ_e of the ferrite is then obtained from [10]

$$\beta_e = (\beta_+ + \beta_-)/2 = \omega\sqrt{\varepsilon\mu_0}(\sqrt{\mu_{e+}} + \sqrt{\mu_{e-}})/2 = \omega\sqrt{\varepsilon\mu_0\mu_e} \tag{2.8}$$

as

$$\mu_e = \left[(\sqrt{\mu_{e+}} + \sqrt{\mu_{e-}})/2\right]^2 . \tag{2.9}$$

In the following, we assume a ferrite (YIG)with the parameters $\mu_0 M_s = 0.188$ T, $\Delta H = 10$ Oe and $\varepsilon_r = 15$, corresponding to the ferrite used in the experiments which will be presented in Sec. 2.5. Fig. 2.4 shows the effective RHCP and LHCP permeabilities defined in (2.5) for an internal bias of $\mu_0\mathbf{H}_0 = 0.2$ T, while Fig. 2.4b shows the isotropic-effective relative permeability defined in (2.9) and the Faraday rotation angle. The results of both graphs are for normal incidence. Figure 2.4b shows that 90° Faraday rotation, corresponding to the PMC boundary case, occurs at $f = 5.19$ GHz, while 45° Faraday rotation, corresponding to the free-space perfect electromagnetic conductor boundary case, occurs at $f = 4.7$ GHz.

2.4.2 Effect of Oblique Incidence at the Air-Ferrite Interface

In practical applications, such as a TEM PMC waveguide (Sec. 2.5), the field incident on the ferrite slab may be oblique, as shown in Fig. 2.5. In this case, the RHCP and LHCP solutions of (2.4) for the normal incidence case become elliptically polarized and transform to [10]

$$\begin{aligned}\beta_\pm^2 =& \omega^2\varepsilon\mu_0 \left\{ \frac{(\mu^2 - \mu - \kappa^2)\sin^2\psi_{t\pm} + 2\mu}{2\left(\cos^2\psi_{t\pm} + \mu\sin^2\psi_{t\pm}\right)} \right\} \\ & \pm \omega^2\varepsilon\mu_0 \left\{ \frac{\left[(\mu^2 - \mu - \kappa^2)^2\sin^4\psi_{t\pm} + 4\kappa^2\cos^2\psi_{t\pm}\right]^{\frac{1}{2}}}{2\left(\cos^2\psi_{t\pm} + \mu\sin^2\psi_{t\pm}\right)} \right\},\end{aligned} \tag{2.10}$$

where $\psi_{t\pm}$ are the RH/LH elliptically polarized refraction angles in the ferrite medium. It is then found, by substituting this expression into (2.3), that the Faraday rotation becomes a function of the angle of propagation, i.e. $\theta = \theta[\beta_\pm(\psi_{t\pm})] = \theta(\psi_{t\pm})$. Furthermore, replacing (2.4) by the same expression and next inserting the result into (2.5) also yields an angle-dependent RH/LH elliptically polarized effective relative permeability $\mu_{e\pm}(\psi_{t\pm})$, and thereby an angle-dependent RH/LH elliptically polarized effective refractive index, $n_{e\pm} = n_{e\pm}(\psi_{t\pm}) =$

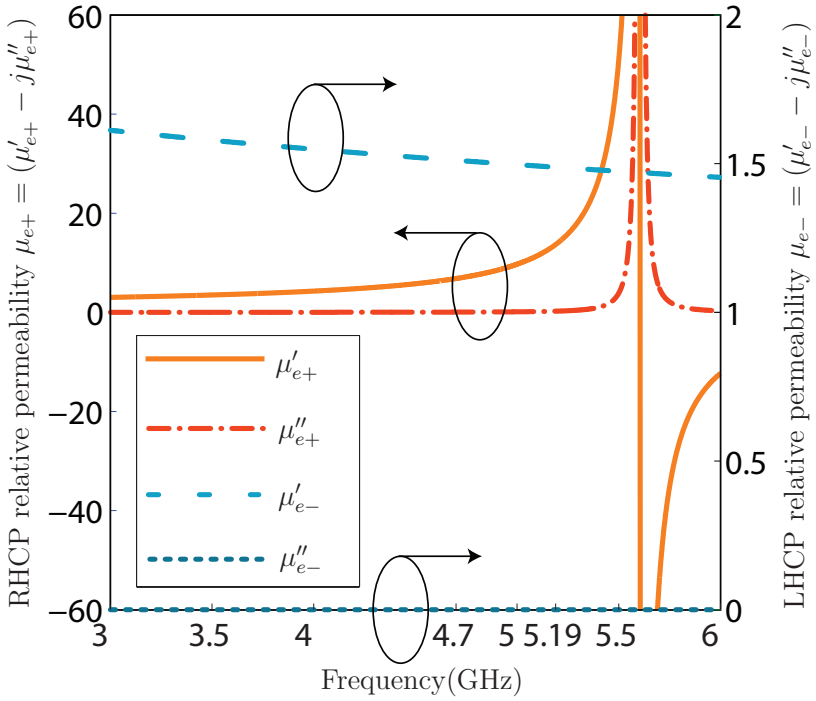

Figure 2.4 Permeability and Faraday rotation angle versus frequency for an unbounded ferrite medium (YIG) with parameters: $\mu_0 M_s = 0.188$ T, $\Delta H = 10$ Oe, $\varepsilon_r = 15$, and $\mu_0 \mathbf{H}_0 = 0.2$ T (internal bias field). The parameters M_s, ΔH and ε_r correspond to the specifications of the ferrite which will be used in the experiment (Sec. 2.5) while the parameter $\mu_0 \mathbf{H}_0$ will be determined in Sec. 2.4.4 to provide an exact PMC at $\theta = 90°$. (a) Real and imaginary parts of $\mu_{e\pm}$ computed by (2.5). (b) Real and imaginary parts of μ_e computed by (2.9), and Faraday rotation angle calculated by (2.3). The $\tan\delta_m$ at 5.19 GHz (PMC) and at 4.7 GHz (free-space perfect electromagnetic conductor (PEMC)) are of 0.0129 and 0.0045, respectively.

$\sqrt{\mu_{e\pm}(\psi_{t\pm})\varepsilon/\varepsilon_0}$. The approximated RH/LH elliptically polarized refraction angle $\psi_{t\pm}$ may be then computed numerically from Snell's law [82],

$$n_i \sin\psi_i = n_{e\pm}(\psi_{t\pm}) \sin\psi_{t\pm}, \tag{2.11}$$

where n_i is the refractive index of air.

Fig. 2.6 shows the effect of oblique incidence on the Faraday rotation angle across the whole range of incidence angles, $\psi_i = 0, \ldots, 90°$. The maximal deviation (for $\psi_i = 90°$) compared to normal incidence are of 1.83% and 1.71% for the cases of PMC (5.19 GHz) and free-space perfect electromagnetic conductor (4.7 GHz), respectively, while the deviations are of 0.91% and 0.86% for $\psi_i = 45°$. So, the effect of oblique incidence is very small and may be neglected for practical purposes. This holds in most cases because the refractive index is generally very large, due to the simultaneously large permittivity and effective permeability (relatively close to resonance for a thin slab), which results into a small refraction angle according to (2.11). Therefore, oblique angles are ignored in the following analysis.

2.4.3 Exact Analysis for Normal Incidence by the Generalized Scattering Matrix Method

The grounded ferrite slab produces both multiple reflections, if some mismatch is present, and phase shifts, corresponding to the multiple trips of the wave in the ferrite slab. These effects not accounted in Secs. 2.3, 2.4.1 and 2.4.2. In order to determine their exact impact on the perfect electromagnetic conductor boundaries, an accurate analysis of the problem is required. The generalized scattering matrix [58, 59, 60, 61] may be used for this purpose. The general problem of reflection and transmission of plane waves in the presence of a bianisotropic slab has been solved in [61]. This subsection explicitly derives the solution of the problem of interest, which is a particular case of [61], to ensure consistency and to provide insight into the physics of the structure. Since, as shown in Sec. 2.4.2, the effect of oblique incidence is negligible, the following generalized scattering matrix analysis restricts to the case of normal incidence for simplicity.

Assume an incident field linearly polarized along the z direction and has unit amplitude, i.e. $\mathbf{E}_i = 1\mathbf{z}$. In order to account for the distinct reflection coefficients for the RHCP and LHCP eigenmodes of the ferrite [10, 2], we decompose this linearly polarized field into a RHCP field and a LHCP field:

$$\mathbf{E}_i = 1/2\left[(\mathbf{z} - j\mathbf{y}) + (\mathbf{z} + j\mathbf{y})\right]. \tag{2.12}$$

At the interface between air and the ferrite slab, the RHCP and LHCP components of the

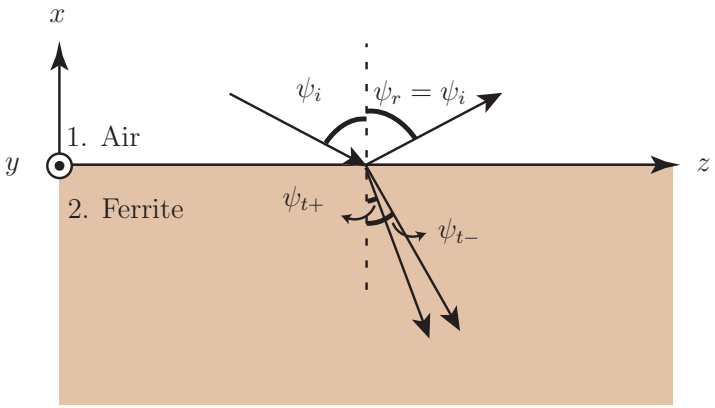

Figure 2.5 Reflection and refraction at the interface between air and a ferrite medium for plane wave oblique incidence.

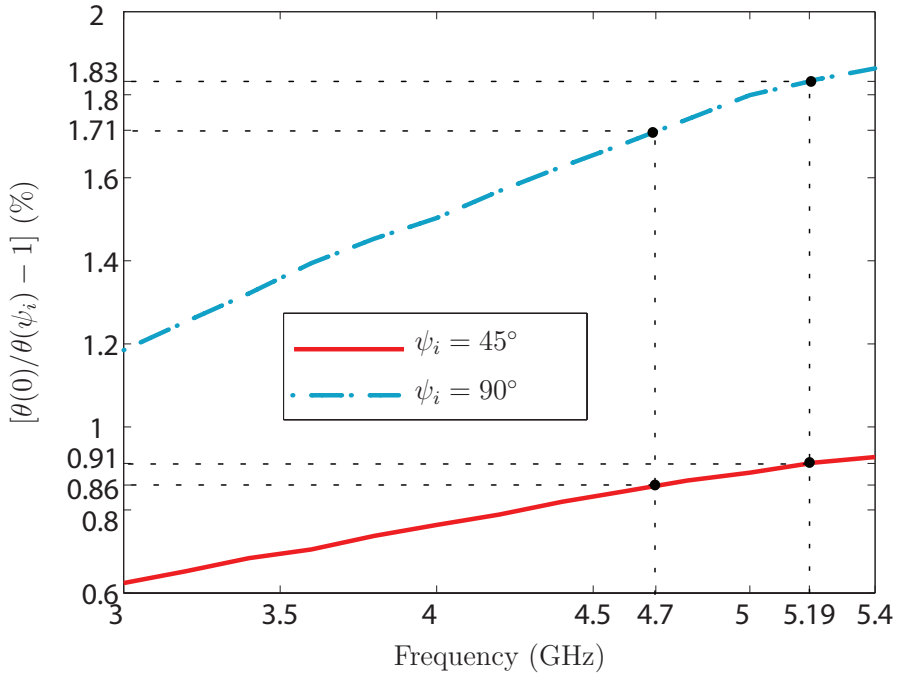

Figure 2.6 Approximate Faraday rotation angle variation due to oblique incidence with the parameters of Fig. 2.4 after refraction through an interface with air (Fig. 2.5) for different incidence angles ψ_i, computed by (2.3) with (2.10), using (2.11).

wave see different reflection coefficients, Γ_+ and Γ_-, respectively. So the reflected field is

$$\mathbf{E}_r = \frac{1}{2}\left[\Gamma_+ (\mathbf{z} - j\mathbf{y}) + \Gamma_- (\mathbf{z} + j\mathbf{y})\right], \tag{2.13}$$

with the following z and y components

$$E_r^z = \frac{1}{2}(\Gamma_+ + \Gamma_-) = E_{rz+} + E_{rz-}, \tag{2.14a}$$

$$E_r^y = -\frac{j}{2}(\Gamma_+ - \Gamma_-) = -j(E_{ry+} - E_{ry-}), \tag{2.14b}$$

where the exact expressions for Γ_+ and Γ_- will be derived next by generalized scattering matrix analysis.

Fig. 2.7 shows the definition of the incident and scattered waves in the grounded ferrite slab for the RHCP and LHCP waves. According to this figure and considering that the incident field is polarized along z, the scattering relation for the z components reads

$$\begin{pmatrix} B_{1\pm}^z \\ B_{3\pm}^z \end{pmatrix} = S_\pm \begin{pmatrix} A_{1\pm}^z \\ A_{3\pm}^z \end{pmatrix}, \tag{2.15}$$

where $S_\pm$ is the total scattering matrix of the grounded ferrite slab for the RHCP/LHCP waves, which may be obtained by conversion of the transmission matrix $T_\pm$ [60] defined by the transmission relation

$$\begin{pmatrix} B_{3\pm}^z \\ A_{3\pm}^z \end{pmatrix} = T_\pm \begin{pmatrix} A_{1\pm}^z \\ B_{1\pm}^z \end{pmatrix}. \tag{2.16}$$

In this relation, $T_\pm = T_{f\pm} T_{1\to 2\pm}$, where $T_{f\pm}$ is the transmission matrix of the ferrite medium, defined by

$$\begin{pmatrix} B_{3\pm}^z \\ A_{3\pm}^z \end{pmatrix} = T_{f\pm} \begin{pmatrix} A_{2\pm}^z \\ B_{2\pm}^z \end{pmatrix} \tag{2.17}$$

and given as

$$T_{f\pm} = \begin{pmatrix} \exp(j\beta_\pm h) & 0 \\ 0 & \exp(-j\beta_\pm h) \end{pmatrix}, \tag{2.18}$$

where $\beta_\pm$ is given by (2.4), and $T_{1\to 2\pm}$ is the transmission matrix of the air-ferrite interface

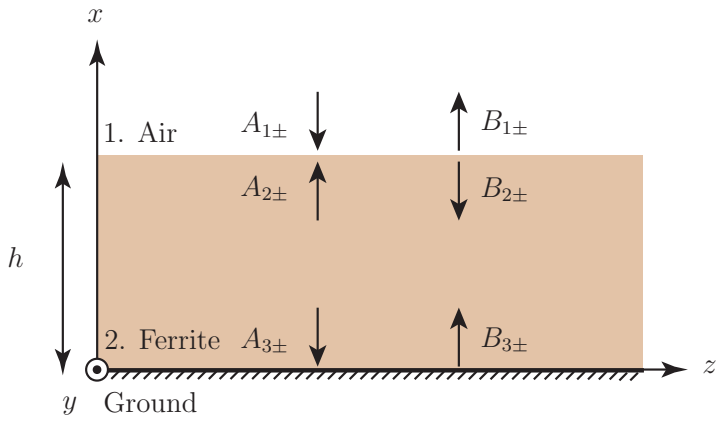

Figure 2.7 Definition of the incident and scattered RHCP (+) and LHCP (−) waves in the grounded ferrite slab for application of the generalized scattering matrix analysis under normal incidence.

defined by

$$\begin{pmatrix} B^z_{2\pm} \\ A^z_{2\pm} \end{pmatrix} = T_{1\to 2\pm} \begin{pmatrix} A^z_{1\pm} \\ B^z_{1\pm} \end{pmatrix} \tag{2.19}$$

and given as

$$T_{1\to 2\pm} = \begin{pmatrix} T_{12\pm} - \frac{R_{12\pm}R_{21\pm}}{T_{21\pm}} & \frac{R_{21\pm}}{T_{21\pm}} \\ -\frac{R_{12\pm}}{T_{21\pm}} & \frac{1}{T_{21\pm}} \end{pmatrix}, \tag{2.20}$$

where $R_{ij\pm}$ and $T_{ij\pm}$ are the local reflection and transmission coefficients of the RHCP/LHCP incident waves from medium i to medium j at the air-ferrite interface. The matrix $T_{1\to 2\pm}$ has been obtained by conversion of the interface scattering matrix $S_{1\to 2\pm}$ [60], which is defined by

$$\begin{pmatrix} B^z_{1\pm} \\ B^z_{2\pm} \end{pmatrix} = S_{1\to 2\pm} \begin{pmatrix} A^z_{1\pm} \\ A^z_{2\pm} \end{pmatrix} \tag{2.21}$$

and given as

$$S_{1\to 2\pm} = \begin{pmatrix} R_{12\pm} & T_{21\pm} \\ T_{12\pm} & R_{21\pm} \end{pmatrix}, \tag{2.22}$$

where $R_{12\pm} = (\eta_{f\pm} - \eta_0)/(\eta_{f\pm} + \eta_0) = -R_{21\pm}$, $T_{12\pm} = 1 + R_{12\pm}$ and $T_{21\pm} = 1 + R_{21\pm}$, where $\eta_{f\pm} = \eta_0\sqrt{\mu_{e\pm}/\varepsilon_r}$ and $\eta_0 = \sqrt{\mu_0/\varepsilon_0}$ and $\mu_{e\pm}$ are RHCP/LHCP effective relative permeabilities defined in (2.5).

The reflected field may now be computed in closed form by the following procedure: i) calculate the closed form expression of $T_\pm = T_{f\pm}T_{1\to 2\pm}$ from the expressions of (2.18) and (2.20); ii) convert the resulting expression for $T_\pm$ into the corresponding scattering matrix to obtain the closed form expression of $S_\pm$ in terms of $\beta_\pm h$ and $R_{12\pm}$ in (2.15); iii) applying the boundary conditions at the PEC ground plane for the electric field, we find $B^z_{3\pm} = -A^z_{3\pm}$; insert this relation into the closed form expression obtained from (2.15), which reduces this equation to a relation between the incident field $A^z_{1\pm}$ and the reflected field $B^z_{1\pm}$; iv) finally, consider a unit amplitude z-polarized incident field, corresponding to $E^z_{i\pm}(h) = A^z_{1\pm} = 1$; this yields the corresponding z components of the scattered (or reflected) field, as $E^z_{r\pm}(h) = B^z_{1\pm}$ for the RHCP and LHCP polarizations; v) the z and y components of the *total* reflected wave are then obtained from (2.14) as

$$\begin{aligned} E^z_r(h) =& \frac{1}{2}\left[R_{12+} - \frac{T_{12+}T_{21+}e^{(-j2\beta_+ h)}}{1+R_{21+}e^{(-j2\beta_+ h)}}\right] \\ &+ \frac{1}{2}\left[R_{12-} - \frac{T_{12-}T_{21-}e^{(-j2\beta_- h)}}{1+R_{21-}e^{(-j2\beta_- h)}}\right], \end{aligned} \tag{2.23a}$$

$$\begin{aligned} E^y_r(h) =& -\frac{j}{2}\left[R_{12+} - \frac{T_{12+}T_{21+}e^{(-j2\beta_+ h)}}{1+R_{21+}e^{(-j2\beta_+ h)}}\right] \\ &+ \frac{j}{2}\left[R_{12-} - \frac{T_{12-}T_{21-}e^{(-j2\beta_- h)}}{1+R_{21-}e^{(-j2\beta_- h)}}\right], \end{aligned} \tag{2.23b}$$

with the possible simplifications mentioned just after (2.22). Alternatively, these expression may be written in terms of the Faraday rotation angle $\theta(x=h) = -[(\beta_+ - \beta_-)/2]h$ [(2.3)] and the effective propagation constant $\beta_e = (\beta_+ + \beta_-)/2$ [(2.8)] as

$$\begin{aligned} &E^z_r(h) = \\ &\frac{\cos(2\beta_e h)\,(R_{12+}+R_{12-}) - \cos(2\theta)(1+R_{12+}R_{12-})}{\left[e^{-j(\beta_e h+\theta)}R_{12-} - e^{j(\beta_e h+\theta)}\right]\left[e^{-j(\beta_e h-\theta)}R_{12+} - e^{j(\beta_e h-\theta)}\right]}, \end{aligned} \tag{2.24a}$$

$$\begin{aligned} &E^y_r(h) = \\ &\frac{\sin(2\beta_e h)\,(R_{12+}-R_{12-}) - \sin(2\theta)(1-R_{12+}R_{12-})}{\left[e^{-j(\beta_e h+\theta)}R_{12-} - e^{j(\beta_e h+\theta)}\right]\left[e^{-j(\beta_e h-\theta)}R_{12+} - e^{j(\beta_e h-\theta)}\right]}. \end{aligned} \tag{2.24b}$$

These equations represent in general a system of four equations, since each of the two relations is complex, involving a magnitude and a phase. The design of a specified grounded ferrite perfect electromagnetic conductor, such as for instance a PMC or a free-space perfect electromagnetic conductor (Fig. 2.3), will consist in seeking, numerically, an optimal solution to this system. It should be noted that perfect local matching at the air-ferrite interface ($R_{12\pm} = 0$), assumed in Secs. 2.3, 2.4.1 and 2.4.2, is not mandatory to achieve the desired perfect electromagnetic conductor, since mismatch may be compensated by multiple reflections and phase shift contributions to the overall reflected field. Furthermore, the system (2.23) or (2.24) does not necessarily admit a solution for the available ferrite material, slab thickness, practical bias field, and desired frequency. In this case, the constraints of (2.2) must be relaxed, which leads to an imperfect electromagnetic boundary.

2.4.4 PMC and Free-Space Perfect Electromagnetic Conductor Realizations

Consider first the example of a PMC boundary, with the same parameters as in Fig. 2.4 and for a ferrite slab of thickness $h = 3$ mm (slab to be used in the experiment of Sec. 2.5). Let us consider as staring guess a Faraday rotation angle of 90°. It may be verified from (2.24b) that $\theta = 90°$ indeed makes the cross-polarized component zero, $E_r^y(h) \to 0$, as $\beta_e h \to m\pi$ ($m \in \mathbb{Z}$), which corresponds to the phase coherence condition of the slab to be further discussed in Sec. 2.5.1; at the same time, (2.24a) splits in the two equations $|E_r^z(h)| = 1$ and $\angle E_r^z(h) = 2\pi m$ ($m \in \mathbb{Z}$), which readily corresponds to the PMC situation of a reflected electric field co-polarized with the incident electric field, according to Fig. 2.3a. The simultaneous resolution of these two equations yields several solution pairs $(\mu_0 \mathbf{H}_0, \omega)$. For the parameters selected, one of these pairs with practical values was found to be $(\mu_0 \mathbf{H}_0, \omega) = (0.2\text{ T}, 5.19\text{ GHz})$. The corresponding co- and cross-components of the electric field are plotted in Fig. 2.8. In fact, the magnetic conductor boundary of this design is not perfect: a residual phase shift of $\angle E_r^z(h) = 12.13°$ exists. However, this small deviation from a PMC will be shown in Sec. 2.5 to still provide excellent results, hardly distinguishable from those of a PMC. It should also be noted that $E_r^z(h)$ does not reach exactly the value of one, because of some dissipation due to proximity to the resonance. As an alternative design, one might choose here the frequency of 5.22 GHz, where the phase shift reduces to 0° without introducing significant cross-polarization (case of the TEM waveguide design of Sec. 2.5.2). Another possible improvement, either at the frequency found or at another specified frequency, would be to relax the constraint of $\theta = 90°$ and seek a better solution in terms of $\mu_0 \mathbf{H}_0$ and θ for this frequency. Of course, if the ferrite slab thickness h can be varied, more freedom is available, and most perfect electromagnetic conductors can be achieved accurately.

For the free-space perfect electromagnetic conductor boundary, the reflected electric field

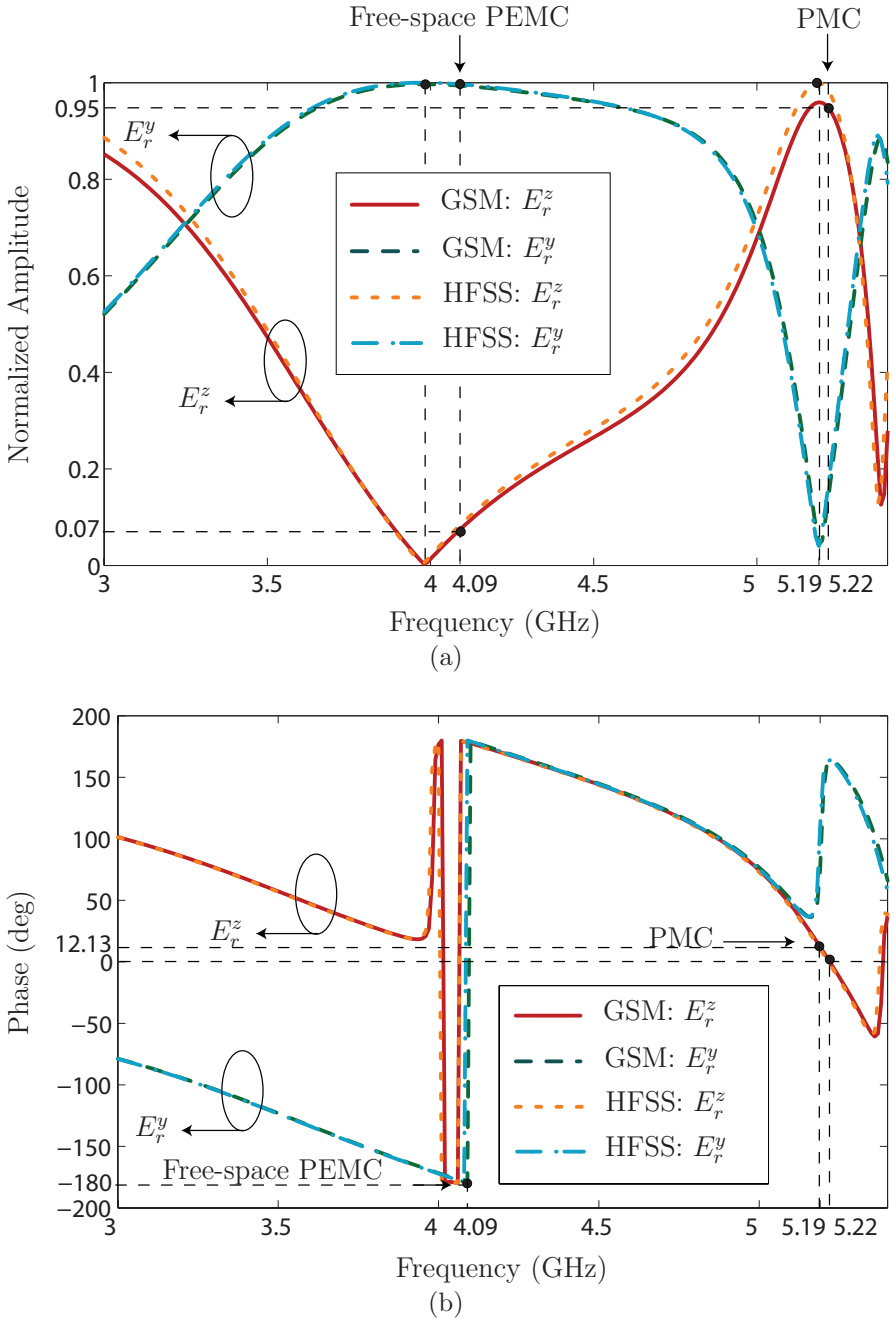

Figure 2.8 Components z and y of the electric field scattered (or reflected) by the grounded ferrite slab computed by the generalized scattering matrix (GSM) method [(2.23)] and compared with HFSS (FEM) results, for a slab of thickness of $h = 3$ mm (sample used in the experiment, Sec. 2.5, and for a Faraday rotation angle of $\theta = 90°$). The ferrite parameters are given in the caption Fig. 2.4, and the bias field $\mathbf{H}_0 = 0.2$ T was obtained from (2.23) as a solution providing the PMC boundary at 5.19 GHz. The incident wave is linearly polarized along the z direction, so the z and y reflected field components correspond to the co- and cross-polarized fields with respect to the incident field. (a) Amplitude. (b) Phase.

should be cross-polarized with respect to the incident electric field, i.e. $E_r^y(h) = 1$ and $E_r^z(h) = 0$, according to Fig. 2.3b. This occurs at 4.09 GHz in Fig. 2.8 where its phase is slightly less than $m\pi$ ($m \in \mathbb{Z}$). The frequency of 4 GHz significantly differs from the 4.7 GHz frequency of Fig. 2.4b, due to the fact that the design was performed (in terms of $\mathbf{H}_0$ and ω) at $\theta = 90°$, far from $\theta = 45°$.

In Fig. 2.8, the generalized scattering matrix results are compared with HFSS (FEM) results, where the transversally infinite slab is emulated by a finite slab surrounded by Floquet boundaries. Excellent agreement is observed between generalized scattering matrix and HFSS results, which both validates the generalized scattering matrix approach and confirms the perfect electromagnetic conductor capability of the proposed grounded ferrite structure.

The proposed PEMC structure does not make an exception to the fundamental tradeoff existing between bandwidth and loss in all resonant materials and structures. Using a ferrite with higher loss, corresponding to a larger line width ΔH, reduces the slope of the $\mu_{e\pm}(\omega)$ functions [see Eq. (2.5) and Fig. (2.4a)], and hence the slopes of both $\beta_e(\omega)$ [Eq. (2.8)] of $\theta(\omega)$ [Eq. (2.3) and Fig. 2.4b]; therefore, the required phase and Faraday rotation angle conditions for the desired boundary will be satisfied over a broader bandwidth. Alternatively, the ferrite may be operated at a larger distance from the ferromagnetic resonance ω_0, where loss is clearly smaller; however, this reduces the magnitude of $\mu_{e\pm}$ [as seen in Fig. (2.4a)], and hence of $\theta(\omega)$ [as seen in Fig. 2.4b], requiring a thicker substrate to compensate, which eventually also increases the loss. So, in all cases a higher bandwidth may be achieved only at the expense of higher loss. A further issue with larger bandwidth is that the subsequent larger loss decreases the magnitude of the reflected fields, leading to imperfectly parallel total (incident + reflected) electric and magnetic fields (Fig. 2.2) and therefore to an imperfect boundary condition. The bandwidth-loss tradeoff also exists in electromagnetic bandgap (EBG) type of artificial magnetic conductor (AMC) surfaces [50, 52], where increasing the bandwidth by complexed metal patterns (e.g. [83]) unavoidably increases the loss.

2.4.5 Effect of Multiple Reflections

To better assess the effects of multiple reflections and related phase shifts, Fig. 2.9 plots the $E_r^z(h)$ (co-polarization) and $E_r^y(h)$ (cross-polarization) components for different number of round-trips inside the ferrite slab. These components are obtained from the iterative

formulas for RHCP/LHCP components, for the normalized incident field $E_i = 1\mathbf{z}$, as

$$\begin{aligned} B^z_{1\pm}(N) =& R_{12_\pm} - T_{12\pm}T_{21\pm}\exp(-j2\beta_\pm h) \\ & \times \sum_{i=1}^{N} \left[-R_{21\pm}\exp(-j2\beta_\pm h)\right]^{i-1}, \end{aligned} \tag{2.25}$$

where N denotes the number of round-trips.

For one round-trip ($N = 1$), a quasi PMC boundary condition is achieved at 4.7 GHz, which, not surprisingly, is equal to the frequency predicted in Fig. 2.4b not taking into account phase shifts and multiple reflections, while the imperfection of the PMC is due to mismatch. For two round-trips ($N = 2$), the PMC point has reached its final frequency of 5.19 GHz, but the free-space perfect electromagnetic conductor point has not converged yet to its final frequency, 4 GHz. For three round trips ($N = 3$), the free-space perfect electromagnetic conductor point has also its final frequency, but the final co-to-cross polarization levels of the PMC (∞) and free-space perfect electromagnetic conductor (0) boundaries have not been reached yet. This is essentially achieved after 7 round trips, beyond which no significant difference compared to the exact formulation with an unlimited number of trips is observed.

The results of Fig. 2.9 show that phase shifts and multiple reflections may have a significant impact on the actual boundary condition seen at the dielectric interface, and must be exactly taken into account for an exact design.

2.4.6 General Perfect Electromagnetic Conductor Admittance

The general perfect electromagnetic conductor boundary admittance Y may be computed by inserting the expressions for the total normally incident plane wave $\mathbf{E}(x) = \mathbf{E}_i\exp[-j\mathbf{k}_0(h-x)] + \mathbf{E}_r\exp[j\mathbf{k}_0(h-x)]$ and $\mathbf{H}(x) = -\frac{1}{\eta_0}\mathbf{x}\times\{\mathbf{E}_i\exp[-j\mathbf{k}_0(h-x)] - \mathbf{E}_r\exp[j\mathbf{k}_0(h-x)]\}$, evaluated at $x = h$, into (2.1a). This yields

$$Y\eta_0\left(\mathbf{E}_i + \mathbf{E}_r\right) = \mathbf{x}\times\left(\mathbf{E}_i - \mathbf{E}_r\right), \tag{2.26}$$

Assuming $\mathbf{E}_i = E^z_i\mathbf{z}$ and writing $\mathbf{E}_r = E^y_r\mathbf{y} + E^z_r\mathbf{z}$ in (2.26), we obtain

$$Y\eta_0\left[E^y_r\mathbf{y} + \left(E^z_i + E^z_r\right)\mathbf{z}\right] = \mathbf{x}\times\left[-E^y_r\mathbf{y} + \left(E^z_i - E^z_r\right)\mathbf{z}\right], \tag{2.27}$$

or

$$Y\eta_0\left[E^y_r\mathbf{y} + \left(E^z_i + E^z_r\right)\mathbf{z}\right] = -\left[\left(E^z_i - E^z_r\right)\mathbf{y} + E^y_r\mathbf{z}\right]. \tag{2.28}$$

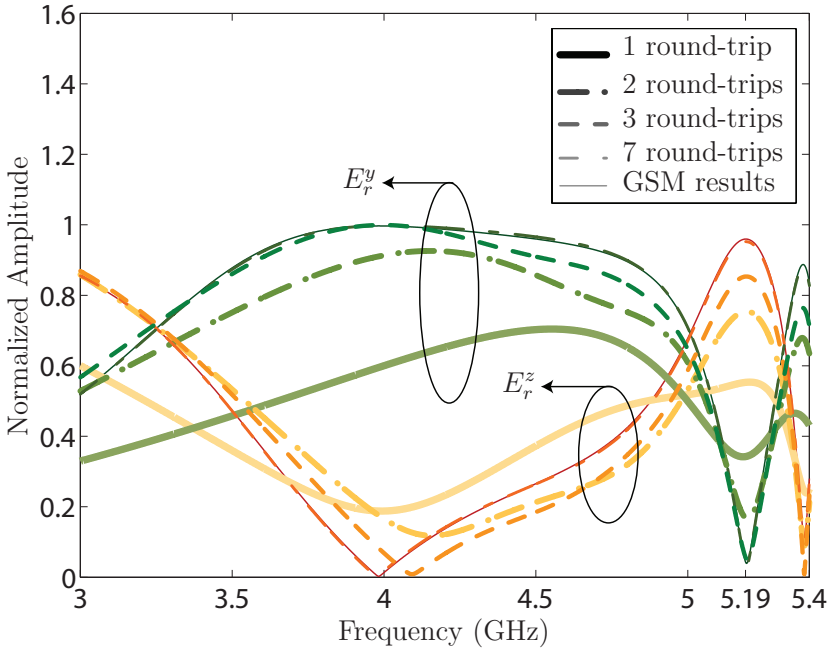

Figure 2.9 Components z (co-polarized) and y (cross-polarized) of the scattered electric field as a function of the number of propagation round trips inside the ferrite slab, computed by (2.25), to show the effect of multiple reflections and related phase shifts caused by mismatch (lossless case).

The y and z components of this equation, respectively, yield the following two distinct expressions for the admittance

$$Y\eta_0 = -\frac{E_i^z - E_r^z}{E_r^y}, \tag{2.29a}$$

$$Y\eta_0 = -\frac{E_r^y}{E_i^z + E_r^z}. \tag{2.29b}$$

However, according to (2.2), the perfect electromagnetic conductor admittance should be a unique value. Therefore, the two expressions for $Y\eta_0$ in (2.29a) and (2.29b) must be equal, which implies

$$(E_r^y)^2 + (E_r^z)^2 = (E_i^z)^2 . \tag{2.30}$$

This relation represents an additional condition for the realization of a perfect electromagnetic conductor boundary by the proposed grounded ferrite structure.

Normalizing again the incident field, $E_i^z = 1$, and substituting the expressions $E_r^z = \pm\sqrt{1-(E_r^y)^2}$ and $E_r^y = \pm\sqrt{1-(E_r^z)^2}$ following (2.30) into (2.29a) and (2.29b), respectively,

the perfect electromagnetic conductor admittance is found as a function of the cross- (E_r^y) and co- (E_r^z) polarized reflected fields as

$$Y\eta_0 = \frac{-1 \mp \sqrt{1-\left(E_r^y\right)^2}}{E_r^y}, \tag{2.31a}$$

$$Y\eta_0 = \mp\sqrt{\frac{1-E_r^z}{1+E_r^z}}. \tag{2.31b}$$

where E_r^z and E_r^y are available analytically in the generalized scattering matrix formulas of (2.23a) and (2.23b), respectively. In these expressions, the signs are determined by the phase shifts occurring in the substrate for the specific design considered.

Following these developments, the complete results for the perfect electromagnetic conductor admittance are summarized in Tab. 2.1.

In the design of Fig. 2.8, it appears that the phase of E_r^y is π, Subsequently substituting $E_r^y = 1\exp(-j\pi)$ and $E_r^z = 0$ of the free-space perfect electromagnetic conductor into (2.29) yields $Y\eta_0 = 1$. Therefore, in this design, the correct sign in (2.31b) is +, and thus $Y\eta_0 = \sqrt{\frac{1-E_r^z}{1+E_r^z}}$. The proper sign in (2.31a) is next found by equalizing this expression with the positive value found for $Y\eta_0$. Figs. 2.10a and 2.10b show the magnitude and phase of $Y\eta_0$, respectively, computed by (2.29) for a lossless grounded ferrite. The perfect electromagnetic conductor condition of (2.30) is satisfied at the frequencies where the curves cross each other. This occurs in the current design at $f = 4.09$ GHz for the free-space perfect electromagnetic conductor case and at $f = 5.22$ GHz for the PMC case. It appears that at the free-space perfect electromagnetic conductor point, $Y\eta_0 = 1.08$ with a phase shift of 0° (ideal situation: $Y\eta_0 = 1, \angle = 0°$), while at the PMC point, $Y\eta_0 = 0.07$ with a phase shift of $\varphi = 0°$ (ideal situation: $Y\eta_0 = 0, \angle = 0$). These results are in agreement with previous observations in Fig. 2.8 and Fig. 2.9.

The effect of loss is quantified in Figs. 2.11a and 2.11b. Losses induce a deviation from the perfect electromagnetic conductor condition of (2.30), particularly at the PMC point in

Table 2.1 Exact perfect electromagnetic conductor (PEMC) boundary conditions with the Faraday grounded ferrite slab.

E_r^z	E_r^y	Boundary	Condition	Admittance Y
arbitrary	arbitrary	general PEMC	$\mathbf{n}\times(\mathbf{H}+Y\mathbf{E}) = \mathbf{n}\cdot(\mathbf{D}-Y\mathbf{B}) = 0$	$\mp\frac{1}{\eta_0}\sqrt{\frac{1-E_r^z}{1+E_r^z}} = \frac{1}{\eta_0}\frac{-1\mp\sqrt{1-\left(E_r^y\right)^2}}{E_r^y}$
0	1	"free-space" PEMC	$\mathbf{n}\times(\mathbf{H}\pm\mathbf{E}/\eta_0) = \mathbf{n}\cdot(\mathbf{D}\mp\mathbf{B}/\eta_0) = 0$	$\pm 1/\eta_0$
1	0	PMC	$\mathbf{n}\times\mathbf{H} = \mathbf{n}\cdot\mathbf{E} = 0$	0
−1	0	PEC	$\mathbf{n}\times\mathbf{E} = \mathbf{n}\cdot\mathbf{H} = 0$	∞

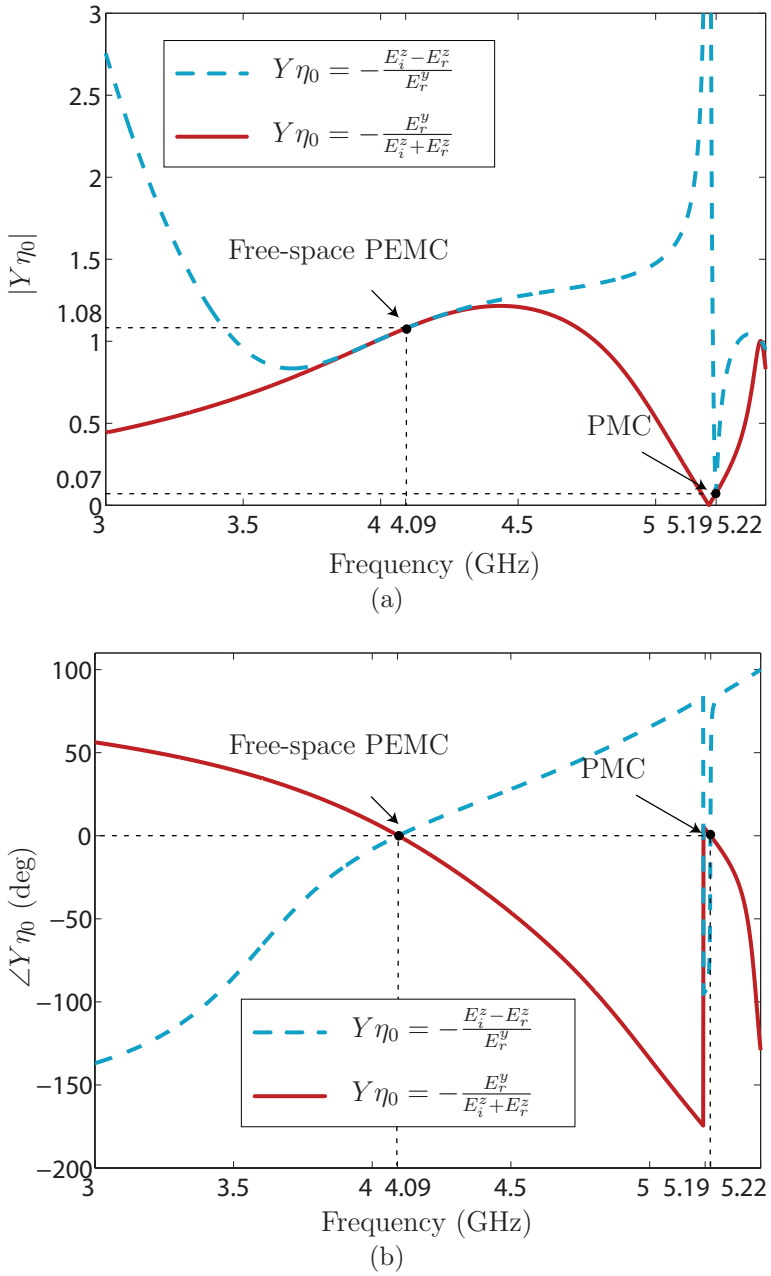

Figure 2.10 Normalized admittance $Y\eta_0$ versus frequency computed by (2.29) from generalized scattering matrix results for the grounded ferrite perfect electromagnetic conductor, assuming a lossless ferrite. (a) Magnitude. (b) Phase.

this design, where the two magnitudes of $Y\eta_0$ are visibly different, so the condition of (2.30) does not hold exactly anymore. In Sec. 2.5.2, we will see that although this PMC boundary is not ideal, it still proves effective for the PMC walls of the TEM waveguide. At the free-space perfect electromagnetic conductor frequency, the effect of loss is less significant, because this point is much farther away from the ferromagnetic resonance frequency, which is 5.5 GHz, as shown in Figs. 2.4.

2.5 PMC-Walls TEM Waveguide

2.5.1 Principle

Conventional hollow waveguides do not support any TEM mode because the transverse voltage gradient in a single-conductor transmission system is zero [51]. However, if the PEC sidewalls of such a waveguide are replaced by PMC walls, then TEM propagation is allowed, since the PMC walls act as "insulators" between the top and the bottom PEC walls so as to provide the required voltage gradient for the existence of a field.

In a transmission line, the TEM mode is cutoff-less and its propagation constant is real and linear (non-dispersive) at all frequencies, $\beta = k_0 = \omega/c$. Consequently, the lateral size of the waveguide does not depend on the operation frequency and, as a result, compared to a conventional waveguide, the structure may be reduced for miniaturization or increased (under the condition that higher modes are properly suppressed) for radiation aperture enhancement. In addition to the cross section, the length of the waveguide is also reduced since the guided wavelength, $\lambda_g = 2\pi/\beta = 2\pi/\sqrt{k_0^2 - (\pi/a)^2}$, where a is the width of the waveguide, is reduced to $\lambda_g = 2\pi/k_0$. The subsequent miniaturization represents an attractive feature of a TEM waveguide.

However, since a PMC does not exist naturally, due to the nonexistence of magnetic charges, it must be generated artificially. In addition, due to causality requirements, such an artificial PMC condition maybe achieved only at *one* frequency. TEM waveguides with artificial PMC sidewalls may be realized in different manners. One approach is to insert dielectric slabs of width $h = \lambda_0/4\sqrt{\varepsilon_{rd} - 1}$ along the sidewalls of the waveguide [84, 85]. Another approach consists in replacing the sidewalls by planar electromagnetic band-gap (EBG) structures [52]. Recently, we demonstrated a grounded ferrite PMC TEM waveguide [80]. We present here, for the sake of illustration of grounded ferrite perfect electromagnetic conductor, an optimized grounded ferrite PMC TEM waveguide, with a deeper description of its operation principle and with a demonstration of its tunability capability.

Fig. 2.12a shows a rectangular waveguide whose PEC sidewalls have been transformed into grounded ferrite PMC walls by inserting ferrite slabs into the waveguide against these

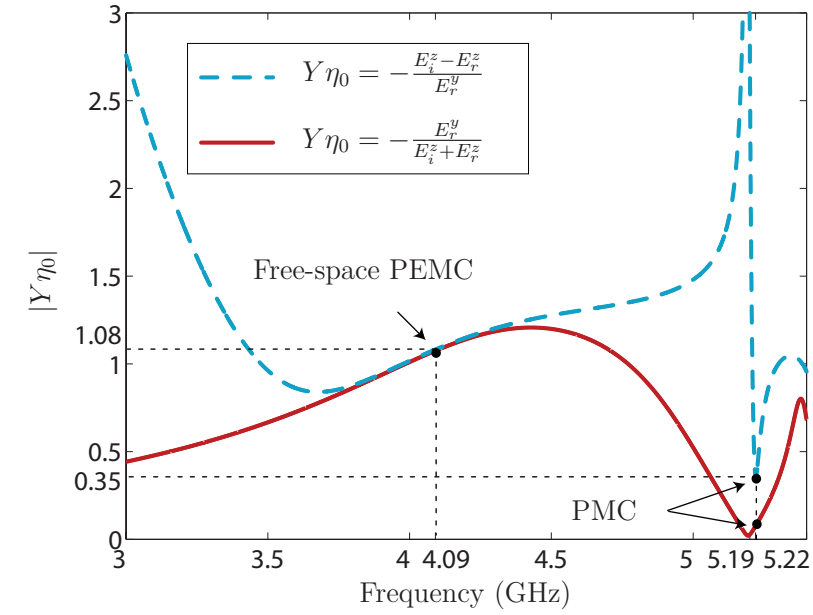

(a)

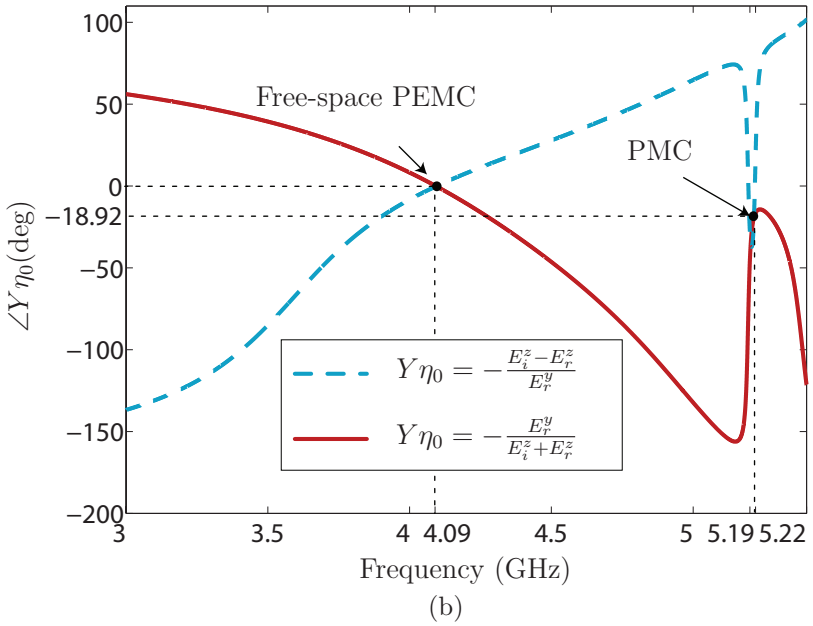

(b)

Figure 2.11 Normalized admittance $Y\eta_0$ versus frequency computed by (2.29) from generalized scattering matrix results for the grounded ferrite perfect electromagnetic conductor, for a lossy ferrite of $\triangle H = 10$ Oe. (a) Magnitude. (b) Phase.

sidewalls. Since $\mathbf{H}_{\tan} = 0$ at the surface of a PMC, we have $\mathbf{H} \| \mathbf{x}$. Moreover, assuming no field variation along y, and considering that $\mathbf{E}_{\text{norm}} = 0$ at the surface of a PMC, we also have $\mathbf{E} \| \mathbf{y}$. This field configuration leads to TEM propagation.

Fig. 2.12b depicts the ray-optic propagation of the TEM wave inside the grounded ferrite PMC waveguide, for which the propagation constants along the x and y directions, β_x and β_y, vanish. As a result, we have in the air region of the waveguide, $\beta^2 = k_0^2 - \beta_x^2 - \beta_y^2 = \omega^2 \mu_0 \varepsilon_0 = k_0$, and thereby a phase velocity equal to the velocity of light, $v_p = \omega/\beta = \omega/k_0 = c$. In fact, the TEM wave propagating in the air region co-exists with a surface wave propagating in the ferrite regions, where the phase shift of each round-trip, $\Delta\phi_f = 2\beta_e h/\cos\psi_t$ [$\psi_t \approx (\psi_{t+} + \psi_{t-})/2$], is equal to the phase shift of the TEM wave in the air $\Delta\phi_a = \beta \Delta z = k_0 2h \tan\psi_t$, as illustrated in Fig. 2.12c. Here, β_e is the *transverse* (x-directed, parallel to $\mathbf{H}_0$) propagation constant, as defined in (2.8), and not the usual *waveguide* longitudinal propagation constant. In order to ensure phase coherence between the air TEM wave and the ferrite surface wave, the equality $\Delta\phi_f = \Delta\phi_a \pm 2m\pi$ ($m \in \mathbb{Z}$) must hold, which leads to the following relation between the wavelength in the air, λ_0, and the *transverse* effective wavelength in the ferrite, $\lambda_e = 2\pi/\beta_e$,

$$\lambda_0/\lambda_e = \sqrt{1 - \cos^2\psi_t} \pm \frac{m\lambda_0 \cos\psi_t}{2h}, \tag{2.32}$$

where it may be noted that in the limit $\psi_t \to 0$ (case of a ferrite with a very high refractive index), this relation simply reduces to $m\lambda_e \to 2h$, which corresponds to a pure transverse resonance inside the ferrite slab.

2.5.2 Full-wave and Experimental Demonstration

To demonstrate the miniaturization of a TEM waveguide using the grounded ferrite PMC structure of Fig. 2.12, a rectangular waveguide (dimensions: $a = 15$ mm and $b = 13$ mm, cutoff: 10 GHz) with the grounded ferrite PMC parameters of Fig. 2.8, operating at $f = 5.2$ GHz, has been designed and compared with a G-band rectangular waveguide (mode: TE_{10}, range: $3.95 - 5.85$ GHz), as shown in Fig. 2.13.

The corresponding full-wave and experimental results are presented in Fig. 2.14. While no signal propagates below cutoff in the empty waveguide [Fig. 2.14a], of course, the grounded ferrite PMC TEM waveguide exhibits a high transmission level (around -1 dB), both in full-wave analysis and in the experiment, at the PMC design frequency of 5.2 GHz. The pass-band of the waveguide is naturally restricted by the dispersion of the ferrite, but it may be sufficient for typical narrow-band applications.

Fig. 2.15 shows that the vectorial electric field distribution in the cross-section of the

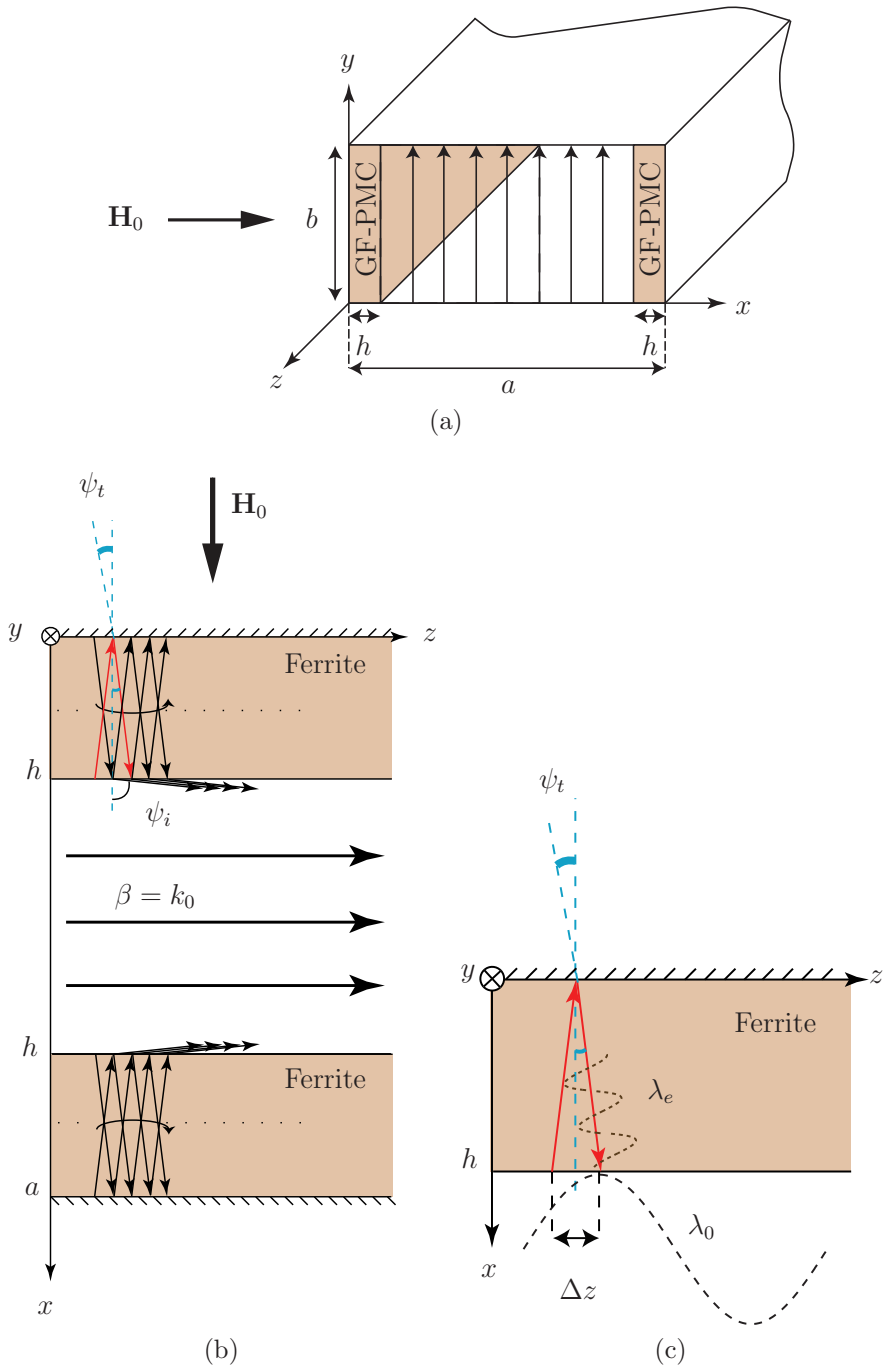

Figure 2.12 Transverse electromagnetic (TEM) rectangular waveguide realized by inserting ferrite slabs against the lateral walls of a rectangular waveguide according to the grounded ferrite PMC (GF-PMC) principle depicted in Fig. 2.3a. (a) Perspective view. (b) Top view with ray-optic illustration of the TEM waveguide phenomenology. (c) Zoom on the ferrite region of (b) to illustrate the phase coherence condition between the TEM wave in the air region and the surface wave in the ferrite slab.

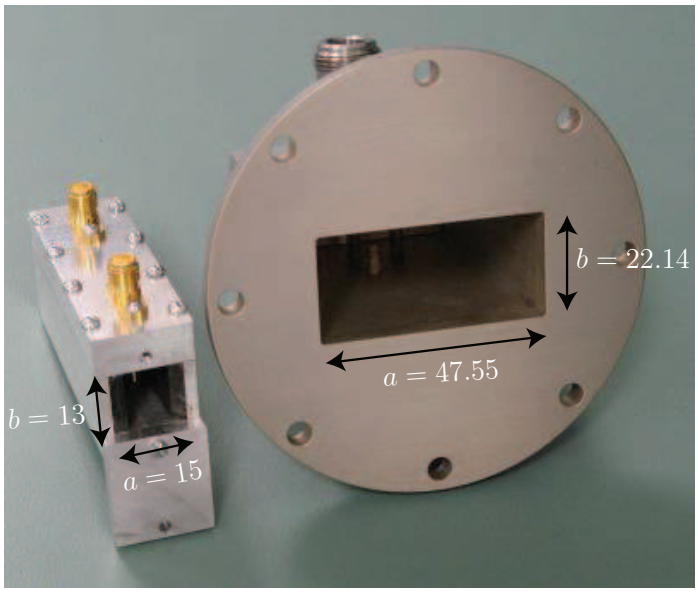

Figure 2.13 Comparison between a G-band rectangular waveguide (3.95 − 5.85 GHz) and a grounded ferrite PMC waveguide (Fig. 2.12) with the parameters of Fig. 2.8 operating in the same frequency range, specifically at $f = 5.2$ GHz, but with a much smaller width (around 3× smaller). The dimensions are in millimeters. The waveguide is excited by a coaxial probe located a quarter-wavelength away from a short-circuiting wall (here removed for visualization).

grounded ferrite PMC waveguide is almost perfectly uniform, as expected for a TEM structure, in contrast to exhibiting the TE_{10} sinusoidal distribution of the empty waveguide, and only marginally departs from the perfectly uniform ideal PMC waveguide distribution near the ferrite interfaces. This slight imperfection is due to the imperfect magnetic boundary condition (Fig. 2.11), but the result is still excellent. In this waveguide design, the phase coherence parameters corresponding to the discussion at the end of Sec. 2.5.1 are $\Delta z = 1.4$ mm, $\lambda_0 = 79.1$ mm ($\Delta z/\lambda_0 = 1/56.5$) and $\lambda_e = 6.1$ mm.

2.5.3 Tunability

The proposed grounded ferrite PMC is a naturally tunable boundary, since varying the bias field changes the frequency of 90° Faraday rotation [10]. Therefore the TEM operation frequency of the grounded ferrite PMC waveguide can be tuned. Figures 2.16a and 2.16b demonstrate this tunability capability.

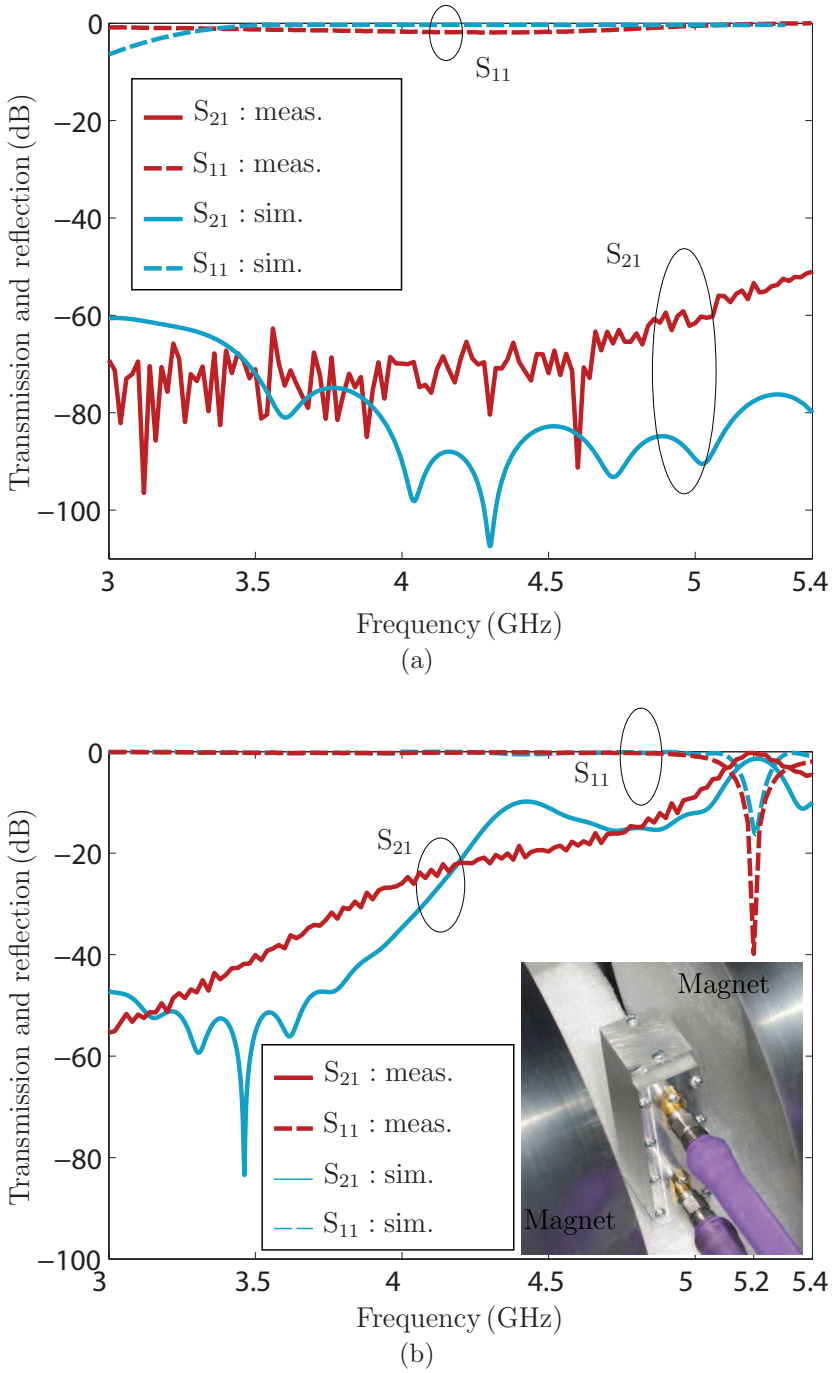

Figure 2.14 Comparative full-wave (CST Microwave Studio) and experimental results for the grounded ferrite PMC TEM rectangular waveguide of Figs. 2.12 and 2.13. (a) Scattering parameters for an empty waveguide of same width, which is a waveguide with cutoff of $f_c = c/(2a) = 10$ GHz. (b) Scattering parameters for the grounded ferrite PMC TEM waveguide. The inset shows grounded ferrite PMC waveguide sandwiched between two biasing magnets.

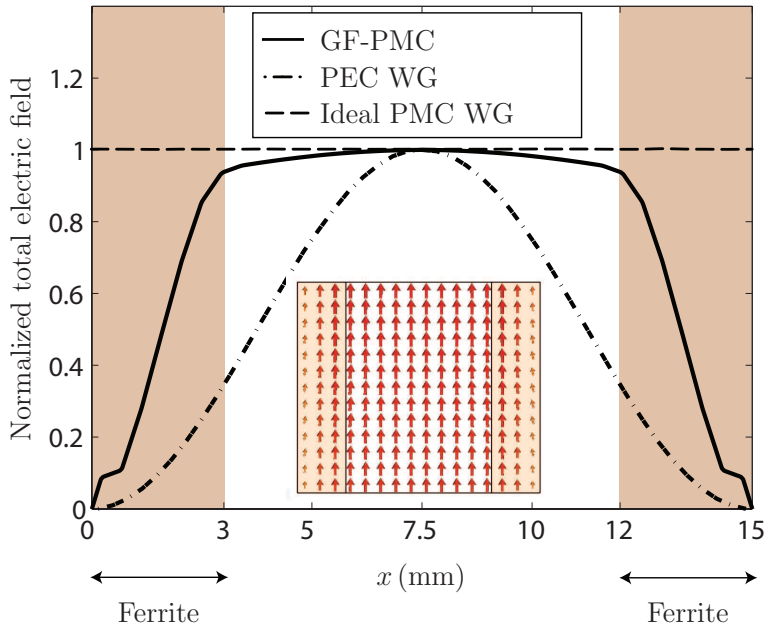

Figure 2.15 Full-wave (CST Microwave Studio) electric field distribution at the half-height of the grounded ferrite PMC (GF-PMC) waveguide of Fig. 2.14b, compared with an ideal PMC waveguide and a PEC waveguide. The inset shows the vectorial field distribution in the entire cross section.

2.6 Conclusion

The realization of arbitrary perfect electromagnetic conductor boundaries by a grounded ferrite slab using Faraday rotation has been proposed, as the first practical realization of a perfect electromagnetic conductor. The structure has been analyzed rigorously by the generalized scattering matrix method, which has been validated by a full-wave commercial software HFSS, to account for mismatch, multiple reflections, phase shifts and loss. The particular case of a grounded ferrite PMC has been demonstrated by full-wave and measurement in the application of a miniaturized and tunable grounded ferrite perfect electromagnetic conductor TEM rectangular waveguide. The grounded ferrite perfect electromagnetic conductor specifically offers a full control over the polarization of the reflected fields, and have therefore a potential for applications in various types of reflectors and radio frequency identifications. As all ferrite components, this structure requires a cumbersome magnet. However, emerging self-biased and integrated nano-structured magnetic materials [86], may soon provide an effective solution to this limitation.

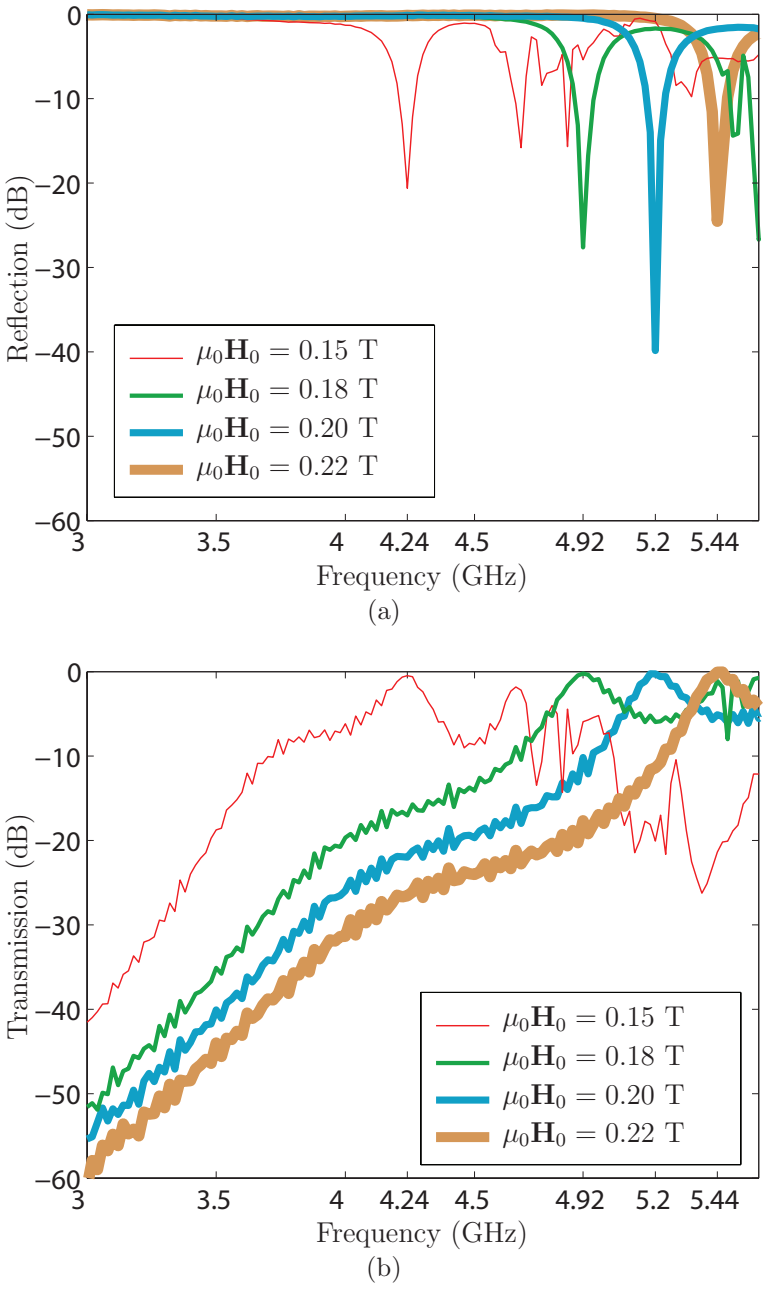

Figure 2.16 Experimental demonstration of the tunability of the grounded ferrite PMC TEM waveguide of Fig. 2.14b with the bias field $\mu_0\mathbf{H}_0$. (a) S_{11}. (b) S_{21}.

CHAPTER 3

ARTICLE 2: BROADBAND AND LOW-BEAM SQUINT LEAKY WAVE RADIATION FROM A UNIAXIALLY ANISOTROPIC GROUNDED SLAB

Attieh Shahvarpour[1], Christophe Caloz[1], and Alejandro Alvarez Melcon[2]
[1]Poly-Grames Research Center, Department of Electrical Engineering,
École Polytechnique de Montréal, Centre de Recherche en Électronique Radiofréquence (CREER),
Montréal, QC, H3T 1J4, Canada.
[2] Universidad Politécnica de Cartagena, 30202 Cartagena, Murcia, Spain.

 A. Shahvarpour, A. Alvarez Melcon, and C. Caloz, "Broadband and low beam-squint leaky-wave radiation from a uniaxially anisotropic grounded slab," *Radio Sci.*, vol. 46, no. RS4006, pp. 1-13, Aug. 2011. doi:10.1029/2010RS004530.

3.1 Abstract

The behavior of leaky and surface modes in uniaxially anisotropic grounded slabs is investigated. First, a TM and TE modal parametric analysis of the structure is performed, based on dispersion relations, comparing the non-dispersive and Drude/Lorentz dispersive anisotropic slabs with an isotropic non-dispersive slab. This analysis reveals that in the case of the isotropic slab, the leaky-wave pointing angle is restricted to the endfire region. In contrast, it is shown, for the first time, that the proposed anisotropic dispersive grounded slab structure provides efficient (in particular highly directive) leaky-wave radiation with a high design flexibility. Toward its lower frequencies, the dominant leaky mode provides full-space conical-beam scanning. At higher frequencies, it provides fixed-beam radiation (at a designable angle) with very low-beam squint. A vertical dipole source is placed inside the slab to excite the relevant leaky-wave mode. The radiation characteristics obtained for this structure confirms the novel low-beam squint and high directivity operation of the dominant leaky mode. Further validation is included using the commercial software tool CST. The structure could be used to conceive antennas either for conical beam-scanning (lower frequency range) or for point-to-point communication and radar systems (higher frequency range).

3.2 Introduction

Leaky-wave antennas feature high directivity and frequency beam scanning capability. They have found many applications in radar, point-to-point communications and MIMO systems. The general theory of leaky-wave antennas and the history of their developments have been reported by [62]. Slitted waveguide [87], holey waveguide [88] and sandwiched line [89] antennas were the first proposed fan-beam leaky-wave antennas, while high-directivity leaky-wave antenna constituted by periodic partially reflective screens over a ground plane [63], or dielectric superstrate layers [64] and several other types performed by various authors [90, 91, 92, 65], enabled the conical-beam radiation.

Over the past decade, intense research has been performed in the area of electromagnetic metamaterials [16, 17, 36]. In the microwave range, transmission line type metamaterials have led to a wealth of component [93, 94]), antenna [95] and system [96] applications. However, most of the planar metamaterial structures were in fact structured transmission lines printed on conventional standard substrate and thus were not "real" metamaterials but rather artificial transmission lines with periodic loads. However, real *meta-substrates*, or artificial dielectric substrates, have recently been introduced [33, 32, 49, 45]. Also, several leaky-wave antennas based on meta-substrates have been reported in the past [41, 42, 66, 67]. However, some of the previous works [41, 42] treated the antenna design problem from an experimental perspective, and detailed indepth studies on the properties and behavior of these new meta-substrates are lacking.

To fill the above gap, this paper presents a detailed investigation of the leaky and surface modes that can propagate in a uniaxially permittivity and permeability anisotropic grounded slab using a spectral domain approach based on transmission line equivalent circuits. The structure is assumed to behave with a Drude dispersive permittivity along the axis perpendicular to the substrate and with a Lorentz permeability in the plane of the substrate. Such a substrate may be implemented in the form of a mushroom-type structure [50, 49, 48], where the Drude dispersive permittivity models the wires and the Lorentz dispersive permeability models the rings between adjacent mushrooms in the plane of the substrate. The complete structure includes two distinct dispersion levels, whose combination leads to the overall structure's dispersion. The first level refers to the dispersive behavior of the grounded slab itself, even present in the case where the slab is isotropic. The second level refers to the Drude and Lorentz model of the artificial materials constituting the slab. It is shown, for the first time, that such a structure can propagate a leaky-wave mode which can support broadband, highly directive and low beam squint radiation in the upper part of the right-handed (RH) region, in contrast to isotropic structures (conventional grounded dielectric slabs). It is also

shown that this novel low beam squint effect cannot be achieved using simple ferrite type materials, even if they also exhibit Lorentz type dispersive permeability response.

A vertical source is introduced in the slab to excite the dominant leaky-mode. By computing the radiation characteristics of this structure the novel low-beam squint and high directivity characteristics of the mode are confirmed. The behavior is further verified using the CST commercial software tool.

The paper first investigates the TM and TE dispersion properties of the uniaxially anisotropic grounded slab. Sec. 3.5 presents a modal parametric analysis, comparing the non-dispersive and Drude/Lorentz dispersive anisotropic slabs with the isotropic non-dispersive slab. As the TM modes are found in this section more appropriate for broadband, low beam squint leaky-wave radiation, Sec. 3.6 employs a vertical point source for the excitation of the TM leaky-modes. Then, the asymptotic far-field radiation properties are computed from the Green functions using the transmission line model of the structure [76]. Finally, in Sec. 3.7 the radiation properties of the isotropic and anisotropic slabs are carefully compared.

3.3 Definition of the Medium

The uniaxially anisotropic medium of interest is represented in Fig. 3.1 along with the TM_z and TE_z field configurations, where z will be the axis perpendicular to the air-dielectric interface in the grounded anisotropic slab which will be studied in Sec. 3.4. The medium is characterized by the following permittivity and permeability tensors

$$\bar{\bar{\varepsilon}} = \begin{pmatrix} \varepsilon_\rho & 0 & 0 \\ 0 & \varepsilon_\rho & 0 \\ 0 & 0 & \varepsilon_z \end{pmatrix}, \tag{3.1a}$$

$$\bar{\bar{\mu}} = \begin{pmatrix} \mu_\rho & 0 & 0 \\ 0 & \mu_\rho & 0 \\ 0 & 0 & \mu_z \end{pmatrix}. \tag{3.1b}$$

For typical artificial substrates, such as mushroom-type structures [50], ε_z and μ_ρ may represent the permittivity and permeability, respectively, due to the presence of the artificial implants, while ε_ρ and μ_z represent the permittivity and permeability, respectively, of a host medium (e.g. teflon) [49].

While the host medium is generally non-dispersive, the constitutive parameters related to the artificial implants are inherently dispersive (i.e. frequency-dependent). In the frequency range where the wires of the mushroom-type structure are electrically short or densely packed

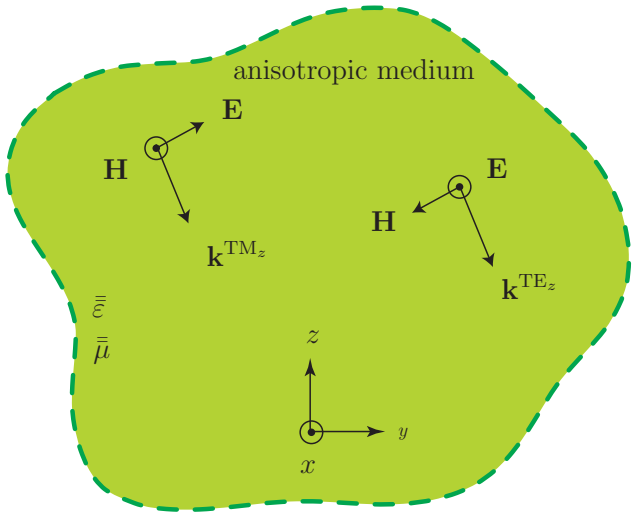

Figure 3.1 Effective uniaxial anisotropic medium (unbounded), characterized by the permittivity and permeability tensors of (3.1) along with the TM_z and TE_z field configurations.

[48], the effective permittivity term ε_z may be modeled by the electric local Drude dispersion expression [12]

$$\frac{\varepsilon_z}{\varepsilon_0} = \varepsilon_r \left[1 - \frac{{\omega_{\mathrm{pe}}}^2}{\omega^2 - j\omega\zeta_{\mathrm{e}}}\right], \tag{3.2}$$

where ε_r is the host medium permittivity, ω_{pe} is the electric plasma frequency, which is related to the lattice constant and ζ_{e} is the damping factor of the structure. Moreover, the effective permeability term μ_ρ may be modeled by the magnetic Lorentz dispersion relation [30]

$$\begin{aligned} \frac{\mu_\rho}{\mu_0} &= 1 - \frac{F\omega^2}{(\omega^2 - {\omega_{\mathrm{m0}}}^2) - j\omega\zeta_{\mathrm{m}}} \\ &= 1 - \frac{F\omega^2}{[\omega^2 - {\omega_{\mathrm{pm}}}^2(1-F)] - j\omega\zeta_{\mathrm{m}}}, \end{aligned} \tag{3.3}$$

where F is a factor related to the geometry of the current loops, ω_{m0} is the resonant frequency of these loops, $\omega_{\mathrm{pm}} = \omega_{\mathrm{m0}}/\sqrt{1-F}$ is the plasma frequency and ζ_{m} is the damping factor of the structure.

Following [49], we assume that the uniaxially anisotropic grounded slab exhibits the dispersive responses of (3.2) and (3.3) in the frequency range of interest. However, at higher frequencies, where the electrical thickness of the substrate becomes relatively large, the permittivity dispersion of (3.2) would have to be modified to follow a non-local model to take into account spatial dispersion [48]. Moreover, as the frequency increases far above the elec-

tric and magnetic plasma frequencies, $\omega_{\rm pe}$ and $\omega_{\rm pm}$, respectively, the artificial mushroom structure progressively looses its homogeneity, since the electrical size of the unit cell grows, and therefore the effective anisotropic medium models of (3.1) with the effective dispersive permittivity and permeability of (3.2) and (3.3), respectively, eventually become inappropriate. However, in the following theoretical study, it is assumed that the medium remains effectively Drude/Lorentz dispersive in a wideband frequency range, as allowed by some unit-cell compression techniques, such as for instance the use of elongated mushroom structures [97] or of nano-structured metamaterials [98]. Such techniques may be used in the future practical implementation of the wideband anisotropic materials.

3.4 Dispersion Relation of the Uniaxially Anisotropic Grounded Slab

Fig. 3.2a shows the grounded uniaxial anisotropic slab of interest. The TM_z and TE_z dispersion relations for this structure are derived by the transverse resonance technique [99] with the help of the source-less transmission line model [75] shown in Fig. 3.2b. They read

$$jZ_c^{\mathrm{TM}_z,\mathrm{TE}_z}\tan\left(\beta_z^{\mathrm{TM}_z,\mathrm{TE}_z}d\right)+Z_{c0}^{\mathrm{TM}_z,\mathrm{TE}_z}=0, \tag{3.4}$$

where $\beta_z^{\mathrm{TM}_z,\mathrm{TE}_z}$and $Z_c^{\mathrm{TM}_z,\mathrm{TE}_z}$ are the TM_z and TE_z phase constants along the z axis and the characteristic impedances of the line, respectively, and

$$\beta_z^{\mathrm{TM}_z}=\pm\sqrt{\omega^2\mu_\rho\varepsilon_z-k_\rho^{\mathrm{TM}_z\,2}}\sqrt{\frac{\varepsilon_\rho}{\varepsilon_z}}, \tag{3.5a}$$

$$Z_c^{\mathrm{TM}_z}=\frac{\pm\sqrt{\omega^2\mu_\rho\varepsilon_z-k_\rho^{\mathrm{TM}_z\,2}}}{\omega\varepsilon_\rho}\sqrt{\frac{\varepsilon_\rho}{\varepsilon_z}}, \tag{3.5b}$$

and

$$\beta_z^{\mathrm{TE}_z}=\pm\sqrt{\omega^2\mu_z\varepsilon_\rho-k_\rho^{\mathrm{TE}_z\,2}}\sqrt{\frac{\mu_\rho}{\mu_z}}, \tag{3.6a}$$

$$Z_c^{\mathrm{TE}_z}=\frac{\omega\mu_z}{\pm\sqrt{\omega^2\mu_z\varepsilon_\rho-k_\rho^{\mathrm{TE}_z\,2}}}\sqrt{\frac{\mu_\rho}{\mu_z}}, \tag{3.6b}$$

where $k_\rho^{\mathrm{TM}_z,\mathrm{TE}_z}=\mathrm{Re}(k_\rho^{\mathrm{TM}_z,\mathrm{TE}_z})+j\mathrm{Im}(k_\rho^{\mathrm{TM}_z,\mathrm{TE}_z})$ are the TM_z and TE_z transverse wave numbers. For later convenience, we also introduce the lighter notations $\mathrm{Re}(k_\rho^{\mathrm{TM}_z,\mathrm{TE}_z})=\beta_\rho$

and $\mathrm{Im}(k_\rho^{\mathrm{TM}_z,\mathrm{TE}_z}) = \alpha_\rho$.

(3.5) and (3.6) are extended transmission line parameters for an anisotropic substrate. They reduce to the standard expressions in the particular case of a conventional isotropic slab [75].

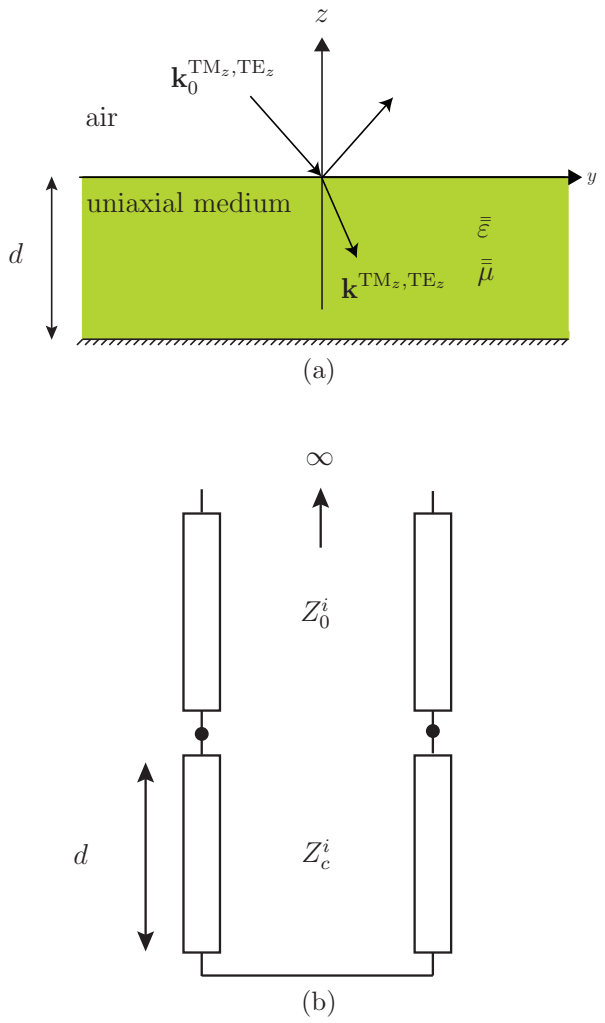

Figure 3.2 Uniaxially anisotropic grounded slab and its transmission line model, where $i \equiv \mathrm{TM}_z, \mathrm{TE}_z$. (a) TM_z and TE_z waves incident onto the slab. (b) Transmission line model (source-less case).

In ((3.4) $Z_{c0}^{\mathrm{TM}_z,\mathrm{TE}_z}$ are the TM_z or TE_z free-space characteristic impedances, respectively,

$$Z_{c0}^{\mathrm{TM}_z} = \frac{k_{z0}^{\mathrm{TM}_z}}{\omega\varepsilon_0}, \tag{3.7a}$$

$$Z_{c0}^{\mathrm{TE}_z} = \frac{\omega\mu_0}{k_{z0}^{\mathrm{TE}_z}}, \tag{3.7b}$$

where $k_{z0}^{\mathrm{TM}_z,\mathrm{TE}_z} = \mathrm{Re}(k_{z0}^{\mathrm{TM}_z,\mathrm{TE}_z}) + j\mathrm{Im}(k_{z0}^{\mathrm{TM}_z,\mathrm{TE}_z})$ are the TM_z and TE_z free-space wave numbers along z and

$$k_{z0}^{\mathrm{TM}_z,\mathrm{TE}_z} = \pm\sqrt{\omega^2\mu_0\varepsilon_0 - k_\rho^{\mathrm{TM}_z,\mathrm{TE}_z{}^2}}. \tag{3.8}$$

The dispersion relations of (3.4) are transcendental. The explicit k_ρ and k_{z0} dispersion curves are obtained numerically by computing their roots versus frequency.

3.5 Dispersion Analysis

In this section, we investigate the effects of uniaxial anisotropy [Eqs. (3.1a) and (3.1b)] and medium dispersion [Eqs. (3.2) and (3.3)] on the behavior [Eq. (3.4)] of the uniaxially anisotropic grounded slab. In order to discriminate these two effects, we first consider the effect of uniaxial anisotropy only (even if such a medium does not exist physically) in Sec. 3.5.1. Later, we add the medium dispersion to determine its specific effect in Sec. 3.5.2.

3.5.1 Effect of Uniaxial Anisotropy (Non-dispersive Medium)

Three case studies will be performed here – two for TM_z modes and one for TE_z modes. For the TM_z modes, we first keep μ_ρ/μ_z constant and vary $\varepsilon_\rho/\varepsilon_z$, to investigate the effect of electric anisotropy. Next (second case), we keep $\varepsilon_\rho/\varepsilon_z$ constant and vary μ_ρ/μ_z, to investigate the effect of magnetic anisotropy. We also consider two different values of $\varepsilon_\rho/\varepsilon_z$ to determine the combined effects of magnetic and electric anisotropies. In the third study, for the TE_z modes, we vary only μ_ρ/μ_z in (3.4) and (3.6), since this is the only parameter related to anisotropy. The three case studies also consider the case of an isotropic grounded slab for comparison.

The first case study (TM_z modes, fixed $\mu_\rho/\mu_z = 1$ and varying $\varepsilon_\rho/\varepsilon_z$) is presented in Fig. 3.3. This figure explicitly indicates, on the dispersion curves of the isotropic case, the surface-waves modes (SW), the leaky-wave modes (LW), and the improper non-physical modes (IN) [62]. These indications are not repeated but can be easily inferred in the cases of Figs. 3.4 and 3.5.

Fig. 3.3 (especially Fig. 3.3a) shows that as $\varepsilon_\rho/\varepsilon_z$ increases, the bandwidth of the surface waves modes decreases progressively until they fully transform into leaky modes. Moreover, the slopes of the resulting leaky modes progressively decrease as $\varepsilon_\rho/\varepsilon_z$ increases, and become almost perfectly flat for electrically very thick slabs, roughly for $d/\lambda_0 > 1/2$ for the parameters considered (λ_0 is the free-space wavelength). This flattening of the dispersive curves has important physical implications and interests for leaky-wave antennas. First, since the

radiation angle of the main beam of a leaky-wave structure is given by $\theta(\omega) \approx \sin^{-1}[\beta_\rho/k_0]$ [62], a flat dispersion curve (i.e. a constant β_ρ/k_0 ratio) leads to a *fixed radiation beam* over a broad bandwidth. This resolves the issue of beam squinting while preserving the leaky-wave benefit of high directivity. This is beneficial to broadband point-to-point communication and sensing applications, where a broadband signal should radiate to a fixed direction without experiencing spatial dispersion of its energy across its spectrum.

Fig. 3.4 shows the results of the second case study (TM_z, fixed $\varepsilon_\rho/\varepsilon_z$ and varying μ_ρ/μ_z). It is seen that the leaky dispersion curves progressively flatten as μ_ρ/μ_z is decreased. Moreover, as expected form the previous study, larger $\varepsilon_\rho/\varepsilon_z$ leads to flatter curves. Therefore, it may be concluded that the flattest (i.e. lowest dispersive) TM response is obtained by maximizing $\varepsilon_\rho/\varepsilon_z$ and minimizing μ_ρ/μ_z.

Fig. 3.5 presents the third case study (TE_z, varying μ_ρ/μ_z).

We observe that the TE_z leaky modes have a very different behavior than the TM_z leaky modes. Here, as μ_ρ/μ_z decreases, the dispersion curves penetrate deeper into the leaky-wave region but they also become more dispersive. Less dispersion flatting is achievable as compared to the TM_z case for a given slab electrical thickness, which makes these modes less attractive for low beam-squint leaky-wave antenna applications. Therefore, in the following, only the TM_z case will be considered.

3.5.2 Effect of Drude/Lorentz Dispersion in Addition to Anisotropy

Sec. 3.5.1 showed that introducing a uniaxial anisotropy of the type given by (3.1a) and (3.1b) into a grounded slab could generate a very broadband quasi non-dispersive leaky-wave TM_z mode, of interest for the low beam-squint radiation of broadband signals. However, as pointed out in Sec. 3.3, the uniaxially anisotropic medium of practical interest are frequency dispersive. So, the question as whether these properties of the grounded slab are preserved in the real case, where the medium exhibits frequency dispersion (in addition to anisotropy), naturally arises. This question will be addressed now.

The permittivity and permeability dispersion curves, given by (3.2) and (3.3), respectively, for the medium of interest (Sec. 3.3), are plotted in Fig. 3.6 for the parameters indicated in the caption (lossless case). The permittivity plasma frequency ω_{pe} and the permeability resonant plasma frequency ω_{pm} are designed to be equal, $\omega_{\mathrm{pe}} = \omega_{\mathrm{pm}} = \omega_{\mathrm{p}}$, so as to avoid the presence of a stop-band between the double-negative and double-positive ε_z and μ_ρ frequency ranges. Moreover, the value ω_{p} ($f = 11$ GHz) was chosen to coincide with the leaky-wave cutoff frequency of the isotropic non-dispersive grounded slab.

The TM_z dispersion curves of the dispersive uniaxially anisotropic grounded slab with the medium dispersion of Fig. 3.6 are shown in Fig. 3.7. They are compared with the isotropic

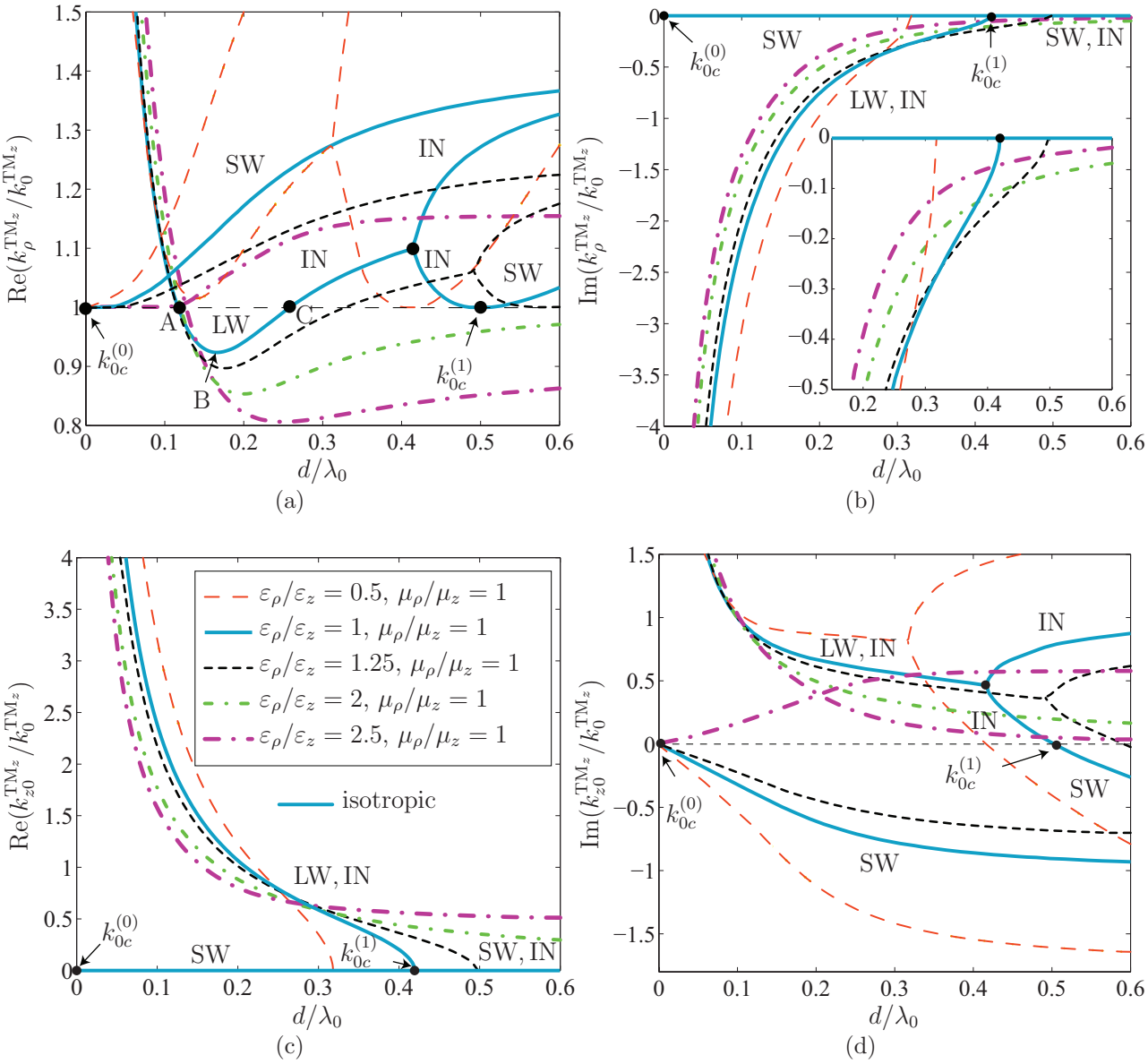

Figure 3.3 TM_z dispersion curves for the uniaxial anisotropic grounded slab with $\varepsilon_\rho = 2\varepsilon_0$ and $\mu_z = \mu_0$, for a fixed μ_ρ/μ_z and various $\varepsilon_\rho/\varepsilon_z$. (a) $\mathrm{Re}(k_\rho^{\mathrm{TM}_z}/k_0^{\mathrm{TM}_z})$. (b) $\mathrm{Im}(k_\rho^{\mathrm{TM}_z}/k_0^{\mathrm{TM}_z})$. (c) $\mathrm{Re}(k_{z0}^{\mathrm{TM}_z}/k_0^{\mathrm{TM}_z})$. (d) $\mathrm{Im}(k_{z0}^{\mathrm{TM}_z}/k_0^{\mathrm{TM}_z})$. The surface-wave (SW), leaky-wave (LW) and improper non-physical (IN) modes are indicated on the curves for the isotropic case. These indications also apply to Figs. 3.4 and 3.5.

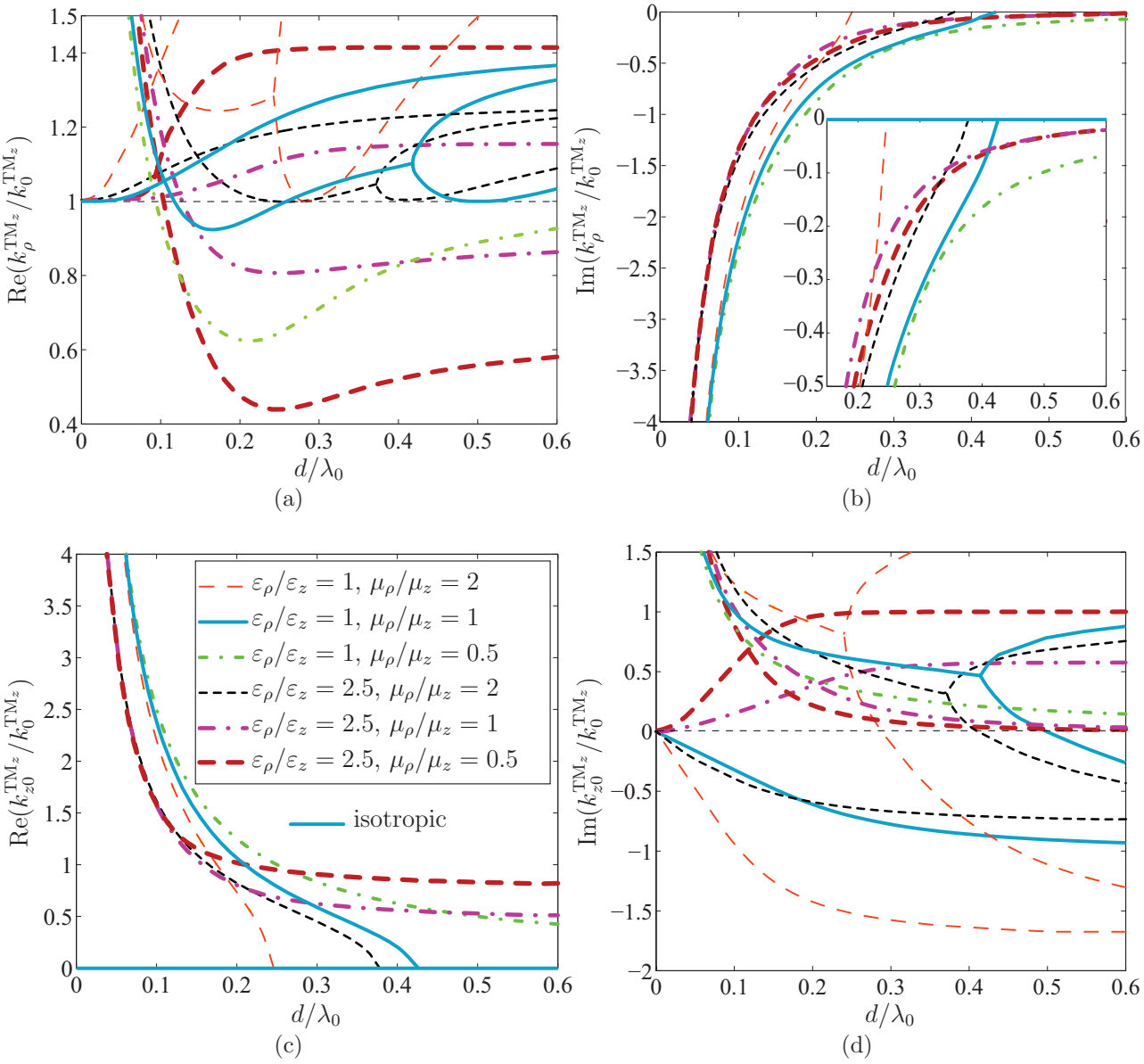

Figure 3.4 TM_z dispersion curves for the uniaxial anisotropic grounded slab with $\varepsilon_\rho = 2\varepsilon_0$ and $\mu_z = \mu_0$, for a fixed $\varepsilon_\rho/\varepsilon_z$ and various μ_ρ/μ_z. (a) $\mathrm{Re}(k_\rho^{\mathrm{TM}_z}/k_0^{\mathrm{TM}_z})$. (b) $\mathrm{Im}(k_\rho^{\mathrm{TM}_z}/k_0^{\mathrm{TM}_z})$. (c) $\mathrm{Re}(k_{z0}^{\mathrm{TM}_z}/k_0^{\mathrm{TM}_z})$. (d) $\mathrm{Im}(k_{z0}^{\mathrm{TM}_z}/k_0^{\mathrm{TM}_z})$.

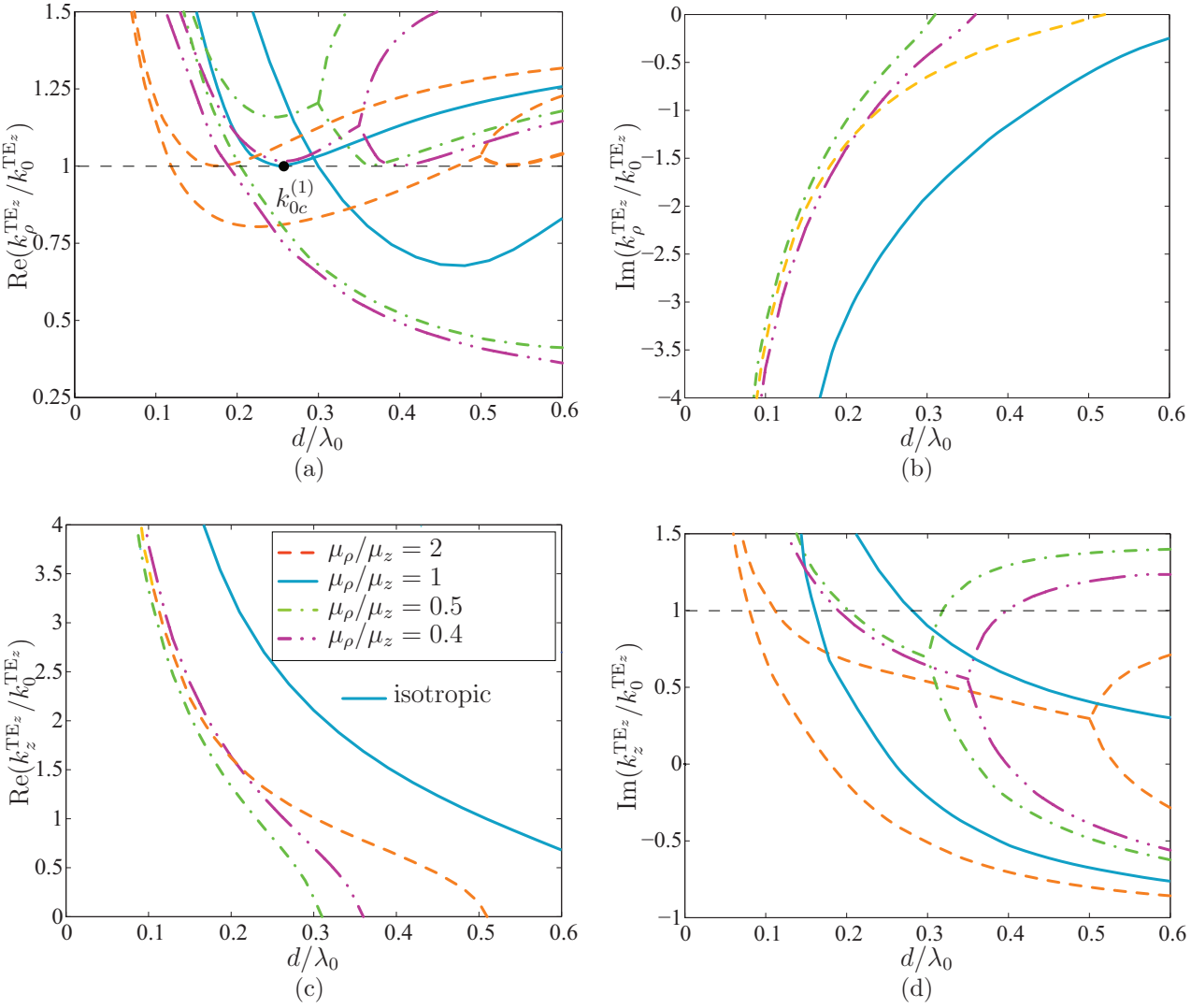

Figure 3.5 TE_z dispersion curves for the uniaxial anisotropic grounded slab with $\varepsilon_\rho = 2\varepsilon_0$ and $\mu_z = \mu_0$, for a fixed $\varepsilon_\rho/\varepsilon_z = 1$ and various μ_ρ/μ_z. (a) $\mathrm{Re}(k_\rho^{\mathrm{TE}_z}/k_0^{\mathrm{TE}_z})$. (b) $\mathrm{Im}(k_\rho^{\mathrm{TE}_z}/k_0^{\mathrm{TE}_z})$. (c) $\mathrm{Re}(k_z^{\mathrm{TE}_z}/k_0^{\mathrm{TE}_z})$. (d) $\mathrm{Im}(k_z^{\mathrm{TE}_z}/k_0^{\mathrm{TE}_z})$.

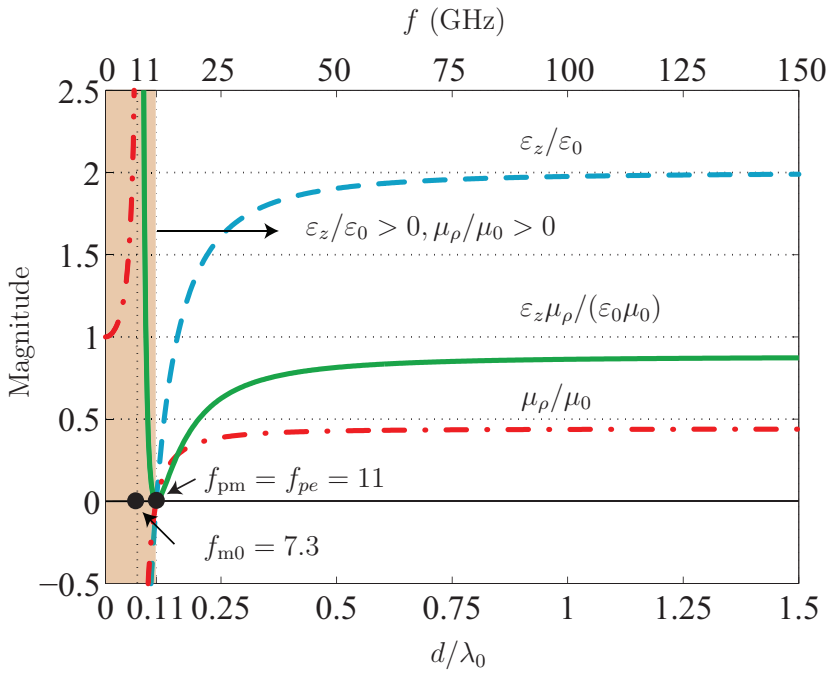

Figure 3.6 Dispersive response for the permittivity $\varepsilon_z/\varepsilon_0$ (Drude model) [Eq. (3.2)] and permeability μ_ρ/μ_0 (Lorentz model) [Eq. (3.3)] for equal electric and magnetic plasma frequencies ($\omega_{\rm pe} = \omega_{\rm pm}$). The parameters are: $F = 0.56$, $\omega_{\rm m0} = 2\pi \times 7.3 \times 10^9$ rad/s, fixing $\omega_{\rm pm} = \omega_{\rm m0}/\sqrt{1-F} = 2\pi \times 11 \times 10^9$ rad/s, $\varepsilon_r = 2$, $\omega_{\rm pe} = \omega_{\rm pm}$, $\zeta_{\rm e} = 0$ and $\zeta_{\rm m} = 0$. The substrate thickness is $d = 3$ mm.

non-dispersive (in terms of the slab medium) and the anisotropic non-dispersive (in terms of the slab medium) cases.

Fig. 3.7 reveals that the low beam-squint property is preserved after the introduction of real medium dispersion, since the anisotropic dispersive (physical) curves still remain very flat. The magnitude of the leakage factor of the anisotropic dispersive mode is comparable to that of a typical leaky-wave antenna, thus allowing high directivity leaky-wave radiation [62].

3.6 Far-Field Radiation Analysis

3.6.1 Green Functions for Vertical Point Source

Sec. 3.5 revealed that the TM_z modes are appropriate for broadband, highly directive and low beam-squint leaky-wave radiation. Such TM_z modes may be excited by a vertical point source excitation embedded in the substrate, as shown in Fig. 3.8a. This excitation reads in the spectral domain $\tilde{\mathbf{J}} = 1/(2\pi)\delta(z - z')\mathbf{a}_z$. The corresponding equivalent transmission line model is shown in Fig. 3.8b, where the vertical point source is modeled by the series voltage

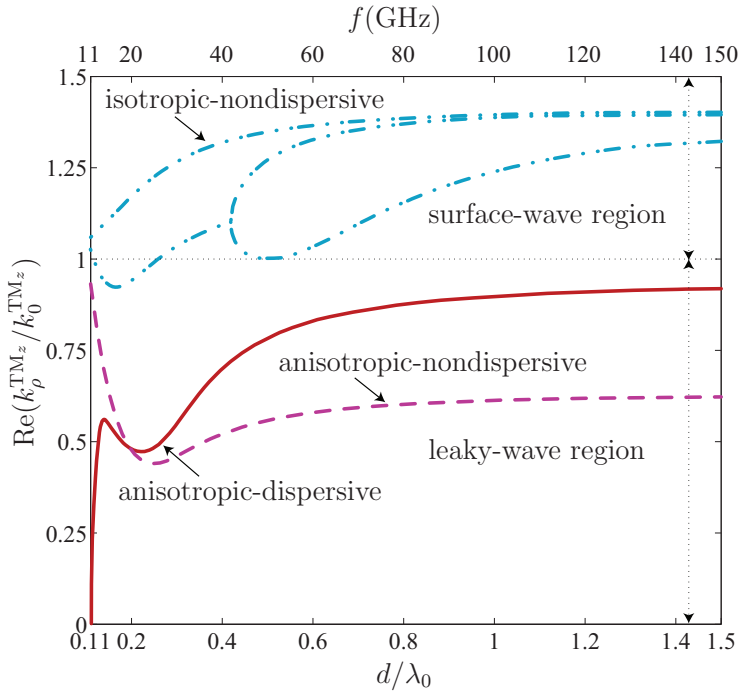

(a)

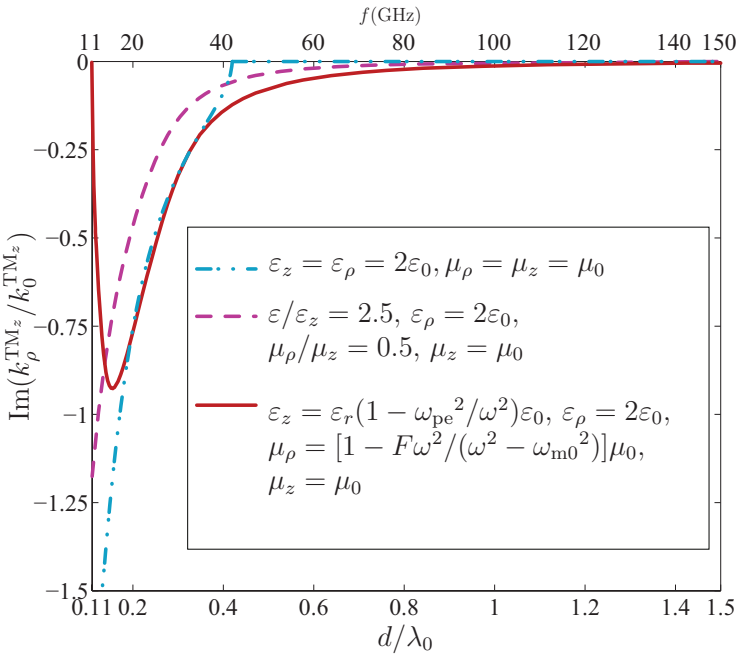

(b)

Figure 3.7 Comparison of the dispersions of the first TM_z leaky modes for different grounded slabs: non-dispersive (slab medium) isotropic ($\varepsilon_z = \varepsilon_\rho = 2\varepsilon_0, \mu_\rho = \mu_z = \mu_0$), non-dispersive (slab medium) anisotropic ($\varepsilon_\rho/\varepsilon_z = 2.5$, $\varepsilon_\rho = 2\varepsilon_0$, $\mu_\rho/\mu_z = 0.5$, $\mu_z = \mu_0$), and dispersive anisotropic ($\varepsilon_z = \varepsilon_r(1 - \omega_{pe}{}^2/\omega^2)\varepsilon_0$ with $\varepsilon_r = 2$, $\varepsilon_\rho = 2\varepsilon_0$, $\mu_\rho = [1 - F\omega^2/(\omega^2 - \omega_{m0}{}^2)]\mu_0$, $\mu_z = \mu_0$). (a) $\mathrm{Re}(k_\rho^{TM_z}/k_0^{TM_z})$. (b) $\mathrm{Im}(k_\rho^{TM_z}/k_0^{TM_z})$. The non specified parameters are equal to those of Fig. 3.6.

source $V_g = |\tilde{\mathbf{J}}| = J_z$ [100] . Using Sommerfeld's choice for the potentials [76], the far fields can be entirely determined by the $\tilde{G}_{\mathrm{A}}^{zz}$ component of the spectral-domain magnetic vector potential dyadic Green function $\bar{\bar{G}}_{\mathrm{A}}$.

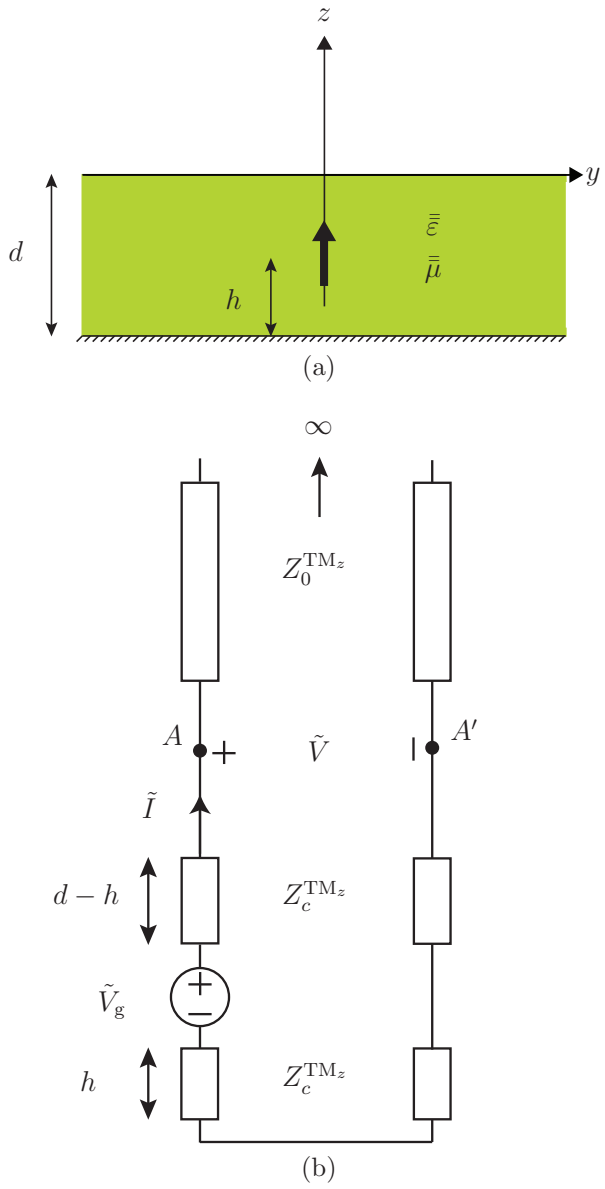

Figure 3.8 Uniaxially anisotropic grounded slab excited by an embedded vertical point source. (a) Physical structure. (b) Transmission line model.

By substituting (3.1) into the spectral-domain Maxwell equations with the above source $\tilde{\mathbf{J}}$ and manipulating the resulting relations, the following relevant equations are found

$$\frac{d^2}{dz^2}\left[\frac{-\omega\varepsilon_z}{k_x^{\mathrm{TM}_z}}\tilde{G}_{\mathrm{EJ}}^{xz,\mathrm{TM}_z}\right] = -\frac{\varepsilon_\rho}{\varepsilon_z}k_z^{\mathrm{TM}_z 2}\left[\frac{-\omega\varepsilon_z}{k_x^{\mathrm{TM}_z}}\tilde{G}_{\mathrm{EJ}}^{xz,\mathrm{TM}_z}\right] + \frac{d}{dz}\tilde{J}_z, \tag{3.9a}$$

$$\frac{d}{dz}\left[\frac{-\omega\varepsilon_z}{k_x^{\mathrm{TM}_z}}\tilde{G}_{\mathrm{EJ}}^{xz,\mathrm{TM}_z}\right] = -j\frac{k_z^{\mathrm{TM}_z}}{\omega\varepsilon_z}k_z^{\mathrm{TM}_z}\left[\frac{-\omega^2\varepsilon_z^2}{{k_\rho^{\mathrm{TM}_z}}^2}\tilde{G}_{\mathrm{EJ}}^{zz,\mathrm{TM}_z}\right], \tag{3.9b}$$

to map the transmission line equations

$$\frac{d^2\tilde{V}}{dz^2} + ZYk_z^2\tilde{V} = \frac{dV_{\mathrm{g}}}{dz}, \tag{3.10a}$$

$$\frac{d\tilde{V}}{dz} = -jZk_z\tilde{I}. \tag{3.10b}$$

By identifying (3.10a) with (3.9a) and (3.10b) with (3.9b), we next obtain the Green functions

$$\tilde{G}_{\mathrm{EJ}}^{xz,\mathrm{TM}_z} = \frac{-k_x^{\mathrm{TM}_z}}{\omega\varepsilon_z}\tilde{V}, \tag{3.11a}$$

$$\tilde{G}_{\mathrm{EJ}}^{zz,TM_z} = \frac{-{k_\rho^{\mathrm{TM}_z}}^2}{\omega^2\varepsilon_z^2}\tilde{I}, \tag{3.11b}$$

where $\tilde{V}$ and $\tilde{I}$ are the spectral domain voltage and current along the equivalent transmission line (see Fig. 3.8b). Next, the relevant magnetic field Green function components are obtained by substituting (3.11) into Maxwell equations

$$\tilde{G}_{\mathrm{HJ}}^{xz,\mathrm{TM}_z} = \frac{k_y^{\mathrm{TM}_z}}{\omega\varepsilon_z}\tilde{I}, \tag{3.12}$$

while $\tilde{G}_{\mathrm{HJ}}^{zz,\mathrm{TM}_z} = 0$ because it is a TM_z mode. The sought for Green function $\tilde{G}_{\mathrm{A}}^{z}z$ is finally obtained by inverting the relation

$$\bar{\bar{\mathbf{G}}}_{\mathrm{HJ}} = \bar{\bar{\mu}}^{-1}\nabla\times\bar{\bar{\mathbf{G}}}_{\mathrm{A}}, \tag{3.13}$$

which yields

$$\tilde{G}_{\mathrm{A}}^{zz} = \frac{-j\mu_\rho}{\omega\varepsilon_z}\tilde{I}. \tag{3.14}$$

These Green functions have been computed following the same procedure as in [100] with extension to the case of uniaxial anisotropy.

3.6.2 Asymptotic Far-Field Expressions

The far field radiated by a z-directed source in a layered medium may be written in terms of the corresponding Green function at the interface with air (at AA' in Fig. 3.8b), $\tilde{G}_{\mathrm{A}}^{zz}(k_x, k_y)$, as $\tilde{g}_{\mathrm{A}}^{zz}(k_x, k_y, z) = \tilde{G}_{\mathrm{A}}^{zz}(k_x, k_y) \exp(-jk_{z0}z)$. The double Fourier transform relating the spectral to the spatial domain Green function reduces then to the value of the integrand at the saddle point [75, 101, 11], resulting in

$$g_{\mathrm{A}}^{zz}(k_x, k_y, z) = jk_0 \cos\theta \tilde{G}_{\mathrm{A}}^{zz}(k_x, k_y) \frac{\exp(-jk_0 r)}{r}, \tag{3.15}$$

The electric field is then calculated from (3.15) as follows [76]

$$E_\theta(x, y, z) = \frac{-1}{2} \omega k_0 \sin(2\theta) \tilde{G}_{\mathrm{A}}^{zz}(k_x, k_y) \frac{\exp(-jk_0 r)}{r}, \tag{3.16}$$

while $E_\phi(x, y, z) = 0$. Equation 3.16 represents the complete far field, which includes contributions from leaky-waves, related to the poles of $\tilde{G}_{\mathrm{A}}^{zz}(k_x, k_y)$ [11], and from the space wave, corresponding to the direct radiation of the dipole to free space through the substrate.

Figure 3.9a compares the theoretical [Eq. (3.16)] and full-wave fields, obtained with CST, radiated by a vertical point source. This source is located at $h = 1.5$ mm from the ground plane in the anisotropic grounded slab [Fig. 3.8a] at $f = 51$ GHz, where $k_\rho/k_0 = 0.78 - j0.07$ (Fig. 3.7) for the parameters of Fig. 3.6. The CST setup emulates the theoretical infinite substrate by a grounded slab of $35\lambda_0 \times 35\lambda_0$ mm terminated by open boundaries, and emulates the point source by a small discrete current source. The figure shows good agreement between theoretical and full-wave results, thus validating the theory presented.

3.7 Leaky-Wave Properties Discussion

In this section, the behavior and the performance of isotropic and double anisotropic (i.e. anisotropic in terms of both the permittivity and permeability) grounded-slabs excited by a vertical point source are compared with the help of the dispersion and the far-field radiation results presented in Secs. 3.5 and 3.6.2, respectively.

3.7.1 Inappropriateness of the Isotropic Structure

The leaky wave radiation from an isotropic grounded slab has several important limitations, due to the following reasons:

– *The leaky-wave pointing angle θ_p is restricted to a small angular range near endfire.* For instance, this range is limited to $68° - 90°$ in Fig. 3.10a. This represents a severe limitation in planar antenna applications, where radiation capability close to broadside

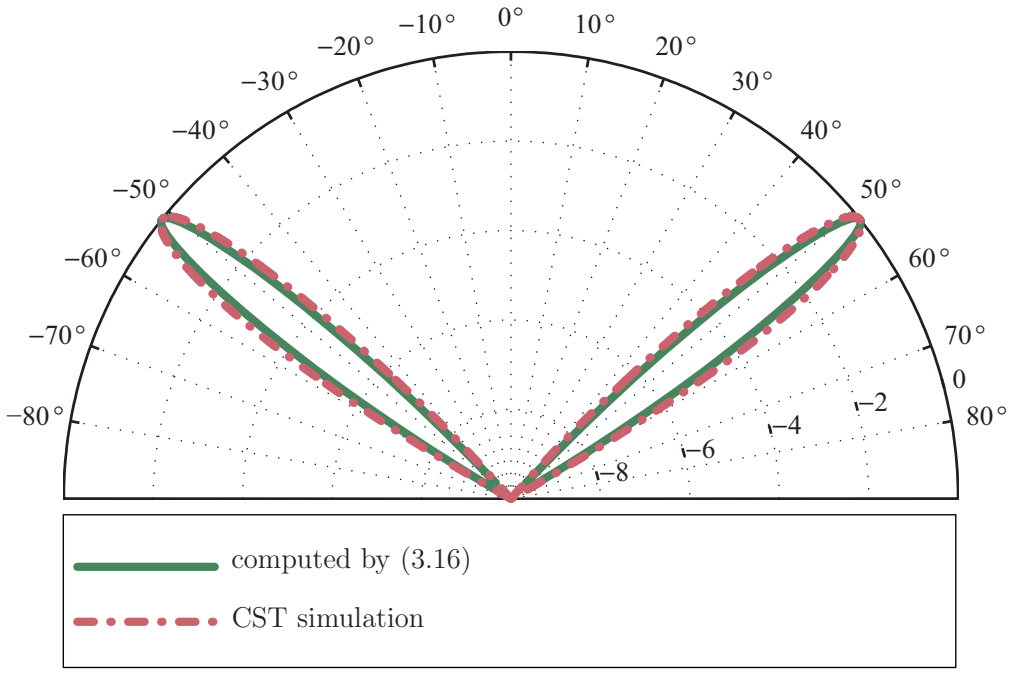

(a)

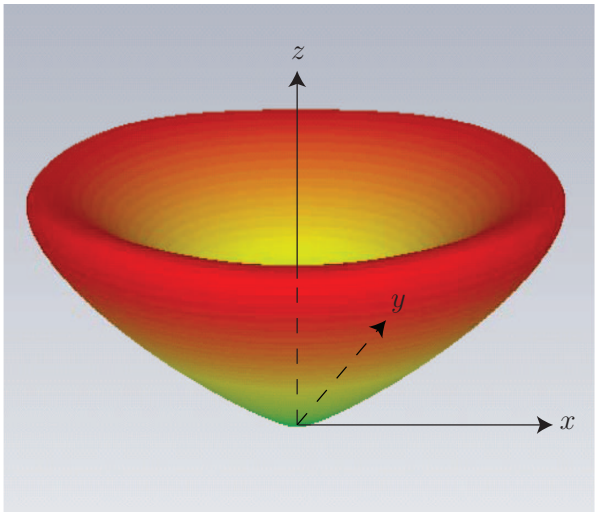

(b)

Figure 3.9 Radiation pattern for a vertical point source located at $h = 1.5$ mm from the ground plane in the anisotropic grounded slab [Fig. 3.8a] at $f = 51$ GHz where $k_\rho/k_0 = 0.78 - j0.07$ (Fig. 3.7) for the parameters of Fig. 3.6. (a) Comparison between theory [Eq. (3.16)] and full-wave (FIT-CST) simulation results. (b) 3D conical pattern.

is usually required, particularly in flush-mounted antenna systems including obstacles in the plane of the antenna. This angular range restriction of θ_p is related, via the scanning law $\theta_\mathrm{p} \simeq \sin^{-1}(\beta_\rho/k_0)$ [62], to the fact that the phase constant β_ρ, cannot reach values significantly smaller than k_0, as shown in Fig. 3.10a. This is due to the relatively small

permittivity ($\varepsilon_r = 2$ in Fig. 3.10a) of the slab. At small permittivities, leakage to free-space is eased by the fact that the wave experiences little trapping inside the slab (no trapping at all in the limiting case $\varepsilon_r \to 1$). As a result, the leakage factor α_ρ (radiation per unit length) is also relatively large, since all the energy tends to radiate directly from the dipole. This behavior is apparent in Fig. 3.3a (solid blue curve). Leakage occurs along the valley-like dispersion curve between points A and C in this graph. As the electrical thickness of the substrate decreases below C, β_ρ decreases to reach a minimum in the leaky-wave region at B. Then, the curve increases again towards k_0 to finally penetrate into the non-physical region at A. As the permittivity increases, the wave becomes more and more trapped inside the slab, and tends to propagate at smaller angles (smaller β_ρ). This results in a deeper penetration into the leaky-wave region, leading to smaller angles of radiation toward the broadside direction, as shown in Fig. 3.11. However, the extension in the scanning range is accompanied with a severe loss of directivity and bandwidth reduction, as will be shown below.

– Due to the effect of wave guidance in the slab, the far-field radiation exhibits a null at endfire, as shown by the $\cos\theta$ factor in (3.15). Therefore, due to this angular factor *the contribution of the leaky wave to the total radiation tends to be suppressed*, since directive and useful leaky-wave radiation occurs only near endfire according to the previous point. As a consequence, radiation is mostly dominated by a space wave, whose beam direction is dictated by the electrical thickness of the substrate. Fig. 3.12 shows the radiation patterns for the isotropic slab computed by (3.16) for various frequencies along the leaky-wave dispersion curve of Fig. 3.10a and at one non-physical frequency where no leaky wave can exist (Fig. 3.7a). Figure 3.12 shows that the radiation angles at these frequencies point at around $\theta = 45°$, which does not correspond at all to the angles predicted by the leaky-wave scanning law in Fig. 3.10a. This also applies to the non-physical grounded-slab frequency (27 GHz). Thus, radiation is not due to the leaky wave but to the space wave. Such a wave does not allow scanning and provides little radiation directivity, as discussed in the next point.

– *The directivity of the structure is low* ($D = 6.61$ dBi at $f = 24.2$ GHz in Fig. 3.12). The leaky-mode radiation, in addition to being limited to the endfire region, it also exhibits a very poor directivity due to the large magnitude of its leakage factor $|\alpha_\rho|$, as shown in Fig. 3.7b. As a result, the aperture size becomes extremely small, which leads to a very low directivity. On the other hand, the space wave, producing the pattern shown in Fig. 3.12, also does not provide high directivity due to its direct radiation to free space.

– *The radiation efficiency (both for the leaky and space waves) is further reduced by the*

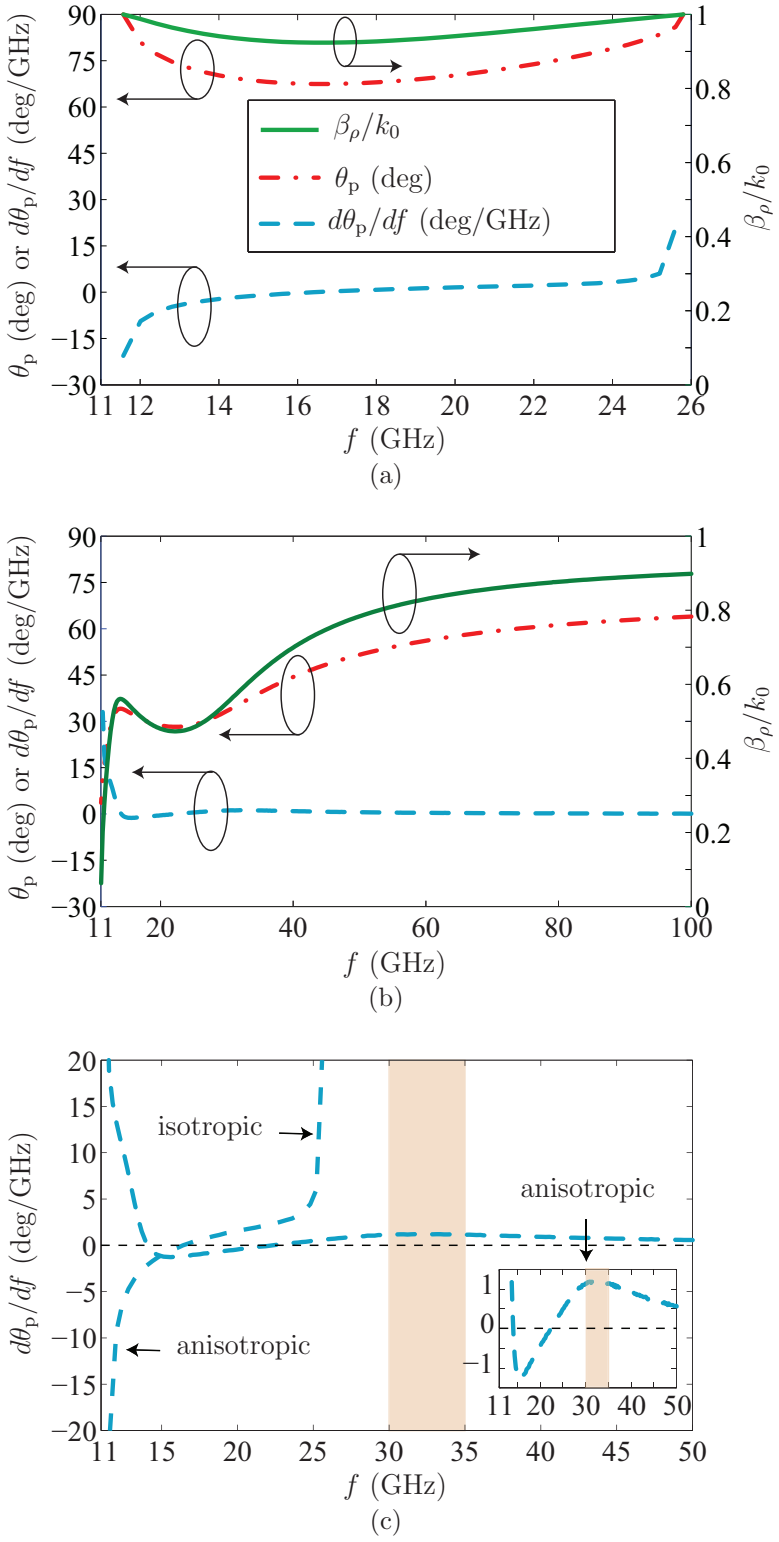

Figure 3.10 Pointing angle of the leaky mode and its variation over frequency calculated from $\theta_\mathrm{p} = \sin^{-1}(\beta_\rho/k_0)$ (*Leaky-Wave Antennas*, by A. Oliner and D. Jackson, 2007) for the slab with the dispersion curves of Fig. 3.7 and $d = 3$ mm. (a) Isotropic slab with $\varepsilon_z = \varepsilon_\rho = 2\varepsilon_0$, $\mu_\rho = \mu_z = \mu_0$. (b) Anisotropic slab with $\varepsilon_z = \varepsilon_r(1 - {\omega_\mathrm{pe}}^2/\omega^2)\varepsilon_0$, $\varepsilon_\rho = 2\varepsilon_0$, $\mu_\rho = [1 - F\omega^2/(\omega^2 - {\omega_\mathrm{m0}}^2)]\mu_0$, $\mu_z = \mu_0$. (c) Comparison of the variations of the pointing angle with respect to frequency for the isotropic and anisotropic substrates.

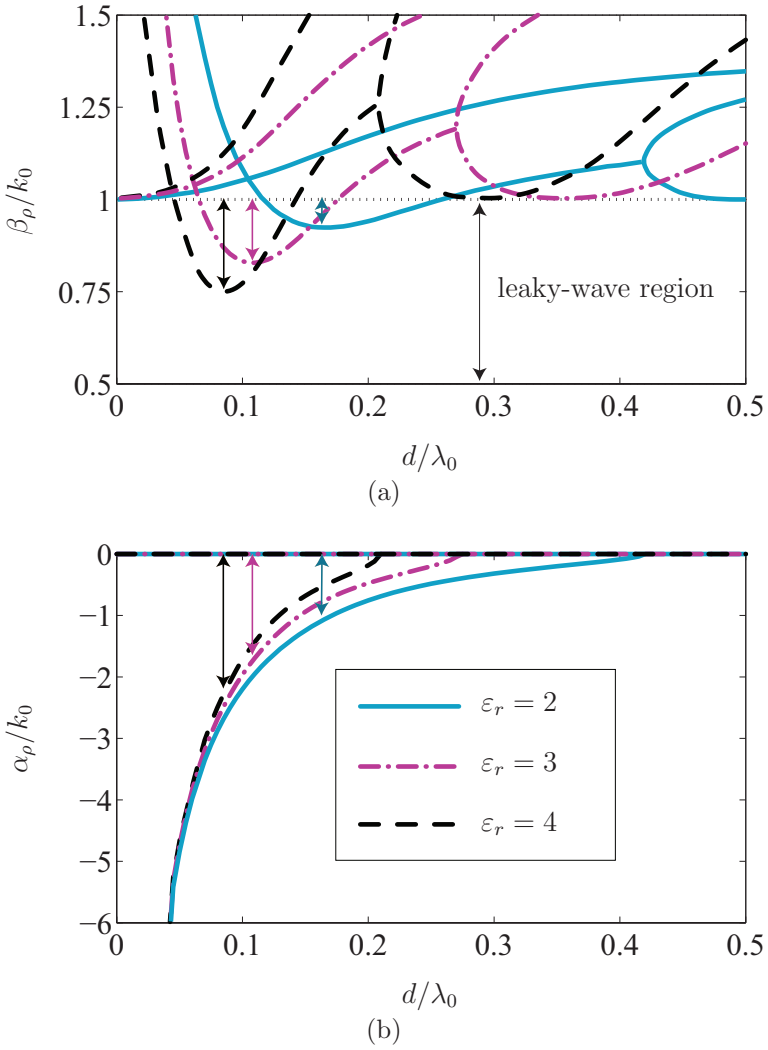

Figure 3.11 Comparison of the leaky-wave behavior of the isotropic grounded slab for different permittivities ($\varepsilon_r = 2, 3, 4$), with $\mu_r = 1$ and $d = 3$ mm.

propagation of the first (cutoff-less) TM_0 surface mode at all frequencies (especially higher), as shown in Fig. 3.7a. This surface mode not only reduces the efficiency by forcing the guidance of part of energy from the source, but also generates diffraction at the end of a practical substrate, which induces back radiation and spurious ripples in the forward radiation pattern.

– *The leaky-mode bandwidth is very narrow.* In fact, there is a trade-off between bandwidth and minimum pointing angle, as shown in Fig. 3.11. Larger bandwidths are achievable with lower permittivities, but this restricts the pointing angle to the deep endfire region. Fig. 3.13 further reveals that the leaky-mode bandwidth decreases as the permittivity is increased, as a result of the decrease of the critical angle of total

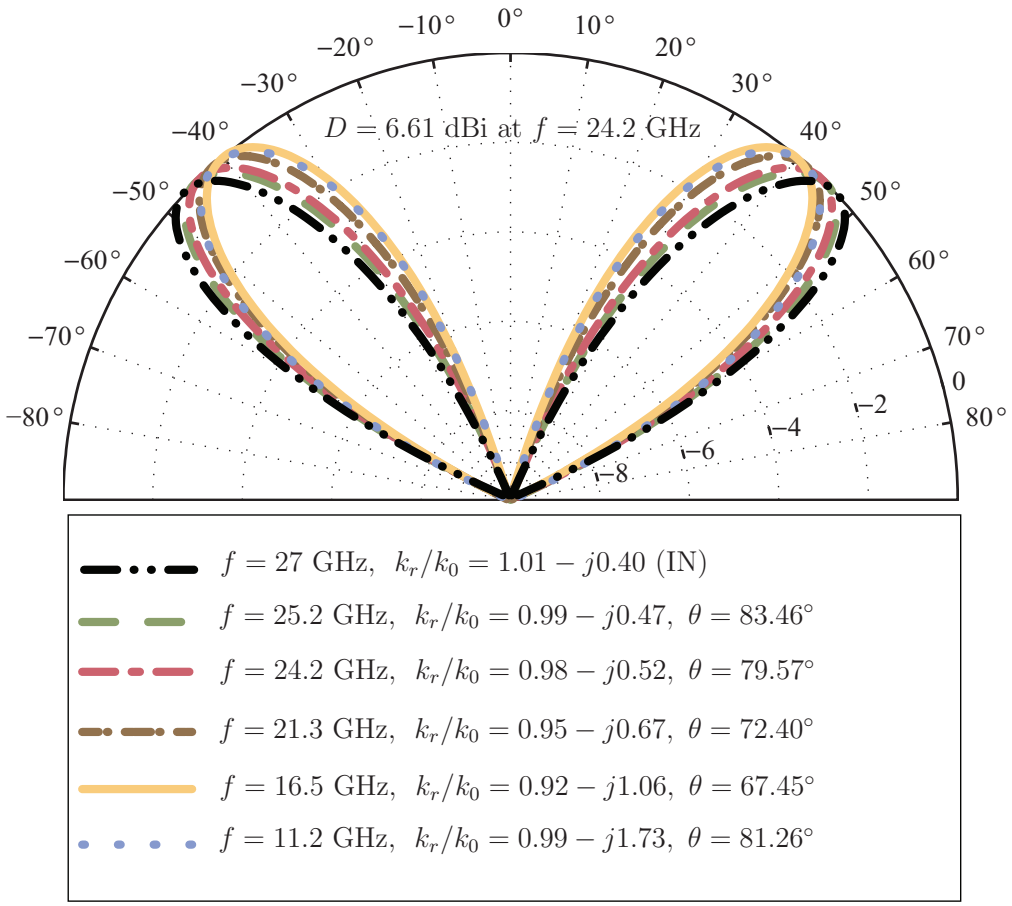

Figure 3.12 The radiation from an isotropic grounded slab for various frequencies from Fig. 3.10a and for the frequency of $f = 27$ GHz, which lies in the improper non-physical (IN) region of the dispersion curve of Fig. 3.7.

internal reflection in the substrate (red line in Fig. 3.13).

Following the above discussion on the pointing angle, Fig. 3.14 confirms that increasing the slab permittivity decreases the minimum pointing angle (and thereby also increases the scanning range toward broadside since near-endfire radiation is always present around the leaky-wave to surface-wave transition region). Fig. 3.14 further confirms the subsequent increase of the leakage factor, which results in a decrease of the directivity.

The points discussed above are general, and the leaky-wave performances of the isotropic grounded slab structure cannot be significantly improved beyond the presented results.

3.7.2 Appropriateness and Performance of the Double Anisotropic Structure

We now explore the leaky-wave radiation properties of the dispersive double anisotropic grounded slab, showing the advantages over the isotropic substrate:

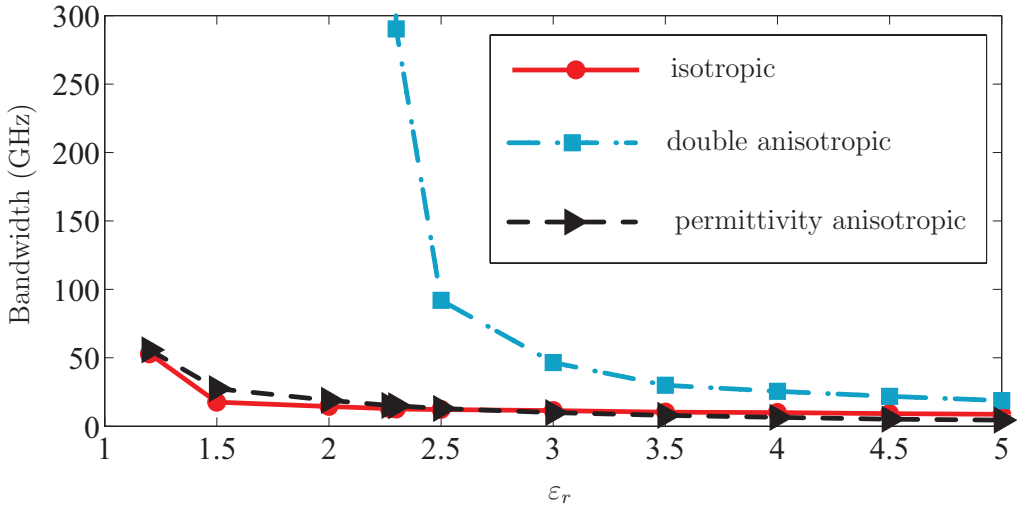

Figure 3.13 Comparison of the leaky-wave bandwidth versus the host medium permittivity ε_r between the isotropic, double anisotropic and permittivity-only anisotropic grounded slabs.

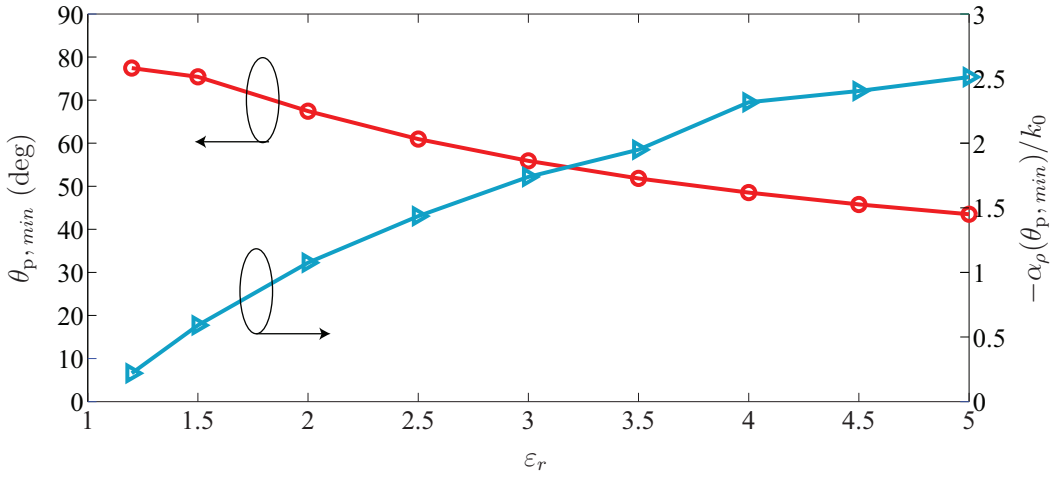

Figure 3.14 Minimum pointing angle $\theta_{\mathrm{p},\,min}$ for the isotropic substrate versus the permittivity ε_r and corresponding leakage factor $\alpha(\theta_{\mathrm{pmin}})/k_0$.

– *A wide range of beam pointing angles is available*, from broadside almost to endfire. For example, in Fig. 3.10b, this range extends from 0° to 65°. The reason for this wide scanning range is apparent in Fig. 3.6, where $0 \leq \varepsilon_z\mu_\rho/(\varepsilon_0\mu_0) < 1$, and therefore $0 \leq \beta_\rho/k_0 < 1$, in the leaky-mode range. In this case, the largest pointing angle is limited to 65° because of the asymptotic behavior of $\varepsilon_z\mu_\rho/(\varepsilon_0\mu_0) \overset{\omega\to\infty}{=} 0.88$, corresponding to $\beta_\rho/k_0 \overset{\omega\to\infty}{=} 0.9$. Larger pointing angles can be achieved by increasing the effective index $\varepsilon_z\mu_\rho$ to values exceeding unity at after some frequency, so that β_ρ reaches k_0 (at the transition region from the leaky-mode to the surface-mode). This is shown in Fig. 3.15,

where the maximum pointing angle $\theta_{\mathrm{p,max}}$, and therefore also the scanning range of the leaky mode is increased by increasing the permittivity of the host medium, ε_r, so as to scan the entire angular range from 0° to 90° (this occurs for a permittivity close to $\varepsilon_r = 2.5$). Figure 3.16 shows the scanning behavior of the leaky mode over the broad frequency range of 11 GHz to 150 GHz. Note the null at broadside, which is due to the vertical point source excitation.

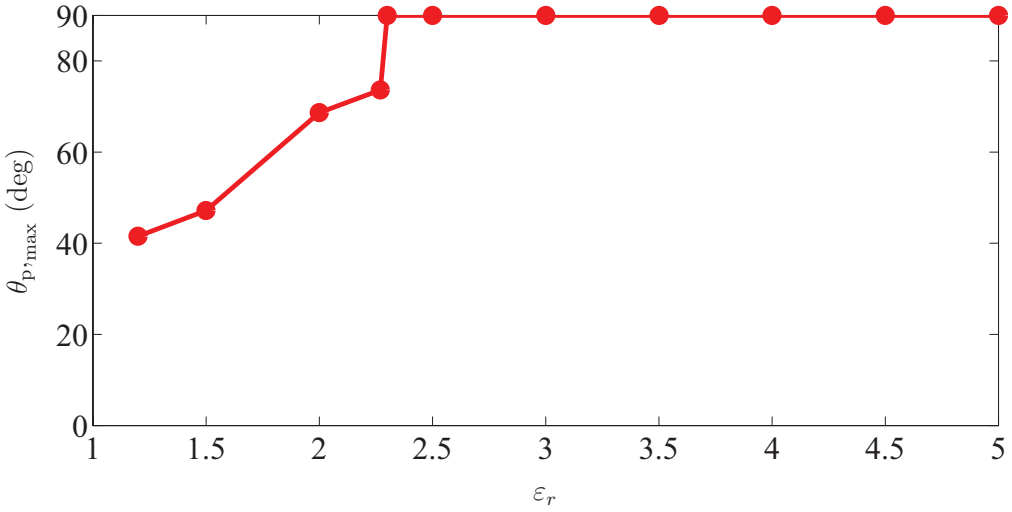

Figure 3.15 Maximum pointing angle of the leaky mode radiation from the double anisotropic grounded slab.

- *The directivity of the leaky-wave radiation may be very high.* Fig. 3.7b shows that the magnitude of the leakage factor, $|\alpha_\rho|$, becomes very small as frequency increases, thereby allowing a large radiating aperture and a very directive beam. Figure 3.16 shows that, according to the behavior of the leakage factor in Fig. 3.7b, the beam becomes extremely directive as the frequency increases.
- *The radiation efficiency of the anisotropic substrate is much higher than that for the isotropic structure*, since no surface modes exist in the leaky-mode frequency range, as shown in Fig. 3.7a. Therefore no energy is coupled inside the dielectric through the surface modes. In the case of the isotropic substrate, the TM_0 surface mode is always present in addition to the leaky mode [see also Fig. 3.7a].
- *The bandwidth of the leaky mode is wider than that for the isotropic structure*, as seen in Fig. 3.7a. Figure 3.6 shows that $\lim_{\omega\to\infty} \varepsilon_z\mu_\rho/(\varepsilon_0\mu_0) < 1$ in the right-handed frequency range. For the reason explained above, this fact prevents radiation at endfire (practically not very useful anyways), but leads to a huge frequency band of operation. Fig. 3.13 shows that by increasing the host medium permittivity ε_r, the bandwidth of the leaky mode decreases as a consequence of the increasing importance of surface

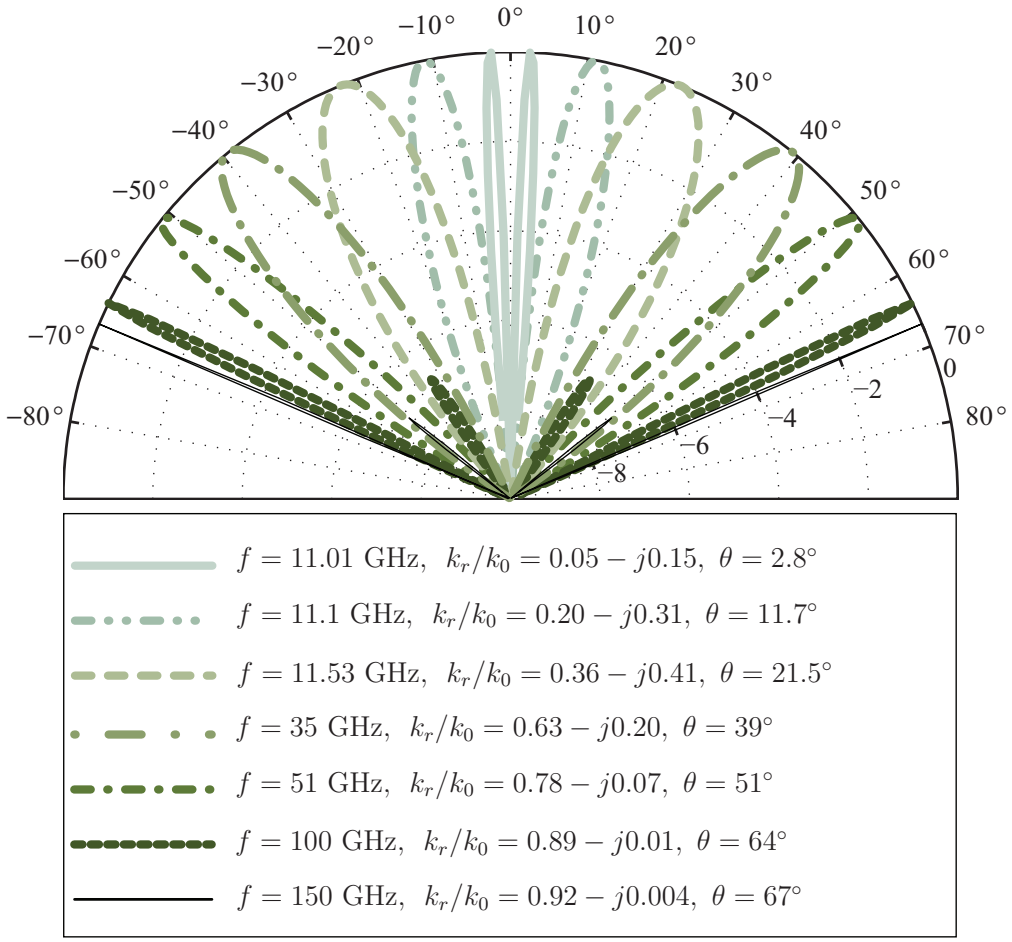

Figure 3.16 The scanning behavior of the double anisotropic substrate in a wide band frequency range.

modes. This effect also occurs in the isotropic case, but the double anisotropic structure always exhibits a much wider bandwidth.

– *The beam squinting is extremely low.* This is a direct consequence of the previous point. Figure 3.10c compares the beam squinting $d\theta_p/df$ of the leaky mode for the isotropic and double anisotropic structures. Close to the plasma frequency ($f = 11$ GHz), the beam squinting of the isotropic and the anisotropic structures are comparable. However, for the anisotropic case, it quickly drops as frequency increases above the plasma frequency; it then reaches a value that is always less than that of the isotropic slab, and remains relatively constant up to very high frequencies. Figure 3.17 shows the beam squinting of the leaky-wave beam for the anisotropic slab in the frequency range of $f = 30-35$ GHz. In accordance with Fig. 3.10c, the beam squinting in the bandwidth of $\Delta f = 5$ GHz is only 7°.

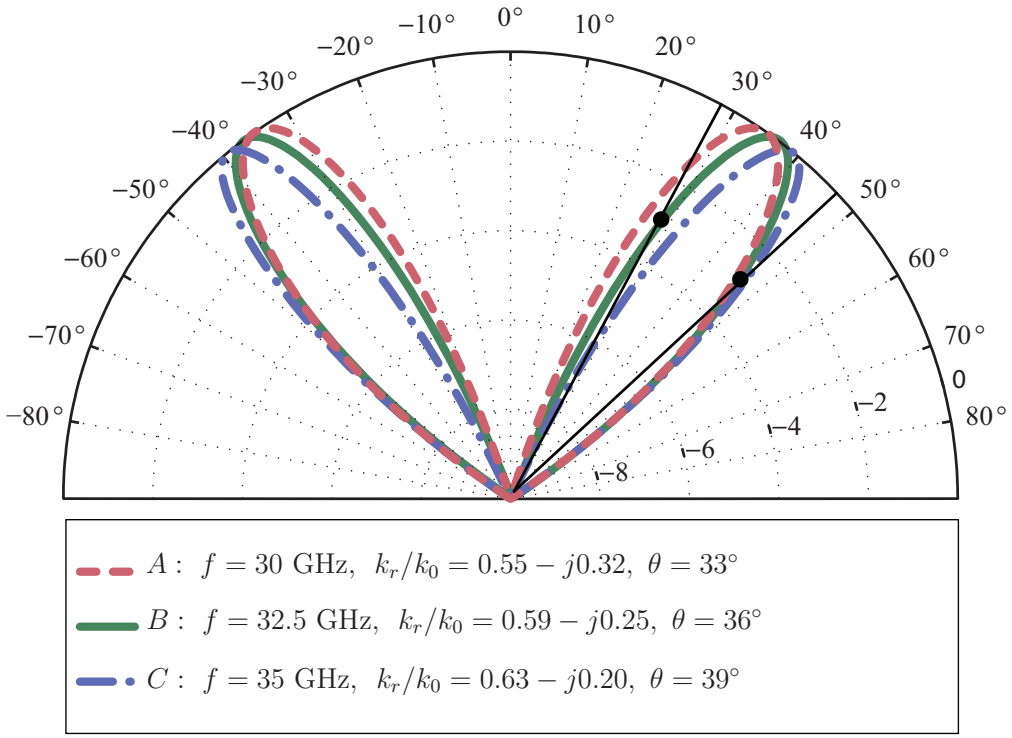

Figure 3.17 Beam squinting of the leaky mode radiation of the anisotropic slab of Fig. 3.10b in the bandwidth of $\Delta f = 5$ GHz for $f = 30 - 35$ GHz.

3.7.3 Importance of the Dispersion Associated with Magnetic Anisotropy

As discussed above, the reason for bandwidth enhancement, and the subsequent reduction of beam squinting, is the fact that $\varepsilon_z\mu_\rho/(\varepsilon_0\mu_0) < 1$ in a wide frequency range, as illustrated in Fig. 3.6. This asymptotic behavior is essentially due to the dispersive contribution of μ_ρ since $\lim_{\omega\to\infty} \varepsilon_z/\varepsilon_0 > 1$. Therefore, the dispersive behavior in μ_ρ should satisfy the condition $\lim_{\omega\to\infty} \mu_\rho/\mu_0 < 1$. This magnetic response is inherent to magneto-dielectric artificial metasubstrates. Thus, such a performance can not be achieved with a substrate that would be only electrically artificial but magnetically conventional. This is because for these materials, $\varepsilon_z/\varepsilon_0 < 1$ only occurs in narrow frequency ranges just above the electric plasma frequency. Figs. 3.13 compares the bandwidths of the electrically artificial slab with that of the double electrically and magnetically artificial (anisotropic and dispersive) slabs. It shows that the bandwidth of the only electrically anisotropic slab is similar to the conventional slab, and much smaller than that of the double anisotropic slab. It is important to note that this behavior cannot either be achieved using a simple ferrite material which has also a Lorentz permeability response [10]. This is because, according to (3.3), in the artificial case the static and infinite frequency limit values of μ_ρ/μ_0 are $\mu_\rho/\mu_0(\omega = 0) = 1$ and

$\mu_\rho/\mu_0(\omega \to \infty) = 1 - F < 1$, respectively (the $\omega \to \infty$ asymptotic diamagnetic response $\mu_\rho < \mu_0$ is a consequence of Lenz's law). In contrast, in the ferrite case, $\mu_\rho/\mu_0(\omega = 0) > 1$ and $\mu_\rho/\mu_0(\omega \to \infty) = 1$.

This demonstrates the importance of the Lorentz-type permeability of (3.3) with $\lim_{\omega\to\infty} \mu_\rho/\mu_0 < 1$, which requires artificial magnetic anisotropy, besides the Drude-type permittivity of (3.2), for very broadband operation.

3.8 Conclusion

A spectral analysis has been applied to the study of the behavior of leaky and surface modes in anisotropic magneto-dielectric meta-substrates. The analysis has shown, for the first time, that an anisotropic grounded slab provides a highly directive leaky-wave radiation with high design flexibility. Toward its lower frequencies, this mode allows full-space conical-beam scanning. At higher frequencies, it provides fixed-beam radiation (at a designable angle) with very low-beam squint, which makes it particularly appropriate for future applications in wide band point-to-point communication and radar systems.

The loss of homogeneity far above the Lorentz resonant frequency in conventional metamaterial substrates, such as the mushroom substrate, would prevent the utilization of the low-beam squint regime of the proposed anisotropic antenna at high frequency. However, it is anticipated that novel periodic structures using unit-cell compression techniques or multiscale nano-structured metamaterials will provide a solution to this issue in the future, henceforth enabling the two operation ranges of the antenna.

CHAPTER 4

ARTICLE 3: RADIATION EFFICIENCY ISSUES IN PLANAR ANTENNAS ON ELECTRICALLY THICK SUBSTRATES AND SOLUTIONS

Attieh Shahvarpour[1], Alejandro Alvarez Melcon[2], and Christophe Caloz[1]
[1]Poly-Grames Research Center, Department of Electrical Engineering,
École Polytechnique de Montréal, Centre de Recherche en Électronique Radiofréquence (CREER),
Montréal, QC, H3T 1J4, Canada.
[2] Universidad Politécnica de Cartagena, 30202 Cartagena, Murcia, Spain.

4.1 Abstract

The paper addresses the problem of the radiation efficiency of planar antennas on electrically thick substrates. First, the non-monotonic dependency of the radiation efficiency of an infinitesimal horizontal electric dipole on grounded and ungrounded substrates versus the substrate electrical thickness is analyzed. Next, the phenomenology of the observed radiation efficiency is explained with the help of a novel substrate dipole approach, which reduces the actual structure to an equivalent source dipole composed of the original dipole and the substrate dipole radiating into free space. It is then shown that the efficiency response of an actual half-wavelength dipole printed on grounded and ungrounded substrates is essentially similar to that of the infinitesimal dipole. Finally, two solutions for enhancing the efficiency at electrical thicknesses where the efficiency is minimal are studied.

4.2 Introduction

Over the past decades, planar antennas have found a myriad of applications due to their low profile, low cost, compatibility with integrated circuits and conformal nature [102]. At the same time, ever increased bandwidth requirements and miniaturization constraints, particularly in arrays [103], have spurred growing interest for the millimeter-wave and terahertz ranges [104, 105, 106].

Unfortunately, in the millimeter-wave and terahertz regimes, the efficiency of planar antennas tends to be very low, because several surface-wave modes are excited and carry and dissipate a significant amount of the source power [77, 78, 79]. This is caused by the large electrical thickness of the substrates, which cannot be chosen to be thinner due to the mechanical rigidity requirements and fabrication constraints [107],[108]. The surface waves may

also cause scan-blindness, while their diffraction at the edges of the substrate introduces ripples in the radiation pattern and produce parasitic back radiation.

To better understand the issue of the low radiation efficiency of planar antennas on the electrically thick substrates, and also devise remedies, a detailed analysis is required. The efficiency versus substrate electrical thickness for a horizontal electric dipole on a grounded substrate was shown in [77, 78, 79], but no detailed analysis and explanation have been reported to our knowledge. Moreover, no solutions have been discussed to mitigate the low-efficiency issue in electrically thick substrates.

In this paper, the radiation efficiency behavior of an infinitesimal horizontal dipole on grounded and ungrounded substrates is analyzed and solutions for enhancing the efficiency at frequencies where the efficiency is close to zero (no radiation) are presented. Next, it is shown that the efficiency behavior of an actual planar antenna, such as a half-wavelength dipole, is qualitatively similar and quantitatively close to that of an infinitesimal horizontal dipole. A novel approach, based on reducing the real structure to an equivalent structure composed of the original source dipole and of a substrate dipole radiating into free space, is proposed to explain the efficiency behavior.

The paper is organized as follows. Section 4.3 defines the radiation efficiency and presents the dependency of the radiation efficiency versus the substrate electrical thickness for the grounded and ungrounded dielectric slab cases. Section 4.4 introduces the substrate dipole concept and applies it to explain the radiation efficiency from the radiated and surface-wave mode powers behaviors. Section 4.5 presents the efficiency behavior of a practical printed half-wavelength dipole. Finally, Sec. 4.6 discusses possible solutions for enhancing the radiation efficiency at the frequency bands where the efficiency reaches its minima.

4.3 Radiation Efficiency

4.3.1 Definition

The radiation efficiency, η, of an antenna is defined as [102]

$$\eta = \frac{P_{\text{rad}}}{P_{\text{tot}}} = \frac{P_{\text{rad}}}{P_{\text{rad}} + P_{\text{loss}}} = \frac{P_{\text{rad}}}{P_{\text{rad}} + P_{\text{ref}} + P_{\text{mat}} + P_{\text{sw}}}, \tag{4.1}$$

where P_{rad} is the radiated power, P_{tot} is the total power, and $P_{\text{loss}} = P_{\text{tot}} - P_{\text{rad}} = P_{\text{ref}} + P_{\text{mat}} + P_{\text{sw}}$ is the lost power, which consists of reflected power due to mismatch (P_{ref}), dissipated power due to dielectric (P_{diel}) and metallic (P_{metal}) material losses ($P_{\text{mat}} = P_{\text{diel}} + P_{\text{metal}}$), and surface wave power (P_{sw}). Equation (4.1) indicates that η is limited by reflection, material and surface wave losses.

In practice, most antennas, perhaps with the exception of electrically small antennas [1], may be easily matched to exhibit a VSWR of less than 2, in which case $P_{\rm ref}$ is generally negligible.

As pointed out in Sec. 4.2, when one moves from low microwave frequencies to millimeter-wave and submillimeter-wave frequencies, the electrical thicknesses of antenna substrates tend to increase. As a consequence, the dielectric loss contribution to $P_{\rm mat}$, $P_{\rm diel}$, which is associated with dielectric heating, tends to decrease, due to reduced electric field density [78]. In contrast, the metal loss contribution to $P_{\rm mat}$, $P_{\rm metal}$, which is associated with metal heating by the Joule effect, tends to increase towards higher frequencies, due to decreased skin depth and subsequently increased electric field density in the metal. Overall, the increase in $P_{\rm metal}$ overweights the decrease in $P_{\rm diel}$, so that $P_{\rm mat}$ increases as frequency increases, as well known by antenna practitioners. In any case, we are here mostly interested in the dependence of the antenna efficiency on the electrical thickness of the substrate *for a given substrate with corresponding dielectric and metallic characteristics*. Therefore, in the forthcoming analysis, we shall ignore the material losses, and the reported efficiencies will represent an *upper bound* to the achievable efficiencies in the presence of loss.

Based on the above considerations, we consider the particular case of (4.1) where $P_{\rm ref} = P_{\rm mat} = 0$, so that only $P_{\rm sw}$ affects the antenna efficiency. The radiation efficiency reduces then to [77, 78, 79]

$$\eta = \frac{P_{\rm rad}}{P_{\rm rad} + P_{\rm sw}}. \tag{4.2}$$

In this expression, $P_{\rm rad}$ and $P_{\rm sw}$ will be next calculated from the radiated and surface-wave time-averaged Poynting vectors, $\mathbf{S}_{\rm r,av}$ and $\mathbf{S}_{\rm sw,av}$, respectively. In the case of an antenna over a grounded substrate, these powers read

$$P_{\rm rad} = \int_0^{2\pi} \int_0^{\pi/2} \mathbf{S}_{\rm rad,av}.\hat{\mathbf{r}} r^2 \sin\theta \, d\theta \, d\phi, \tag{4.3a}$$

$$P_{\rm sw} = \int_0^{2\pi} \int_{-d}^{\infty} \mathbf{S}_{\rm sw,av}.\hat{\boldsymbol{\rho}} \rho \, dz \, d\phi, \tag{4.3b}$$

where $P_{\rm rad}$ is obtained by integration over a half sphere in free space above of the antenna and $P_{\rm sw}$ is obtained by integration over a cylinder extending from the ground plane through the

1. Although this section and Sec. 4.4 deal with an infinitesimal dipole, for the sake of emphasizing the fundamentals of the interactions between a radiator and the substrate upon which it is placed, the practical antennas of interest in this paper are *not* electrically small antennas. Section 4.5 will show that the results in these two sections essentially hold for the case of half-wavelength antennas, which may be easily matched.

substrate with the thickness of d to infinity above the antenna. In the case of an antenna over an ungrounded substrate, one must add integrals corresponding to radiation and surface-wave propagation at the other side of the substrate.

The Poynting vectors in (4.3) will be computed using the classical spectral-domain transmission-line modeling technique for a horizontal infinitesimal electrical dipole placed at the surface of the substrate [75, 109]. The details are provided in Appendix C.

4.3.2 Dependence on the Electrical Thickness

Figs. 4.1a and 4.2a show a grounded substrate and an ungrounded substrate, respectively, excited by an infinitesimal horizontal dipole. Both substrates have a thickness d, a permittivity $\varepsilon_{\rm d} = \varepsilon_{\rm rd}\varepsilon_0$ and a permeability μ_0. Throughout the paper, the considered substrate is RT/Duroid 6006 with $\varepsilon_{\rm rd} = 6.15$ and $d = 2.5$ mm, unless otherwise specified.

The corresponding responses versus the electrical thickness of the substrate for the grounded and ungrounded substrate cases, computed from the transmission-line models of Figs. 4.1b and 4.2b, are presented in Figs. 4.3 and 4.4, respectively, where the sub-figures (a), (b), (c) and (d) show the radiation efficiencies, the surface-wave modes, the radiated powers and the surface-wave powers, respectively. The bottom abscissae refer to the free-space electrical thicknesses, d/λ_0, where λ_0 denotes the free-space wavelength, while the labeled points in the top abscissae refer to the surface-wave cutoff effective electrical thicknesses, $d/\lambda_{\rm eff}^{\rm cutoff}$. In the latter, $\lambda_{\rm eff}^{\rm cutoff}$ is the cutoff effective wavelength, which is related to the transmission-line (z-directed) substrate effective wavelength,

$$\lambda_{\rm eff} = 2\pi/k_{\rm zd}, \tag{4.4}$$

where, as shown in Fig. 4.5,

$$(k_{\rm zd})^2 = \omega^2\mu_0\varepsilon_{\rm d} - k_\rho^2, \tag{4.5}$$

by $\lambda_{\rm eff}^{\rm cutoff} = \lambda_{\rm eff}(k_{\rm z0} = 0)$, yielding [110]

$$\begin{aligned}\lambda_{\rm eff}^{\rm cutoff} &= \frac{2\pi}{\sqrt{\varepsilon_{\rm rd}(k_0^{\rm cutoff})^2 - k_\rho^2}} \\ &= \frac{2\pi}{\sqrt{\varepsilon_{\rm rd}(k_0^{\rm cutoff})^2 - [(k_0^{\rm cutoff})^2 - (\cancel{k_{\rm z0}})^2]}} \\ &= \frac{2\pi}{k_0^{\rm cutoff}\sqrt{\varepsilon_{\rm rd} - 1}} = \frac{\lambda_0^{\rm cutoff}}{\sqrt{\varepsilon_{\rm rd} - 1}}.\end{aligned} \tag{4.6}$$

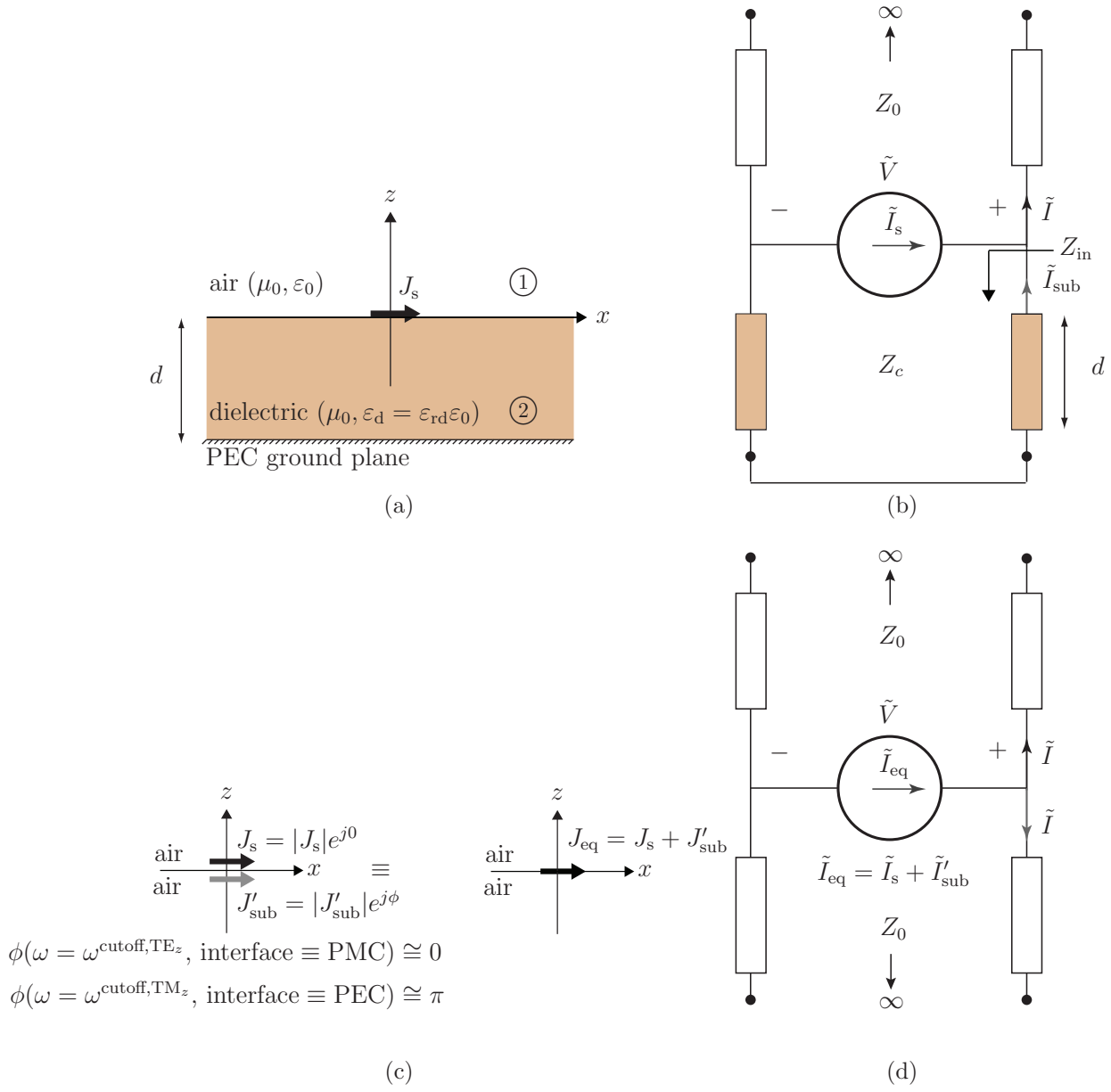

Figure 4.1 *Grounded* (PEC) dielectric substrate excited by an infinitesimal horizontal electric dipole. (a) Structure. (b) Transmission-line model. (c) Equivalent free-space dipole pair $J_{eq} = J_s + J'_{sub}$ formed by the source dipole J_s and the auxiliary substrate dipole J'_{sub}. (d) Equivalent transmission-line model of the equivalent free-space dipole pair radiating into free-space.

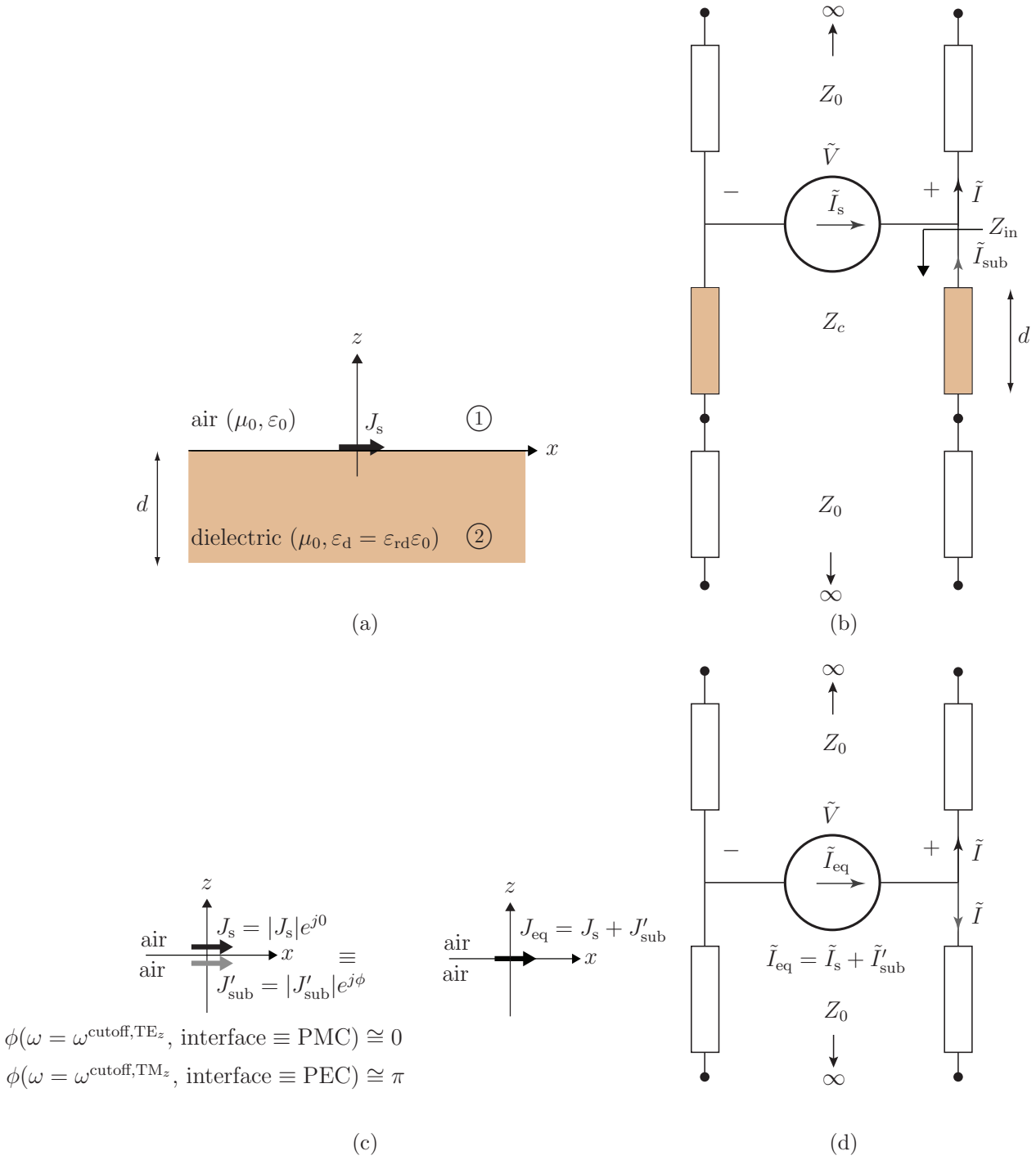

Figure 4.2 *Ungrounded* dielectric substrate excited by an infinitesimal horizontal electric dipole. (a) Structure. (b) Transmission-line model. (c) Equivalent free-space dipole pair $J_{eq} = J_s + J'_{sub}$ formed by the source dipole J_s and the auxiliary substrate dipole J'_{sub}. (d) Equivalent transmission-line model of the equivalent free-space dipole pair radiating into free-space.

Two interesting facts may be observed in Figs. 4.3 and 4.4 [77, 78, 79, 108]. First, as seen in Fig. 4.3a and 4.4a, the efficiency does not decay monotonically, but goes through successive peaks and valleys, as the electrical thickness is increased. Second, in the grounded case the maxima (resp. minima) of the radiation efficiency correspond to the TE (resp. TM) surface-wave cutoffs, as seen by comparing Figs. 4.3a and 4.3b, while in the ungrounded case, the maxima correspond to the degenerated TE and TM surface-wave cutoffs, as seen by comparing Figs. 4.4a and 4.4b. Moreover, striking differences between the grounded and ungrounded cases are the fact that in the latter case the radiation efficiency decreases much faster, the efficiency peaks are smaller and no zero efficiency point is observed. Section 4.4 will explain these observations.

4.4 Explanation of the Radiation Efficiency Response versus the Substrate Thickness

Since the radiation efficiency [Eq. (4.2)] involves the radiated power and the surface-wave power, we shall now consider these powers, first separately and next combined, to explain the radiation efficiency response observed in Sec. 4.3.2.

4.4.1 Radiated Power

The dependence of the radiated power on the electrical thickness may be best understood with the help of an *auxiliary substrate dipole* modeling the substrate and its ground plane if present.

Substrate Dipole

The aforementioned substrate dipole is represented in Figs. 4.1c and 4.2c for the grounded substrate and ungrounded substrate cases, respectively. By definition, this substrate dipole, J'_{sub}, is a fictitious dipole which is collocated [2] with the source dipole, J_{s}, and whose combination with J_{s} *in free-space*,

$$J_{\text{eq}} = J_{\text{s}} + J'_{\text{sub}}, \tag{4.7}$$

produces the same electromagnetic far-fields as the source in the original substrate structures (Figs. 4.1a and 4.2a) in the half-space $z > 0$, hence the subscript "eq", standing for "equivalent". Thus, the substrate dipole J'_{sub}, even though it is radiating in free space, fully accounts for the presence of the substrate and its ground plane if present.

2. Note that this substrate dipole is *not* an image dipole in the classical sense [111], which refers to some mirror symmetry, since it is collocated with the physical dipole source without any symmetry feature.

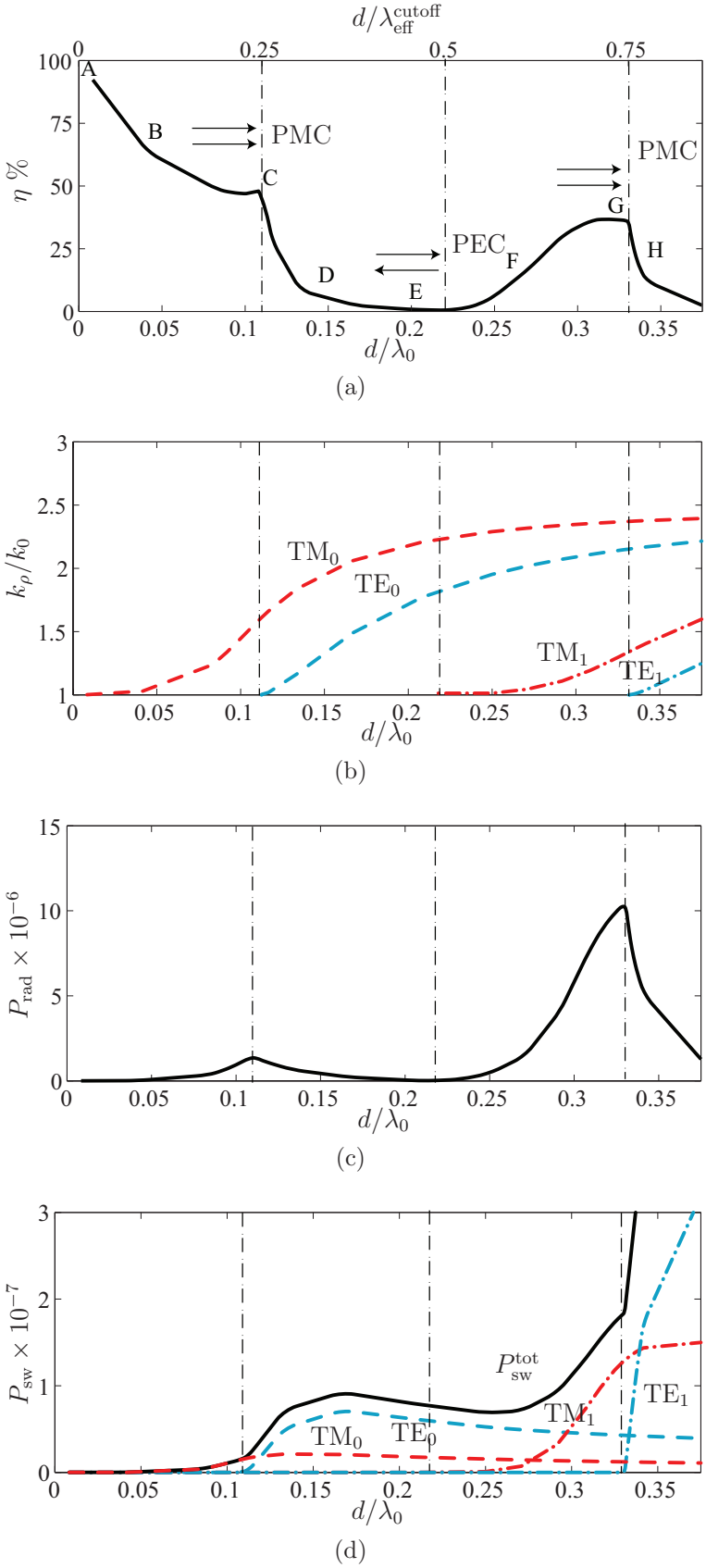

Figure 4.3 Response to an infinitesimal horizontal dipole on a *grounded* substrate (Fig. 4.1a) versus the electrical thickness of the substrate. (a) Radiation efficiency [Eq. (4.2)]. (b) TM_z and TE_z surface modes [poles of (C.11)]. (c) Radiated power [Eq. (4.3a)]. (d) Surface-modes powers [Eq. (4.3b)].

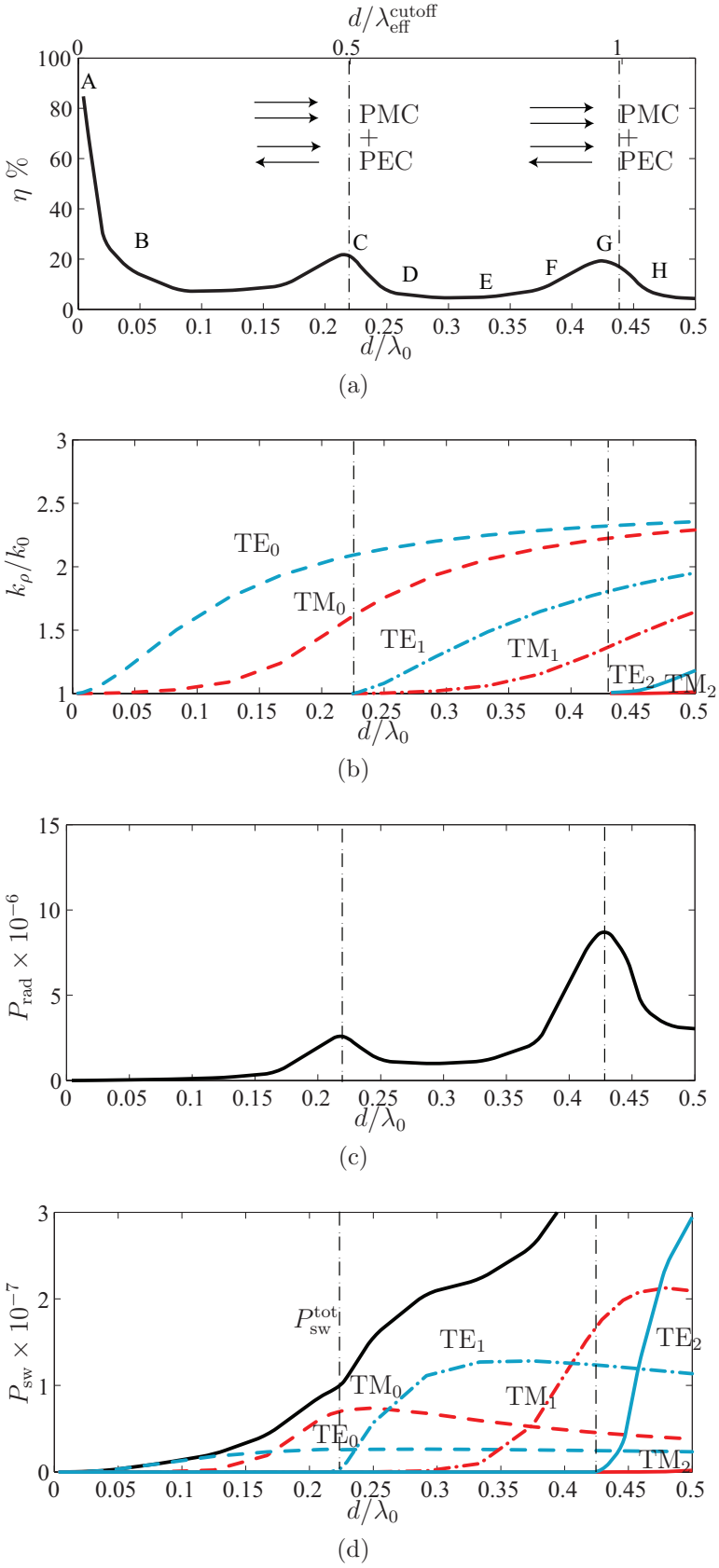

Figure 4.4 Response to an infinitesimal horizontal dipole on an *ungrounded* substrate (Fig. 4.2a) versus the electrical thickness of the substrate. (a) Radiation efficiency [Eq. (4.2)]. (b) TM_z and TE_z surface modes [poles of (C.11)]. (c) Radiated power [Eq. (4.3a)]. (d) Surface-modes powers [Eq. (4.3b)].

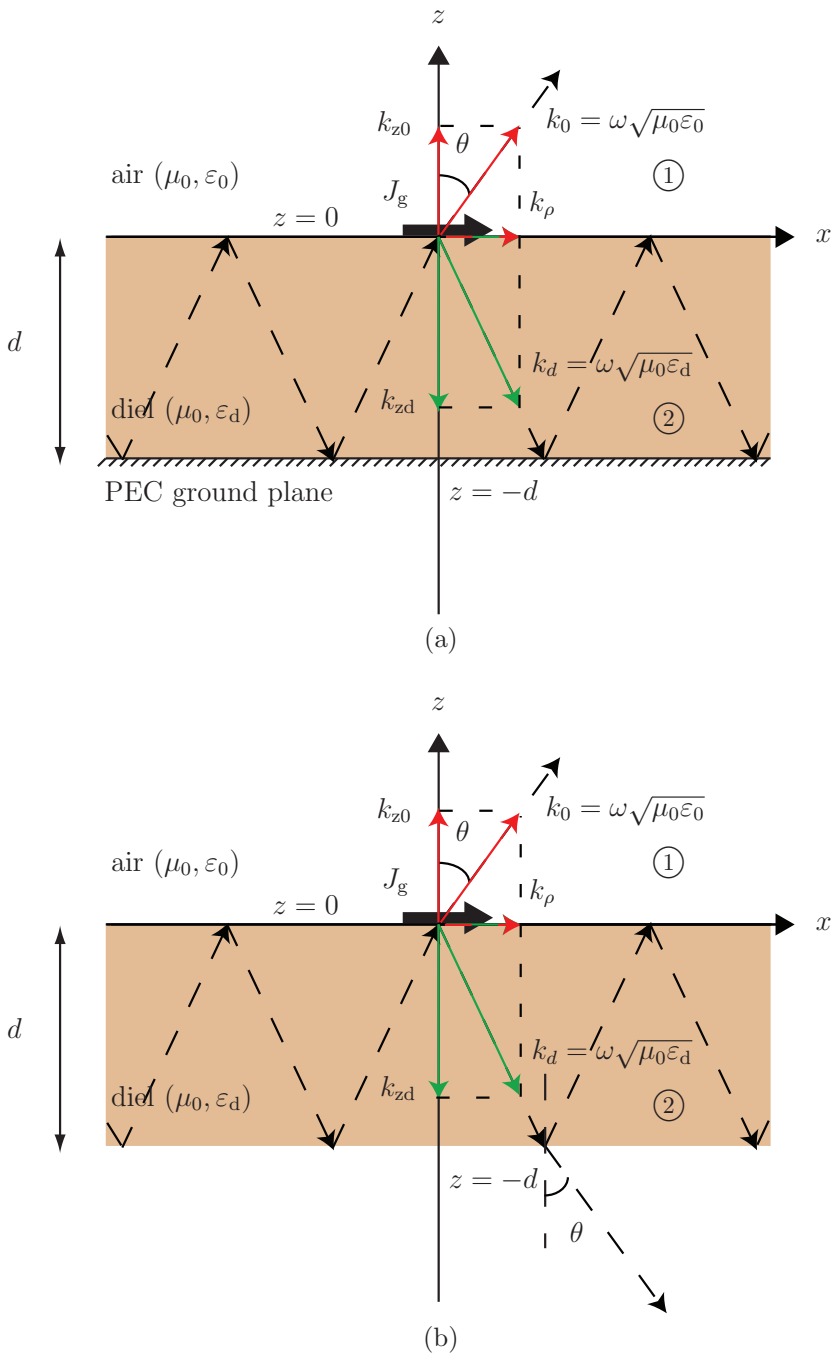

Figure 4.5 Ray-optics representation of wave propagation in the air and in the dielectric (only one leaky-wave ($\theta < 90°$) or surface-wave ($\theta = 90°$) is shown) in the grounded substrate and ungrounded substrate cases. (a) Grounded case. (b) Ungrounded case.

The above definition of the substrate dipole and the subsequent relation (4.7) correspond to the transmission-line models shown in Figs. 4.1d and 4.2d, which are equivalent to the transmission-line models of Figs. 4.1b and 4.2b for the grounded substrate and ungrounded

substrate cases, respectively. Note that the models of Figs. 4.1d and 4.2d do not represent any computational benefit over the models of Figs. 4.1b and 4.2b, since J'_{sub} in the former has to be determined from the latter, but only provide a simple model for the forthcoming explanation of the radiation efficiency behavior observed in Figs. 4.3a and 4.4a.

The spectral current $\tilde{I}$ in Figs. 4.1b and 4.2b is composed of the sum of the spectral source dipole current, $\tilde{I}_{\text{s}}$, and spectral substrate dipole current, $\tilde{I}_{\text{sub}}$,

$$\tilde{I} = \tilde{I}_{\text{s}} + \tilde{I}_{\text{sub}}. \tag{4.8}$$

The current $\tilde{I}_{\text{sub}}$ is the transmission-line equivalent substrate current, where the substrate is characterized by its characteristic impedance, Z_c, thickness, d, and input impedance, Z_{in}. The current $\tilde{I}$ is also present in the equivalent transmission-line model of Figs. 4.1d and 4.2d, respectively. This model consist of a simple transmission-line of impedance Z_0, modeling free space, excited in its center by the equivalent current

$$\tilde{I}_{\text{eq}} = \tilde{I}_{\text{s}} + \tilde{I}'_{\text{sub}}. \tag{4.9}$$

which is essentially the Fourier transform of (4.7). Note that (4.7) represents a *spatial electromagnetic* current density whereas (4.9) represents its *spectral equivalent* current model. The relation between $\tilde{I}'_{\text{sub}}$ in (4.9) and $\tilde{I}_{\text{sub}}$ in (4.8) is derived in Appendix D. It reads

$$\tilde{I}'_{\text{sub}} = \tilde{I}_{\text{sub}} \left(1 - \frac{Z_{\text{in}}}{Z_0}\right). \tag{4.10}$$

According to the models of Figs. 4.1c and 4.2c, the original structures excited by the source dipole J_s are simply equivalent to free space excited by J_{eq}. Therefore, the radiated power is expected to be proportional to J_{eq}. According to (4.7), to determine J_{eq}, one only needs to determine J'_{sub} since J_s is known. This will be accomplished by determining the nature of an equivalent boundary at $z = 0$, from which the image J'_{sub} of J_{s} will follow, hence yielding J_{eq}.

Air-Dielectric Interface Equivalent Boundary Conditions

As shown in Sec. 4.4.1, the radiated power is the power radiated by J_{eq} in free-space, which is the sum of the known source dipole J_{s} and the substrate dipole J'_{sub}. To determine the radiated power, one must therefore find out how J'_{sub} is related to J_{s}. This relation can be established by determining the boundary conditions induced by the surface-wave modes at the air-dielectric interface.

In surface waves, the vertical phase shift of a wave round-trip in the substrate (Fig. 4.5)

is a multiple of 2π, i.e. $k_{\rm zd}d + \phi_{-d} + k_{\rm zd}d + \phi_0 = 2m\pi$ ($m \in \mathbb{N}$) [110], or

$$k_{\rm zd}d = m\pi - \frac{\phi_{-d} + \phi_0}{2}, \tag{4.11}$$

where ϕ_{-d} and ϕ_0 are the dielectric reflection phases at $z = -d$ and $z = 0$, respectively.

The corresponding transmission-line input impedance at the air-dielectric interface in Figs. 4.1b and 4.2b can then be determined using [2]

$$Z_{\rm in} = Z_c \frac{Z_L + jZ_c \tan(k_{\rm zd}d)}{Z_c + jZ_L \tan(k_{\rm zd}d)}, \tag{4.12}$$

where Z_L is the load impedance at $z = -d$.

The surface-wave wavenumber, k_ρ, is purely real, assuming a lossless substrate, and k_ρ approaches k_0 towards cutoff. Exactly at cutoff, $\theta = 90^\circ$ and $k_\rho = k_0$, and hence $k_{\rm z0} = (k_0^2 - k_\rho^2)^{1/2} = 0$, which corresponds to the limit of grazing propagation at the air-dielectric interface in the air. Let us now examine the vectorial field configurations at the $\rm TE_z$ and $\rm TM_z$ cutoffs at the air-dielectric interface [3]. These configurations are shown in Fig. 6. In the TE case, the electric field, **E**, in the air is purely tangential, while the magnetic field, **H**, is purely normal, and hence the interface is equivalent to a PMC boundary, so that $\phi_0 = 0$ in (4.11). Conversely, in the TM case, **H** is purely tangential, while **E** is purely normal, and hence the interface is equivalent to a PEC boundary, so that $\phi_0 = \pi$ in (4.11).

We shall next determine the values of $Z_{\rm in}$ in (4.12) and $d/\lambda_{\rm eff}^{\rm cutoff}$ in (4.6), which both depend on $k_{\rm zd}d$ in (4.11) for the grounded and ungrounded substrates cases. The forthcoming results are summarized in Tab. 4.1.

Grounded Substrate Case Because of the PEC boundary condition at $z = -d$, we have $Z_L^{\rm TE,TM} = 0$ and $\phi_{-d} = \pi$. Inserting the former result into (4.12) leads to

$$Z_{\rm in}^{\rm TE,TM} = jZ_c \tan(k_{\rm zd}d). \tag{4.13}$$

For the TE-cutoff case, inserting $\phi_0 = 0$ (cutoff) and $\phi_{-d} = \pi$ (ground) into (4.11) yields $k_{\rm zd}^{\rm cutoff}d = (2m-1)\pi/2$ and hence, from (4.13), $Z_{\rm in} = \infty$, which corresponds to a PMC condition (Fig. 4.6). Therefore, $J'_{\rm sub}$ is *in phase* with $J_{\rm s}$, which maximizes $J_{\rm eq}$, as confirmed in Fig. 4.7a at $\theta = 90^\circ$ (angular variation to be discussed below), and hence maximizes the radiated power, as observed in Fig. 4.3c. Note that in this TE-cutoff case, from (4.4), $d/\lambda_{\rm eff}^{\rm cutoff} = k_{\rm zd}d/(2\pi) = (2m-1)/4$ (Fig. 4.3b).

For the TM-cutoff case, inserting $\phi_0 = \pi$ (cutoff) and $\phi_{-d} = \pi$ (ground) into (4.11) yields

3. For the sake of notational brevity, we shall omit the z subscript in $\rm TE_z$ and $\rm TM_z$ in the remainder of the paper.

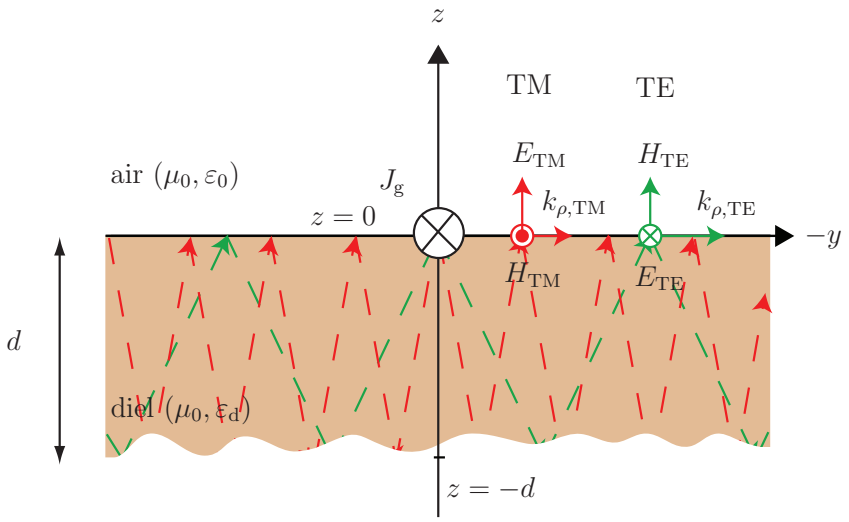

Figure 4.6 Vectorial field configurations at the TE and TM cutoffs.

$k_{zd}^{cutoff} d = (m-1)\pi$ and hence, $Z_{in} = 0$, which corresponds to a PEC condition (Fig. 4.6) and $d/\lambda_{eff}^{cutoff} = (m-1)/2$ (Fig. 4.3b). In this case, J'_{sub} is *out of phase* with J_s, which nullifies [4] J_{eq}, as confirmed in Fig. 4.7a at $\theta = 90°$ (angular variation to be discussed below), and hence minimizes the radiated power, as observed in Fig. 4.3c.

Let us now explain the variation of $\tilde{I}_{eq}$ versus the angle θ. For the ease of the argument, let us consider that the dipole – grounded substrate system operates in the receive mode, while the transmit mode follows by reciprocity. The angle θ is then the angle of incidence of a plane wave impinging on the system. We will first provide a qualitative explanation and next a quantitative explanation.

For any surface-wave mode, the angle $\theta = 90°$ at a given frequency of the incident wave corresponds to a situation where the mode is excited so as to propagate in a grazing fashion at the surface of the substrate in the air and in a zigzagging fashion under the critical angle of total internal reflection in the dielectric. This corresponds to the cutoff frequency of the mode. Consequently, based on the above considerations, $\theta = 90°$ corresponds to frequencies indicated in Tab. 4.1, where the TE-PMC and TM-PEC conditions occur (dashed lines in Fig. 4.7a). In region $\theta < 90°$, the surface-wave mode, has transformed into a leaky-wave mode (left of the dashed lines in Fig. 4.7a). Since the electromagnetic fields are also functions of θ through k_ρ, according to $\sin\theta = k_\rho/k_0$, via (C.8) in Appendix C, at each angle of incidence θ there is a specific frequency where the total tangential magnetic field for the TE modes or the total tangential electric field for the TM modes vanishes at the air-dielectric interface, which leads to TE-PMC and TM-PEC boundary conditions at the interface, respectively. This

4. Since J'_{sub} is the image of J_s with respect to the plane $z = 0$, $J'_{sub} = -J_s$.

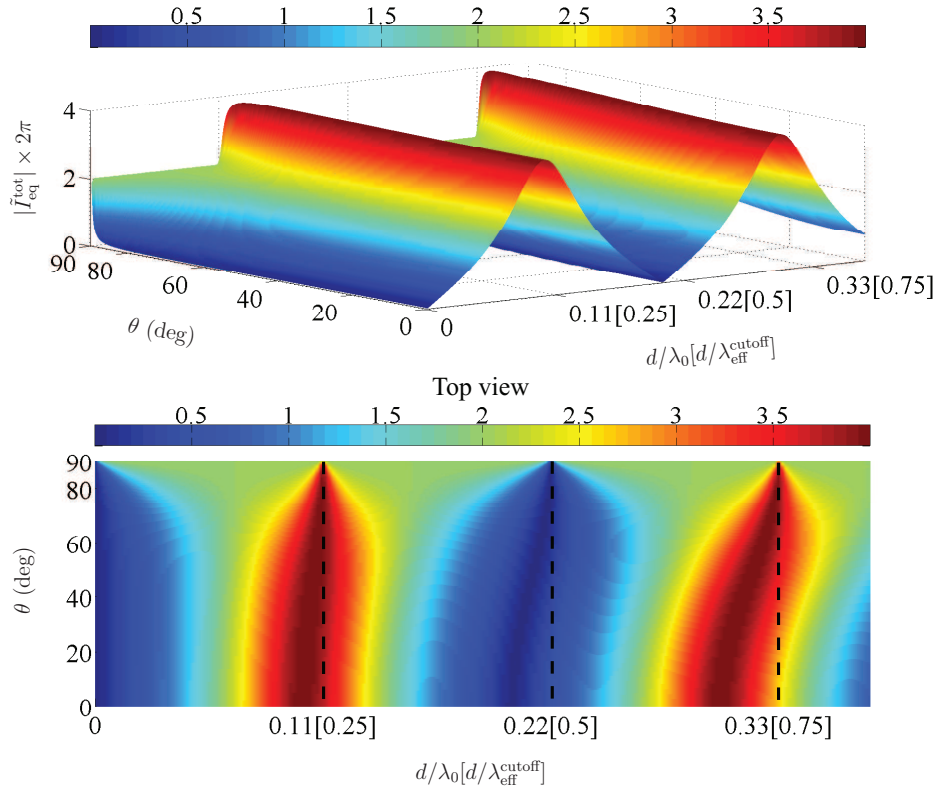

(a)

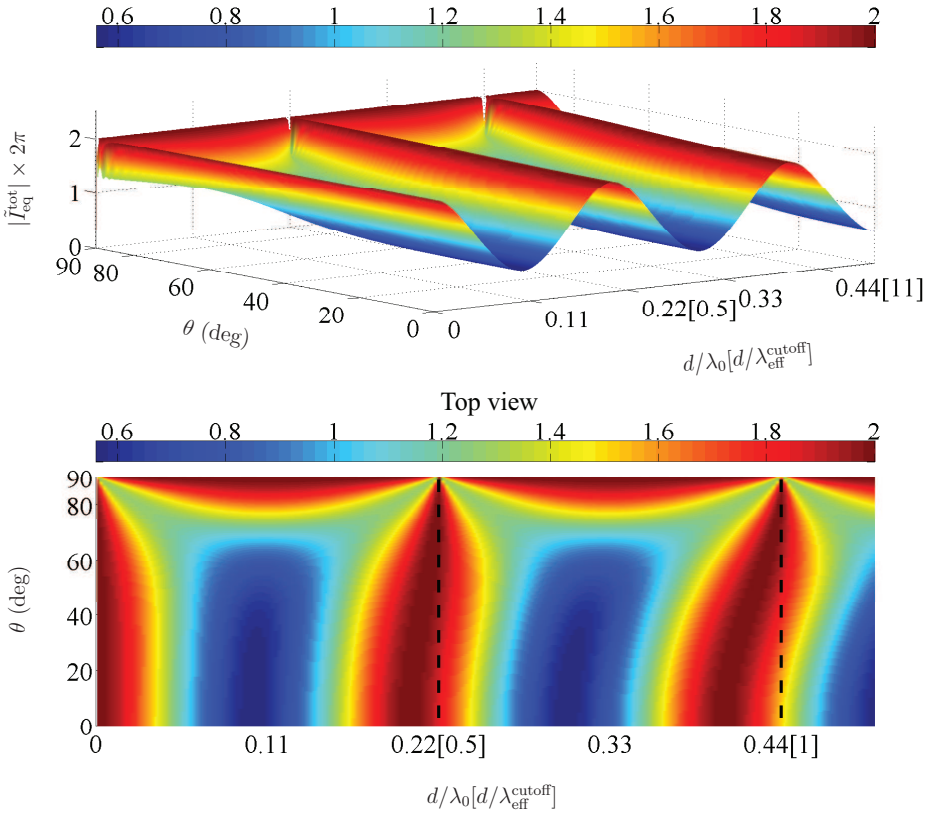

(b)

Figure 4.7 Magnitude of the total equivalent dipole current $\tilde{I}_{eq}^{tot} = \tilde{I}_{eq}^{TE} + \tilde{I}_{eq}^{TM}$ [Eq. (4.9)] versus the electrical thickness of the substrate and the angle of radiation. (a) Grounded case. (b) Ungrounded case.

Table 4.1 Values of ϕ_0, ϕ_{-d}, $k_{\mathrm{zd}}d$, Z_{in} and $d/\lambda_{\mathrm{eff}}^{\mathrm{cutoff}}$ at the TE and TM surface-wave mode cutoffs for the grounded and ungrounded substrates.

	grounded substrate	ungrounded substrate
TE	$\phi_0 = 0$ $\phi_{-d} = \pi$ $k_{\mathrm{zd}}^{\mathrm{cutoff}}d = (2m-1)\pi/2$ $Z_{\mathrm{in}} = \infty$ (PMC) $d/\lambda_{\mathrm{eff}}^{\mathrm{cutoff}} = (2m-1)/4$	$\phi_0 = 0$ $\phi_{-d} = 0$ $k_{\mathrm{zd}}^{\mathrm{cutoff}}d = m\pi$ $Z_{\mathrm{in}} = \infty$ (PMC) $d/\lambda_{\mathrm{eff}}^{\mathrm{cutoff}} = m/2$
TM	$\phi_0 = \pi$ $\phi_{-d} = \pi$ $k_{\mathrm{zd}}^{\mathrm{cutoff}}d = (m-1)\pi$ $Z_{\mathrm{in}} = 0$ (PEC) $d/\lambda_{\mathrm{eff}}^{\mathrm{cutoff}} = (m-1)/2$	$\phi_0 = \pi$ $\phi_{-d} = \pi$ $k_{\mathrm{zd}}^{\mathrm{cutoff}}d = (m-1)\pi$ $Z_{\mathrm{in}} = 0$ (PEC) $d/\lambda_{\mathrm{eff}}^{\mathrm{cutoff}} = (m-1)/2$

frequency is shifted below the cutoff frequency, as will be shown mathematically below. As a result, for all the angles $\theta = 0^\circ \rightarrow 90^\circ$ there is a frequency where $\tilde{I}_{\mathrm{eq}}$ reaches a maximum or minimum due to the TE-PMC or TM-PEC conditions, respectively, as shown in Fig. 4.7a, and this variation covers a given bandwidth, increasing with the electrical thickness, below each cutoff. Since the efficiency results from the integration of $\tilde{I}_{\mathrm{eq}}$ over all the k_ρ's or, equivalently, all the θ's, the aforementioned increasing bandwidths lead to increasing-bandwidth efficiency plateaux for increasing electrical thickness, as was observed in Fig. 4.3a.

Inserting the relation $\sin\theta = k_\rho/k_0$ into (4.5) yields $k_{\mathrm{zd}} = k_0\sqrt{\varepsilon_{\mathrm{rd}} - \sin^2\theta}$. Inserting this last expression into (4.13) results into

$$Z_{\mathrm{in}}^{\mathrm{TE,TM}} = jZ_c^{\mathrm{TE,TM}} \tan\left(k_0 d\sqrt{\varepsilon_{\mathrm{rd}} - \sin^2\theta}\right). \tag{4.14}$$

This relation shows that the input impedance, and hence the frequency at which the aforementioned PMC or PEC conditions occur, depends on the radiation angle, as observed in Fig. 4.7a. Specifically,

$$Z_{\mathrm{in}}^{\mathrm{TE,TM}}(\theta = 90^\circ) = jZ_c^{\mathrm{TE,TM}} \tan\left(k_0 d\sqrt{\varepsilon_{\mathrm{rd}} - 1}\right), \tag{4.15a}$$

$$Z_{\mathrm{in}}^{\mathrm{TE,TM}}(\theta = 0^\circ) = jZ_c^{\mathrm{TE,TM}} \tan\left(k_0 d\sqrt{\varepsilon_{\mathrm{rd}}}\right), \tag{4.15b}$$

where, for $\theta = 90^\circ$, the PMC and PEC occur at $k_0 d = (2m-1)\pi/2\sqrt{\varepsilon_{\mathrm{rd}} - 1}$ and $k_0 d = (m-1)(2\pi)/\sqrt{\varepsilon_{\mathrm{rd}} - 1}$, respectively, and for $\theta = 0^\circ$, the PMC and PEC occur at $k_0 d = (2m-1)\pi/2\sqrt{\varepsilon_{\mathrm{rd}}}$ and $k_0 d = (m-1)(2\pi)/\sqrt{\varepsilon_{\mathrm{rd}} - 1}$, respectively. As a result, the ratios of both the PMC and

PEC frequencies at $\theta = 90^\circ$ and at $\theta = 0^\circ$ is given by the constant

$$\frac{\omega^{\theta=90^\circ}}{\omega^{\theta=0^\circ}} = \sqrt{\frac{\varepsilon_{\rm rd}}{\varepsilon_{\rm rd}-1}} > 1, \tag{4.16}$$

indicating that $\omega^{\theta=90^\circ} > \omega^{\theta=0^\circ}$, as observed in Fig. 5a. Equation 4.16 corresponds to the frequency shift of

$$\Delta\omega = \omega^{\theta=90^\circ} - \omega^{\theta=0^\circ} = \left(1 - \sqrt{\frac{\varepsilon_{\rm rd}}{\varepsilon_{\rm rd}-1}}\right)\omega^{\theta=90^\circ}, \tag{4.17}$$

indicating that the frequency shift between the $\theta = 90^\circ$ and $\theta = 0^\circ$ PMC or PEC frequencies increases linearly with frequency, as also observed in Fig. 4.7a.

Ungrounded Substrate Case In the ungrounded substrate, the TE and TM surface-wave mode cutoffs are degenerate. Therefore the equivalent boundary conditions seen by $J_{\rm s}$ at the cutoff frequencies depend on the combined effects of the TE and TM cutoffs. At the cutoff, at $z = -d$, we have $Z_L^{\rm TE} = \infty$, $Z_L^{\rm TM} = 0$, $\phi_{-d}^{\rm TE} = 0$ and $\phi_{-d}^{\rm TM} = \pi$. Inserting these results for $Z_L^{\rm TE,TM}$ into (4.12) leads to

$$Z_{\rm in}^{\rm TE} = -jZ_c^{\rm TE}\cot(k_{\rm zd}d), \tag{4.18a}$$

$$Z_{\rm in}^{\rm TM} = jZ_c^{\rm TM}\tan(k_{\rm zd}d). \tag{4.18b}$$

For the TE-cutoff case, inserting $\phi_0 = 0$ (cutoff) and $\phi_{-d} = 0$ (cutoff, no ground and TE) into (4.11) yields $k_{\rm zd}^{\rm cutoff}d = m\pi$ and hence $Z_{\rm in} = \infty$ a PMC condition (Fig. 4.6) and $d/\lambda_{\rm eff}^{\rm cutoff} = m/2$ (Fig. 4.4b). For the TM-cutoff case, inserting $\phi_0 = \pi$ (cutoff) and $\phi_{-d} = \pi$ (cutoff, no ground and TM) into (4.11) yields $k_{\rm zd}^{\rm cutoff}d = (m-1)\pi$ and hence $Z_{\rm in} = 0$ a PEC condition (Fig. 4.6) and $d/\lambda_{\rm eff}^{\rm cutoff} = (m-1)/2$ (Fig. 4.4b). These TE and TM boundary conditions are handled separately in the computation of the radiated power, using superposition, and, as in the grounded case, the TE part contributes a maximal radiated power while the TM part contributes a minimal radiated power, due to in phase and out of phase $J'_{\rm sub}$ and $J_{\rm s}$, respectively. As a result, the total (TE + TM) radiated power is maximal at the degenerated cutoff frequencies, as confirmed in Fig. 4.7b at $\theta = 90^\circ$ (angular variation to be discussed below), and hence maximizes the radiated power, as observed in Fig. 4.4c. As in the grounded case, at $\theta = 90^\circ$, the field is propagating in the air at a grazing angle along the substrate, and therefore the field configurations in the air correspond to PMC and PEC boundary conditions for the TE and TM modes, respectively. Since the cutoffs are $\lambda_{\rm eff}^{\rm cutoff}/2$ apart, the TE and

TM input impedances from one cutoff to the next one transform from an open to another open and from a short to another short, respectively. Therefore, they cross a short and an open for the TE and TM modes, respectively [Eq. (4.18)], at some intermediate frequency in-between. Consequently, corresponding additional maxima occur between adjacent cutoffs, as seen in Fig. 4.7b.

Let us now explain the variation of $\tilde{I}_{\rm eq}$ versus θ. As in the grounded substrate case, at each angle of incidence θ and at a specific frequency slightly shifted from the cutoff frequencies, the total tangential magnetic field for the TE modes vanishes at the air-dielectric interface, which leads to TE-PMC boundary condition at the interface. As a result, as shown in Fig. 4.7b at all the angles $\theta = 90^\circ \rightarrow 0^\circ$ there is a frequency where the TE-PMC condition is satisfied. Moreover, it is observed in Fig. 4.7b that as θ decreases towards 0°, the additional maxima between the cutoffs progressively transform into minima. To explain the reason of this variation, let us consider the variations of the input impedance $Z_{\rm in}$ of the ungrounded substrate as the angle decreases from $\theta = 90^\circ$ to $\theta = 0^\circ$. In the ungrounded substrate case, the load impedance $Z_L^{\rm TE,TM} = Z_0^{\rm TE,TM}$ [Eq. (4.12)] is a function of the angle of incidence. This is in contrast with the grounded substrate case whose ground plane has a load impedance which is independent of θ. The variations of Z_L with the angle affects the input impedance and therefore the position of the maxima and minima of $\tilde{I}_{\rm eq}$. As the angle decreases from $\theta = 90^\circ$ to $\theta = 0^\circ$, $k_{z0}^{\rm TE,TM} = k_0\sqrt{1-\sin^2\theta}$ varies from $k_{z0}^{\rm TE,TM} = 0$ to $k_{\rm z0}^{\rm TE,TM} = k_0$. Therefore, $Z_0^{\rm TE} = \omega\mu_0/k_{\rm z0}^{\rm TE}$ starts to decrease from infinity to the free-space impedance $\eta_0 = \sqrt{\mu_0/\varepsilon_0}$ while $Z_0^{\rm TM} = k_{\rm z0}^{\rm TM}/\omega\varepsilon_0$ increases from zero to η_0. After θ has decreased beyond some point, $Z_L^{\rm TM}$ starts to increase significantly from zero and converges to $Z_L^{\rm TE}$ so that the variations of its corresponding input impedance follow the same maxima and minima with respect to the frequency as the TE mode.

Finally, the total radiated power is a result of integration over all the k_ρ or all the angles, which results into the radiated power maxima observed at the cutoffs in Fig. 4.4c.

4.4.2 Surface-Wave Power

As observed in Figs. 4.3d and 4.4d, the surface-wave modes carry and dissipate part of the energy provided by the source. Let us examine in some details how this energy varies versus the electrical thickness of the substrate and how it is distributed between the TE and TM modes.

Globally, the total surface-wave power tends to increase with increasing electrical thickness. This is intuitively very understandable since the number of surface waves increases with the electrical thickness. Specifically, the increase in surface wave power tends to be maximal at the cutoff frequencies, since each of these frequencies corresponds to the onset of

new modes, one TE or TM mode in the grounded substrate case and one TE-TM mode pair in the ungrounded substrate case. However, this is not systematically the case, because the radiated power behavior depends on *all* the surface-wave modes. For instance, no surface-wave power increase is observed at the onset of the TM_1 mode in the grounded substrate case. This is because the decay in the TM_0 and TE_0 powers toward this frequency, due to reduction of phase matching, is exceeding the power increase induced by the onset of the TM_1 mode.

Note that the surface-wave power increase is sharper for the TE modes than for the TM modes. This is due to the fact that the former have their electric field perfectly co-polarized with the source whereas the latter have their electrical field perfectly cross-polarized with the source. In the ungrounded substrate case, this effect is apparent only when looking at the TE and TM surface-wave contribution separately since the TE and TM cutoffs are degenerate.

4.4.3 Radiation Efficiency

According to its definition (2), the radiation efficiency, observed in Figs. 4.3a and 4.4a, depends only on the radiated and surface-wave powers. Therefore, it may be completely explained from the radiated and surface-wave powers, which were presented in Secs. 4.4.1 and 4.4.2 and plotted in Figs. 4.3c–4.3d and 4.4c–4.4d. We shall thus explain here the radiation efficiency behavior versus electrical length by comparing the relative amounts of radiated and surface-wave powers. The reader is referred to Figs. 3a and 4a for the electric length regions to be considered next.

Region A

At the lowest frequencies, just above DC, only one (grounded case) or two (ungrounded case) surface waves propagate, and these waves carry only a very small fraction of the power. The TM_0 wave carries almost no power because its field is essentially (exactly at DC) cross-polarized with the source dipole. For the ungrounded case, the TE_0 mode is always co-polarized with the source, but it is essentially (completely at DC) shorted by the ground due to the extremely small (zero at DC) electrical thickness of the substrate. As result of the very small surface-wave power, most of the energy radiates to free-space, and therefore the radiation efficiency is very high.

Region B

As the electrical thickness increases towards the second cutoff frequency (TE_0 for the grounded case, TE_1 and TM_1 for the ungrounded case), the efficiency decreases monotonically,

due to increased coupling to the surface waves. For the grounded case, this decrease is relatively slow whereas for the ungrounded case it is quite abrupt. The reason for this difference is the fact that the TE_0 mode (always perfectly co-polarized with the source), propagating only in the ungrounded case, is now less shorted than in Region A due to the increased electrical thickness of the substrate.

Region C

As the electrical thickness is further increased close the second cutoff frequency, the surface-wave and radiated powers both increase, but the increase rate of the latter exceeds that of the former, due to the radiated power maximum. Consequently, the radiation efficiency reaches a local maximum at this point.

Region D

Just above the second cutoff frequency, the onset of additional surface-wave modes increases the surface-wave power, and hence reduces the radiated power, which decreases the radiation efficiency.

Region E

For the grounded substrate, the radiation efficiency reaches zero at the TM_1 cutoff frequency, while for the ungrounded substrate, it only becomes minimum, due to corresponding radiated powers.

Region F

Next, the radiation efficiency increases towards a next local maximum, due to a high increase rate in the radiated power.

Region G

The radiation efficiency reaches then its second maximum at the TE_1 cutoff for the grounded case and at the TE_2-TM_2 cutoff for the ungrounded case.

Region H

The radiation efficiency keeps varying according to the cycle of Regions D to G, although it is progressively decreasing on average due to the increased number of propagating surface waves.

Note that the radiation efficiency maxima are smaller in the ungrounded case, due to the existence of a larger number of surface waves.

4.5 Half-wavelength Dipole Antenna Extension

The previous two sections considered the theoretical case of an *infinitesimal horizontal dipole radiator* for simplicity. The question now is whether the results obtained for this infinitesimal dipole radiator hold in the case of a *practical planar antenna*.

The main planar antennas are patch antennas, planar dipole antennas and planar traveling-wave antennas. Patch antennas do not work on electrically thick substrates [78] because, being cavity-type structures, they loose resonance when higher-order modes start to be excited [112]. Traveling-wave antennas are much more complex and less common, and they therefore are not considered in this paper. The remaining type, to be considered, is then the planar dipole antenna type.

From the fact that the radiation from a real (finite-size) dipole antenna is equivalent to the superposition of the radiation contributions from infinitesimal dipole elements distributed in an array along the extent of the real dipole, it may be anticipated that the results obtained in the previous two sections for a single infinitesimal dipole should, at least qualitatively, hold for the real dipole case.

Figure 4.8 compares the radiation efficiency behaviors of the infinitesimal dipole and a half-wavelength dipole on the grounded substrate (Fig. 4.8a) and on the ungrounded substrate (Fig. 4.8b), respectively. The efficiency of the half-wavelength dipole is computed from the method of moments engine of the Advanced Design System (ADS) software. The comparison confirms the expectation of the previous paragraph: the behavior of the dipole antenna radiation efficiency is qualitatively similar to that of the infinitesimal dipole.

4.6 Solutions to the Low Radiation Efficiency Issue

Let us now examine possible solutions to enhance the efficiency of a dipole antenna on an electrically thick substrate with a given permittivity and thickness. Consider the most unfavorable situation where the electrical thicknesses at the specified frequency corresponds to minimal efficiency (little or no radiation) (see Figs. 4.3a and 4.4a). As pointed out in Sec. 4.2, this situation may frequently occur in millimeter-wave and terahertz antennas, where a reasonably thick substrate for sufficient rigidity typically entails the propagation of several surface waves [107]. In this case, we have for the grounded substrate $d/\lambda_{\text{eff}}^{\text{cutoff}} = 0.5$, meaning that a TM-PEC condition is seen at $z = 0$, while for an ungrounded substrate minimal efficiency occurs at about $d/\lambda_0 = 0.35$, between two cutoff frequency pairs.

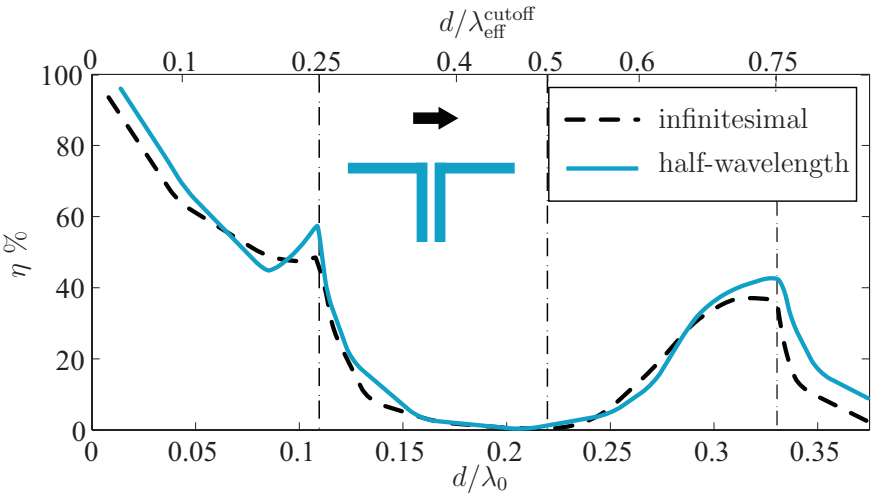

(a)

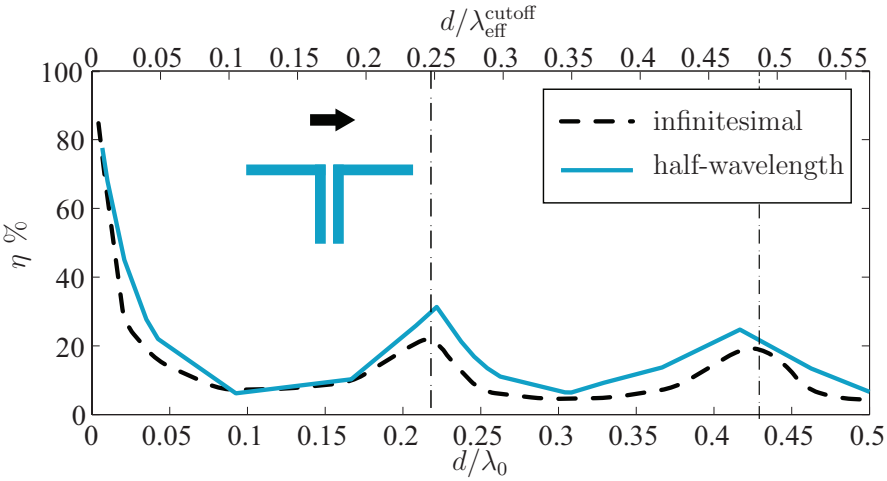

(b)

Figure 4.8 Comparison of the radiation efficiency behaviors of the infinitesimal dipole and the half-wavelength dipole on the grounded and ungrounded substrates, computed from the Green function analysis and from full-wave simulation, respectively. (a) Grounded substrate. (b) Ungrounded substrate.

4.6.1 Enhancement Principle

The efficiency enhancement presented here is based on manipulating the boundaries at $z = 0$, so that the substrate dipole J_{sub} interferes constructively with the source dipole J_{s} at the desired electrical thickness. In other words, as shown in Sec. 4.4, the input impedance of the transmission-line equivalent circuit at the air-dielectric interface controls the positions of the maxima and minima of the radiation efficiency. The maximal and minimal efficiencies are achieved when the air-dielectric interface behaves as a PMC plane and PEC boundary plane, respectively. Therefore, in order to maximize a minimum of the radiation efficacy, the air-dielectric PEC has to be transformed to a PMC. For this purpose, one needs to replace the PEC boundary at $z = -d$ by a PMC which transforms the boundary at $z = 0$ from a PEC to a PMC.

Although a PMC boundary does not exist naturally, it can be realized artificially [53, 52, 50, 113]. In the following, two efficiency enhancement PMC boundary realizations, a quarter-wavelength grounded dielectric slab and an electromagnetic bandgap grounded slab, depicted in Figs. 4.9 and 4.12, respectively, are presented and compared. Since both of the PMC boundaries possess a PEC ground plane, they are not practical for the ungrounded substrate case. Therefore, in the following the efficiency enhancement is only examined for the grounded substrate case (Fig. 4.1a).

4.6.2 Enhancement Solutions

Quarter-Wavelength Grounded Dielectric Slab

The quarter-wavelength grounded dielectric slab was introduced in [53], and the detailed descriptions of Sec. 4.4.1 straightforwardly apply to it. The PMC condition is achieved at the air-dielectric interface at the frequency corresponding to $d_{\text{PMC}}/\lambda_0 = 1/(4\sqrt{\varepsilon_{\text{r, PMC}} - 1})$, where $\varepsilon_{\text{r, PMC}}$ and d_{PMC} are the permittivity and the thickness of the dielectric slab, respectively (Fig. 4.9b).

In order to remedy the aforementioned minimal radiation efficiency issue, such a quarter-wavelength grounded dielectric slab PMC (Fig. 4.9b) is added at the bottom of the original slab (Fig. 4.9a) so as to form a two-layer configuration (Fig. 4.9c). A PMC is then seen at $z = 0$, at the frequency corresponding to $d_{\text{PMC}}/\lambda_0 = 1/(4\sqrt{\varepsilon_{\text{r, PMC}} - 1})$.

The substrate of the additional layer could be chosen the same as the original substrate. This corresponds to increasing the thickness of the original substrate $(\mu_0, \varepsilon_{\text{d}})$ by a thickness $\lambda_{\text{eff}}^{\text{cutoff}}/4$, which will shift the maxima of the original substrate toward the lower frequencies. In the case of technological constraints regarding the acceptable thickness of overall antenna, the additional PMC substrate could be realized under the form of a thin high-permittivity

grounded layer. It should be noted that this method is practical only in the cases where the original substrate would be constrained to be fixed, due to design limitations (such as in millimeter-wave and terahertz antennas), and could not be substituted by a thinner or lower-permittivity substrate. The following provides an example of efficiency enhancement corresponding to the latter case.

In order to generate a PMC at $z = 0$, one now needs to add at the bottom of the original substrate another substrate providing there a PMC. This may be achieved by a dielectric slab with $\varepsilon_{\mathrm{r,\ PMC}} = 10.2$ (RT/duroid 6010) and $d_{\mathrm{PMC}} = 1$ mm. Fig. 4.10 compares the efficiencies of the original and PMC grounded dielectric substrates, where it is seen that the minimum efficiency of the original structure has become maximal.

Electromagnetic Bandgap Grounded Slab

Electromagnetic bandgap (EBG) structures may act as PMC boundaries at their resonant frequency. These structures have been used for the gain enhancement of electrically thin planar antennas [114]. However, in electrically thin antennas the EBG is in the near-field of the patch or dipole radiator and therefore behaves more as parasitic scattering surface than as a real (homogeneous) PMC, which requires extensive full-wave optimization and may alter the radiation pattern.

Here, an EBG structure similar to the one proposed in [52] (shown in Fig. 4.12) is used for the realization of the PMC boundary, and the PEC plane of the original substrate (Fig. 4.12 is replaced by the EBG-PMC structure (Fig. 4.12b) so as to form the configuration shown in Fig. 4.12c.

Similar to the previous method, this method of enhancement is useful in antenna systems where design constraints, fabrication limitations or mechanical rigidity requirements prevent the substitution of the original electrically thick substrate by an electrically thin one.

In contrast to the case EBG utilizations reported in works such as [114], the EBG structure here is in the far-field of the dipole, since the antenna is operated at frequencies where the substrate is electrically thick. Therefore, the EBG is essentially seen by the dipole as a uniform PMC surface, immune of parasitic effects and operating as predicted from plane wave incidence analysis.

The advantage of the EBG-PMC method to the quarter-wavelength-dielectric-PMC is that it can be realized by thin-film deposition followed by metal deposition at the back of the substrate, which does represent a significant thickness increase with respect to the original antenna. However, the EBG approach entails higher loss and lower bandwidth, as will be shown in the forthcoming example.

In order to satisfy the PMC condition at $d/\lambda_{\mathrm{eff}}^{\mathrm{cutoff}} = 0.5$, an EBG structure is designed

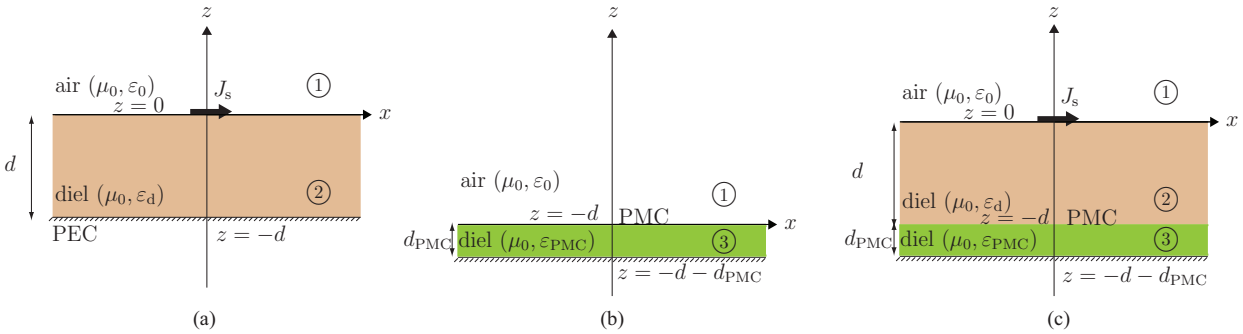

Figure 4.9 Quarter-wavelength grounded dielectric PMC boundary configuration for the enhancement of the radiation efficiency at the minima of the radiation efficiency of the original grounded substrate (Fig. 4.3a). (a) Original grounded substrate. (b) Quarter-wavelength dielectric PMC boundary structure. (c) Substituting the PEC ground plane of the grounded substrate by the quarter-wavelength PMC structure.

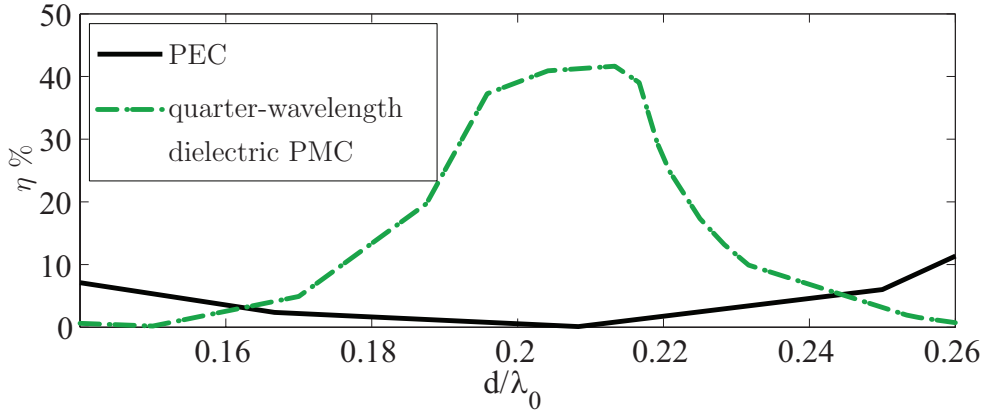

Figure 4.10 Comparison between the efficiency of the original and the PMC grounded substrates.

on a dielectric with $\varepsilon_{\mathrm{r,\,PMC}} = 10.2$ (RT/duroid 6010) and $d_{\mathrm{PMC}} = 0.254$ mm. To confirm the PMC frequency of the EBG, the phases of the waves reflected from a PEC plane and the EBG structure are compared. The frequency where the phase difference between the two reflected fields is 180° is the PMC frequency of the EBG structure. Figure 4.11 shows the full-wave simulation results for the differential unwrapped phase between the reflected fields from a PEC plane and the EBG structure. It is seen that the phase difference of is 180° is achieved at $d/\lambda_{\mathrm{eff}}^{\mathrm{cutoff}} = 0.5$, corresponding to the PMC frequency.

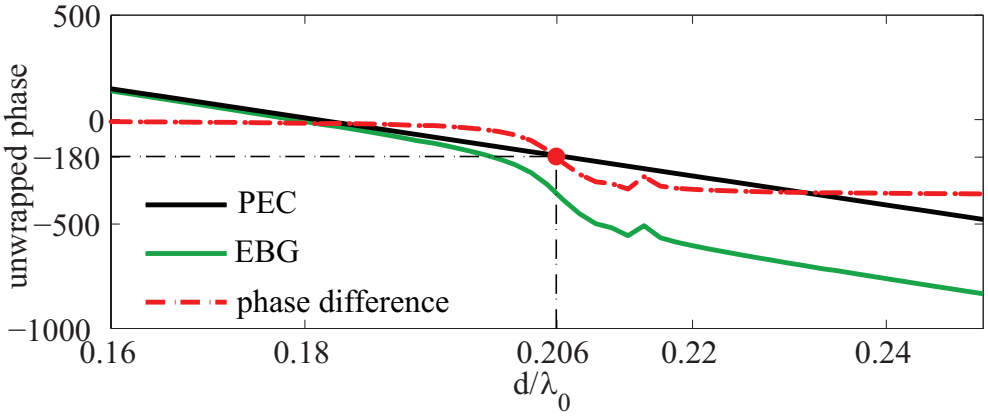

Figure 4.11 Full-wave HFSS simulation results for the differential unwrapped phase between the reflected fields from a PEC plane and the EBG structure.

Figure 4.13 compares the efficiencies of the original and EBG-PMC grounded substrates. It is seen that by using PMC, the minimum efficiency in the original substrate becomes maximal.

4.7 Conclusions

The radiation efficiency response of an infinitesimal horizontal electric dipole on grounded and ungrounded substrates versus the substrate electrical thickness up to thicknesses beyond the wavelength has been analyzed. To simplify the explanation of the non-monotonically decaying response of the efficiency, a substrate dipole approach has been introduced, which reduces the actual structure to an equivalent source dipole composed of the original dipole and the substrate dipole radiating into free space. It has next been shown that the efficiency response of a half-wavelength dipole printed on grounded and ungrounded substrate is essentially similar to that of the infinitesimal dipole. Finally, two solutions for enhancing the efficiency at electrical thicknesses where the efficiency is minimal have been compared. This study provides guidelines for the efficient design of millimeter-wave and terahertz antennas

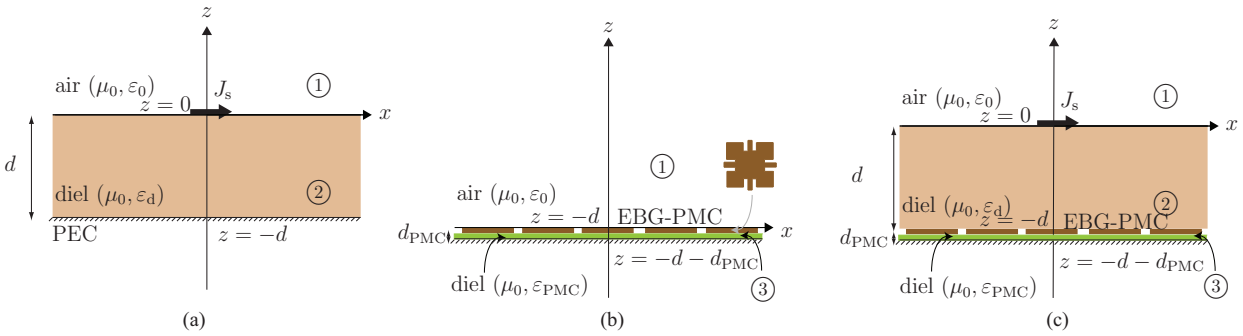

Figure 4.12 EBG-PMC boundary configuration for the enhancement of the radiation efficiency at the minima of the radiation efficiency of the original grounded substrate (Fig. 4.3a). (a) Original grounded substrate. (b) EBG-PMC boundary structure. (b) Substituting the PEC ground plane of the original grounded substrate by the EBG-PMC structure.

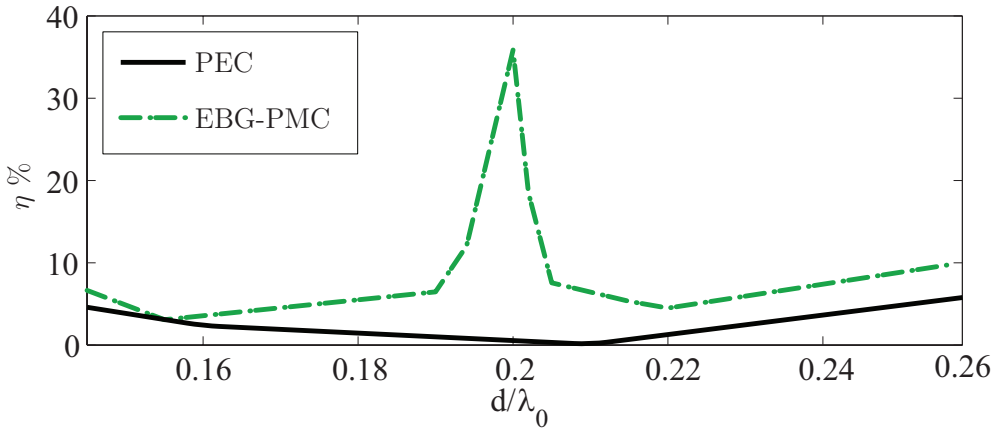

Figure 4.13 Comparison between the efficiency of the PEC and the EBG-PMC grounded substrate.

whose substrates tend to be inherently electrically thick.

CHAPTER 5

EFFECT OF SUBSTRATE ANISOTROPY ON RADIATION EFFICIENCY

5.1 Abstract

The effect of substrate anisotropy on radiation efficiency behavior of a horizontal electric dipole printed on an electrically thick substrate is studied. To simplify the analysis, first, various cases of non-dispersive anisotropic substrates are analyzed and the appropriate anisotropy for the highest level of efficiency with the smoothest variations is chosen. Next, a mushroom-type artificial substrate which has the desired anisotropy for the efficiency enhancement behavior is studied. This substrate is uniaxially anisotropic with Drude-dispersive permittivity along the axis of the wires and Lorentz-dispersive permeability along the perpendicular axis to the loops between the two adjacent mushrooms. The results provide fundamental and useful guidelines for the design of high-efficiency antennas.

5.2 Introduction

In Chapter 4, the radiation efficiency behavior of a horizontal electric dipole printed on an electrically thick conventional isotropic substrate was analyzed. The reasons for the oscillatory behavior of the efficiency versus the electrical thickness and the TE/TM surface-wave modes cutoffs coincidence with the maxima/minima of the radiation efficiency, were discussed.

As explained in Chapter 1, substrate anisotropy can be employed in engineering novel interesting applications which may not be achieved by using isotropic substrates. For instance, Chapter 3 demonstrated how the substrate anisotropy is able to enhance and control the radiation properties of the substrate leaky-wave modes excited by a vertical electric dipole.

The goal of this chapter is to study and discuss the effect of substrate anisotropy on the radiation efficiency of a horizontal electric dipole printed on a grounded substrate. To this end, we will benefit from the knowledge obtained in Chapter 4 about the radiation efficiency behavior of a horizontal dipole for the simpler case of an isotropic substrate. Furthermore, we assume that the anisotropy of the substrate is uniaxial and similar to the substrate discussed in Chapter 3 [Eq. (3.1)].

In Sec. 5.3, to simplify the study, we start from the analysis of various *non-dispersive* uniaxially anisotropic substrates and show how the anisotropy governs the efficiency behavior of

the dipole. Afterwards, in Sec. 5.4, we extend the study to the more complicated case of artificial anisotropic substrates with *dispersive* Drude permittivity along the axis perpendicular to the substrate and with Lorentz permeability in the plane of the substrate. This substrate is in the form of the dispersive anisotropic substrate of Chapter 3 [Eqs. (3.2) and (3.3)], which may be practically realized by a mushroom-type artificial magneto-dielectric substrate [50, 49, 48], where the Drude dispersive permittivity models the wires and the Lorentz dispersive permeability models the rings between adjacent mushrooms.

5.2.1 Radiation Efficiency Computation

Figure 5.1a illustrates the anisotropic grounded substrate with the permittivity and permeability tensors $\bar{\bar{\varepsilon}}$ and $\bar{\bar{\mu}}$, respectively, in the form of

$$\bar{\bar{\varepsilon}} = \begin{pmatrix} \varepsilon_\rho & 0 & 0 \\ 0 & \varepsilon_\rho & 0 \\ 0 & 0 & \varepsilon_z \end{pmatrix}, \tag{5.1a}$$

$$\bar{\bar{\mu}} = \begin{pmatrix} \mu_\rho & 0 & 0 \\ 0 & \mu_\rho & 0 \\ 0 & 0 & \mu_z \end{pmatrix}, \tag{5.1b}$$

excited by an infinitesimal electric dipole along the x axis, J_x.

Similar to Chapter 4, it is assumed that the substrate shown in Fig. 5.1a is loss-less, and that the only source of loss in the system is the energy trapped by the surface-wave modes in the substrate. Therefore, the radiation efficiency η can be calculated from the radiated power $P_{\rm rad}$ and surface-wave power $P_{\rm sw}$ using the following equation [77, 78, 79]

$$\eta = \frac{P_{\rm rad}}{P_{\rm rad} + P_{\rm sw}}, \tag{5.2}$$

where $P_{\rm rad}$ and $P_{\rm sw}$ are calculated from the radiated and surface-wave time-averaged Poynting vectors, $\mathbf{S}_{\rm r,av}$ and $\mathbf{S}_{\rm sw,av}$, respectively, and read

$$P_{\rm rad} = \int_0^{2\pi} \int_0^{\pi/2} \mathbf{S}_{\rm rad,av}.\hat{\mathbf{r}} r^2 \sin\theta \, d\theta \, d\phi, \tag{5.3a}$$

$$P_{\rm sw} = \int_0^{2\pi} \int_{-d}^{\infty} \mathbf{S}_{\rm sw,av}.\hat{\boldsymbol{\rho}} \rho \, dz \, d\phi, \tag{5.3b}$$

where d is the thickness of the substrate and $P_{\rm rad}$ and $P_{\rm sw}$ are obtained by integration over

the half sphere in free space above the antenna and by integration over a cylinder extending from the ground plane through the substrate to infinity above the antenna, respectively.

To compute the radiated and surface-wave time-averaged Poynting vectors, $\mathbf{S}_{\mathrm{rad/sw,av}} = \frac{1}{2}\mathrm{Re}[\mathbf{E} \times \mathbf{H}^*]$, the far-field electric and magnetic fields $\mathbf{E}$ and $\mathbf{H}$, respectively, should be calculated. For this purpose, the spectral-domain transmission-line modeling of the horizontal infinitesimal electrical dipole placed at the air-dielectric interface of the substrate [75, 109] is employed, which is shown in Fig. 5.1b. In this approach, the spatial domain far-field electric fields radiated by an infinitesimal dipole along the x axis, $\mathbf{E}(x, y, z)$, is calculated from the spatial domain magnetic vector potentials $\overline{\overline{\mathbf{G}}}_A(x, y, z)$ as follows

$$\mathbf{E}(x, y, z) = -j\omega\overline{\overline{\mathbf{G}}}_A(x, y, z) \cdot \mathbf{x}, \tag{5.4}$$

and the corresponding magnetic fields are obtained via the Maxwell equations. The Sommerfeld choice for vector potential Green functions leads to $\bar{\bar{\mathbf{G}}}_A = (\mathbf{x}G_A^{xx} + \mathbf{z}G_A^{zx})\,\mathbf{x}$, where G_A^{xx} and G_A^{zx} are the x and z potential Green function components, respectively, due to $\tilde{J}_x$ [76].

The spatial domain vector potential Green functions G_{A}^{xx} and G_{A}^{zx} are calculated by the inverse Fourier transformation of the spectral domain vector potential Green functions $\tilde{G}_{\mathrm{A}}^{xx}$ and $\tilde{G}_{\mathrm{A}}^{zx}$, respectively, that are related to the transmission line model of the grounded substrate as follows

$$\tilde{G}_{\mathrm{A}}^{xx} = \frac{1}{j\omega}\tilde{V}^{\mathrm{TE}_z}, \tag{5.5a}$$

$$\tilde{G}_{\mathrm{A}}^{zx} = \frac{\mu_\rho}{jk_y}\left(\frac{k_x k_y}{k_\rho^2}\tilde{I}^{\mathrm{TM}_z} - \frac{k_x k_y}{k_\rho^2}\tilde{I}^{\mathrm{TE}_z}\right), \tag{5.5b}$$

where $\tilde{V}^{\mathrm{TE}_z}$, $\tilde{I}^{\mathrm{TE}_z}$ and $\tilde{I}^{\mathrm{TM}_z}$ are the spectral-domain voltage and current for the TE_z modes and the spectral-domain current for the TM_z modes, while k_x, and k_y are the wave numbers along the x and y axes and ${k_\rho}^2 = {k_x}^2 + {k_y}^2$ is the square of the transverse wave number, with ${k_\rho^{TM_z}}^2 + {k_z^{\mathrm{TM}_z}}^2 = \omega^2\mu_\rho\varepsilon_z = {k^{\mathrm{TM}_z}}^2$ and ${k_\rho^{\mathrm{TE}_z}}^2 + {k_z^{\mathrm{TE}_z}}^2 = \omega^2\mu_z\varepsilon_\rho = {k^{\mathrm{TE}_z}}^2$ where $k_z^{\mathrm{TM}_z,\mathrm{TE}_z}$ is the longitudinal wave number and $k^{\mathrm{TM}_z,\mathrm{TE}_z}$ is the wave number for the $\mathrm{TM}_z/\mathrm{TE}_z$ modes, respectively.

The details of the spectral domain transmission-line modeling is provided in Appendix B (particularly Sec. B.2 which is devoted to the horizontal dipole excitation), while Appendix E presents the calculation of the radiation efficiency for a uniaxially anisotropic material with the tensorial permittivity and permeability of (5.1).

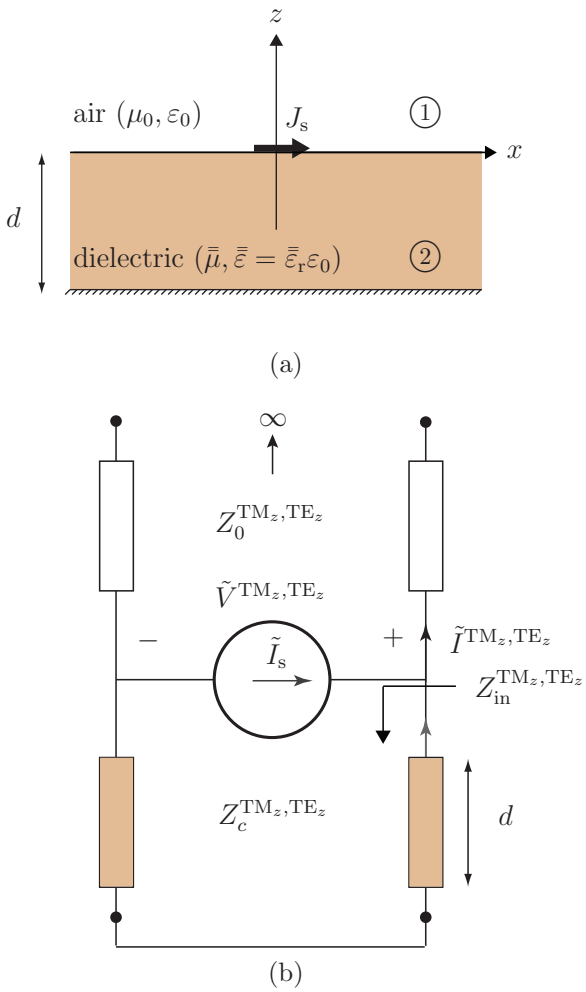

Figure 5.1 Uniaxially anisotropic grounded substrate excited by an infinitesimal horizontal electric dipole. (a) Structure. (b) Transmission-line model.

5.3 Non-Dispersive Uniaxially Anisotropic Substrates

To simplify the analysis of the effects of substrate anisotropy on the radiation efficiency, let us first analyze non-dispersive anisotropic substrates.

5.3.1 Definition of Various Cases of Study

To study the effect of anisotropy on the radiation efficiency, 5 different cases of uniaxially anisotropic grounded substrate (Fig. 5.1a), with the constitutive tensorial parameters of (5.1), are examined and compared. In order to make the comparison reasonable, the permittivity and permeability of each case are chosen so that at each frequency, all the 5 substrate cases

possess equal effective electrical dimensions with respect to the effective electrical wavelength

$$\lambda_{\text{eff}} = \frac{2\pi}{k^{\text{TM}_z,\text{TE}_z}}. \tag{5.6}$$

Since ${k^{\text{TM}_z}}^2/\omega^2 = \mu_\rho \varepsilon_z$ and ${k^{\text{TE}_z}}^2/\omega^2 = \mu_z \varepsilon_\rho$, in order to get equal effective electrical dimensions for the TE_z and TM_z modes at any fixed frequency, one should choose $\mu_\rho \varepsilon_z = \mu_z \varepsilon_\rho = n\mu_0\varepsilon_0$, where n is the square of the TM_z and TE_z refractive indices.

The cases under study are summarized in Table 5.1. As seen in the table, case 1 has the properties of an isotropic substrate, while the cases 2-5 are uniaxially anisotropic. The value of $n = 6.15$ and the thickness of the substrate $d = 2.5$ mm are chosen so that case 1 reduces to the isotropic grounded substrate of Chapter 4. The values for the permittivity and permeability tensors elements of the cases are defined so that they present high and low values for the ratios μ_ρ/μ_z and $\varepsilon_\rho/\varepsilon_z$.

Table 5.1 Various uniaxially anisotropic substrate cases ($\mu_\rho \varepsilon_z = \mu_z \varepsilon_\rho = n\mu_0\varepsilon_0$), with $d = 2.5$ mm and $n = 6.15$.

case	μ_ρ/μ_0	$\varepsilon_z/\varepsilon_0$	μ_z/μ_0	$\varepsilon_\rho/\varepsilon_0$	μ_ρ/μ_z	$\varepsilon_\rho/\varepsilon_z$
case 1 (conventional isotropic)	1	n	1	n	1	1
case 2 (anisotropic)	1	n	$\sqrt{n}/2$	$2\sqrt{n}$	$2/\sqrt{n}$	$2/\sqrt{n}$
case 3 (anisotropic)	1	n	$2\sqrt{n}$	$\sqrt{n}/2$	$1/(2\sqrt{n})$	$1/(2\sqrt{n})$
case 4 (anisotropic)	$\sqrt{n}/2$	$2\sqrt{n}$	1	n	$\sqrt{n}/2$	$\sqrt{n}/2$
case 5 (anisotropic)	$2\sqrt{n}$	$\sqrt{n}/2$	1	n	$2\sqrt{n}$	$2\sqrt{n}$

5.3.2 Results and Discussion

Figures 5.2a, 5.3a, 5.4a, 5.5a, and 5.6a illustrate the radiation efficiency of the substrate cases 1, 2, 3, 4 and 5, respectively, versus the electrical thickness d/λ_0, while Figs. 5.2b, 5.3b, 5.4b, 5.5b, and 5.6b present the TE_z and TM_z surface-wave modes for each case 1, 2, 3, 4 and 5, respectively. From these figures, the following observations can be made about the radiation efficiency behavior of each grounded substrate case.

Oscillatory Radiation Efficiency Variations

Comparing the radiation efficiency and the corresponding surface-wave modes for each case reveals that in all the anisotropic cases 2-4, the oscillatory behavior of the radiation efficiency is preserved. The efficiency variations follow the same rule as in the isotropic substrate case 1, which was thoroughly explained in Chapter 4. As seen in the figures, in all

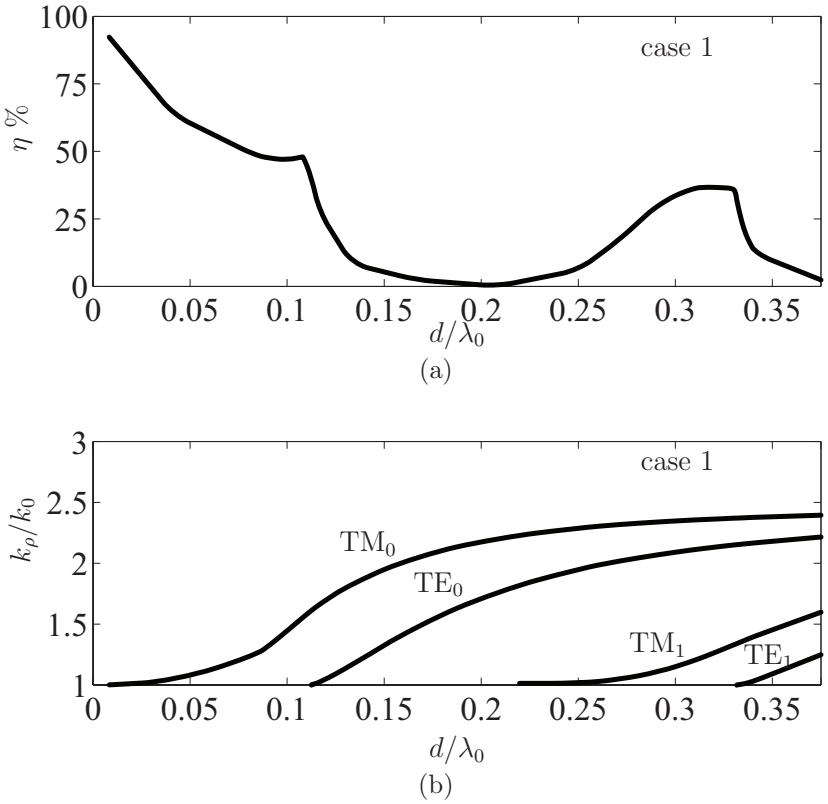

Figure 5.2 Response to an infinitesimal horizontal dipole on the isotropic grounded substrate (Fig. 5.1a) of *case 1* versus the electrical thickness of the substrate. (a) Radiation efficiency [Eq. (5.2)]. (b) TM_z and TE_z surface modes.

the cases, the efficiency maxima/minima occur at the TE_z/TM_z modes cutoffs, respectively. However, in case 5 (Fig 5.6a), as opposed to the other cases, the efficiency does not increase uniformly towards its maxima at the TE_z cutoffs. The following discussion addresses this feature of the anisotropic substrate case 5.

Figure 5.7b compares the radiated power for the cases 1-5. In this figure, it is evident that as opposed to the cases 1-4, the radiated power in case 5 does not increase uniformly towards its maxima at the TE_z cutoffs. Based on this figure, it is concluded that the non-uniform increase of the efficiency close to the maxima are related to the radiated power behavior and *not* the surface-wave powers. Therefore, the rest of the analysis is concentrated on the radiated power behavior.

As explained in Sec. 5.2.1, the radiated power is controlled by the spectral domain vector potentials $\tilde{G}_{\rm A}^{xx}$ and $\tilde{G}_{\rm A}^{zx}$ through equations (5.5a) and (5.5b). Let us now compare $\tilde{G}_{\rm A}^{xx}$ and $\tilde{G}_{\rm A}^{zx}$ variations for the cases 1 and 5. Figures 5.8a and 5.8b show $\tilde{G}_{\rm A}^{xx}$ and $\tilde{G}_{\rm A}^{zx}$ for the case 1, respectively, versus the electrical thickness d/λ_0 and the angle of radiation θ from the z axis, while Figs. 5.9a and 5.9b are for $\tilde{G}_{\rm A}^{xx}$ and $\tilde{G}_{\rm A}^{zx}$ of case 5, respectively. To simplify the

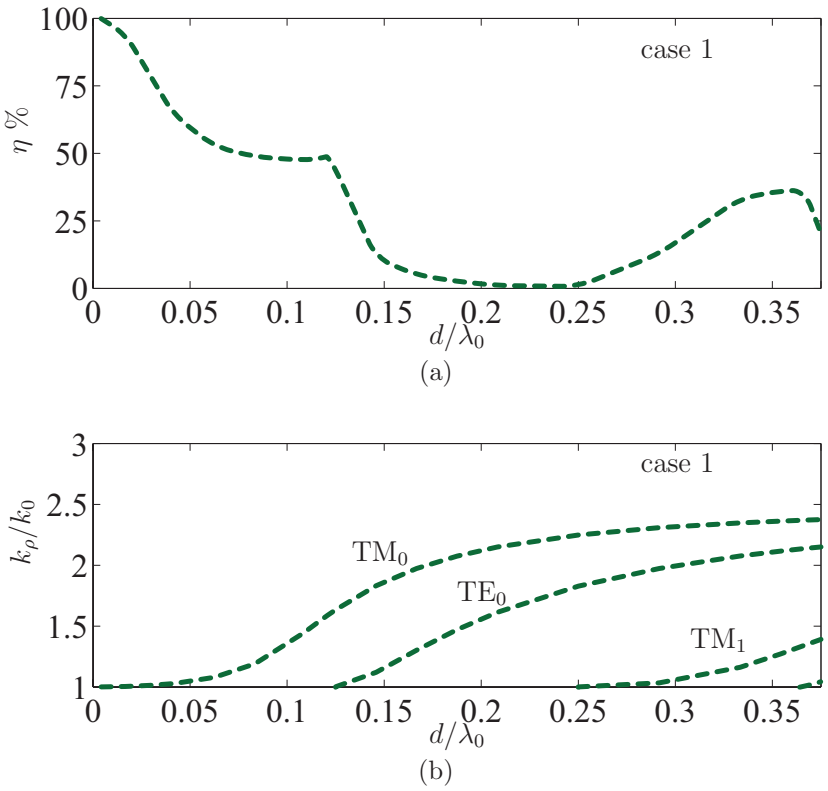

Figure 5.3 Response to an infinitesimal horizontal dipole on the uniaxially anisotropic grounded substrate (Fig. 5.1a) of *case 2* versus the electrical thickness of the substrate. (a) Radiation efficiency [Eq. (5.2)]. (b) TM_z and TE_z surface modes.

comparison and in order to only focus on the values whose contribution in the radiated power is strong, all the figures are limited to $-21 < \log\left(\left|\tilde{G}_{\mathrm{A}}^{xx,zx}\right|\right) < 0$. Figure. 5.8 demonstrates that in the isotropic substrate of case 1, the radiation at low frequencies close to DC is mostly due to $\tilde{G}_{\mathrm{A}}^{zx}$ or the E_z component contribution. However, as the electrical thickness increases, $\tilde{G}_{\mathrm{A}}^{zx}$ decreases rapidly. Therefore, after the second surface-wave mode cutoff (TE_0), the maxima/minima of the radiated power are only controlled by the maxia/minia of $\tilde{G}_{\mathrm{A}}^{xx}$ or the E_x component through V^{TE_z} of the transmission-lime model (Fig. 5.1b), which occur at $\mathrm{TE}_z/\mathrm{TM}_z$ modes cutoffs, respectively (see Chapter 4). However, this is not the case for the anisotropic substrate of case 5 shown in Fig. 5.9. For this case, the contribution of $\tilde{G}_{\mathrm{A}}^{zx}$ to the radiated power, which is oscillatory due to the variations of $I^{\mathrm{TM}_z} - I^{\mathrm{TE}_z}$ of the transmission-line model (Fig. 5.1b), is not ignorable as compared to $\tilde{G}_{\mathrm{A}}^{xx}$. Consequently, in case 5, the radiated power and therefore the radiation efficiency is affected by the maxima/minima of both $\tilde{G}_{\mathrm{A}}^{xx}$ and $\tilde{G}_{\mathrm{A}}^{zx}$.

Let us take an example of the case 5, such as the frequency band between the TM_1 ($d/\lambda_0 = 0.1$) and TM_2 ($d/\lambda_0 = 0.2$) cutoffs. At the TM_1 cutoff, both $\tilde{G}_{\mathrm{A}}^{xx}$ and $\tilde{G}_{\mathrm{A}}^{zx}$ are

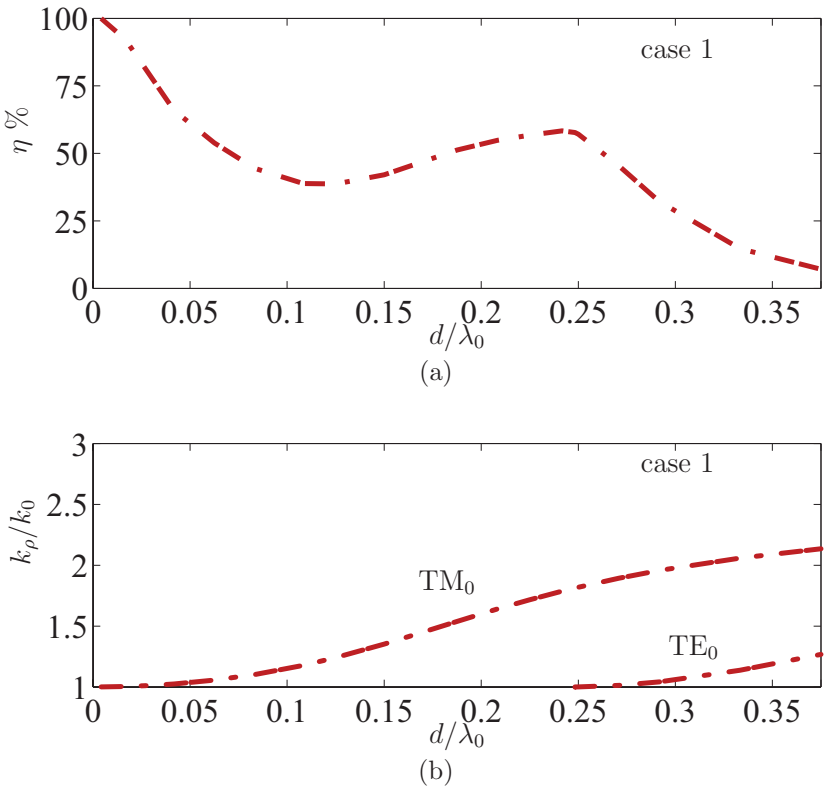

Figure 5.4 Response to an infinitesimal horizontal dipole on the uniaxially anisotropic grounded substrate (Fig. 5.1a) of *case 3* versus the electrical thickness of the substrate. (a) Radiation efficiency [Eq. (5.2)]. (b) TM_z and TE_z surface modes.

minimum, corresponding to a minimum in the radiated power. As the frequency increases, the contribution of $\tilde{G}_{\rm A}^{zx}$ and consequently the radiated power start to increase towards its maximum at $d/\lambda_0 = 0.13$. After this point, $\tilde{G}_{\rm A}^{zx}$ starts to decrease again and therefore the radiated power decreases as well. However, as the contribution of $\tilde{G}_{\rm A}^{xx}$ increases towards its maximum at the TE_1 cutoff corresponding to $d/\lambda_0 = 0.15$, the radiated power starts to increase. In addition, $\tilde{G}_{\rm A}^{zx}$ starts to increase again towards its next maximum at $d/\lambda_0 = 0.16$. Therefore, the combined effect of the increase in $\tilde{G}_{\rm A}^{xx}$ and $\tilde{G}_{\rm A}^{zx}$ leads to a maximum radiated power at $d/\lambda_0 = 0.16$. After this electrical thickness, both $\tilde{G}_{\rm A}^{xx}$ and $\tilde{G}_{\rm A}^{zx}$ and therefore the radiated power decrease towards to next cutoff, TM_2 at $d/\lambda_0 = 0.2$. The same behavior repeats as the electrical thickness increases.

The reasons for which $\tilde{G}_{\rm A}^{zx}$ is stronger in the anisotropic substrate case 5 as compared to the isotropic substrate case 1 lies in the fact that $\tilde{G}_{\rm A}^{zx}$ is directly proportional to μ_ρ [Eq. 5.5b] which has a large value for the case 5 as compared to the other cases including the case 1. As a proof to this explanation, Fig. 5.10 plots $\tilde{G}_{\rm A}^{zx}/(\mu_\rho/\mu_0)$ from (5.5b), and shows that by removing the factor μ_ρ in $\tilde{G}_{\rm A}^{zx}$, the contribution of $\tilde{G}_{\rm A}^{zx}$ decreases dramatically, specially for

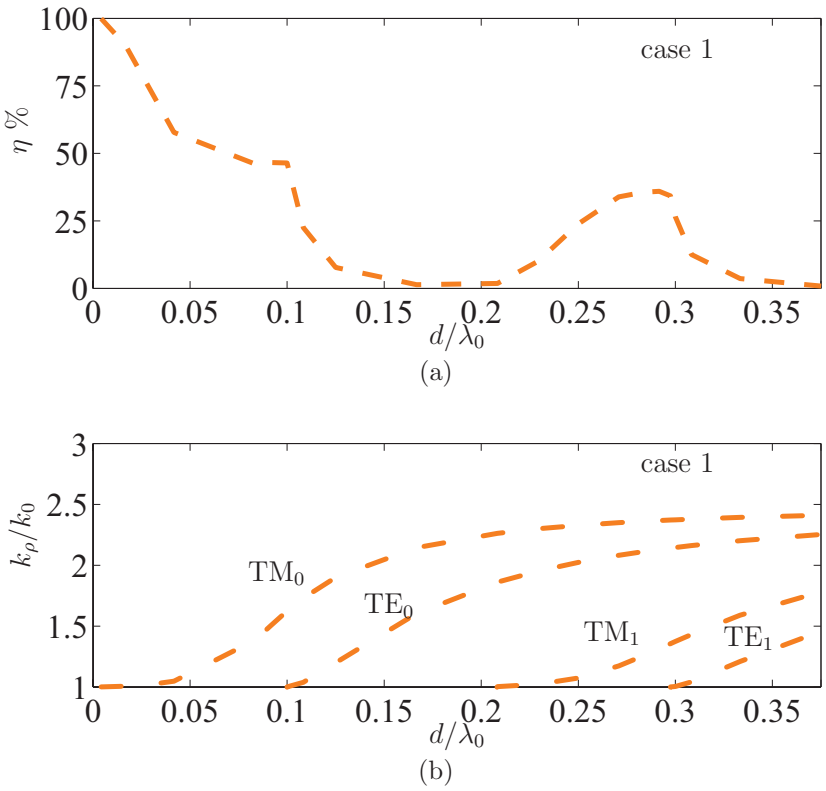

Figure 5.5 Response to an infinitesimal horizontal dipole on the uniaxially anisotropic grounded substrate (Fig. 5.1a) of *case 4* versus the electrical thickness of the substrate. (a) Radiation efficiency [Eq. (5.2)]. (b) TM_z and TE_z surface modes.

high electrical thicknesses. This results reveal that for a horizontal electric current excitation, μ_ρ plays an important rule in controlling the amplitude of the electric field along the z axis, E_z, and therefore the radiated power and the radiated efficiency.

Number of Surface-Wave Modes

According to the surface-wave modes graphs for the different substrates of cases 1-5, demonstrated in Figs .5.2b, .5.3b, .5.4b, .5.5b, and .5.6b, the number of surface-wave modes in a fixed frequency range is not the same for the different cases. Particularly, case 3 and case 5 with 2 and 8 surface modes, respectively, possess the least and most numbers of surface-wave modes as compared to the other cases.

In Chapter 4 it was shown that the input impedance $Z_{\mathrm{in}}^{\mathrm{TM}_z,\mathrm{TE}_z}$ for the TE_z and TM_z of the substrates transmission models, shown in Fig. 5.1b, defines the position of the surface-wave cutoffs. As shown in Appendix B, $Z_{\mathrm{in}}^{\mathrm{TM}_z,\mathrm{TE}_z}$ reads

$$Z_{\mathrm{in}}^{\mathrm{TM}_z,\mathrm{TE}_z} = Z_{\mathrm{c}}^{\mathrm{TM}_z,\mathrm{TE}_z} \tan\left(\beta^{\mathrm{TM}_z,\mathrm{TE}_z} d\right) \tag{5.7}$$

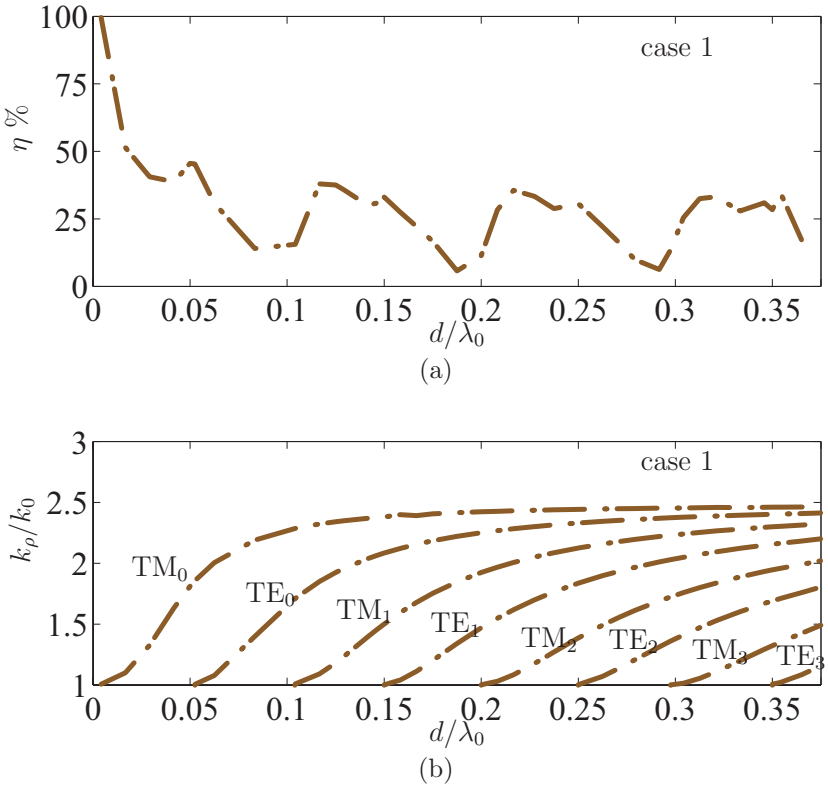

Figure 5.6 Response to an infinitesimal horizontal dipole on the uniaxially anisotropic grounded substrate (Fig. 5.1a) of *case 5* versus the electrical thickness of the substrate. (a) Radiation efficiency [Eq. (5.2)]. (b) TM_z and TE_z surface modes.

where $Z_{\mathrm{c}}^{\mathrm{TM}_z,\mathrm{TE}_z}$ is the characteristic impedance and $\beta^{\mathrm{TM}_z,\mathrm{TE}_z}$ is the propagation constant of the anisotropic material for the TE_z and TM_z modes expressed as

$$Z_c^{\mathrm{TM}_z} = k_z^{\mathrm{TM}_z}/(\omega\varepsilon_\rho)\sqrt{\varepsilon_\rho/\varepsilon_z}, \tag{5.8a}$$

$$\beta^{\mathrm{TM}_z} = \sqrt{\varepsilon_\rho/\varepsilon_z}\,k_z^{\mathrm{TM}_z}, \tag{5.8b}$$

and

$$Z_c^{\mathrm{TE}_z} = \omega\mu_z/k_z^{\mathrm{TE}_z}\sqrt{\mu_\rho/\mu_z}, \tag{5.9a}$$

$$\beta^{\mathrm{TE}_z} = \sqrt{\mu_\rho/\mu_z}\,k_z^{\mathrm{TE}_z}. \tag{5.9b}$$

As demonstrated in Chapter 4, at the TM_z cutoffs $Z_{\mathrm{in}}^{\mathrm{TM}_z} = 0$ and therefore from (5.7) $\beta^{\mathrm{TM}_z,\mathrm{cutoff}}d = (2m-1)\pi/2$ $(m \in \mathbb{N})$, while at the TE_z cutoffs $Z_{\mathrm{in}}^{\mathrm{TE}_z} = \infty$, which corresponds

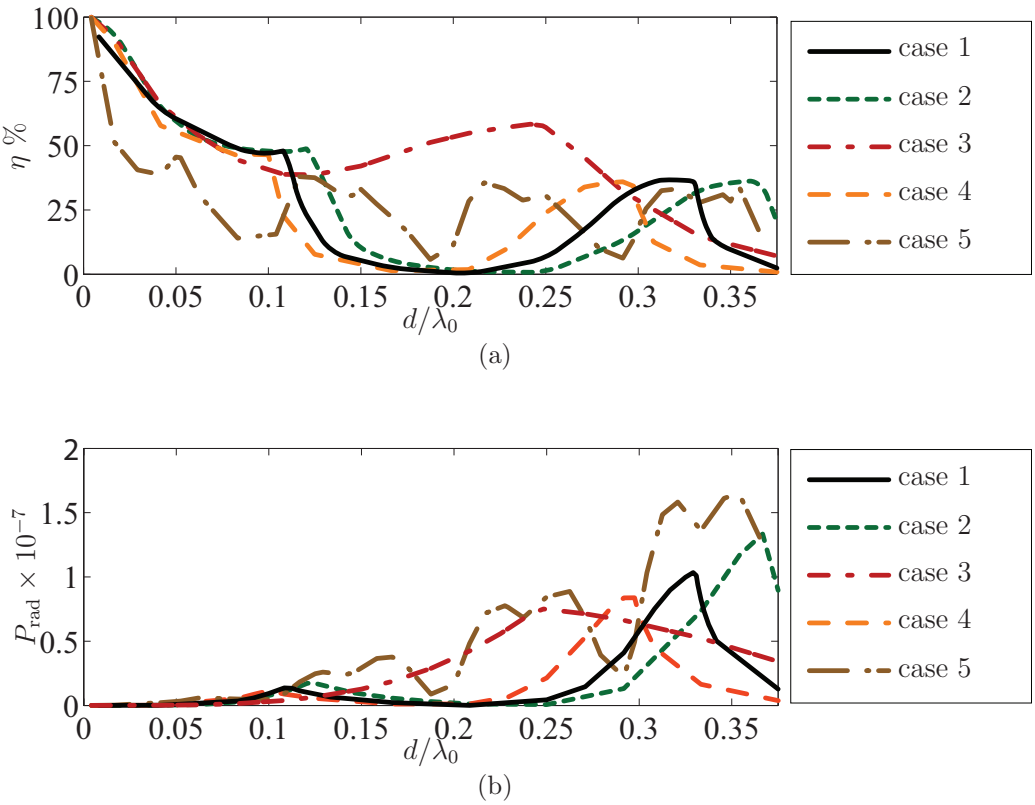

Figure 5.7 Comparison between the radiation efficiency behaviors and radiated powers for the grounded substrates of cases 1-5. (a) Radiation efficiency η. (b) Radiated power P_{rad}.

to $\beta^{\text{TE}_z,\text{cutoff}}d = (m-1)\pi$. Therefore, from (5.8b) and (5.9b), it is concluded that the cutoffs of the TM_z and TE_z modes occur at $k_z^{\text{TM}_z,\text{cutoff}}d = \sqrt{\varepsilon_z/\varepsilon_\rho}(2m-1)\pi/2$ and $k_z^{\text{TE}_z,\text{cutoff}}d = \sqrt{\mu_z/\mu_\rho}(m-1)\pi$, where $k_z^{\text{TM}_z,\text{TE}_z}$ is inversely proportional to the effective wavelength along the z axis. As a result, the position of the TM_z and TE_z cutoffs are controlled by the ratios $\sqrt{\varepsilon_\rho/\varepsilon_z}$ and $\sqrt{\mu_\rho/\mu_z}$, respectively. The larger these ratios are, the closer the cutoffs of the TM_z and TE_z cutoffs will be and vice versa. As shown in Table 5.1, the smallest $\sqrt{\varepsilon_\rho/\varepsilon_z}$ and $\sqrt{\mu_\rho/\mu_z}$ belong to the case 3 while the largest ratios are related to the case 5. Consequently, in a fixed frequency range, case 3 and 5 have the smallest and the largest number of the surface-wave modes, as compared to the other cases.

Comparison between the Radiation Efficiencies of All the Cases

Figure 5.7a compares the efficiency behavior versus the electrical thickness of the cases 1-5. It shows that the efficiency variations of the anisotropic substrates of cases 3 and 5 deviate immensely from the radiation efficiency of the other cases 1,2 and 4, where the case 3 has the smoothest efficiency variations with a wider frequency range for which the efficiency

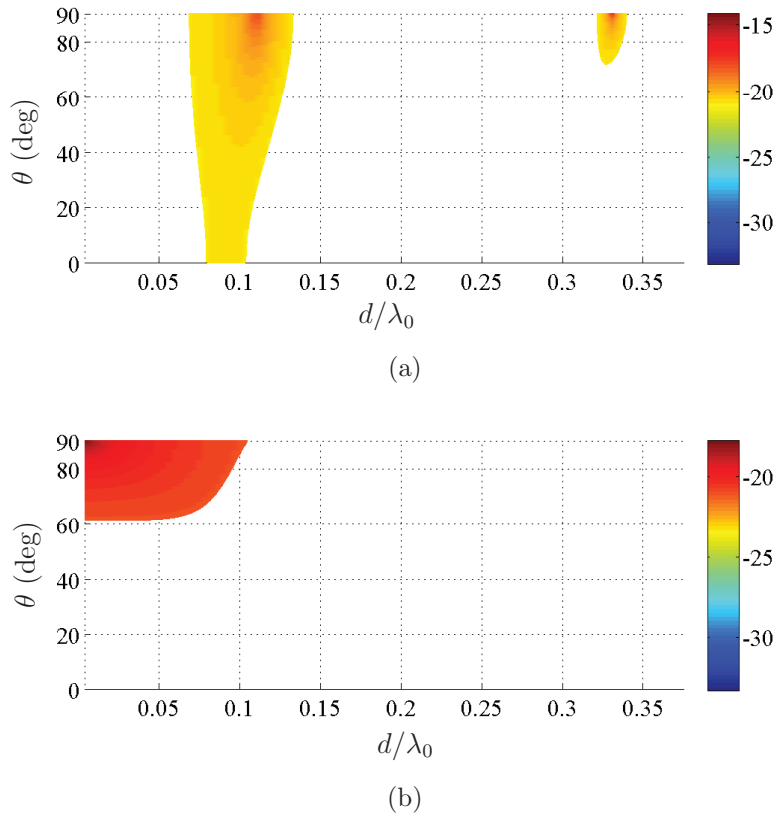

Figure 5.8 Spectral domain Green functions $\tilde{G}_{\mathrm{A}}^{xx}$ and $\tilde{G}_{\mathrm{A}}^{zx}$ for the isotropic substrate of case 1, limited in the range of $-21 < \log\left(\left|\tilde{G}_{\mathrm{A}}^{xx,zx}\right|\right) < 0$. (a) $\tilde{G}_{\mathrm{A}}^{xx}$. (b) $\tilde{G}_{\mathrm{A}}^{xx}$.

is relatively high, while case 5 has the sharpest oscillations and the lowest level of efficiency.

This phenomenon can be explained by considering the number of the excited modes in each case and in a fixed frequency range, as discussed above. For example, in case 3 with the least number of surface-wave modes, the second surface-wave mode (TE_0) occurs much farther from the previous TM_0 mode as compared to the other cases. Therefore, the efficiency varies smoothly towards its maximum at the TE_0 cutoff, and in a wider frequency range the efficiency remains close to its maximum level. Moreover, since the number of surface-wave modes and therefore the surface-wave power are less than for the other cases, its maximum level is higher with respect to the other cases. In contrast, for case 5, since in a fixed frequency range the number of surface-wave modes is larger, the efficiency varies rapidly from a maximum at the TE_z cutoff to a minimum at the TM_z cutoff. In addition, since the number of surface-wave modes is more and therefore the surface-wave power is sronger than in the other cases, the level of the radiation efficiency is lower than cases 1-4.

Based on the above results and discussion, it is concluded that substrates with lower ratios

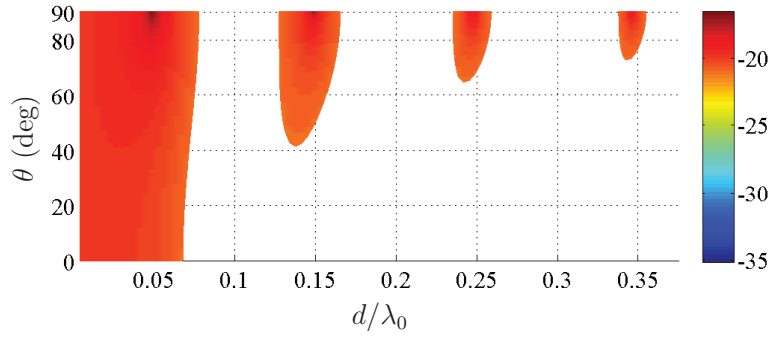

(a)

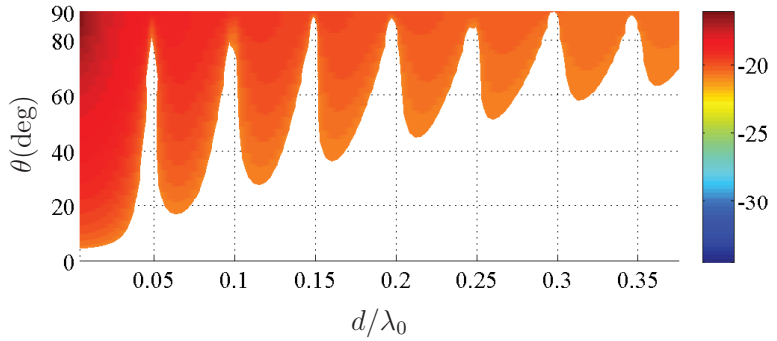

(b)

Figure 5.9 Spectral domain Green functions $\tilde{G}_{\mathrm{A}}^{xx}$ and $\tilde{G}_{\mathrm{A}}^{zx}$ for the anisotropic substrate of case 5, limited in the range of $-21 < \log\left(\left|\tilde{G}_{\mathrm{A}}^{xx,zx}\right|\right) < 0$. (a) $\tilde{G}_{\mathrm{A}}^{xx}$. (b) $\tilde{G}_{\mathrm{A}}^{xx}$.

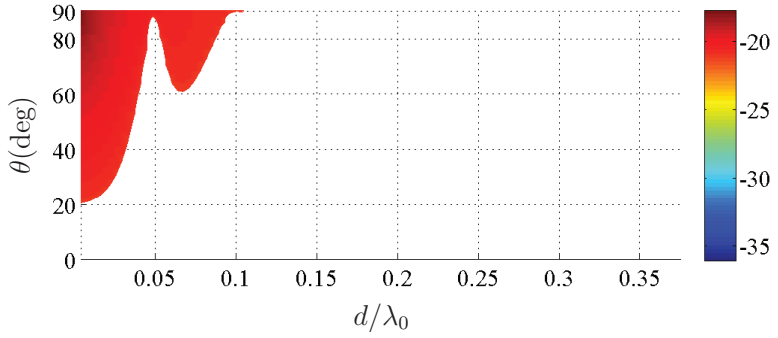

Figure 5.10 $\tilde{G}_{\mathrm{A}}^{zx}/(\mu_\rho/\mu_0)$, limited in the range of $-21 < \log\left(\left|\tilde{G}_{\mathrm{A}}^{xx,zx}\right|\right) < 0$.

$\sqrt{\mu_\rho/\mu_z}$ and $\sqrt{\varepsilon_\rho/\varepsilon_z}$, and therefore a lower number of surface-wave modes, have a smoother variation of the efficiency with a higher level, which is desired in many communication applications.

5.4 Dispersive Anisotropic Substrate

In the previous section it was demonstrated that for the uniaxially anisotropic substrate, lowering the ratios $\sqrt{\mu_\rho/\mu_z}$ and $\sqrt{\varepsilon_\rho/\varepsilon_z}$ results in achieving high radiation efficiency level with smoother variations. Such a substrate may be engineered artificially and therefore, as opposed to the anisotropic substrates of cases 2-5 studied in the previous section, the artificial anisotropic substrate will possess dispersive constitutive parameters. In the following section, an artificial substrate which can satisfy a relatively low $\sqrt{\mu_\rho/\mu_z}$ condition in a large frequency bandwidth, and therefore a high-level radiation efficiency with smooth variations is demonstrated and discussed.

5.4.1 Dispersive Material Definition

The discussions of Chapters 1 and 3 show that the artificial anisotropic mushroom-type magneto-dielectric substrate may be a good candidate to satisfy the condition of low $\sqrt{\mu_\rho/\mu_z}$. In this structure, and in the electrical thicknesses where the mushroom-type structure wires are electrically short or densely packed [48], the effective permittivity along the axis of wires z, ε_z, may be modeled by the electric local Drude dispersion expression [12]

$$\frac{\varepsilon_z}{\varepsilon_0} = \varepsilon_r \left[1 - \frac{{\omega_{\rm pe}}^2}{\omega^2 - j\omega\zeta_{\rm e}}\right], \tag{5.10}$$

where ε_r is the host medium permittivity, $\omega_{\rm pe}$ is the electric plasma frequency and $\zeta_{\rm e}$ is the damping factor of the structure. However, the permittivity in the ρ plane, ε_ρ remains equal to the permittivity of the host medium ε_r. In addition, the effective permeability in the xy plane, μ_ρ, may be modeled by the magnetic Lorentz dispersion relation [30]

$$\begin{aligned}\frac{\mu_\rho}{\mu_0} &= 1 - \frac{F\omega^2}{(\omega^2 - {\omega_{\rm m0}}^2) - j\omega\zeta_{\rm m}} \\ &= 1 - \frac{F\omega^2}{[\omega^2 - {\omega_{\rm pm}}^2(1-F)] - j\omega\zeta_{\rm m}},\end{aligned} \tag{5.11}$$

where F is a factor related to the geometry of the current loops, $\omega_{\rm m0}$ is the resonant frequency of these loops, $\omega_{\rm pm}$ is the plasma frequency and $\zeta_{\rm m}$ is the damping factor of the structure. However, the permeability along the z axis remains similar to the one of the host medium μ_0.

As it is expressed in (5.11) and seen in Fig. 5.11, as the frequency increases above the Lorentz-permeability magnetic plasma frequency $\omega_{\rm pm}$, the permittivity tends to $1 - F < 1$. Since in this structure $\mu_z/\mu_0 = 1$, in the frequency bands above the plasma frequency

$\mu_\rho/\mu_z < 1$ which is desired for a high efficiency with smooth variations. Unfortunately, in this structure, as expressed in (5.10) and shown in Fig. 5.11, the condition of low $\sqrt{\varepsilon_\rho/\varepsilon_z}$ cannot be satisfied, since after the electric plasma frequency $\varepsilon_z < \varepsilon_\rho = \varepsilon_r\varepsilon_0$. However, the next section shows that only the low $\mu_\rho/\mu_z < 1$ is enough to immensely enhance the efficiency.

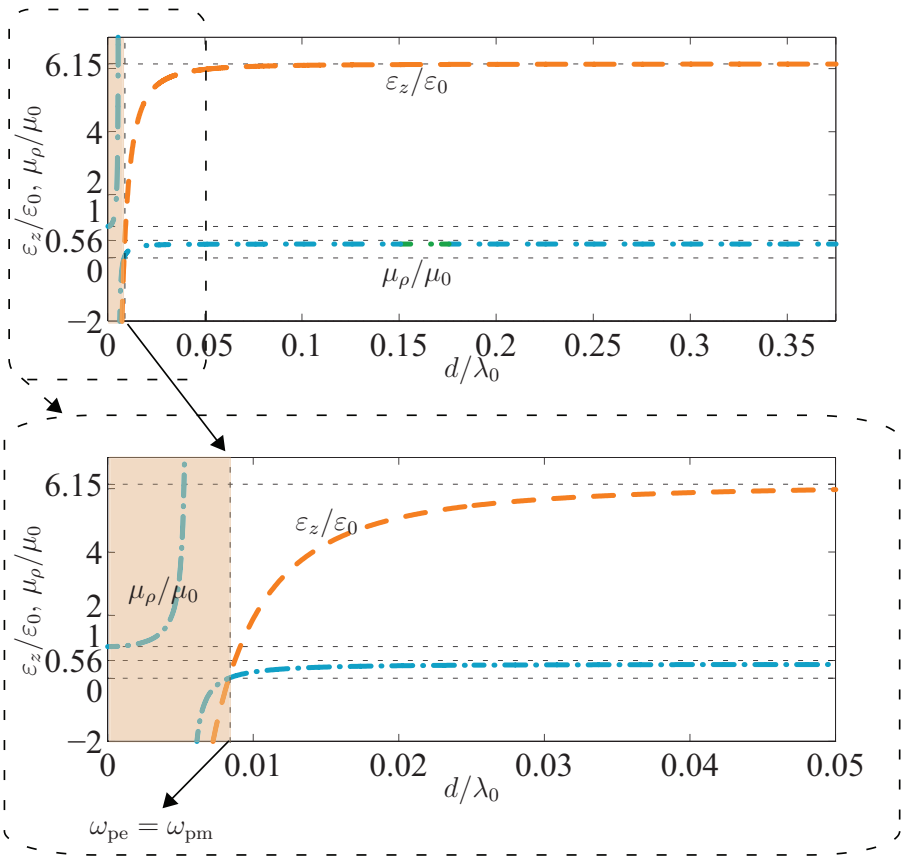

Figure 5.11 Drude permittivity along the z axis, ε_z, and Lorentz permeability in the ρ plane μ_ρ of the dispersive uniaxially anisotropic substrate with $\varepsilon_r = 6.15$, $\zeta_{\rm e} = 0$, $F = 0.56$, $\zeta_{\rm m} = 0$, and $\omega_{\rm pe} = \omega_{\rm pm} = 1$ GHz.

5.4.2 Results

Figures 5.12a and 5.12b show the efficiency and the surface-wave modes, respectively, for the dispersive anisotropic artificial dielectric with the parameters of Fig. 5.11, while Fig. 5.13 compares its efficiency with the one of the host medium without any implants which is similar to the isotropic substrate of case 1 in Sec. 5.3. According to Fig. 5.12b, due to the low $\sqrt{\mu_\rho/\mu_z}$, the substrate only supports two surface-wave modes in a wide frequency range. Therefore, as shown in Fig. 5.12a the efficiency has smooth-variations and high-level efficiency below the cutoff of the $\rm TE_0$ mode. As this mode starts to propagate, the radiation efficiency drops

abruptly due to the corresponding surface-wave power of the TE_0 mode which is strongly coupled to the horizontal source.

Figure 5.13 demonstrates that the radiation efficiency performance of the Drude-permittivity and Lorentz-permeability uniaxially anisotropic substrate is significantly enhanced as compared to the isotropic case 1.

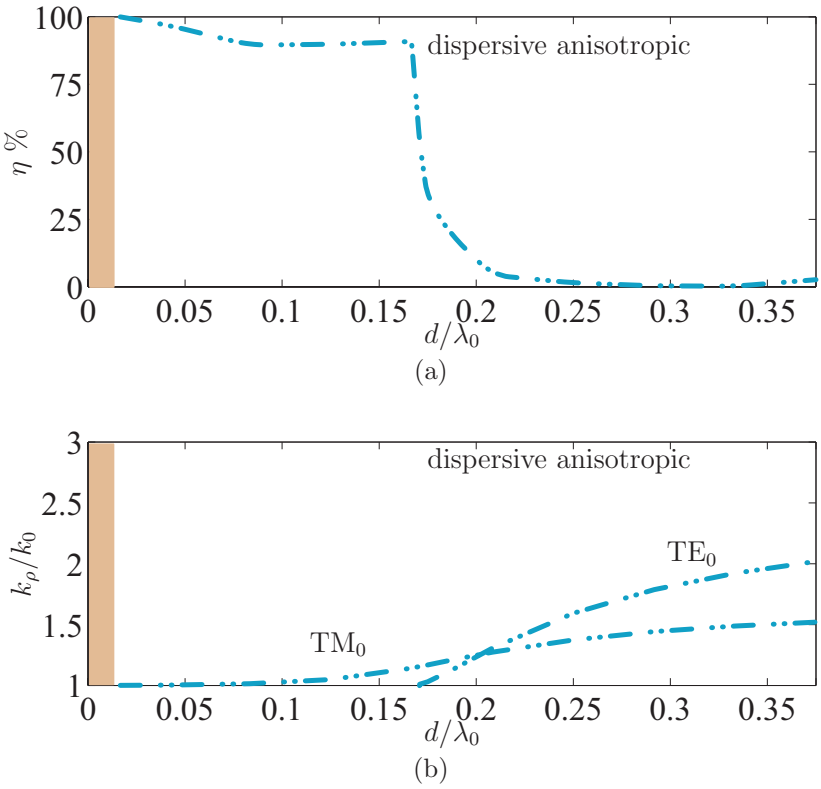

Figure 5.12 Response to an infinitesimal horizontal dipole on the dispersive uniaxially anisotropic grounded substrate (Fig. 5.1a) versus the electrical thickness of the substrate. (a) Radiation efficiency [Eq. (5.2)]. (b) TM_z and TE_z surface modes.

5.5 Conclusions

The radiation efficiency behavior of a horizontal electric dipole on an electrically thick uniaxially anisotropic substrate was studied. To analyze the effect of anisotropy on the radiation efficiency, first, different non-dispersive uniaxially anisotropic substrate cases were considered. The best type of anisotropy which leads to a high-level smooth-variations efficiency was chosen and discussed. Afterwards, a mushroom-type uniaxially anisotropic artificial substrate with Drude-dispersive permittivity along the axis of wires and Lorentz-dispersive permeability along the perpendicular axis to the loop between the two adjacent mushrooms

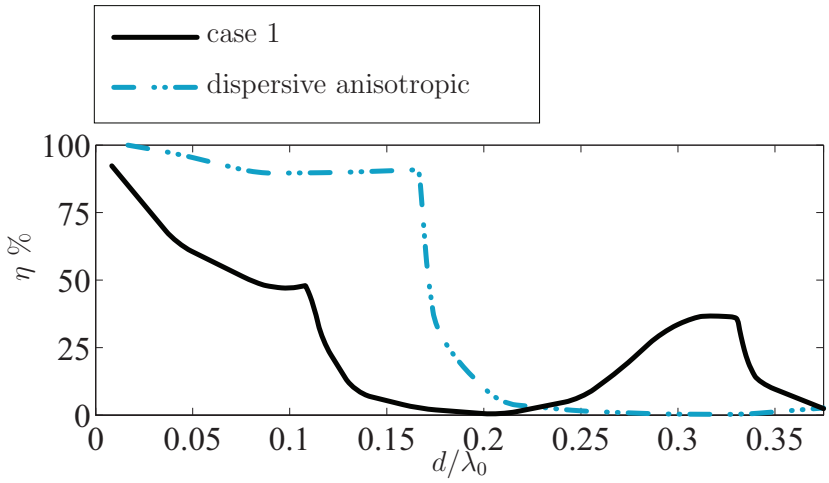

Figure 5.13 Comparison between the radiation efficiency behaviors of the isotropic grounded (case 1) and the dispersive anisotropic substrates.

was considered. This substrate has the potential of providing the desired anisotropy for an enhanced efficiency. This work offers fundamental guidelines which may be helpful in the design of high-efficiency antennas.

CHAPTER 6

GENERAL DISCUSSION

As explained in Chapter 1, *anisotropic artificial* substrates possess several qualities and offer important properties such as:

1. *Artificial* substrates have the potential of providing electromagnetic properties that are not readily available in nature.
2. The effective electromagnetic properties of *artificial* substrates can be controlled by engineering the characteristics of the implants in the substrates. Consequently, specific substrates can be designed for specific applications.
3. As opposed to isotropic substrates, the properties of *anisotropic* substrates are different in different directions, and as a result, the electromagnetic wave interacts with the material differently in the different directions.
4. The anisotropy of *anisotropic artificial* substrates can be controlled in the different directions by controlling the properties of the implants.

As a result of the mentioned properties, artificial substrates provide several unique characteristics and also significant degrees of freedom in the design of microwave devices which may lead to novel applications.

This thesis is motivated by the following main factors:

1. Lack of sufficient analysis on anisotropic properties of the artificial substrates is evident in the literature.
2. Potentially, novel microwave applications and devices may be enabled by rigorously analyzing and also exploring anisotropic properties of the artificial substrates, with all their unique characteristics and benefits as explained above.

As a consequence of the above mentioned motivations, the objectives of the thesis are focus on the following aspects:

1. Electromagnetic analysis of the properties of anisotropic artificial substrates.
2. Investigation of the novel microwave applications of anisotropic artificial substrates.

Along the path towards achieving the goals of the thesis and in order to acquire the basic knowledge to study anisotropic artificial substrates, it may be beneficial to pursue the following methodology:

1. It is favorable to first better understand the cases of well-known natural anisotropic substrates such as ferrimagnetic materials, where for these anisotropic materials, concrete sets of studies and analysis methods are already available in the literature. This approach may in turn lead to interesting applications.
2. To study some of the applications of the artificial anisotropic materials, it is required to first study some dark zones in the literature about the explanation and analysis of some specific phenomena which occurs in the isotropic (conventional) substrates.

To address the objectives of the thesis, and based on the methodology mentioned above, some basic problems such as realization of fundamental boundary conditions, analysis and realization of special leaky-wave antennas and analysis and explanation of the radiation efficiency behavior of planar antennas on isotropic and anisotropic electrically thick substrates, are studied. To tackle these problems, various electromagnetic analysis methods, such as employing generalized scattering matrix (GSM) and spectral domain transmission-line modeling based on multilayered Green functions are chosen.

The thesis starts with the exploration of the unique properties of the natural anisotropic ferrimagnetic materials for the purpose of obtaining the basic available knowledge in the literature about anisotropic materials. This effort is directed towards the realization of the fundamental recently introduced concept of perfect electromagnetic conductor (PEMC). PEMC is a generalized description of electromagnetic boundary conditions, including perfect electric conductor (PEC) and perfect magnetic conductor. It has found an important place in electromagnetics and may enable many future applications in microwaves. However, the PEMC boundaries had only been introduced theoretically and were not practically realized. This thesis establishes the following contributions and advances regarding PEMC boundaries:

1. It introduces a practical implementation of generalized perfect electromagnetic conductor boundaries by exploiting the Faraday rotation principle and ground reflection in the ferrite materials which are inherently anisotropic.
2. To our knowledge, it was the first reported practical approach for the realization of the PEMC boundaries.
3. The grounded-ferrite PEMC boundary structure is rigorously analyzed by generalized scattering matrix (GSM).
4. A tunable (transverse electromagnetic) TEM-waveguide application of grounded ferrite PMC, which is a special case of the PEMC boundaries, is provided, along with its experimental validation.

After obtaining basic knowledge about the natural anisotropic materials, we step towards analyzing the more complicated case of artificial anisotropic materials, where there is not

enough in-depth analysis available in the literature. For this purpose, a leaky-wave antenna application of a special type of anisotropic magneto-dielectric material is proposed and analyzed. Leaky-wave antennas perform as high directivity and frequency beam scanning antennas and due to their properties they enable many applications in radar, point-to-point communications and MIMO systems. The contributions of the thesis in the field of leaky-wave antennas are as follow:

1. It provides a rigorous spectral domain transmission-line model based on dyadic Green function analysis of a specific type of anisotropic magneto-dielectric substrates.
2. It presents a novel broadband and low beam squint two-dimensional leaky-wave antenna application which is particularly appropriate for future applications in wide band point-to-point communication and radar systems.
3. A comparison between the performance of isotropic (conventional) and artificial anisotropic leaky-wave antennas clearly demonstrates that isotropic dielectric slabs do not perform as an efficient leaky-wave antenna.

The accomplishments of the last project, such as acquired knowledge about uniaxially anisotropic artificial magneto-dielectric materials and their radiating properties and also establishing a rigorous method for modeling and analyzing these materials, motivated us to study another important electromagnetic problem which is related to the explanation of radiation efficiency behavior of planar antennas on electrically thick substrates and also the effect of anisotropy on the efficiency properties. Planar antennas have found many applications in communication systems, however toward millimeter-wave and terahertz regime, their radiation efficiency degrades due to the increase of the number of surface modes which carry part of the energy in the substrate. Although the oscillatory behavior of the radiation efficiency versus the electrical thickness was already known and reported in several publications, a clear explanation of its reasons was not reported so far. The contributions of this thesis regarding the issues of planar antennas on electrically thick substrates are as follow:

1. This project includes the interpretation and analysis of the radiation efficiency behavior of a planar dipole antenna on electrically thick substrates.
2. For the analysis, a novel substrate-dipole method is introduced which simplifies the problem by modelling the substrate and reducing the problem to an equivalent dipole radiating in the free-space.
3. It provides two solutions for the efficiency enhancement at the electrical thickness where the efficiency is minimal.
4. Finally, the effect of the anisotropy of the substrate on the efficiency behavior is studied

and guidelines for designing an efficient planar antenna on anisotropic substrates are provided.

CHAPTER 7

CONCLUSIONS AND FUTURE WORKS

7.1 Conclusions

This thesis consists of selected articles related to the electromagnetic analysis and exploration of novel microwave applications of anisotropic artificial substrates and of natural anisotropic and isotropic substrates, as initial steps to ease the understanding of the artificial anisotropic substrates.

In the following, a summary of the contributions of the thesis based on its objectives, which were discussed in Chapter 1, is presented.

Chapter 2 presents the first article entitled "Arbitrary Electromagnetic Conductor Boundaries Using Faraday Rotation in a Grounded Ferrite Slab". In this article, for the first time, a practical solution for the realization of the perfect electromagnetic conductor (PEMC) boundary as a novel concept which exhibits interesting properties and a vast potential for microwave applications has been presented. The realization method employs Faraday rotation and ground reflection of a normally incident plane wave on a grounded ferrite slab. A detailed description of the operation phenomenology of the structure and the exact electromagnetic analysis based on the generalized scattering matrix method has been provided. The specific case of perfect magnetic conductor (PMC) has been experimentally validated by using a tunable transverse electromagnetic (TEM) waveguide with grounded ferrite PMC lateral walls.

Chapter 3 is dedicated to the article "Broadband and Low Beam Squint Leaky-Wave Radiation from a Uniaxially Anisotropic Grounded Slab". In this article, a broadband and low beam squint anisotropic magneto-dielectric 2D leaky-wave antenna excited by a vertical electric source has been presented. A spectral domain transmission line modelling of the structure and its Green functions have been provided for the rigorous analysis of the structure. A TM_z dispersion analysis of the structure has been performed for Drude/Lorentz dispersive anisotropic grounded slabs as well as for an isotropic non-dispersive grounded slab. The analysis of the isotropic slab has shown that the pointing angle of the leaky-wave radiation is limited to the endfire region which is suppressed by the inherent radiation null of the slab at endfire. Therefore, the radiation is dominated by the space-wave which has low directivity and is incapable of beam scanning. In contrast, the anisotropic grounded slab provides a highly directive 2D leaky-wave radiation with high design flexibility. At its lower frequencies,

it provides full-space conical-beam scanning while at higher frequencies, it provides fixed-beam, low-beam squint radiation (at a designable angle). As a result, this antenna may be appropriate for wide-band point-to-point communication and radar systems.

Chapter 4 presents the article entitled "Radiation Efficiency Issues in Planar Antennas on Electrically Thick Substrates and Solutions". In this article, the analysis of the non-monotonically decaying behavior of the radiation efficiency of an infinitesimal horizontal electric dipole on grounded and ungrounded substrates versus the substrate electrical thickness has been presented. To simplify the interpretation of the response of the efficiency, a substrate dipole has been introduced which models the substrate and the ground plane (if present). The substrate dipole reduces the actual structure to an equivalent source dipole radiating into free space which is composed of the original dipole and the substrate dipole. Next, it has been demonstrated that the efficiency behavior of an actual planar antenna such as a half-wavelength dipole printed on grounded and ungrounded substrates is essentially similar to that of the infinitesimal dipole. Eventually, two radiation efficiency enhancement solutions at electrical thicknesses where the efficiency is minimal have been introduced. This article provides design guidelines for the efficient millimeter-wave and terahertz antennas whose substrates tend to be inherently electrically thick.

Chapter 5 is an extension to Chapter 4. In this chapter, the effect of substrate anisotropy on the radiation efficiency behavior of a horizontal electric dipole on the substrate has been analyzed. The appropriate anisotropy which provides the highest efficiency with less oscillation has been introduced.

7.2 Future Works

This section presents the possible future extensions of the work that has been done in this thesis.

7.2.1 Rotating Field-Polarization Waveguide Application of the Grounded-Ferrite Perfect Electromagnetic Conductor (PEMC) Boundaries

In Chapter 2, an application of a special case of the PEMC boundaries, which is the PMC boundary, was demonstrated. The application was a TEM waveguide realized by grounded-ferrite PMC sidewalls. Exploring other applications of the PEMC boundaries which can be realized by the proposed grounded ferrite slab could be a future extension of this thesis.

One of the applications of the PEMC boundaries was theoretically proposed in [57]. This application is a rotating field-polarization waveguide which is shown in Fig. 7.1. In [57] it is shown that when the walls of a waveguide is covered by the PEMC boundaries, the

polarization of the electromagnetic field propagating inside the waveguide is tilted by some angles. The amount of rotation of the field is controlled by the admittance Y of the PEMC.

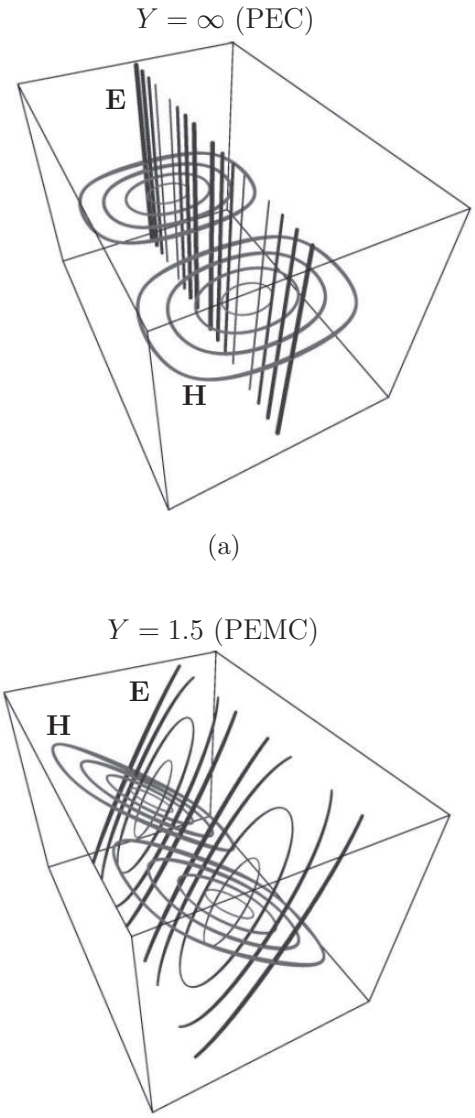

Figure 7.1 PEMC waveguide. (a) $Y = \infty$ (PEC). (b) $Y = 1.5$ (PEMC). Taken from "Possible applications of perfect electromagnetic conductor (PEMC) media," in Proc. EuCap, 2006, by A. Sihvola and I. V. Lindell. ©2006 IEEE

The rotating field-polarization waveguide may be practically realized by the proposed practical grounded-ferrite PEMC in Chapter 2. Since the proposed grounded-ferrite is tunable by adjusting the DC bias field (Sec. 2.5.3), the admittance of the grounded-ferrite PEMC, and therefore the rotation angle of the field inside the waveguide, can be tuned by adjusting

the bias field. This waveguide may find applications in demultiplexers or tunable polarization converters.

7.2.2 Grounded-Ferrite PMC Application for Gain Enhancement of a Low-Profile Patch Antenna

A conductive sheet ground plane is usually used in many antennas as a reflector or ground plane to redirect the radiation in the receiver direction, to enhance the gain of the antenna and also to shield the objects in the backside [102]. However, if the radiating element is oriented horizontally above the ground plane and also very close to it, for miniaturization purposes, the current on the radiating element and its image with respect to the ground plane will be out of phase and they will have destructive interference, which degrades the gain of the antenna. This problem is usually addressed by increasing the distance between the radiator and the ground plane to a quarter-wavelength, as illustrated in Fig.7.2a, to compensate the phase-reversal effect of the ground plane. As a consequence of this distance between the radiator and ground plane, the current on the antenna and its image will have a constructive interference in the far-field, which leads to an enhancement in the gain of the antenna. Unfortunately, this approach is not desired in many cases, since it makes the antenna structure bulky with a minimum thickness of a quarter-wavelength.

An approach to enhance the gain of a low-profile horizontal antenna is to substitute the PEC ground plane by a PMC ground plane [50]. This approach is proposed based on the principle that the image of a horizontal current above a PMC boundary is in-phase with the current. Therefore the current and its image will have a constructive interference and as a result a maximized gain.

As explained in Chapters 2 and 4, PMC boundaries do not exist naturally, however it can be realized artificially [53, 52, 50, 113]. So far several groups have used EBG structures at their PMC operation frequency for the gain enhancement of planar antennas [50, 114]. However, in this case, the EBG is in the near-field of the radiator and therefore acts more as a parasitic scattering surface than as a homogeneous PMC and may alter the antenna radiation pattern which is not desired.

Employing the homogenous grounded-ferrite PMC, which was introduced in Chapter 2, may be a solution for the gain enhancement of planar antennas. A rigorous analysis on the effect of the grounded ferrite PMC and its anisotropy on the antenna performance is required. This may not only lead to the gain enhancement of the antenna but also may unveil interesting properties of planar antennas on the grounded ferrite material.

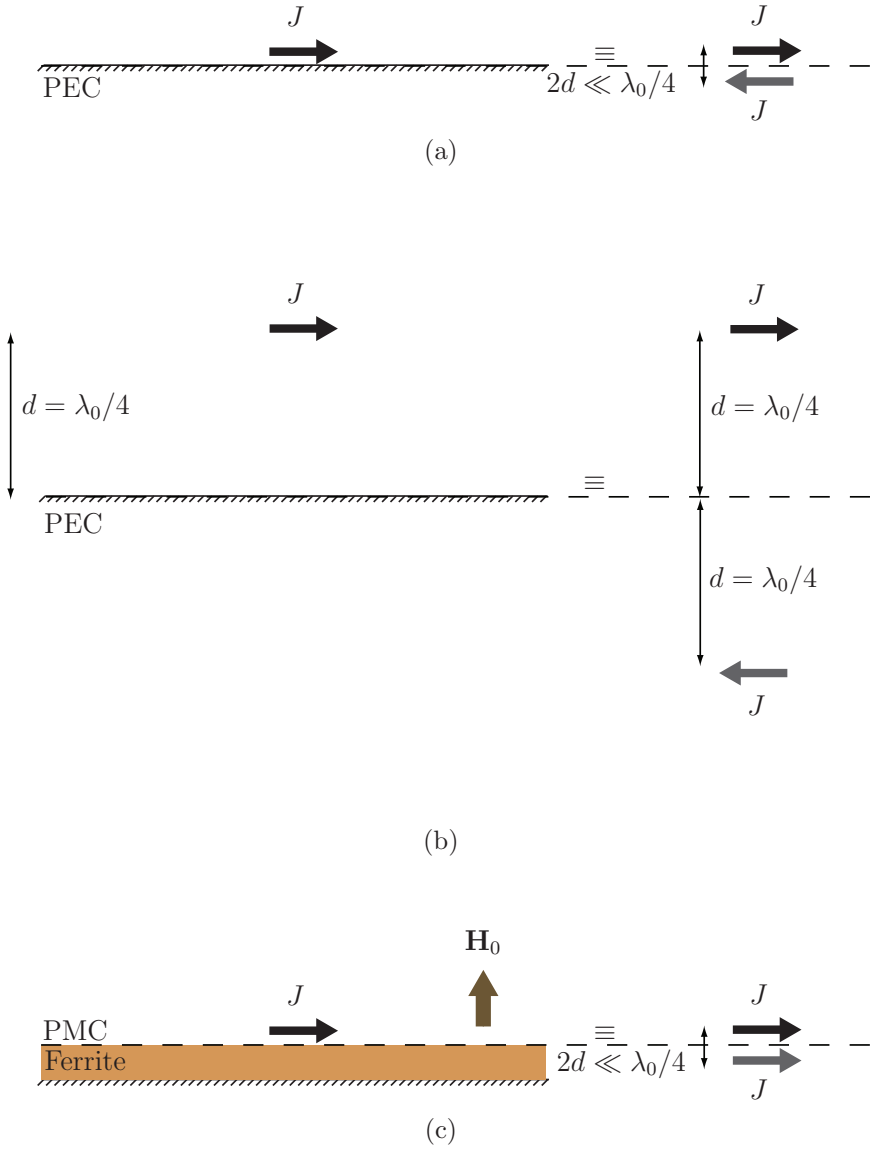

Figure 7.2 A horizontal antenna above the ground plane. (a) The antenna is very close to the ground plane. (a) The antenna is placed at a quarter-wavelength distance from the ground plane. (b) The antenna above and close to the grounded-ferrite PMC boundary (proposed antenna gain-enhancement solution).

7.2.3 Practical Demonstration of the Oscillatory Variations of the Radiation Efficiency versus Frequency for a Horizontal Electric Dipole on an Electrically Thick Substrate

Chapter 4 theoretically discussed the variations of the radiation efficiency of a horizontal electric dipole on an electrically thick substrate versus frequency. In order to acquire more insight into the efficiency variations of the horizontal dipole on an electrically thick substrate, and to practically validate the theory of the efficiency variations suggested in [77, 78, 79] and also demonstrated by full-wave simulation in Chapter 4 for a half-wavelength dipole, it is required to measure the radiation efficiency variations of horizontal dipole antennas versus frequency. For this purpose, in this project, 10 half-wavelength dipole antennas were designed on a similar substrate to the one used in Chapter 4 (RT/Duroid 6006 with $\varepsilon_{\mathrm{rd}} = 6.15$ and $d = 2.5$ mm), at different frequencies mostly around the maxima and minima of the efficiency curve of Fig. 4.8a, to specifically validate the efficiency behavior shown in this figure. Figure. 7.3 illustrates the 10 prototypes with their corresponding frequencies.

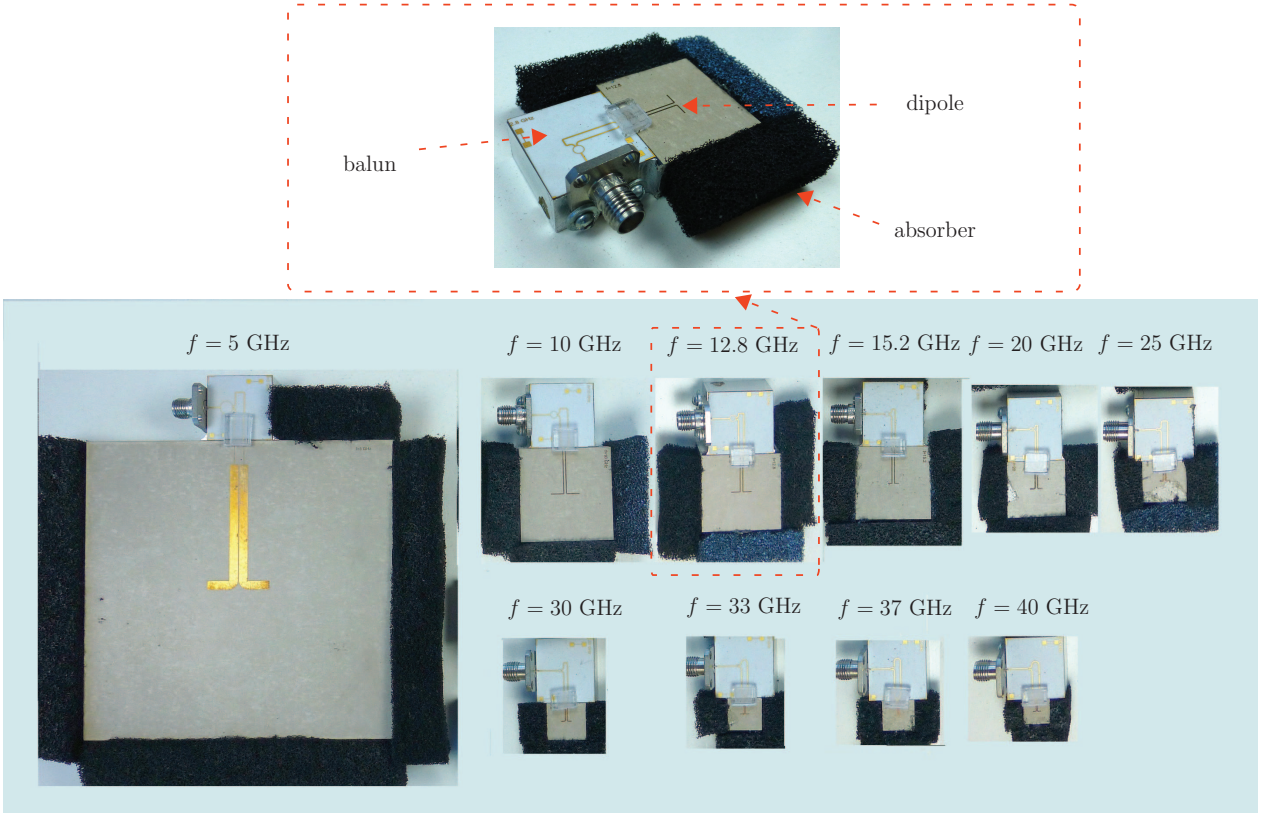

Figure 7.3 10 prototypes of printed half-wavelength dipole on a grounded substrate of RT/Duroid 6006 with $\varepsilon_{\mathrm{rd}} = 6.15$ and $d = 2.5$ mm.

For the efficiency measurement, the Wheeler cap method was not appropriate [115] since the antennas with their electrically thick substrate could not get fully covered by the radiansphere [1]. The second alternative method, which was chosen in this project, was the calculation of the radiation efficiency η by using the measured directivity D and gain G of each antenna, through the following equation [102]

$$\eta = \frac{\mathrm{G}}{\mathrm{D}}. \tag{7.1}$$

Gain measurement of an antenna has a well-known procedure and it is performed by employing standard antennas. Directivity measurement is more complicated and time-consuming than the gain measurement, since in this measurement, the radiated field should be integrated over a sphere around the antenna since

$$\mathrm{D} = \frac{4\pi U_{\mathrm{m}}}{P}, \tag{7.2}$$

where U_{m} is the maximum of the radiation intensity $U(\theta, \phi)$ and P is the total radiated power which reads

$$P = \int_0^{2\pi} \int_0^{\pi} U(\theta, \phi) \sin\theta d\theta d\phi. \tag{7.3}$$

Unfortunately, our performed measurements were not successful due to the following reasons:

1. Since the purpose of the measurement is to compare the radiation efficiency of the samples at the different frequencies from 5 GHz up to 40 GHz, the measurement system had to operate accurately in a wide frequency range, which unfortunately was not the case for our system. Specially, the problem occurred in the frequency range around 25 GHz, which was a critical point as it coincides with the first minimum of the efficiency curve. Unfortunately, the efforts for solving the problem were not successful, and continuing the measurement in other antenna labs was out of the time-frame of the project.
2. Another problem was related to mechanical sensitivity of the antennas. Each antenna consists in two parts, the dipole on the electrically thick substrate, and the feeding network, including a balun on a thin alumina substrate. The balun was not designed on the same substrate as the antenna to avoid any radiation. Since the substrates of the antenna and the balun were different they had to be connected by gold wire

1. The *radiansphere* is the boundary between the near-field and the far-field of a small antenna and its radius is one radianlength which is $\lambda_0/2\pi$ [115].

bondings which were very thin and sensitive to any mechanical force. Since during the directivity measurement, the antennas had to rotate degree-by-degree in θ and ϕ directions, to obtain an integration of the radiation intensity, they were under unwanted mechanical stress which usually resulted in breaking the wire bonding.

As explained above, due to the importance of the practical validation of the radiation efficiency variations versus frequency, which was presented in Chapter 4, performing a standard, stable and reliable measurement system for the efficiency measurement in a wide frequency range and fabricating more durable prototypes is suggested as a possible future extension of this thesis.

7.2.4 Bandwidth Enhancement of a Patch Antenna Using a Wire-Ferrite Substrate

Size constraints in communication systems motivated many studies on the miniaturization of all microwave components, including patch antennas. In the case of a patch antenna, the main miniaturization problem is that decreasing the size of the antenna generally reduces its bandwidth, which limits its operation in most modern communication schemes and standards.

It has been established that the bandwidth of a patch antenna can be enhanced by increasing the ratio of μ/ε [37], where μ and ε are the permeability and permittivity of the substrate, since

$$\text{Bandwidth} = \frac{96\sqrt{\mu/\varepsilon}t/\lambda_0}{\sqrt{2}\left[4 + 17\sqrt{\mu\varepsilon}\right]}, \tag{7.4}$$

where, t is the thickness of the substrate and λ_0 is the free-space wavelength. As expressed in this equation, for a substrate with a fixed refractive index $n = \sqrt{\mu\varepsilon}$, by increasing the ratio of μ/ε the bandwidth increases.

Ferrite materials exhibit a high μ near their ferrimagnetic resonance and therefore, they have been studied for the bandwidth enhancement of patch antennas [33]. However, they have a high permittivity, in the order of 10 to 15 [10], and therefore they cannot provide a high μ/ε ratio. On the other hand, magneto-dielectric substrates may exhibit a relatively high μ/ε ratio at a given frequency, but they are bulky, hard to manufacture, and they suffer from high dispersion which defeats the original purpose of bandwidth enhancement [39].

We propose here a solution for the bandwidth enhancement of a patch antenna which solves the aforementioned issues encountered in the pure ferrite and in the magneto-dielectric approaches. This solution is based on the wire-ferrite composite material proposed by Dewar in [116], which consists of a 2D array of dielectric-coated conductive wires embedded in the ferrite material. In this proposal, the ferrite material provides a high permeability associated

with its ferrimagnetic resonance, while its high bulk permittivity is reduced by the wire Drude permittivity near its plasma frequency. This idea was conceptually proposed in [117], but the bandwidth enhancement of the patch on the real substrate was not demonstrated in this paper. In fact, it is unclear whether this could have been done with the structure considered in [117], which consisted of a 2D array of *uncoated* wires in a ferrite medium, where the electric and magnetic responses tend to cancel each other due to Lenz law [116].

Wire-Ferrite Medium and Design Principles

The considered coated wire-ferrite medium is a 2D lattice of dielectric coated conductive wires embedded in a magnetized ferrite host medium [116], as shown in Fig. 7.4, where r_1, r_2 and p are the radius of the dielectric coating, radius of the wires and lattice constant, respectively, $\mathbf{H}_0$, ε_f, $\bar{\bar{\mu}}$ and t are the bias field, permittivity, permeability tensor and the thickness of the ferrite, respectively, and ε_c is the permittivity of the coating.

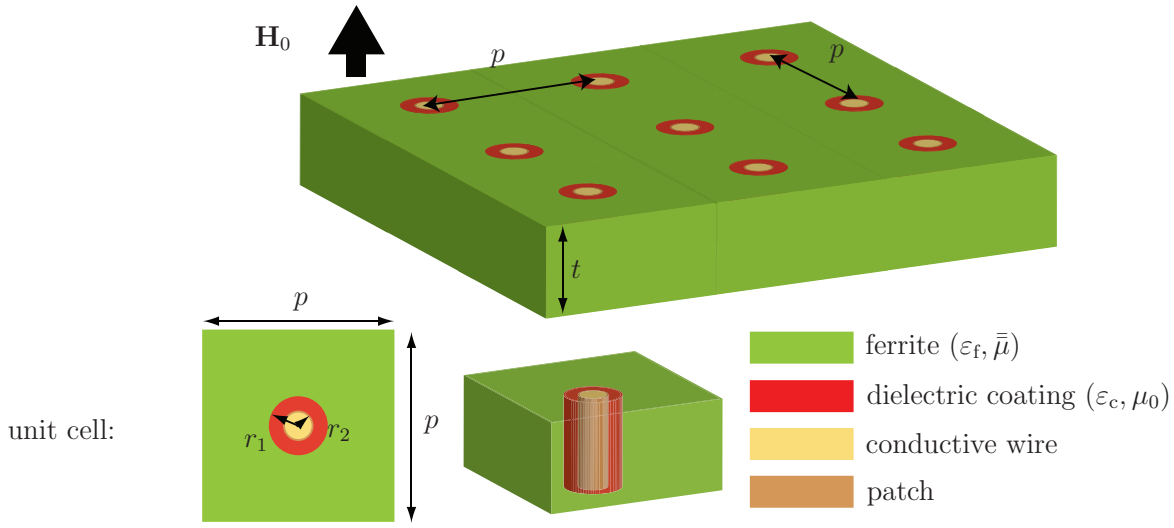

Figure 7.4 Wire-ferrite medium substrate.

Since the wires are coated by a dielectric material, the electric and magnetic responses of the structure are essentially decoupled and the structure exhibits a Drude permittivity due to the wires and a Lorentz permeability due to the ferrite host medium [116, 43].

The wire-ferrite structure should be designed in the following fashion. First, the permittivity must be minimized by exploiting the Drude response of the wires. Second, the dispersion must be kept moderate, so as to avoid losing the bandwidth enhancement benefit. Third, one must ensure that the frequency range of operation lies below the Bragg scattering limit, beyond which the effective medium properties are lost [118]. The design consists in optimizing the available degrees of freedom to meet these three requirements.

Fig. 7.5 shows the effective constitutive parameters of the preliminary designed wire-ferrite structure with the parameters shown in the caption. Fig. 7.5a demonstrates the calculated

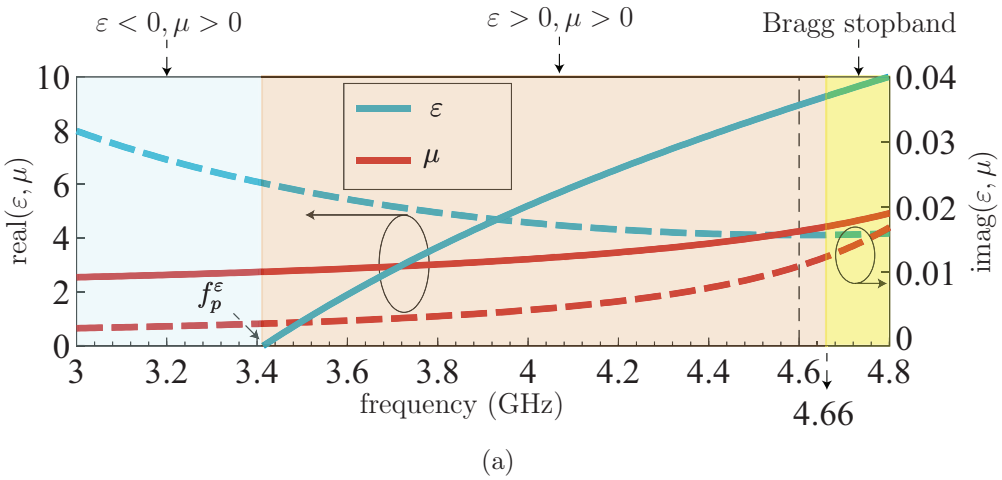

(a)

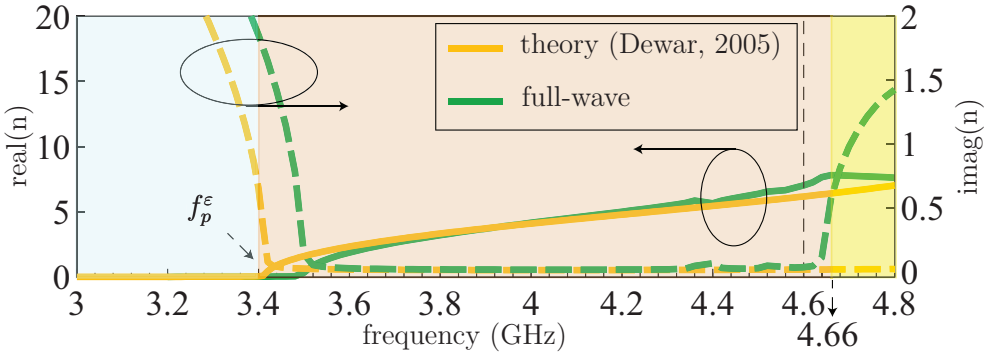

(b)

Figure 7.5 Effective constitutive parameters of the wired-ferrite substrate supporting the patch antenna (Fig. 7.4) with $r_1 = 0.35$ mm, $r_2 = 0.11$ mm, $p = 4.1$ mm, $\mathbf{H}_0 = 1382$ G and a ferrite host medium with the saturation magnetization of $4\pi \mathrm{M_s} = 1600$ G, line width of $\triangle H = 5$ Oe, $\varepsilon_\mathrm{f} = 14.6$ and $t = 1$ mm. (a) Theoretical (Dewar, 2005) effective permeability and permittivity (f_p^{ε} as the plasma frequency of the Drude permittivity). (b) Full-wave simulated and theoretical effective refractive index.

theoretical effective Drude permittivity and Lorentz permeability [116], whereas Fig. 7.5b shows the effective refractive index extracted from the full-wave simulation and calculated by the theory [116]. This Bragg scattering limit occurs at $f = 4.66$ GHz. Since the theoretical formula of [116] for the effective permeability and permittivity does not hold in the bandgap, the bandgap is not predicted by the theory and therefore there is no agreement between the extracted refractive index from the full-wave simulation and the theoretical values in the corresponding frequency range. In this design, the operation frequency is located below the Bragg limit at $f = 4.6$ GHz.

Bandwidth Enhancement Demonstration

To demonstrate the bandwidth enhancement by the wire-ferrite structure, three patch antennas with equal patch size (equal refractive index) and substrate size, are compared using full-wave simulation: 1) the actual wire-ferrite structure of Fig. 7.4, 2) the effective medium of the wire-ferrite structure with the parameters of Fig. 7.5 ($\varepsilon|_{f=4.6\text{ GHz}} = 8.94 - j0.02$ and $\mu|_{f=4.6\text{ GHz}} = 4.25 - j0.01$.) and 3) the conventional, non-magnetic dielectric with an equal refractive index calculated by Fig. 7.5b ($n|_{f=4.6\text{ GHz}} = 6.17 - j0.01$ and $\mu = \mu_0$). In order to avoid radiation pattern squinting due to the magnetic displacement effect, the antenna maybe excited from its two ends.

Fig. 7.6 compares the bandwidths of the patch antenna on the three different substrates. The figure shows that the relative -10 dB bandwidth of the patch on the wire-ferrite, effective and conventional substrates are 2.2%, 1.8% and 1.3%, respectively. Based on these results, the wire-ferrite structure and its effective medium exhibit a bandwidth enhancement of 70% and 42%, respectively, compared to the conventional dielectric substrate. The difference between the achieved bandwidth from the actual wire-ferrite and its effective structure may be due to anisotropy of the ferrite material which is not accounted for by the theoretical formulas of the material.

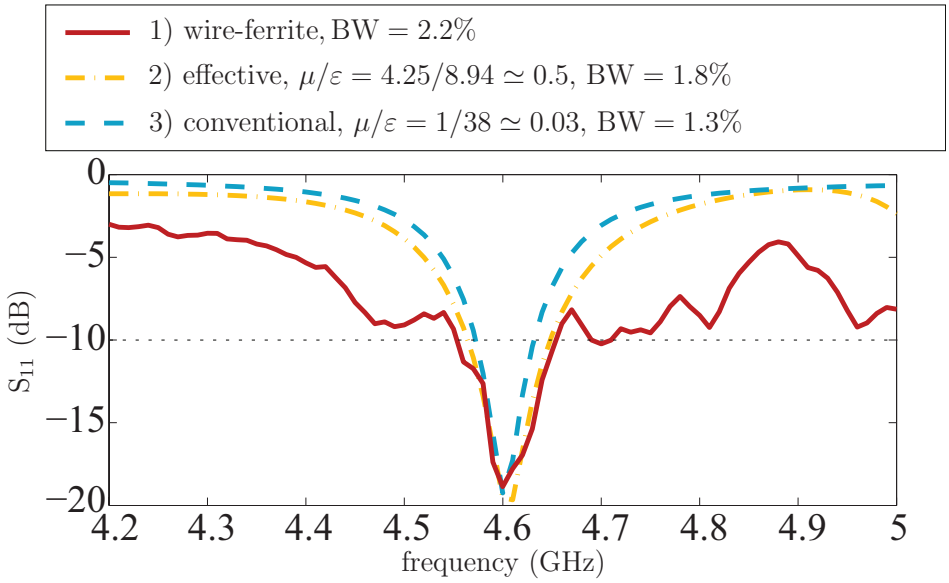

Figure 7.6 Comparison between the bandwidth of a patch antenna on the 1) wire-ferrite structure (Fig. 7.4), 2) its effective medium (Fig. 7.5a) and 3) a conventional dielectric substrate with the same refractive index (Fig. 7.5b), achieved by the full-wave simulation.

Problems for Future Study

In [116], the analytical expressions for the effective permittivity and permeability are calculated under the assumption that the ferrimagnetic material is isotropic [116], which is not precise and suggests that the analytical effective permittivity and permeability may not be accurate. In addition, in our analysis, the anisotropy of the wire-medium structure is not considered. Therefore, in this work it is assumed that the structure has effective isotropic permittivity and permeability. This assumption may explain the deviation of the patch antenna bandwidth for the actual structure and the effective substrate shown in Fig. 7.6. As a result, although the preliminary results of the full-wave simulation of the patch on the actual structure and its comparison with a conventional substrate shows that the structure has the potential of bandwidth enhancement, an in-depth study of the structure, including calculating the accurate effective parameters considering the anisotropy of the ferrite and the wire-medium, is required to exactly explain the behavior of the structure and its effect on the radiation properties of the patch antenna.

REFERENCES

[1] R. P. Feynman, R. B. Leighton, and M. Sands, *The Feynman Lectures on Physics*. Addison-Wesley, 1964, vol. 2.

[2] D. M. Pozar, *Microwave Engineering*. Wiley, 2005.

[3] M. W. Barsoum, *Fundamentals of Ceramics*. Institute of Physics Publishing, 2003.

[4] M. E. Tobar, J. Krupka, E. N. Ivanov, and R. A. Woode, "Anisotropic complex permittivity measurements of mono-crystalline rutile between 10 and 300 k," *J. Appl. Phys.*, vol. 83, no. 3, pp. 1604–1609, 1998.

[5] R. S. Toneva, N. N. Antonov, and I. G. Mironenko, "Permittivity of thin ferroelectrics layers at microwaves," *Ferroelectrics*, vol. 22, no. 1, pp. 789–790, 1978.

[6] Y. Lin, X. Chen, S. W. Liu, C. L. Chen, J.-S. Lee, Y. Li, Q. X. Jia, and A. Bhalla, "Epitaxial nature and anisotropic dielectric properties of (Pb, Sr)TiO_3 thin films on $NdGaO_3$ substrates," *Appl. Phys. Lett.*, vol. 86, p. 142902, 2005.

[7] Z. Shen, J. Liu, J. Grins, M. Nygren, P. Wang, Y. Kan, H. Yan, and U. Sutter, "Effective grain alignment in $Bi_4Ti_3O_{12}$ ceramics by superplastic-deformation-induced directional dynamic ripening," *Adv. Mater.*, vol. 17, no. 6, pp. 676–680, 2005.

[8] W. Chang, S. W. Kirchoefer, J. A. Bellotti, S. B. Qadri, J. M. Pond, J. H. Haeni, and D. G. Schlom, "In-plane anisotropy in the microwave dielectric properties of $SrTiO_3$ films," *J. Appl. Phys.*, vol. 98, no. 2, p. 024107, 2005.

[9] S. Gevorgian, *Ferroelectrics in Microwave Devices, Circuits and Systems: Physics, Modeling, Fabrication and Measurements*. Springer, 2009.

[10] B. Lax and K. J. Button, *Microwave Ferrites and Ferrimagnetics*. McGraw-Hill, 1962.

[11] R. E. Collin, *Field Theory of Guided Waves*. Wiley & IEEE Press, 1991.

[12] S. A. Tretyakov, *Analytical Modeling in Applied Electromagnetics*. Artech House, 2003.

[13] A. H. Sihvola, *Electromagnetic Mixing Formulas and Applications*. The Institution of Electrical Engineers, 1999.

[14] V. G. Veselago, "The electrodynamics of substances with simultaneous negative values of ε and μ," *Soviet Physics Uspekhi*, vol. 10, no. 4, pp. 509–514, 1968.

[15] I. Lindell, A. Sihvola, S. A. Tretyakov, and A. J. Viitanen, *Electromagnetic Waves in Chiral and Bi-isotropic Media*. Artech House, 1994.

[16] C. Caloz and T. Itoh, *Electromagnetic Metamaterials, Transmission Line Theory and Microwave Applications*. Wiley & IEEE Press, 2006.

[17] N. Engheta and R. W. Ziolkowski, *Electromagnetic Metamaterials: Physics and Engineering Explorations*. Wiley & IEEE Press, 2006.

[18] W. E. Kock, "Metal-lens antennas," *Proc. of IRE*, vol. 34, pp. 828–836, 1946.

[19] ——, "Metallic delay lenses," *Bell Syst. Tech. J.*, vol. 27, pp. 58–82, 1948.

[20] S. B. Cohn, "Analysis of the metal-strip delay structure for microwave lenses," *J. Phys.*, vol. 20, pp. 257–262, 1949.

[21] ——, "Electrolytic tank measurements for microwave metallic delay lens media," *J. Appl. Phys.*, vol. 21, pp. 674–680, 1950.

[22] G. Estrin, "The effective permeability of an array of thin conducting disks," *J. Appl. Phys.*, vol. 21, pp. 667–670, July 1950.

[23] J. Brown, "Artificial dielectrics," *Progress in Dielectrics*, vol. 2, pp. 195–225, 1960.

[24] W. Rotman, "Plasma simulation by artificial dielectrics and parallel-plate media," *IRE Trans. Antennas Propagat.*, vol. AP-10, no. 1, 1962.

[25] K. E. Golden, "Plasma simulation with an artificial dielectric in a horn geometry," *IEEE Trans. Antennas Propagat.*, vol. 13, no. 4, pp. 587–594, 1965.

[26] I. J. Bahl and K. Gupta, "A leaky-wave antenna using an artificial dielectric medium," *IEEE Trans. Antennas Propagat.*, vol. 22, no. 1, pp. 119–122, 1974.

[27] ——, "Frequency scanning leaky-wave antennas using artificial dielectrics," *IEEE Trans. Antennas Propagat.*, vol. 23, no. 4, pp. 584–589, 1975.

[28] J. B. Pendry, A. J. Holden, W. J. Stewart, and I. Youngs, "Extremely low frequency plasmons in metallic mesostructures," *Phys. Rev. Lett.*, vol. 76, no. 25, pp. 4773–4776, 1996.

[29] J. B. Pendry, A. J. Holden, D. J. Robbins, and W. J. Stewart, "Low frequency plasmons in thin-wire structures," *J. Phys. Condens. Matter*, vol. 10, no. 22, pp. 4785–4809, 1998.

[30] ——, "Magnetism from conductors and enhanced nonlinear phenomena," *IEEE Trans. Microwave Theory Tech.*, vol. 47, no. 11, pp. 2075–2084, 1999.

[31] D. R. Smith, W. J. Padilla, D. C. Vier, S. C. Nemat-Nasser, and S. Schultz, "Composite medium with simultaneously negative permeability and permittivity," *Phys. Rev. Lett.*, vol. 84, no. 18, pp. 4184–4187, 2000.

[32] H. Mosallaei and K. Sarabandi, "Design and modeling of patch antenna printed on magneto-dielectric embedded-circuit metasubstrate," *IEEE Trans. Antennas Propagat.*, vol. 55, no. 1, pp. 45–52, 2007.

[33] P. M. T. Ikonen, K. N. Rozanov, A. V. Osipov, P. Alitalo, and S. A. Tretyakov, "Magnetodielectric substrates in antenna miniaturization: potentials and limitations," vol. 54, no. 11, pp. 3391–3399, 2006.

[34] R. W. Ziolkowski and F. Auzanneau, "Passive artificial molecule realization of dielectric materials," *J. Appl. Phys.*, vol. 82, no. 7, 1997.

[35] P. A. Belov, R. Marqués, S. I. Maslovski, I. S. Nefedov, M. Silversinha, C. R. Simovskiand, and S. A. Tretyakov, "Strong spatial dispersion in wire media in the very large wavelength limit," *Physical Rev B*, vol. 67, pp. 113 103(1–4), 2003.

[36] F. Capolino, Ed., *Metamaterials Handbook*. CRC, 2009.

[37] R. C. Hansen and M. Bruke, "Antenna with magneto−dielectrics," *Microwave Opt. Technol. Lett.*, vol. 26, no. 2, pp. 75–78, 2000.

[38] H. Mosallaei and K. Sarabandi, "Magneto-dielectrics in electromagnetics: concept and applications," *IEEE Trans. Antennas propagat.*, vol. 52, no. 6, pp. 1558–1567, 2004.

[39] P. Ikonen, S. Maslovski, C. Simovski, and S. Tretyakov, "On artificial magneto−dielectric loading for improving the impedance bandwidth properties of microstrip antennas," vol. 54, no. 6, pp. 1654–1662, 2006.

[40] A. Shahvarpour, S. Couture, , and C. Caloz, "Bandwidth enhancement of a patch antenna using a wire-ferrite substrate," in *Proc. IEEE AP-S Int. Antennas Propagat. (APS)*, Chicago, IL, July 2012.

[41] C. A. Allen, C. Caloz, and T. Itoh, "A novel metamaterial-based two-dimensional conical-beam antenna," in *Proc. IEEE MTT-S Int. Microwave Symp. Dig*, Fort Worth, TX, USA, June 2004.

[42] C. A. Allen, K. M. K. H. Leong, C. Caloz, and T. Itoh, "A two-dimensional edge excited metamaterial-based leaky-wave antenna," in *Proc. IEEE AP-S International Symposium*, Washington, DC, USA, June 2005.

[43] S. Couture, J. Gauthier, T. Kodera, and C. Caloz, "Experimental demonstration and potential applications of a tunable NRI ferrite-wire metamaterial," *IEEE Antennas Wirel. Propag. Lett.*, vol. 9, pp. 1022–1025, 2010.

[44] H. V. Nguyen, J. Gauthier, J. M. Fernandez, M. Sierra−Castaner, and C. Caloz, "Metallic wire substrate (MWS) for miniaturization in planar microwave application," *in Proc. Asia-Pacific Microwave Conference APMC*, 2006.

[45] M. Coulombe, H. V. Nguyen, and C. Caloz, "Substrate integrated artificial dielectric (SIAD) structure for miniaturized microstrip circuits," *IEEE Antennas and Wireless Propagat. Lett.*, vol. 6, pp. 575–579, 2007.

[46] S. Couture, A. Parsa, and C. Caloz, "Size-independent zeroth order electric plasmonic cavity resonator," *Microwave Opt. Technol. Lett.*, vol. 53, no. 4, pp. 927–932, 2011.

[47] M. Coulombe and C. Caloz, "Reflection-type artificial dielectric substrate microstrip dispersive delay line (DDL) for analog signal processing," *IEEE Trans. Microwave Theory Tech.*, vol. 57, no. 7, pp. 1714–17 232, 2009.

[48] A. B. Yakovlev, M. G. Silveirinha, O. Luukkonen, C. R. Simovskiand, I. S. Nefedov, and S. A. Tretyakov, "Characterization of the surface-waves and leaky-waves propagation on wire medium slab and mushroom structures based on local and nonlocal homogenization models," *IEEE Trans. Microwave Theory Tech.*, vol. 57, no. 11, pp. 2700–2714, 2009.

[49] H. V. Nguyen and C. Caloz, "Anisotropic backward-wave meta-susbtrate and its application to a microstrip leaky-wave antenna," in *Proc. CNC/ USNC URSI National Radio Science Meeting*, Ottawa, ON, Canada, July 2007.

[50] D. Sievenpiper, L. Zhang, and E. Y. R. F. J. Broas, N. G. Alexópolous, "High-impedance electromagnetic surfaces with a forbidden frequency band," *IEEE Trans. Microwave Theory Tech.*, vol. 47, no. 11, pp. 2059–2074, 1999.

[51] R. F. Harrington, *Time-Harmonic Electromagnetic Fields.* Wiley-IEEE Press, 2001.

[52] F. R. Yang, K. P. Ma, Y. Qian, and T. Itoh, "A novel TEM waveguide using uniplanar compact photonic bandgap (UC-PBG) structure," *IEEE Trans. Antennas Propagat.*, vol. 47, no. 11, pp. 2092–2098, 1999.

[53] P. S. Kildal, E. Lier, and J. A. Aas, "Artificially soft and hard surfaces in electromagnetics and their applications," in *Proc. IEEE AP-S International Symposium*, Syracuse, NY, USA, June 1988, pp. 832–835.

[54] I. V. Lindell and A. H. Sihvola, "Perfect electromagnetic conductor," *J. Electromagn. Waves App.*, vol. 19, no. 7, pp. 861–869, 2005.

[55] ——, "Realization of the PEMC boundary," *IEEE Trans. Antennas Propagat.*, vol. 53, no. 9, pp. 3012–3018, 2005.

[56] J. A. Stratton, *Electromagnetic Theory.* McGraw-Hill, 1941.

[57] A. Sihvola and I. V. Lindell, "Possible applications of perfect electromagnetic conductor (PEMC) media," in *Proc. European Conference (EuCap)*, Nov. 2006.

[58] T. Itoh, Ed., *Numerical Techniques for Microwave and Millimeter-Wave Passive Structures.* Wiley-IEEE Press, 1989.

[59] W. C. Chew, *Waves and Fields in Inhomogeneous Media.* John Wiley, 1999.

[60] A. F. Peterson, S. L. Ray, and R. Mittra, *Computational Methods for Electromagnetics.* Wiley-IEEE Press, 1997.

[61] J. L. Tsalamengas, "Interaction of electromagnetic waves with general bianisotropic slabs," *IEEE Trans. Microwave Theory Tech.*, vol. 40, no. 10, pp. 1870–1878, 1992.

[62] A. Oliner and D. Jackson, "Leaky-wave antennas," in *Antenna Engineering Handbook*, 4^{st} ed., J. Volakis, Ed. McGraw-Hill, 2007, ch. 11.

[63] G. V. Trentini, "Partially reflecting sheet arrays," *IRE Trans. Antennas Propagat.*, vol. 4, pp. 666–671, 1956.

[64] D. R. Jackson and A. A. Oliner, "A leaky-wave analysis of the high-gain printed antenna configuration," *IEEE Trans. Antennas Propagat.*, vol. 36, no. 7, pp. 905–910, 1988.

[65] T. Zhao, D. R. Jackson, J. T. Williams, H. Y. Yang, and A. A. Oliner, "2-D periodic leaky-wave antenna-part i: metal patch design," *IEEE Trans. Antennas Propagat.*, vol. 53, no. 11, pp. 3505–3514, 2005.

[66] G. Lovat, P. Burghignoli, F. Capolino, D. R. Jackson, and D. R. Wilton, "Analysis of directive radiation from a line source in a metamaterial slab with low permittivity," *IEEE Trans. Antennas Propagat.*, vol. 54, no. 3, pp. 1017–1030, 2006.

[67] P. Burghignoli, G. Lovat, F. Capolino, D. R. Jackson, and D. R. Wilton, "Directive leaky-wave radiation from a dipole source in a wire-medium slab," *IEEE Trans. Antennas Propagat.*, vol. 56, no. 5, pp. 1329–1339, 2008.

[68] N. G. Alexopoulos, "Integrated-circuit structures on anisotropic slabs," *IEEE Trans. Microwave Theory Tech.*, vol. 38, no. 10, pp. 847–881, 1985.

[69] C. M. Krowne, "Green's functions in the spectral domain for biaxial and uniaxial anisotropic planar dielectric structures," *IEEE Trans. Antennas Propagat.*, vol. 32, no. 12, pp. 1273–1281, 1984.

[70] J. L. Tsalamengas, "Electromagnetic fields of elementary dipole antennas embedded in stratified general gyrotropic media," *IEEE Trans. Antennas Propagat.*, vol. 37, no. 3, pp. 399–403, 1989.

[71] F. Mesa, R. Marques, and M. Horno, "An efficient numerical spectral domain method to analyze a large class of nonreciprocal planar transmission lines," *IEEE Trans. Microwave Theory Tech.*, vol. 40, no. 8, pp. 1630–1640, 1992.

[72] F. Mesa and M. Horno, "Computation of proper and improper modes in multilayered bianisotropic waveguides," *IEEE Trans. Microwave Theory Tech.*, vol. 43, no. 1, pp. 233–235, 1995.

[73] R. Marques and M. Horno, "Propagation of quasi-static modes in anisotropic transmission lines: application to MIC line," *IEEE Trans. Microwave Theory Tech.*, vol. 33, no. 10, pp. 927–932, 1985.

[74] G. W. Hansen, "Integral equation formulations for inhomogeneous anisotropic media Green's dyad with applications to microstrip transmission line propagation and leakage," *IEEE Trans. Microwave Theory Tech.*, vol. 43, no. 6, pp. 1359–1363, 1995.

[75] L. B. Felsen and N. Marcuvitz, *Radiation and Scattering of Waves.* Prentice-Hall/IEEE Press, 1996.

[76] J. R. Mosig, "Integral equation techniques," in *Numerical Techniques for Microwave and Millimeter-Wave Passive Structures*, T. Itoh, Ed. Wiley InterSci., 1989, ch. 3.

[77] N. G. Alexopoulos, P. B. Katehi, and D. B. Rutledge, "Substrate optimization for integrated circut antennas," *IEEE Trans. Microwave Theory Tech.*, vol. 31, no. 7, pp. 550–557, 1983.

[78] D. M. Pozar, "Considerations for millimeter wave printed antennas," *IEEE Trans. Antennas Propagat.*, vol. 31, no. 5, pp. 740–747, 1983.

[79] N. G. Alexopoulos and D. R. Jackson, "Fundamental superstrate (cover) effects on printed circuit antennas," *IEEE Trans. Antennas Propagat.*, vol. 32, no. 8, pp. 807–816, 1984.

[80] C. R. Simovski, S. H. Shahvarpour, and C. Caloz, "Grounded ferrite perfect magnetic conductor and application to waveguide miniaturization," *IEEE-MTTS Int. Microwave Symp. Digest*, pp. 25–28, 2009.

[81] A. Shahvarpour, T. Kodera, A. Parsa, and C. Caloz, "Realization of an effective free-space perfect electromagnetic conductor (PEMC) boundary by a grounded ferrite slab using Faraday rotation," *in Proc. European Microwave Conf. (EuMC)*, pp. 731–734, 2009.

[82] B. Lax, J. A. Weiss, N. W. Harris, and G. F. Dionne, "Quasi-optical reflection circulator," *IEEE Trans. Microwave Theory Tech.*, vol. 41, no. 12, pp. 2190–2197, 1993.

[83] J. Yeo, J.-F. Ma, and R. Mittra, "GA-based design of artificial magnetic ground planes (AMGS) utilizing frequency-selective surfaces for bandwidth enhancement of microctrip antennas," *Microwave Opt. Technol. Lett.*, vol. 44, no. 1, pp. 6–13, 2005.

[84] R. G. Heeren and J. R. Baird, "An inhomogeneously filled rectangular waveguide capable of supporting TEM propagation," *IEEE Trans. Microwave Theory Tech.*, vol. 19, no. 11, pp. 884–885, 1971.

[85] M. N. M. Kehn and P. S. Kildal, "Miniaturized rectangular hard waveguides for use in multifrequency phased arrays," *IEEE Trans. Antennas Propagat.*, vol. 53, no. 1, pp. 100–109, 2005.

[86] L.-P. Carignan, M. Massicotte, C. Caloz, A. Yelon, , and D. Ménard, "Magnetization reversal in arrays of Ni nanowires with different diameters," *IEEE Trans. Mag.*, vol. 45, no. 10, pp. 4070–4073, 2009.

[87] W. W. Hansen, "Radiating electromagnetic waveguide," Patent U.S. Patent 2,402,622, June, 1940.

[88] J. N. Hines and J. R. Upson, "A wide aperture tapered-depth scanning antenna," Ohio State Univ. Res. Found., Ohio, Tech. Rep., Dec. 1957.

[89] W. Rotman and N. Karas, "The sandwich wire antenna: a new type of microwave line source radiator," *IRE Conv. Rec., part 1*, p. 166, 1957.

[90] A. Ip and D. R. Jackson, "Radiation from cylindrical leaky-waves," *IEEE Trans. Antennas Propagat.*, vol. 38, no. 4, pp. 482–488, 1990.

[91] D. R. Jackson, A. A. Oliner, and A. IP, "Leaky-wave propagation and radiation from a narrow-beam multiple-layer dielectric structure," *IEEE Trans. Antennas Propagat.*, vol. 4, no. 3, pp. 344–348, 1993.

[92] A. P. Feresidis and J. C. Vardaxoglou, "High-gain planar antenna using optimized partially reflective surfaces," vol. 148, no. 6, pp. 345–350, 2001.

[93] A. Lai, C. Caloz, and T. Itoh, "Composite right/left-handed transmission line metamaterials," *IEEE Microwave Magazine*, vol. 5, no. 3, pp. 34–50, 2004.

[94] G. V. Eleftheriades, "Enabling RF/microwave devices using negative-refractive-index transmission-line (NRI-TL) metamaterials," *IEEE Antennas Propagat. Magazine*, vol. 49, no. 2, pp. 34–51, 2007.

[95] C. Caloz, T. Itoh, and A. Rennings, "CRLH metamaterial traveling-wave and resonant antennas," *IEEE Antennas Propagat. Magazine*, vol. 50, no. 5, pp. 25–39, 2008.

[96] S. Gupta and C. Caloz, "Analog signal processing in transmission line metamaterial structures," *Radioengineering*, vol. 18, no. 2, pp. 155–167, June 2009.

[97] M. Coulombe, S. F. Koodiani, and C. Caloz, "Compact elongated mushroom (EM)-EBG structure for enhancement of patch antenna array performances," *IEEE Trans. Antennas Propagat.*, vol. 58, no. 4, pp. 1076–1086, 2010.

[98] L. P. Carignan, A. Yelon, D. Ménard, and C. Caloz, "Ferromagnetic nanowire metamaterials: theory and applications," *IEEE Trans. Microwave Theory Tech.*, vol. 59, no. 10, pp. 2568–2586, 2011.

[99] N. Marcuvitz, *Waveguide Handbook*. McGraw-Hill, 1951.

[100] T. M. Grzegorczyk and J. R. Mosig, "Full-wave analysis of antennas containing horizontal and vertical metallizations embedded in planar multilayered media," vol. 51, no. 11, pp. 3047–3054, 2003.

[101] J. R. Mosig and F. E. Gardiol, *Advances in Electronics and Electron Physics*. Academic Press, 1982.

[102] C. A. Balanis, *Antenna Theory: Analysis and Design*, 3rd ed. Wiley, 2005.

[103] R. J. Mailloux, *Phased Array Antenna Handbook*, 2nd ed. Wiley, 2005.

[104] J. Federici and L. Moeller, "Review of terahertz and subterahertz wireless communications," *J. Appl. Phys.*, vol. 107, p. 111101, 2010.

[105] T. Kleine-Ostmann and T. Nagatsuma, "A review on terahertz communications research," *J. Infrared, Millim. Terahertz Waves*, vol. 32, pp. 143–171, 2011.

[106] H.-J. Song and T. Nagatsuma, "Present and future of terahertz communications," *IEEE Trans. on Terahertz Science Tech.*, vol. 1, no. 1, pp. 256–263, 2011.

[107] D. Dragoman and M. Dragoman, "Terahertz fields and applications," *Progress in Quantum Electronics*, vol. 28, pp. 1–66, 2004.

[108] G. M. Rebeiz, "Millimeter-wave and terahertz integrated circuit antennas," *Proceedings of the IEEE*, vol. 80, no. 11, pp. 1748–1770, 1992.

[109] A. Shahvarpour, A. A. Melcon, , and C. Caloz, "Analysis of the radiation properties of a point source on a uniaxially anisotropic meta-substrate and application to a high-efficiency antenna," in *Proc. 40th European Microwave Conf. (EuMC)*, Paris, Ontario, Sept 2010, pp. 1424–1428.

[110] C. A. Balanis, *Advanced Engineering Electromagnetics*. Wiley, 1989.

[111] I. V. Lindell, *Methods for Electromagnetic Field Analysis*. Prentice-Hall/IEEE Press, 1992.

[112] K. R. Carver and J. W. Mink, "Microstrip antenna technology," *IEEE Trans. Antennas Propagat.*, vol. 29, no. 1, pp. 2–24, 1981.

[113] A. Shahvarpour, T. Kodera, A. Parsa, and C. Caloz, "Arbitrary electromagnetic conductor boundaries using Faraday rotation in a grounded ferrite slab," *IEEE Trans. Microwave Theory Tech.*, vol. 58, no. 11, pp. 2781–2793, 2010.

[114] F. Yang and Y. Rahmat-Samii, "Reflection phase characterizations of the EBG ground plane for low profile wire antenna applications," *IEEE Trans. Antennas Propag.*, vol. 51, no. 10, pp. 2691–2703, 2003.

[115] H. A. Wheeler, "The radiansphere around a small antenna," *Proc. IRE.*, pp. 1325–1331, 1959.

[116] G. Dewar, "Minimization of losses in a structure having a negative index of refraction," *New J. Phys.*, vol. 7, no. 161, 2005.

[117] I. S. Nefedov, A.-C. Tarot, , and K. Mahdjoubi, "Wire media-ferrite substrate for patch antenna miniaturization," in *Proc. Antenna Technology: Small and Smart Antennas Metamaterials and Applications (IWAT)*, Cambridge, 2007, pp. 101–104.

[118] C. R. Simovski and S. Tretyakov, "Local constitutive parameters of metamaterials from an effective-medium perspective," *Phys. Rev. B*, vol. 75, p. 195111, 2007.

[119] S. T. Peng and A. A. Oliner, "Guidance and leakage properties of a class open dielectric waveguides: Part 1-mathematical formulations," *IEEE Trans. Microwave Theory Tech.*, vol. 29, no. 9, pp. 843–855, Sept. 1981.

[120] A. Oliner and D. Jackson, "Leaky-wave antennas," in *Modern Antenna Handbook*, C. A. Balanis, Ed. John Wiley, 2008, ch. 7.

[121] P. Lampariello, F. Frezza, and A. A. Oliner, "The transition region between bound-wave and leaky-wave ranges for a partially dielectric-loaded open guiding structure," *IEEE Trans. Microwave Theory Tech.*, vol. 38, no. 12, pp. 1831–1836, 1990.

[122] J. R. Mosig and A. A. Melcon, "Green's functions in lossy layered media: integration along the imaginary axis and asymptotic behavior," *IEEE Trans. Antennas Propagat.*, vol. 51, no. 12, pp. 3200–3208, 2003.

Appendix A

Definition of Proper and Improper Modes in a Dielectric Slab

A.1 Physical Interpretation of the Signs of the Wave Numbers

In order to facilitate the discussions of this section, it is appropriate to first provide a physical interpretation of the signs of the real and imaginary parts of the transverse (ρ) and longitudinal (z) wave numbers. For this purpose, we write the spatial dependencies in the air for the structure of Fig. 3.2a as follows

$$\begin{aligned} e^{-j\mathbf{k}_0.\mathbf{r}} &= e^{-j\mathbf{k}_\rho.\boldsymbol{\rho}} e^{-j\mathbf{k}_{z0}.\mathbf{z}} = e^{-jk_\rho\rho} e^{-jk_{z0}z} \\ &= e^{-j\mathrm{Re}(k_\rho)\rho} e^{\mathrm{Im}(k_\rho)\rho} e^{-j\mathrm{Re}(k_{z0})z} e^{\mathrm{Im}(k_{z0})z}, \end{aligned} \tag{A.1}$$

where we recall the assumed time dependence of $e^{+j\omega t}$ and that the TM and TE superscripts are implicit. By phase continuity, the transverse wave number in the slab is the same as in the air, while the longitudinal wave number in the slab $k_{z\mathrm{d}}$ has a similar form as in the air and just requires the substitution of k_{z0} by $k_{z\mathrm{d}}$.

The physical interpretation of the signs of the wave numbers is given in Tab. A.1.

Table A.1 Physical interpretation of the signs of the transverse and longitudinal wave numbers.

		k_ρ (transverse)	k_{z0} (longitudinal)
Re	< 0	incoming along ρ	incoming along z
	> 0	outgoing along ρ	outgoing along z
Im	< 0	decaying along ρ	decaying along z
	$= 0$	constant along ρ	constant along z
	> 0	growing along ρ	growing along z

A.2 Definition of the Proper and Improper Modes

Typical modes in a dielectric slab, classified in terms of the signs of $\mathrm{Im}(k_\rho)$ and $\mathrm{Im}(k_{z0})$ (Tab. A.1) and further characterized by the values of $\mathrm{Re}(k_\rho)$ and $\mathrm{Re}(k_{z0})$, are listed in Tab. A.2 [36, 119, 75]. It has been also assumed that $\mathrm{Re}(k_{z0}) > 0$ and $\mathrm{Re}(k_\rho) > 0$, which excludes the possibility for backward waves.

Table A.2 Typical modes in a dielectric slab ($k_{\rm d} = \omega\sqrt{\mu_{\rm d}\varepsilon_{\rm d}}$ represents the wave number in the medium with effective permeability $\mu_{\rm d}$ and permittivity $\varepsilon_{\rm d}$).

	$\mathrm{Im}(k_\rho) < 0$	$\mathrm{Im}(k_\rho) = 0$
$\mathrm{Im}(k_{z0}) < 0$	impossible (if no loss)	surface mode for $1 < \mathrm{Re}(k_\rho/k_0) < k/\omega$ and $\mathrm{Re}(k_{z0}/k_0) = 0$
$\mathrm{Im}(k_{z0}) > 0$	leaky mode if $0 < \mathrm{Re}(k_\rho/k_0) < 1$ non-physical if $\mathrm{Re}(k_\rho/k_0) > 1$	non-physical if $1 < \mathrm{Re}(k_\rho/k_0) < k/\omega$ and $\mathrm{Re}(k_{z0}/k_0) = 0$

According to Tab. A.2, in a dielectric slab two physical modes known as surface-wave and leaky-wave modes may exist. Surface-wave modes are the non-radiative modes of the structure which carry the energy inside the dielectric. As shown in Fig. A.1a, for a lossless dielectric, surface-wave modes propagate without decaying in the substrate along the axis of propagation ρ ($\mathrm{Im}(k_\rho) = 0$), while decaying along the z axis ($\mathrm{Im}(k_{z0}) < 0$) and therefore they are named *proper* modes. Leaky-modes are the radiative modes of the dielectric slab. They radiate progressively along the z axis while propagating along ρ and therefore they decay along the axis ρ ($\mathrm{Im}(k_\rho) < 0$). However these modes amplify along the z axis ($\mathrm{Im}(k_{z0}) > 0$) and therefore they are called *improper* modes. Figure A.1b illustrates the ray-optics representation of a leaky-mode propagation in a dielectric slab and demonstrates how the leaky-wave radiation along the z axis has an amplifying nature ($\mathrm{Im}(k_{z0}) > 0$) [1]. The non-physical modes in Tab. A.2 are the mathematical poles of the dispersion relation of the structure which do not have any physical meaning.

In order to demonstrate the proper and improper modes, the particular and simple case of the isotropic grounded dielectric slab which was presented in Chapter 3 is considered. The corresponding TM_z and TE_z dispersion curves for the dielectric slab with $\varepsilon_{\rm d} = 2\varepsilon_0$ and $\mu_{\rm d} = \mu_0$ are shown in Figs. A.2 and A.3, respectively. Four distinct types of modes are indicated in Fig. A.2, according to Tabs. A.1 and A.2 [121, 120]. Type 1, with $1 < \mathrm{Re}(k_\rho^{\mathrm{TM}_z})/k_0 < \sqrt{\varepsilon}$, $\mathrm{Im}(k_\rho^{\mathrm{TM}_z}) = 0$, $\mathrm{Re}(k_{z0}^{\mathrm{TM}_z}) = 0$, and $\mathrm{Im}(k_{z0}^{\mathrm{TM}_z}) < 0$ (proper mode), corresponds to surface modes of the slab. Types 2 and 3, with $1 < \mathrm{Re}(k_\rho^{\mathrm{TM}_z})/k_0 < \sqrt{\varepsilon}$, $\mathrm{Im}(k_\rho^{\mathrm{TM}_z}) = 0$, $\mathrm{Re}(k_{z0}^{\mathrm{TM}_z}) = 0$, and $\mathrm{Im}(k_{z0}^{\mathrm{TM}_z}) > 0$ (improper mode), represent nonphysical modes. Type 4 includes three frequency bands. The $0.11 < d/\lambda_0 < 0.26$ band, with $\mathrm{Re}(k_\rho^{\mathrm{TM}_z})/k_0 < 1$, $\mathrm{Im}(k_\rho^{\mathrm{TM}_z}) < 0$, $\mathrm{Re}(k_{z0}^{\mathrm{TM}_z}) > 0$, and $\mathrm{Im}(k_{z0}^{\mathrm{TM}_z}) > 0$ (improper mode), supports a leaky mode, while the other two frequency bands, $d/\lambda_0 < 0.11$ and $0.26 < d/\lambda_0 < 0.41$, include nonphysical modes since $\mathrm{Re}(k_\rho^{\mathrm{TM}_z}/k_0^{\mathrm{TM}_z}) > 1$. These modes are summarized in Tab. A.3.

Similar comments hold for the TE_z modes, shown in Fig. A.3.

1. It should be noted that practically, the amplifying behavior of the leaky-wave radiation does not last for $z \to \infty$ and after a certain distance from the radiating aperture along the z axis, the radiation starts to decay again [120].

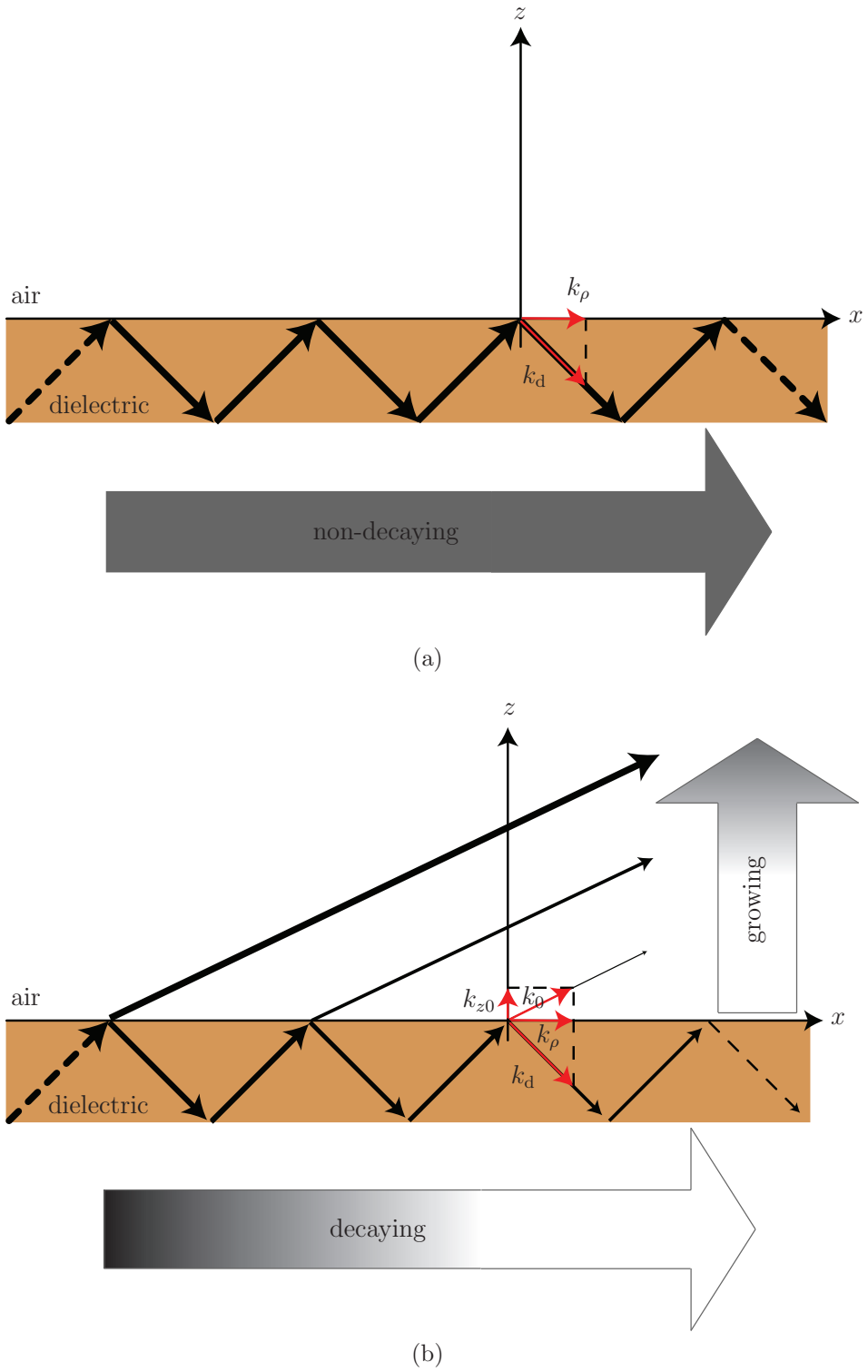

Figure A.1 Ray-optics representation of surface-wave and leaky-wave modes propagation in a dielectric slab. (a) Surface-wave modes. (b) Leaky-wave Modes.

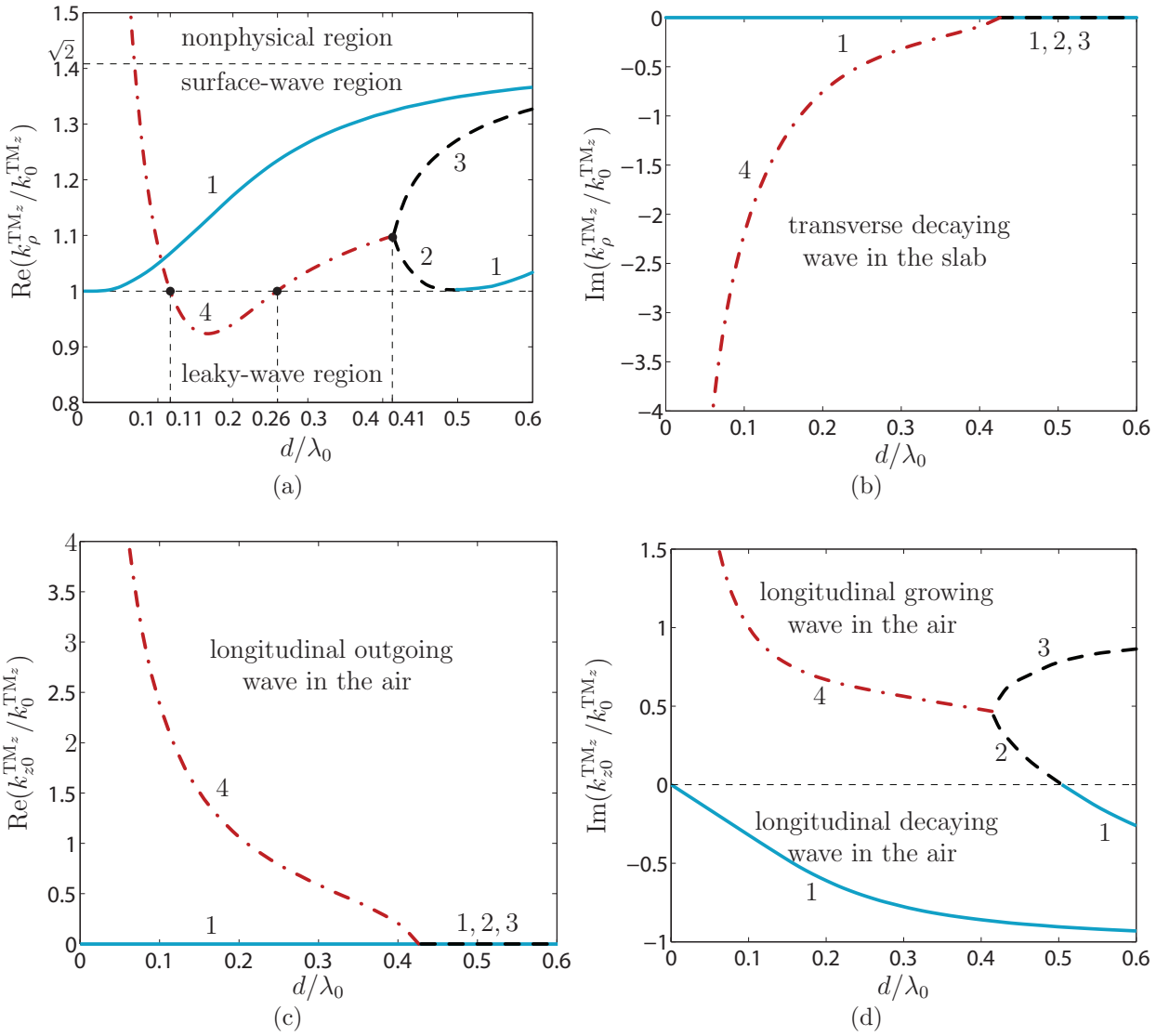

Figure A.2 TM_z dispersion curves for an isotropic grounded slab with $\varepsilon_\mathrm{d} = 2\varepsilon_0$, $\mu_\mathrm{d} = \mu_0$. (a) $\mathrm{Re}(k_\rho^{\mathrm{TM}_z}/k_0^{\mathrm{TM}_z})$. (b) $\mathrm{Im}(k_\rho^{\mathrm{TM}_z}/k_0^{\mathrm{TM}_z})$. (c) $\mathrm{Re}(k_{z0}^{\mathrm{TM}_z}/k_0^{\mathrm{TM}_z})$. (d) $\mathrm{Im}(k_{z0}^{\mathrm{TM}_z}/k_0^{\mathrm{TM}_z})$.

Table A.3 Characteristics of the different TM_z modes shown in the dispersion curves of Fig. A.2. SW, LW and IN stand for surface-wave, leaky-wave and non-physical modes, respectively.

	$\mathrm{Re}(k_\rho{}^{\mathrm{TM}_z}/k_0^{\mathrm{TM}_z})$	$\mathrm{Im}(k_\rho{}^{\mathrm{TM}_z}/k_0^{\mathrm{TM}_z})$	$\mathrm{Re}(k_{z0}^{\mathrm{TM}_z}/k_0^{\mathrm{TM}_z})$	$\mathrm{Im}(k_{z0}^{\mathrm{TM}_z}/k_0^{\mathrm{TM}_z})$	nature
Mode 1	$1 < < \sqrt{\varepsilon_\mathrm{d}}$	$= 0$	$= 0$	< 0	SW
Mode 2	$1 < < \sqrt{\varepsilon_\mathrm{d}}$	$= 0$	$= 0$	> 0	IN
Mode 3	$1 < < \sqrt{\varepsilon_\mathrm{d}}$	$= 0$	$= 0$	> 0	IN
Mode 4	> 1	< 0	> 0	> 0	IN
	< 1	< 0	> 0	> 0	LW

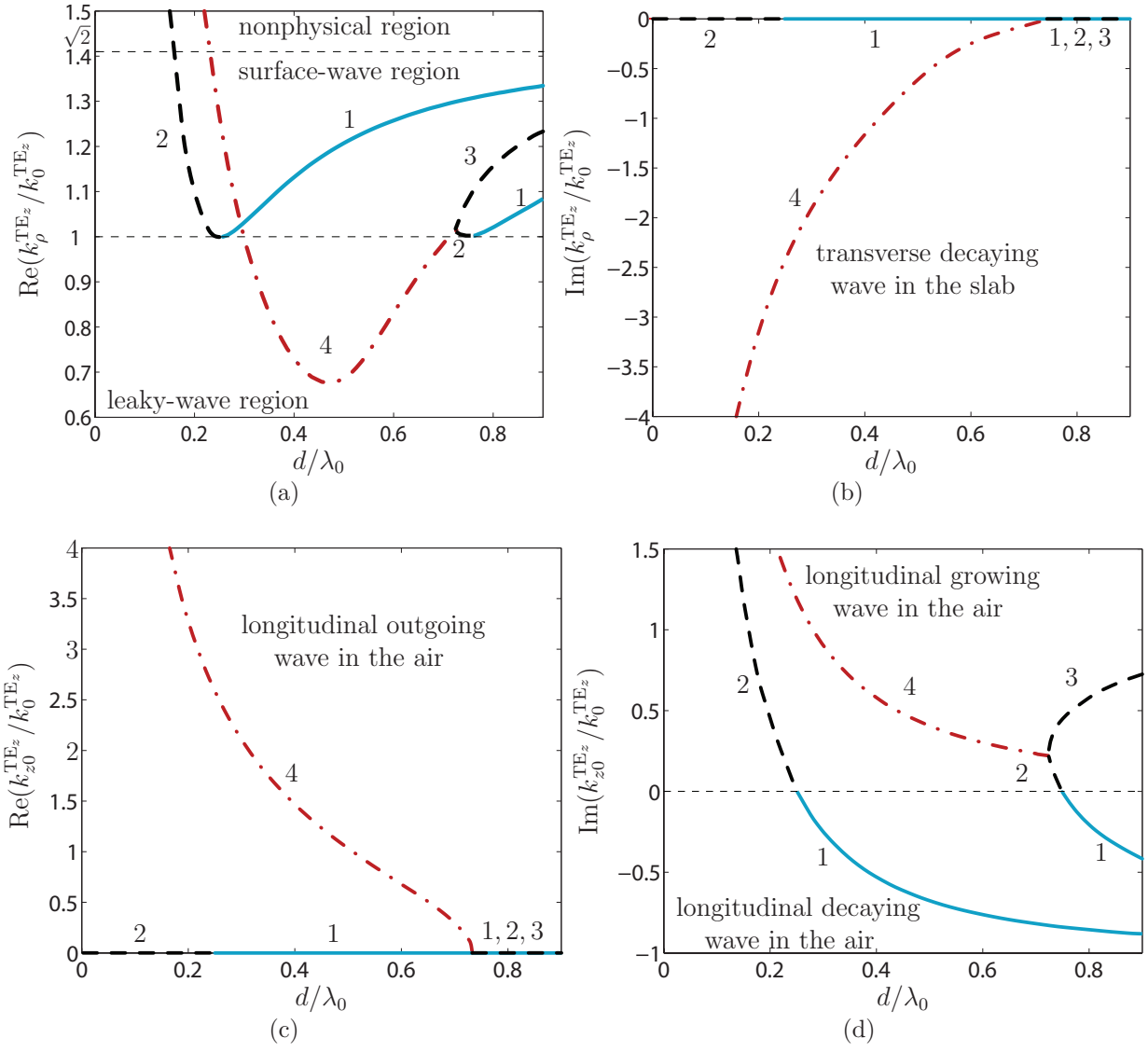

Figure A.3 TE_z dispersion curves for an isotropic grounded slab with $\varepsilon_\mathrm{d} = 2\varepsilon_0$, $\mu_\mathrm{d} = \mu_0$. (a) $\mathrm{Re}(k_\rho^{\mathrm{TE}_z}/k_0^{\mathrm{TE}_z})$. (b) $\mathrm{Im}(k_\rho^{\mathrm{TE}_z}/k_0^{\mathrm{TE}_z})$. (c) $\mathrm{Re}(k_{z0}^{\mathrm{TE}_z}/k_0^{\mathrm{TE}_z})$. (d) $\mathrm{Im}(k_{z0}^{\mathrm{TE}_z}/k_0^{\mathrm{TE}_z})$.

Appendix B

Spectral Domain Transmission-Line Modeling of a Uniaxially Anisotropic Medium

This section presents the spectral domain transmission-line modeling of the uniaxially anisotropic medium of Chapters 3 and 5 with the permittivity and permeability tensors of (3.1).

For simplicity, we start from the source-less problem and we derive the spectral transmission-line models for the TM_z and TE_z modes. Afterwards we extend the results for the cases of horizontal and vertical infinitesimal electric dipole sources and we derive the corresponding field Green functions.

B.1 Source-less Problem

The source-less spectral-domain transmission line model of a medium, assuming the time dependence $e^{+j\omega t}$, can be expressed under the form of the following relations between the spectral voltage $\tilde{V}$ and spectral current $\tilde{I}$ [75]

$$\frac{d\tilde{V}}{dz} = -jZk_z\tilde{I}, \tag{B.1a}$$

$$\frac{d\tilde{I}}{dz} = -jYk_z\tilde{V}, \tag{B.1b}$$

where Y, Z and k_z are the admittance, the impedance and the z component of the wave vector $\mathbf{k}$ of the medium, respectively, of the equivalent transmission line directed along the z axis. The corresponding voltage wave equation is obtained by deriving (B.1a) with respect to z and substituting (B.1b) into the resulting equation, which reads

$$\frac{d^2\tilde{V}}{dz^2} + ZYk_z^2\tilde{V} = 0, \tag{B.2}$$

and admits the voltage solution

$$\tilde{V} = \tilde{V}^{+} e^{-j\sqrt{ZY}k_z z} + \tilde{V}^{-} e^{j\sqrt{ZY}k_z z}, \tag{B.3}$$

where $\tilde{V}^{+}$ and $\tilde{V}^{-}$ are constant. The current solution is obtained by inserting this result into (B.1b), which yields

$$\tilde{I} = \sqrt{\frac{Y}{Z}} \left(\tilde{V}^{+} e^{-j\sqrt{ZY}k_z z} - \tilde{V}^{-} e^{j\sqrt{ZY}k_z z} \right). \tag{B.4}$$

The propagation constant β and the characteristic impedance Z_c of the equivalent transmission line are deduced by comparing (B.2) to (B.4) with the standard transmission line relations, and read

$$\beta = \sqrt{ZY}k_z, \tag{B.5a}$$

$$Z_c = \sqrt{\frac{Z}{Y}}. \tag{B.5b}$$

The transmission line parameters $\tilde{V}$, $\tilde{I}$, Z and Y for the TM_z and TE_z modes in the anisotropic medium of Fig. 3.1 will next be determined by inserting the tensors of (3.1) into source-less Maxwell equations,

$$\nabla \times \mathbf{H} = j\omega\bar{\bar{\varepsilon}}\mathbf{E}, \tag{B.6a}$$

$$\nabla \times \mathbf{E} = -j\omega\bar{\bar{\mu}}\mathbf{H}, \tag{B.6b}$$

and by manipulating the resulting equations so as to obtain two final equations with the same form as (B.1).

B.1.1 TM_z Modes

Inserting (3.1) into (B.6) for the TM_z modes ($H_z = 0$) and writing the resulting equations in the spectral domain, where $\partial/\partial x \to jk_x^{\mathrm{TM}_z}$ and $\partial/\partial y \to jk_y^{\mathrm{TM}_z}$, yields

$$-\frac{d}{dz}\tilde{H}_y = j\omega\varepsilon_\rho \tilde{E}_x, \tag{B.7a}$$

$$\frac{d}{dz}\tilde{H}_x = j\omega\varepsilon_\rho \tilde{E}_y, \tag{B.7b}$$

$$jk_x^{\mathrm{TM}_z}\tilde{H}_y - jk_y^{\mathrm{TM}_z}\tilde{H}_x = j\omega\varepsilon_z \tilde{E}_z, \tag{B.7c}$$

$$jk_y^{\mathrm{TM}_z}\tilde{E}_z - \frac{d}{dz}\tilde{E}_y = -j\omega\mu_\rho \tilde{H}_x, \tag{B.7d}$$

$$\frac{d}{dz}\tilde{E}_x - jk_x^{\mathrm{TM}_z}\tilde{E}_z = -j\omega\mu_\rho \tilde{H}_y, \tag{B.7e}$$

$$jk_x^{\mathrm{TM}_z}\tilde{E}_y - jk_y^{\mathrm{TM}_z}\tilde{E}_x = 0. \tag{B.7f}$$

Several possibilities exist for reducing (B.7) into two equations of the form of (B.1). A simple possibility consists in seeking a relation between $\tilde{E}_z$ and $\tilde{E}_x$ (or, equivalently, $\tilde{E}_y$) only, by eliminating all the other field components. This may be accomplished by the following algebraic manipulations.

First, derive (B.7c) with respect to z, substitute (B.7a) and (B.7b) into the resulting equation, and eliminate $\tilde{E}_y$ by using (B.7f), which yields

$$\frac{\varepsilon_z}{\varepsilon_\rho}\frac{d\tilde{E}_z}{dz} = -j\frac{{k_\rho^{\mathrm{TM}_z}}^2}{k_x^{\mathrm{TM}_z}}\tilde{E}_x, \tag{B.8}$$

where ${k_\rho^{\mathrm{TM}_z}}^2 = {k_x^{\mathrm{TM}_z}}^2 + {k_y^{\mathrm{TM}_z}}^2$ is the square of the TM_z transverse wave number. This relation has a form similar to that of (B.1).

Next, another relation can be established in the following manner. Substituting $\tilde{H}_y$ obtained from (B.7c) into (B.7e) yields

$$\frac{d\tilde{E}_x}{dz} + \left[-jk_x^{\mathrm{TM}_z} + j\frac{{k^{\mathrm{TM}_z}}^2}{k_x^{\mathrm{TM}_z}}\right]\tilde{E}_z = -j\omega\mu_\rho\frac{k_y^{\mathrm{TM}_z}}{k_x^{\mathrm{TM}_z}}\tilde{H}_x, \tag{B.9}$$

where

$$k^{\mathrm{TM}_z\,2} = \omega^2 \mu_\rho \varepsilon_z = k_\rho^{\mathrm{TM}_z\,2} + k_z^{\mathrm{TM}_z\,2} \tag{B.10}$$

is the square of the TM_z wave number and $k_z^{\mathrm{TM}_z}$ is the TM_z longitudinal wave number. Substitute $\tilde{E}_y$ from (B.7f) into (B.7d) and insert the resulting expression of $\tilde{H}_x$ into (B.9). This leads to the following relation

$$\left[\frac{k_\rho^{\mathrm{TM}_z\,2}}{k_x^{\mathrm{TM}_z\,2}}\right] \frac{d}{dz}\tilde{E}_x = j k_x^{\mathrm{TM}_z} \left[\frac{-k_z^{\mathrm{TM}_z\,2}}{k_x^{\mathrm{TM}_z\,2}}\right] \tilde{E}_z, \tag{B.11}$$

which also exhibits a form similar to that of (B.1).

An exact mapping with (B.1) is achieved by rewriting (B.8) and (B.11) as

$$\frac{d}{dz}\left[-\frac{k_\rho^{\mathrm{TM}_z\,2}}{k_x^{\mathrm{TM}_z\,2}}\tilde{E}_x\right] = -j\left(\frac{k_z^{\mathrm{TM}_z}}{\omega\varepsilon_z}\right) k_z^{\mathrm{TM}_z}\left[\frac{-\omega\varepsilon_z}{k_x^{\mathrm{TM}_z}}\tilde{E}_z\right], \tag{B.12a}$$

$$\frac{d}{dz}\left[-\frac{\omega\varepsilon_z}{k_x^{\mathrm{TM}_z}}\tilde{E}_z\right] = -j\left(\frac{\omega\varepsilon_\rho}{k_z^{\mathrm{TM}_z}}\right) k_z^{\mathrm{TM}_z}\left[-\frac{k_\rho^{\mathrm{TM}_z\,2}}{k_x^{\mathrm{TM}_z\,2}}\tilde{E}_x\right], \tag{B.12b}$$

where the TM_z equivalent transmission line parameters are identified as

$$\tilde{V}^{\mathrm{TM}_z} = -\frac{k_\rho^{\mathrm{TM}_z\,2}}{k_x^{\mathrm{TM}_z\,2}}\tilde{E}_x, \tag{B.13a}$$

$$\tilde{I}^{\mathrm{TM}_z} = -\frac{\omega\varepsilon_z}{k_x^{\mathrm{TM}_z}}\tilde{E}_z, \tag{B.13b}$$

$$Z^{\mathrm{TM}_z} = \frac{k_z^{\mathrm{TM}_z}}{\omega\varepsilon_z}, \tag{B.13c}$$

$$Y^{\mathrm{TM}_z} = \frac{\omega\varepsilon_\rho}{k_z^{\mathrm{TM}_z}}, \tag{B.13d}$$

where $\tilde{V}^{\mathrm{TM}_z}$, $\tilde{I}^{\mathrm{TM}_z}$, Z^{TM_z} and Y^{TM_z} are the TM^z spectral voltage, current, impedance and admittance, respectively. Inserting (B.13) in (B.5) yields then

$$\beta_z^{\mathrm{TM}_z} = \sqrt{Z^{\mathrm{TM}_z} Y^{\mathrm{TM}_z}} k_z^{\mathrm{TM}_z} = \sqrt{\frac{\varepsilon_\rho}{\varepsilon_z}} k_z^{\mathrm{TM}_z}. \tag{B.14a}$$

$$Z_c^{\mathrm{TM}_z} = \sqrt{\frac{Z^{\mathrm{TM}_z}}{Y^{\mathrm{TM}_z}}} = \frac{k_z^{\mathrm{TM}_z}}{\omega\sqrt{\varepsilon_\rho \varepsilon_z}} = \frac{k_z^{\mathrm{TM}_z}}{\omega\varepsilon_\rho} \sqrt{\frac{\varepsilon_\rho}{\varepsilon_z}}, \tag{B.14b}$$

where $\beta^{\mathrm{TM}_z}$and $Z_c^{\mathrm{TM}_z}$ are the TM_z propagation constant and characteristic impedance, respectively. It may be verified that substitution of $\varepsilon_\rho = \varepsilon_z = \varepsilon$ and $\mu_\rho = \mu_z = \mu$ in (B.12) reduces to the TM_z transmission line model of an isotropic medium [75].

B.1.2 TE_z Modes

The TE_z ($E_z = 0$) transmission line parameters are obtained by a dual approach as that used in Sec. B.1.1 for the TM_z parameters. The TE_z spectral Maxwell equations read

$$jk_y^{\mathrm{TE}_z} \tilde{H}_z - \frac{d\tilde{H}_y}{dz} = j\omega\varepsilon_\rho \tilde{E}_x, \tag{B.15a}$$

$$\frac{d\tilde{H}_x}{dz} - jk_x^{\mathrm{TE}_z} \tilde{H}_z = j\omega\varepsilon_\rho \tilde{E}_y, \tag{B.15b}$$

$$jk_x^{\mathrm{TE}_z} \tilde{H}_y - jk_y^{\mathrm{TE}_z} \tilde{H}_x = 0, \tag{B.15c}$$

$$-\frac{d\tilde{E}_y}{dz} = -j\omega\mu_\rho \tilde{H}_x, \tag{B.15d}$$

$$\frac{d\tilde{E}_x}{dz} = -j\omega\mu_\rho \tilde{H}_y, \tag{B.15e}$$

$$jk_x^{\mathrm{TE}_z} \tilde{E}_y - jk_y^{\mathrm{TE}_z} \tilde{E}_x = -j\omega\mu_z \tilde{H}_z. \tag{B.15f}$$

Here, we seek a relation between $\tilde{H}_z$ and $\tilde{H}_x$ (or, equivalently, $\tilde{H}_y$) only, by eliminating all the other field components. First, derive (B.15f) with respect to z, substitute (B.15d) and

(B.15e) into the resulting equation, and eliminate $\tilde{H}_y$ by using (B.15c), which yields

$$\frac{\mu_\rho}{\mu_z}\left(k_\rho^{\mathrm{TE}_z 2}\right)\tilde{H}_x = jk_x^{\mathrm{TE}_z}\frac{d\tilde{H}_z}{dz}, \tag{B.16}$$

where $k_\rho^{\mathrm{TE}_z 2} = k_x^{\mathrm{TE}_z 2} + k_y^{\mathrm{TE}_z 2}$ is the square of the TE_z transverse wave number, which constitutes the first of the two sought relations of the same form as (B.1). The other relation is obtained as follows. Substituting $\tilde{E}_y$ obtained from (B.15f) in (B.15b) yields

$$\frac{d\tilde{H}_x}{dz} + \left[-jk_x^{\mathrm{TE}_z} + j\frac{k^{\mathrm{TE}_z 2}}{k_x^{\mathrm{TE}_z}}\right]\tilde{H}_z = j\omega\varepsilon_\rho\frac{k_y^{\mathrm{TE}_z}}{k_x^{\mathrm{TE}_z}}\tilde{E}_x, \tag{B.17}$$

where

$$k^{\mathrm{TE}_z 2} = \omega^2\mu_z\varepsilon_\rho = k_\rho^{\mathrm{TE}_z 2} + k_z^{\mathrm{TE}_z 2} \tag{B.18}$$

is the square of the TE_z wave number and $k_z^{\mathrm{TE}_z}$ is the TE_z longitudinal wave number. Substitute $\tilde{H}_y$ from (B.15c) into (B.15a) and insert the resulting expression of $\tilde{E}_x$ into (B.17). This leads to the following relation

$$\left[\frac{k_\rho^{\mathrm{TE}_z 2}}{k_x^{\mathrm{TE}_z 2}}\right]\frac{d}{dz}\tilde{H}_x = jk_x^{\mathrm{TE}_z}\left[\frac{-k_z^{\mathrm{TE}_z 2}}{k_x^{\mathrm{TE}_z 2}}\right]\tilde{H}_z. \tag{B.19}$$

An exact mapping with (B.1) is achieved by rewriting (B.16) and (B.19) as

$$\frac{d}{dz}\left[\frac{-\omega\mu_z}{k_y}\tilde{H}_z\right] = -j\left(\frac{\omega\mu_\rho}{k_z^{\mathrm{TE}_z}}\right)k_z^{\mathrm{TE}_z}\left[\frac{-k_\rho^{\mathrm{TE}_z 2}}{k_x^{\mathrm{TE}_z}k_y^{\mathrm{TE}_z}}\tilde{H}_x\right], \tag{B.20a}$$

$$\frac{d}{dz}\left[\frac{-k_\rho^{\mathrm{TE}_z 2}}{k_x^{\mathrm{TE}_z}k_y^{\mathrm{TE}_z}}\tilde{H}_x\right] = -j\left(\frac{k_z^{\mathrm{TE}_z}}{\omega\mu_z}\right)k_z^{\mathrm{TE}_z}\left[\frac{-\omega\mu_z}{k_y^{\mathrm{TE}_z}}\tilde{H}_z\right], \tag{B.20b}$$

where the TE_z equivalent transmission line parameters are identified as

$$\tilde{V}^{\mathrm{TE}_z} = \frac{-\omega\mu_z}{k_y^{\mathrm{TE}_z}}\tilde{H}_z, \tag{B.21a}$$

$$\tilde{I}^{\mathrm{TE}_z} = \frac{-{k_\rho^{\mathrm{TE}_z}}^2}{k_x^{\mathrm{TE}_z} k_y^{\mathrm{TE}_z}} \tilde{H}_x, \tag{B.21b}$$

$$Z^{\mathrm{TE}_z} = \frac{\omega \mu_\rho}{k_z^{\mathrm{TE}_z}}, \tag{B.21c}$$

$$Y^{\mathrm{TE}_z} = \frac{k_z^{\mathrm{TE}_z}}{\omega \mu_z}, \tag{B.21d}$$

where $\tilde{V}^{\mathrm{TE}_z}$, $\tilde{I}^{\mathrm{TE}_z}$, Z^{TE_z} and Y^{TE_z} are the TE^z spectral voltage, current, impedance and admittance, respectively. Inserting (B.21) yields then

$$\beta_z^{\mathrm{TE}_z} = \sqrt{Z^{\mathrm{TE}_z} Y^{\mathrm{TE}_z}} k_z^{\mathrm{TE}_z} = \sqrt{\frac{\mu_\rho}{\mu_z}} k_z^{\mathrm{TE}_z}, \tag{B.22a}$$

$$Z_c^{\mathrm{TE}_z} = \sqrt{\frac{Z^{\mathrm{TE}_z}}{Y^{\mathrm{TE}_z}}} = \frac{\omega \sqrt{\mu_z \mu_\rho}}{k_z^{\mathrm{TE}_z}} = \frac{\omega \mu_z}{k_z^{\mathrm{TE}_z}} \sqrt{\frac{\mu_\rho}{\mu_z}}, \tag{B.22b}$$

where $\beta^{\mathrm{TE}_z}$and $Z_c^{\mathrm{TE}_z}$ are the TE_z propagation constant and characteristic impedance, respectively. It may be verified that substitution of $\varepsilon_\rho = \varepsilon_z = \varepsilon$ and $\mu_\rho = \mu_z = \mu$ in B.20 reduces to the TE_z transmission line model of an isotropic medium [75].

B.2 Horizontal Infinitesimal Electric Dipole Source

The transmission line parameters $\tilde{V}$, $\tilde{I}$, Z and Y for the TM_z and TE_z modes in the anisotropic medium of Fig. 3.1 excited by a horizontal current source $\mathbf{J} = J_x \mathbf{a}_x$, will be determined by inserting the tensors of (3.1) into Maxwell equations,

$$\nabla \times \mathbf{H} = j\omega \bar{\bar{\varepsilon}} \mathbf{E} + \mathbf{J}, \tag{B.23a}$$

$$\nabla \times \mathbf{E} = -j\omega \bar{\bar{\mu}} \mathbf{H}, \tag{B.23b}$$

and by manipulating the resulting equations so as to obtain two final equations with the form

of

$$\frac{d\tilde{V}}{dz} = -jZk_z\tilde{I}, \tag{B.24a}$$

$$\frac{d\tilde{I}}{dz} = -jYk_z\tilde{V} + \tilde{I}_{\mathrm{g}}, \tag{B.24b}$$

where $\tilde{I}_{\mathrm{g}}$ is the current source transmission-line model of the horizontal electric dipole $\mathbf{J} = J_x\mathbf{a}_x$ as seen in Figs. 4.1a and 4.1b.

B.2.1 TM$_z$ Modes

Inserting (3.1) into (B.23) for the TM$_z$ modes ($H_z = 0$) and writing the resulting equations in the spectral domain, using the transformations $\partial/\partial x \rightarrow jk_x^{\mathrm{TM}_z}$ and $\partial/\partial y \rightarrow jk_y^{\mathrm{TM}_z}$, assuming a horizontal electric infinitesimal dipole $\tilde{\mathbf{J}} = 1/2\pi\delta(z - z')\mathbf{a}_x$, and following the approach similar to the one used in Sec.B.1.1 yields the TM$_z$ transmission line equations in the form of (B.24) as follows

$$\frac{d}{dz}\left[\frac{-\omega\varepsilon_z}{k_x^{\mathrm{TM}_z}}\tilde{G}_{\mathrm{EJ}}^{zx,\mathrm{TM}_z}\right] = -\,j\left(\frac{\omega\varepsilon_\rho}{k_z^{\mathrm{TM}_z}}\right)k_z^{\mathrm{TM}_z}\left[\frac{-{k_\rho}^2}{{k_x^{\mathrm{TM}_z}}^2}\tilde{G}_{\mathrm{EJ}}^{xx,\mathrm{TM}_z}\right] + \tilde{J}_x, \tag{B.25a}$$

$$\frac{d}{dz}\left[\frac{-{k_\rho^{\mathrm{TM}_z}}^2}{{k_x^{\mathrm{TM}_z}}^2}\tilde{G}_{\mathrm{EJ}}^{xx,\mathrm{TM}_z}\right] = -\,j\left(\frac{k_z^{\mathrm{TM}_z}}{\omega\varepsilon_z}\right)k_z\left[\frac{-\omega\varepsilon_z}{k_x^{\mathrm{TM}_z}}\tilde{G}_{\mathrm{EJ}}^{zx,\mathrm{TM}_z}\right], \tag{B.25b}$$

where $\tilde{G}_{\mathrm{EJ}}^{xx,\mathrm{TM}_z}$ and $\tilde{G}_{\mathrm{EJ}}^{zx,\mathrm{TM}_z}$ are the spectral domain electric field Green functions along the x and z axes, respectively, produced by the electric source along the x axis, and similar to Sec. B.1.1, $k_z^{\mathrm{TM}_z}$ is the longitudinal wave number, ${k_\rho^{\mathrm{TM}_z}}^2 = {k_x^{\mathrm{TM}_z}}^2 + {k_y^{\mathrm{TM}_z}}^2$ is the square of the transverse wave number and ${k_\rho^{\mathrm{TM}_z}}^2 + {k_z^{\mathrm{TM}_z}}^2 = \omega^2\mu_\rho\varepsilon_z = {k^{\mathrm{TM}_z}}^2$, where k^{TM_z} is the TM$_z$ wave number. The analogy of the equivalent transmission line model of (B.25) with (B.24) results in

$$V^{\mathrm{TM}_z} = -\frac{k_\rho^2}{k_x^2}\tilde{G}_{\mathrm{EJ}}^{xx}, \tag{B.26a}$$

$$I^{\mathrm{TM}_z} = -\frac{\omega\varepsilon_z}{k_x}\tilde{G}_{\mathrm{EJ}}^{zx}, \tag{B.26b}$$

$$Z^{\mathrm{TM}_z} = \frac{k_z^{\mathrm{TM}_z}}{\omega\varepsilon_z}, \tag{B.26c}$$

$$Y^{\mathrm{TM}_z} = \frac{\omega\varepsilon_\rho}{k_z^{\mathrm{TM}_z}}, \tag{B.26d}$$

$$I_g^{\mathrm{TM}_z} = \frac{1}{2\pi}, \tag{B.26e}$$

From (B.26a) and (B.26b) the TM_z modes electric field Green functions for the horizontal source are calculated as follows

$$\tilde{G}_{\mathrm{EJ}}^{xx,\mathrm{TM}_z} = \frac{-{k_x^{\mathrm{TM}_z}}^2}{{k_\rho^{\mathrm{TM}_z}}^2}\tilde{V}^{\mathrm{TM}_z}, \tag{B.27a}$$

$$\tilde{G}_{\mathrm{EJ}}^{zx,\mathrm{TM}_z} = \frac{-k_x^{\mathrm{TM}_z}}{\omega\varepsilon_z}\tilde{I}^{\mathrm{TM}_z}, \tag{B.27b}$$

while $Z_c^{\mathrm{TM}_z} = k_z^{\mathrm{TM}_z}/(\omega\varepsilon_\rho)\sqrt{\varepsilon_\rho/\varepsilon_z}$ and $\beta^{\mathrm{TM}_z} = \sqrt{\varepsilon_\rho/\varepsilon_z}k_z^{\mathrm{TM}_z}$.

The magnetic Green functions are computed from substituting (B.27) into spectral domain Maxwell equations as follows

$$\tilde{G}_{\mathrm{HJ}}^{xx,\mathrm{TM}_z} = \frac{k_x^{\mathrm{TM}_z}k_y^{\mathrm{TM}_z}}{{k_\rho^{\mathrm{TM}_z}}^2}\tilde{I}^{\mathrm{TM}_z}, \tag{B.28a}$$

$$\tilde{G}_{\mathrm{HJ}}^{zx,\mathrm{TM}_z} = 0. \tag{B.28b}$$

Substituting $\varepsilon_\rho = \varepsilon_z = \varepsilon$ and $\mu_\rho = \mu_z = \mu$ in the above equations reduces them to the transmission-line model and Green functions of an isotropic medium [75].

B.2.2 TE$_z$ Modes

The TE$_z$ ($E_z = 0$) transmission line model is obtained by an approach dual to that used in Sec. B.1.1 used for the TM$_z$ parameters. The resulting equations are

$$\frac{d}{dz}\left[\frac{-{k_\rho^{\mathrm{TE}_z}}^2}{k_x^{\mathrm{TE}_z}k_y^{\mathrm{TE}_z}}\tilde{G}_{\mathrm{HJ}}^{xx,\mathrm{TE}_z}\right] = -\,j\left(\frac{k_z^{\mathrm{TE}_z}}{\omega\mu_z}\right)k_z^{\mathrm{TE}_z}\left[\frac{-\omega\mu_z}{k_y^{\mathrm{TE}_z}}\tilde{G}_{\mathrm{HJ}}^{zx,\mathrm{TE}_z}\right] + \tilde{J}_x, \tag{B.29a}$$

$$\frac{d}{dz}\left[\frac{-\omega\mu_z}{k_y^{\mathrm{TE}_z}}\tilde{G}_{\mathrm{HJ}}^{zx,\mathrm{TE}_z}\right] = -\,j\left(\frac{\omega\mu_\rho}{k_z^{\mathrm{TE}_z}}\right)k_z^{\mathrm{TE}_z}\left[\frac{-{k_\rho^{\mathrm{TE}_z}}^2}{k_x^{\mathrm{TE}_z}k_y^{\mathrm{TE}_z}}\tilde{G}_{\mathrm{HJ}}^{xx,\mathrm{TE}_z}\right], \tag{B.29b}$$

where $\tilde{G}_{\mathrm{HJ}}^{xx,\mathrm{TE}_z}$ and $\tilde{G}_{\mathrm{HJ}}^{zx,\mathrm{TE}_z}$ are the spectral domain magnetic field Green functions along the x and z axes, respectively, produced by the electric source along the x axis, and the same as Sec. B.1.2, $k_z^{\mathrm{TE}_z}$ is the longitudinal wave number, ${k_\rho^{\mathrm{TE}_z}}^2 = {k_x^{\mathrm{TE}_z}}^2 + {k_y^{\mathrm{TE}_z}}^2$ is the square of the transverse wave number and ${k_\rho^{\mathrm{TE}_z}}^2 + {k_z^{\mathrm{TE}_z}}^2 = \omega^2\mu_z\varepsilon_\rho = {k^{\mathrm{TE}_z}}^2$, where k^{TE_z} is the TE$_z$ wave number. The analogy of the equivalent transmission line model of (B.29) and (B.24) leads to

$$I^{\mathrm{TE}_z} = -\frac{k_\rho^2}{k_x k_y}\tilde{G}_{\mathrm{HJ}}^{xx}, \tag{B.30a}$$

$$V^{\mathrm{TE}_z} = -\frac{\omega\mu_z}{k_y}\tilde{G}_{\mathrm{HJ}}^{zx}, \tag{B.30b}$$

$$Z^{\mathrm{TE}_z} = \frac{\omega\mu_\rho}{k_z^{\mathrm{TE}_z}}, \tag{B.30c}$$

$$Y^{\mathrm{TE}_z} = \frac{k_z^{\mathrm{TE}_z}}{\omega\mu_z}, \tag{B.30d}$$

$$I_g^{\mathrm{TE}_z} = \frac{1}{2\pi}. \tag{B.30e}$$

From (B.30a) and (B.30b), the TE$_z$ modes magnetic field Green functions for the horizontal source, are calculated as follows

$$\tilde{G}_{\mathrm{HJ}}^{xx,\mathrm{TE}_z} = -\frac{k_x^{\mathrm{TE}_z}k_y^{\mathrm{TE}_z}}{{k_\rho^{\mathrm{TE}_z}}^2}\tilde{I}^{\mathrm{TE}_z}, \tag{B.31a}$$

$$\tilde{G}_{\mathrm{HJ}}^{zx,\mathrm{TE}_z} = -\frac{k_y^{\mathrm{TE}_z}}{\omega\mu_z}\tilde{V}^{\mathrm{TE}_z}, \tag{B.31b}$$

while $Z_c^{\mathrm{TE}_z} = \omega\mu_z/k_z^{\mathrm{TE}_z}\sqrt{\mu_\rho/\mu_z}$ and $\beta^{\mathrm{TE}_z} = \sqrt{\mu_\rho/\mu_z}k_z^{\mathrm{TE}_z}$. The electric Green functions are computed by substituting (B.31) into spectral domain Maxwell equations as follows

$$\tilde{G}_{\mathrm{EJ}}^{xx,\mathrm{TE}_z} = -\frac{{k_y^{\mathrm{TE}_z}}^2}{{k_\rho^{\mathrm{TE}_z}}^2}\tilde{V}^{\mathrm{TE}_z}, \tag{B.32a}$$

$$\tilde{G}_{\mathrm{EJ}}^{zx,\mathrm{TE}_z} = 0. \tag{B.32b}$$

Substituting $\varepsilon_\rho = \varepsilon_z = \varepsilon$ and $\mu_\rho = \mu_z = \mu$ in the above equations reduces them to the transmission-line model and Green functions of an isotropic medium [75].

B.3 Vertical Infinitesimal Electric Dipole Source

A vertical electric dipole source along the z axis $\mathbf{J} = J_z\mathbf{a}_z$ only excites the TM_z modes of the structure. The TE_z modes cannot be excited by this source since they have no electric field component along the z axis ($E_z = 0$). Therefore, in the following only the TM_z modes are considered.

The equivalent transmission-line parameters of the structure (Fig. 3.1) will be determined by inserting the tensors of (3.1) into Maxwell equations expressed in (B.23) with $\mathbf{J} = J_z\mathbf{a}_z$. For this purpose, similar to the case of a horizontal source on the anisotropic substrate, explained in Sec.B.2, a spectral domain transformation is applied to the Maxwell equations, where the spectral domain infinitesimal vertical electric dipole source reads $\tilde{\mathbf{J}} = 1/(2\pi)\delta(z-z')\mathbf{a}_z$. For the purpose of achieving the transmission-line models of the structure, we may follow the same procedure as in Sec.B.2.1, which leads to

$$\begin{aligned}\frac{\partial}{\partial z}\left[-\frac{\omega\varepsilon_z}{k_y^{\mathrm{TM}_z}}\tilde{G}_{\mathrm{EJ}}^{zz,\mathrm{TM}_z}\right] = &-j\left(\frac{\omega\varepsilon_\rho}{k_z^{\mathrm{TM}_z}}\right)k_z^{\mathrm{TM}_z}\left[-\frac{{k_\rho^{\mathrm{TM}_z}}^2}{k_x^{\mathrm{TM}_z}k_y^{\mathrm{TM}_z}}\tilde{G}_{\mathrm{EJ}}^{xz,\mathrm{TM}_z}\right]+\\ &\left[-\frac{j}{k_y^{\mathrm{TM}_z}}\frac{\partial}{\partial z}\left(\frac{1}{2\pi}\delta(z-z')\right)\right],\end{aligned} \tag{B.33a}$$

$$\frac{\partial}{\partial z}\left[-\frac{{k_\rho^{\mathrm{TM}_z}}^2}{k_x^{\mathrm{TM}_z}k_y^{\mathrm{TM}_z}}\tilde{G}_{\mathrm{EJ}}^{xz,\mathrm{TM}_z}\right]=-j\left(\frac{k_z^{\mathrm{TM}_z}}{\omega\varepsilon_z}\right)k_z^{\mathrm{TM}_z}\left[\frac{-\omega\varepsilon_z}{k_y^{\mathrm{TM}_z}}\tilde{G}_{\mathrm{EJ}}^{zz,\mathrm{TM}_z}\right]+\frac{\omega\mu_\rho}{k_y^{\mathrm{TM}_z}}\frac{1}{2\pi}\delta(z-z'), \tag{B.33b}$$

where $\tilde{G}_{\mathrm{EJ}}^{xz,\mathrm{TM}_z}$ and $\tilde{G}_{\mathrm{EJ}}^{zz,\mathrm{TM}_z}$ are the electric field Green functions along the x and z axes produced by the source along the z axis. As seen in the (B.33a), the first order derivative of $\tilde{G}_{\mathrm{EJ}}^{zz,\mathrm{TM}_z}$ is associated with the derivative of the infinitesimal source $\tilde{\mathbf{J}}=1/(2\pi)\delta(z-z')\mathbf{a}_z$ with respect to z. Since the derivative of a dirac function is undefined, the above equation does not lead to any physically meaningful model. Therefore, we further manipulate (B.33) in order to achieve the following transmission-line equation

$$\frac{d^2\tilde{V}}{dz^2}+ZYk_z^2\tilde{V}=\frac{dV_{\mathrm{g}}}{dz}, \tag{B.34}$$

where the derivative of the series voltage source V_{g} with respect to the z axis is associated to the *second* derivative of the voltage [100], where the solution of the above equation for the case of a dirac source is physical.

For obtaining the transmission-line model in the form of (B.34), we derive the both sides of (B.33b) with respect to z and then substitute $\partial/\partial z\left[-\omega\varepsilon_z/k_y^{\mathrm{TM}_z}\tilde{G}_{\mathrm{EJ}}^{zz,\mathrm{TM}_z}\right]$ form (B.33a) into the resulting equation. Further multiplying the both sides by $k_y^{\mathrm{TM}_z}/\omega\mu_\rho$ and simplifying the equation yields

$$\begin{aligned}\frac{\partial^2}{\partial z^2}\left[-\frac{{k_\rho^{\mathrm{TM}_z}}^2}{\omega\mu_\rho k_x^{\mathrm{TM}_z}}\tilde{G}_{\mathrm{EJ}}^{xz,\mathrm{TM}_z}\right]=&-\left(\frac{\varepsilon_\rho}{\varepsilon_z}\right){k_z^{\mathrm{TM}_z}}^2\left[-\frac{{k_\rho^{\mathrm{TM}_z}}^2}{\omega\mu_\rho k_x^{\mathrm{TM}_z}}\tilde{G}_{\mathrm{EJ}}^{xz,\mathrm{TM}_z}\right]+\\&\left[1-\left(\frac{{k_z^{\mathrm{TM}_z}}^2}{\omega^2\mu_\rho\varepsilon_z}\right)\right]\frac{\partial}{\partial z}\frac{1}{2\pi}\delta(z-z').\end{aligned} \tag{B.35}$$

Substituting $\left[1-\left({k_z^{\mathrm{TM}_z}}^2/\omega^2\mu_\rho\varepsilon_z\right)\right]={k_\rho^{\mathrm{TM}_z}}^2/\omega^2\mu_\rho\varepsilon_z$ into (B.35) and multiplying the both sides of the resulting equation by $\omega^2\mu_\rho\varepsilon_z/{k_\rho^{\mathrm{TM}_z}}^2$ transforms (B.35) to

$$\frac{\partial^2}{\partial z^2}\left[-\frac{\omega\varepsilon_z}{k_x^{\mathrm{TM}_z}}\tilde{G}_{\mathrm{EJ}}^{xz,\mathrm{TM}_z}\right]=-\left(\frac{\varepsilon_\rho}{\varepsilon_z}\right){k_z^{\mathrm{TM}_z}}^2\left[-\frac{\omega\varepsilon_z}{k_x^{\mathrm{TM}_z}}\tilde{G}_{\mathrm{EJ}}^{xz,\mathrm{TM}_z}\right]+\frac{\partial}{\partial z}\left(\frac{1}{2\pi}\delta(z-z')\right), \tag{B.36}$$

which is in the form of (B.34).

To obtain the relation between $\tilde{G}_{\mathrm{EJ}}^{zz,\mathrm{TM}_z}$ and $\tilde{G}_{\mathrm{EJ}}^{xz,\mathrm{TM}_z}$, in the form of a transmission-line

equation, we use the spectral domain Maxwell equations and we manipulate them so as to find the following source-less spectral domain transmission-line model

$$\frac{d\tilde{V}}{dz} = -jZ^{\mathrm{TM}_z} k_z^{\mathrm{TM}_z} \tilde{I}, \tag{B.37}$$

which leads to

$$\frac{\partial}{\partial z}\left[-\frac{\omega\varepsilon_z}{k_x^{\mathrm{TM}_z}}\tilde{G}_{\mathrm{EJ}}^{xz,\mathrm{TM}_z}\right] = -j\left(\frac{k_z^{\mathrm{TM}_z}}{\omega\varepsilon_z}\right) k_z^{\mathrm{TM}_z}\left[-\frac{\omega^2\varepsilon_z^2}{{k_\rho^{\mathrm{TM}_z}}^2}\tilde{G}_{\mathrm{EJ}}^{zz,\mathrm{TM}_z}\right]. \tag{B.38}$$

In summary, the spectral transmission-line models for a vertical source along the z axis, are found as

$$\frac{d^2}{dz^2}\left[\frac{-\omega\varepsilon_z}{k_x^{\mathrm{TM}_z}}\tilde{G}_{\mathrm{EJ}}^{xz,\mathrm{TM}_z}\right] = -\frac{\varepsilon_\rho}{\varepsilon_z}{k_z^{\mathrm{TM}_z}}^2\left[\frac{-\omega\varepsilon_z}{k_x^{\mathrm{TM}_z}}\tilde{G}_{\mathrm{EJ}}^{xz,\mathrm{TM}_z}\right] + \frac{d}{dz}\tilde{J}_z, \tag{B.39a}$$

$$\frac{d}{dz}\left[\frac{-\omega\varepsilon_z}{k_x^{\mathrm{TM}_z}}\tilde{G}_{\mathrm{EJ}}^{xz,\mathrm{TM}_z}\right] = -j\frac{k_z^{\mathrm{TM}_z}}{\omega\varepsilon_z}k_z^{\mathrm{TM}_z}\left[\frac{-\omega^2\varepsilon_z^2}{{k_\rho^{\mathrm{TM}_z}}^2}\tilde{G}_{\mathrm{EJ}}^{zz,\mathrm{TM}_z}\right], \tag{B.39b}$$

which by their mapping to the transmission line equations (B.34) and (B.37), the transmission-line elements are found as follows

$$\tilde{V}^{\mathrm{TM}_z} = -\frac{\omega\varepsilon_z}{k_x^{\mathrm{TM}_z}}\tilde{G}_{\mathrm{EJ}}^{xz,\mathrm{TM}_z}, \tag{B.40a}$$

$$\tilde{I}^{\mathrm{TM}_z} = -\frac{\omega^2\varepsilon_z^2}{{k_\rho^{\mathrm{TM}_z}}^2}\tilde{G}_{\mathrm{EJ}}^{zz,\mathrm{TM}_z}, \tag{B.40b}$$

$$Z^{\mathrm{TM}_z}Y^{\mathrm{TM}_z} = -\left(\frac{\varepsilon_\rho}{\varepsilon_z}\right), \tag{B.40c}$$

$$V_g^{\mathrm{TM}_z} = \frac{1}{2\pi}. \tag{B.40d}$$

From (B.40a) and (B.40b) the TM_z electric field Green functions for the vertical source are calculated as follows

$$\tilde{G}_{\mathrm{EJ}}^{xz,\mathrm{TM}_z} = -\frac{k_x^{\mathrm{TM}_z}}{\omega\varepsilon_z}\tilde{V}^{\mathrm{TM}_z}, \tag{B.41a}$$

$$\tilde{G}_{\mathrm{EJ}}^{zz,\mathrm{TM}_z} = -\frac{{k_\rho^{\mathrm{TM}_z}}^2}{\omega^2 \varepsilon_z^2} \tilde{I}^{\mathrm{TM}_z}. \tag{B.41b}$$

The relevant magnetic field Green function components are obtained by substituting (B.41) into Maxwell equations which yields

$$\tilde{G}_{\mathrm{HJ}}^{xz,TM_z} = \frac{k_y^{\mathrm{TM}_z}}{\omega \varepsilon_z} \tilde{I}^{\mathrm{TM}_z}, \tag{B.42a}$$

$$\tilde{G}_{\mathrm{HJ}}^{zz,\mathrm{TM}_z} = 0. \tag{B.42b}$$

Appendix C

Computation of the Radiation Efficiency of a Horizontal Infinitesimal Dipole on an Isotropic Substrate

As seen in Sec. 4.3.1, the computation of the radiation efficiency of the horizontal infinitesimal dipole on a grounded and ungrounded substrates requires the computation the radiated ($\mathbf{S}_{\text{rad,av}}$) and surface-wave ($\mathbf{S}_{\text{sw,av}}$) time-averaged Poynting vectors. For this purpose, we derive here the electric field, $\mathbf{E}$, and magnetic field,$\mathbf{H}$, from which the Poynting vectors will follow as $\mathbf{S}_{\text{rad/sw,av}} = \frac{1}{2}\text{Re}[\mathbf{E} \times \mathbf{H}^*]$. The fields can be calculated from the spectral-domain Green functions of the structure.

C.1 Spectral Domain Green Functions

In a multilayered structure, the Green functions in each layer may be computed using a transmission-line model. Assuming the harmonic time dependence $\exp(+j\omega t)$, the transmission-line models for the TM_z and TE_z modes are obtained via a transverse spectral-domain transformation. The substitutions $\partial/\partial x \rightarrow jk_x^{\text{TM}_z}$ and $\partial/\partial y \rightarrow jk_y^{\text{TM}_z}$ associated with this transformation into Maxwell equations,

$$\nabla \times \mathbf{H} = j\omega\varepsilon\mathbf{E} + \mathbf{J}, \quad \nabla \times \mathbf{E} = -j\omega\mu_0\mathbf{H}, \tag{C.1}$$

with the spectral horizontal electric point source $\tilde{\mathbf{J}} = (1/2\pi)\delta(z - z')\hat{\mathbf{x}}$ (positioned at $x' = y' = 0$) yields the transmission-line (Figs. 4.1b and 4.2b) system of equations [75]

$$\frac{d\tilde{I}^i}{dz} = -jY^i k_z^i \tilde{V}^i + \tilde{I}_g, \quad \frac{d\tilde{V}^i}{dz} = -jZ^i k_z^i \tilde{I}^i, \tag{C.2}$$

where $\tilde{V}^i$, $\tilde{I}^i$, Z^i, Y^i, $\tilde{I}_{\text{g}}$ and k_z^i are the spectral-domain voltage and current, impedance, admittance, current source and the wave number along the z axis of the transmission line, respectively, for $i \equiv \text{TM}_z/\text{TE}_z$. The corresponding characteristic impedance, $Z_c^i = \sqrt{Z^i/Y^i}$, and propagation constant, $\beta^i = \sqrt{Z^i Y^i} k_z^i$, directly follow from these equations.

C.1.1 Field Green Functions

The TM_z-mode ($H_z = 0$) electric field Green functions are found as

$$\tilde{G}_{\mathrm{EJ}}^{xx,\mathrm{TM}_z} = \frac{-{k_x^{\mathrm{TM}_z}}^2}{{k_\rho^{\mathrm{TM}_z}}^2}\tilde{V}^{\mathrm{TM}_z},\ \tilde{G}_{\mathrm{EJ}}^{zx,\mathrm{TM}_z} = \frac{-k_x^{\mathrm{TM}_z}}{\omega\varepsilon}\tilde{I}^{\mathrm{TM}_z}, \tag{C.3}$$

where $Z_c^{\mathrm{TM}_z} = k_z^{\mathrm{TM}_z}/(\omega\varepsilon)$ and $\beta^{\mathrm{TM}_z} = k_z^{\mathrm{TM}_z}$. In these expressions, $\tilde{G}_{EJ}^{xx,\mathrm{TM}_z}$ and $\tilde{G}_{\mathrm{EJ}}^{zx,\mathrm{TM}_z}$ are the spectral electric field Green function x and z components, respectively, due to an x-directed electric source, $k_z^{\mathrm{TM}_z}$ is the longitudinal wave number, ${k_\rho^{\mathrm{TM}_z}}^2 = {k_x^{\mathrm{TM}_z}}^2 + {k_y^{\mathrm{TM}_z}}^2$ is the square of the transverse wave number and ${k^{\mathrm{TM}_z}}^2 = {k_\rho^{\mathrm{TM}_z}}^2 + {k_z^{\mathrm{TM}_z}}^2 = \omega^2\mu_0\varepsilon$ is the TM_z wave number in the layer considered.

The magnetic field Green functions are then obtained by substituting (C.3) into spectral-domain Maxwell equations as

$$\tilde{G}_{\mathrm{HJ}}^{xx,TM_z} = \frac{k_x^{\mathrm{TM}_z}k_y^{\mathrm{TM}_z}}{{k_\rho^{\mathrm{TM}_z}}^2}\tilde{I}^{\mathrm{TM}_z},\ \tilde{G}_{\mathrm{HJ}}^{zx,\mathrm{TM}_z} = 0. \tag{C.4}$$

Similarly, the TE_z-mode ($E_z = 0$) magnetic field and electric field Green functions are found as

$$\tilde{G}_{\mathrm{HJ}}^{xx,\mathrm{TE}_z} = -\frac{k_x^{\mathrm{TE}_z}k_y^{\mathrm{TE}_z}}{{k_\rho^{\mathrm{TE}_z}}^2}\tilde{I}^{\mathrm{TE}_z},\ \tilde{G}_{\mathrm{HJ}}^{zx,\mathrm{TE}_z} = -\frac{k_y^{\mathrm{TE}_z}}{\omega\mu_0}\tilde{V}^{\mathrm{TE}_z}, \tag{C.5}$$

and

$$\tilde{G}_{\mathrm{EJ}}^{xx,\mathrm{TE}_z} = -\frac{{k_y^{\mathrm{TE}_z}}^2}{{k_\rho^{\mathrm{TE}_z}}^2}\tilde{V}^{\mathrm{TE}_z},\ \tilde{G}_{\mathrm{EJ}}^{zx,\mathrm{TE}_z} = 0, \tag{C.6}$$

where the definitions of the different terms are analogous to those of the TM_z case.

C.1.2 Vector Potential Green Functions

One of the possible choices for the vector potential Green functions is the Sommerfeld choice. In this choice, for an x-directed source, the electric vector potential Green function is $\bar{\bar{\mathbf{G}}}_{\mathrm{F}} = 0$ while the magnetic vector potential Green function is $\bar{\bar{\mathbf{G}}}_{\mathrm{A}} = (\mathbf{x}G_{\mathrm{A}}^{xx} + \mathbf{z}G_{\mathrm{A}}^{zx})\,\mathbf{x}$, where G_{A}^{xx} and G_{A}^{zx} are the x and z potential Green function components, respectively, due to $\tilde{J}_x$

[76]. Using [51],

$$\bar{\bar{\mathbf{G}}}_{\mathrm{HJ}} = \bar{\bar{\mu}}^{-1} \nabla \times \bar{\bar{\mathbf{G}}}_{\mathrm{A}}, \tag{C.7}$$

where $\bar{\bar{\mathbf{G}}}_{\mathrm{HJ}} = \bar{\bar{\mathbf{G}}}_{\mathrm{HJ}}^{\mathrm{TM}_z} + \bar{\bar{\mathbf{G}}}_{\mathrm{HJ}}^{\mathrm{TE}_z}$ is the total magnetic field Green functions with $\bar{\bar{\mathbf{G}}}_{\mathrm{HJ}}^{\mathrm{TM}_z}$ and $\bar{\bar{\mathbf{G}}}_{\mathrm{HJ}}^{\mathrm{TE}_z}$ obtained from (C.4) and (C.5), respectively, with $k_{\rho,x,y}^{\mathrm{TM}_z} = k_{\rho,x,y}^{\mathrm{TE}_z} = k_{\rho,x,y}$ due to phase matching. Substituting $\tilde{G}_{\mathrm{HJ}}^{xx,\mathrm{TM}_z}$ and $\tilde{G}_{\mathrm{HJ}}^{zx,\mathrm{TM}_z}$ from (C.4) and $\tilde{G}_{\mathrm{HJ}}^{xx,\mathrm{TE}_z}$ and $\tilde{G}_{\mathrm{HJ}}^{zx,\mathrm{TE}_z}$ from (C.5) into (C.7) finally yields

$$\tilde{G}_{\mathrm{A}}^{xx} = \frac{1}{j\omega} \tilde{V}^{\mathrm{TE}_z}, \tag{C.8a}$$

$$\tilde{G}_{\mathrm{A}}^{zx} = \frac{\mu_0}{jk_y} \left(\frac{k_x k_y}{k_\rho^2} \tilde{I}^{\mathrm{TM}_z} - \frac{k_x k_y}{k_\rho^2} \tilde{I}^{\mathrm{TE}_z} \right). \tag{C.8b}$$

C.2 Powers Computation

The radiated and surface-wave powers are computed from the vector potential Green functions in the spatial domain, which are obtained by inverse-Fourier-transforming their spectral-domain counterparts via (C.8) as

$$G_A(x,y,z) = \frac{1}{2\pi} \int_{-\infty}^{+\infty} \int_{-\infty}^{+\infty} \tilde{G}_{\mathrm{A}}(k_x k_y, z) e^{jk_x x} e^{jk_y y} \, dk_x \, dk_y. \tag{C.9}$$

From this expression, the far-field electric field radiated by an x-directed dipole is obtained as

$$\mathbf{E}(x,y,z) = -j\omega \overline{\overline{\mathbf{G}}}_{\mathrm{A}}(x,y,z) \cdot \mathbf{x}, \tag{C.10}$$

and the corresponding magnetic field is obtained via Maxwell equations.

C.2.1 Radiated Power

Since the dipole is assumed to be placed at the air-dielectric interface (at $z = 0$), the radiating spectral Green function dependence on the z axis is that of a purely spherical outgoing wave. Therefore, we have $\tilde{G}_{\mathrm{A}}(k_x, k_y, z) = \tilde{g}_{\mathrm{A}}(k_x, k_y) \exp(-jk_{\mathrm{z0}} z)$, where k_{z0} is the propagation constant along z in free space and $\tilde{g}_{\mathrm{A}}(k_x, k_y)$ is the spectral part in each of the equations (C.8) evaluated at the air-dielectric interface. Under the far-field ($k_\rho \rho \to \infty$ and

$k_0 r \to \infty$) asymptotic approximation [75, 101], the far-field Green function associated with the space wave (C.9) reduces to

$$G_{\mathrm{A}}(x,y,z) = jk_0 \cos\theta \tilde{g}_{\mathrm{A}}(k_x,k_y)\frac{\exp(-jk_0 r)}{r}, \tag{C.11}$$

where k_0 is the free-space wave number. Inserting this expression into (C.10), and computing the corresponding magnetic field from Maxwell equations, determines the Poynting vector $\mathbf{S}_{\mathrm{rad,av}} = \frac{1}{2}\mathrm{Re}[\mathbf{E}\times\mathbf{H}^*]$, and hence the radiated power P_{rad} may be computed using (4.3a).

C.2.2 Surface-Wave Power

Under the surface-wave far-field ($k_\rho \rho \to \infty$) condition, and in the case of a lossless dielectric, (C.9) reduces to [122]

$$G_{\mathrm{A}}(\rho) = -\pi j \sum_i H_0^{(2)}(k_{\rho_i}\rho) k_{\rho_i} R_i^{xx/zx}, \tag{C.12}$$

where R_i^{xx} and R_i^{zx} are the residues of $\tilde{G}_{\mathrm{A}}^{xx}$ and $\tilde{G}_{\mathrm{A}}^{zx}$, respectively at the poles k_{ρ_i} corresponding to the different surface waves. The surface-wave far-field is obtained by substituting (C.12) into (C.10) as

$$E_\phi = (-j\omega)\pi j \sin\phi \sum_i H_0^{(2)}(k_{\rho_i}\rho) k_{\rho_i} R_i^{xx}, \tag{C.13a}$$

$$E_z = (j\omega)\pi j \sum_i H_0^{(2)}(k_{\rho_i}\rho) k_{\rho_i} R_i^{zx}. \tag{C.13b}$$

From these relations and the surface-wave far-field conditions $E_\rho = 0$ and $H_\rho = 0$, the magnetic field is obtained from Maxwell equations as

$$H_\phi = \frac{1}{j\omega\mu_0}\left[(-j\omega)\pi j \sum_i H_1^{(2)}(k_{\rho_i}\rho) k_{\rho_i}^2 R_i^{zx}\right], \tag{C.14a}$$

$$H_z = \frac{1}{j\omega\mu_0}\sin\phi\left[(-j\omega)\pi j \sum_i H_1^{(2)}(k_{\rho_i}\rho) k_{\rho_i}^2 R_i^{xx}\right]. \tag{C.14b}$$

Appendix D

Relation between $\tilde{I}'_{\mathbf{sub}}$ and $\tilde{I}_{\mathbf{sub}}$

The Kirchhoff relations for the transmission-line models of Figs.4.1b and 4.2b are

$$\tilde{V} = \tilde{I} Z_0 = -\tilde{I}_{\rm sub} Z_{\rm in}, \tag{D.1a}$$

$$\tilde{I}_{\rm s} = \tilde{I} - \tilde{I}_{\rm sub}, \tag{D.1b}$$

while for the equivalent models of Figs. 4.1d and 4.2d they are

$$\tilde{V} = \tilde{I} Z_0, \tag{D.2a}$$

$$\tilde{I}_{\rm eq} = 2\tilde{I}, \tag{D.2b}$$

where $\tilde{I}_{\rm eq}$ was defined in (4.9).

Substituting (D.1b) and (D.2b) into (4.9) yields

$$\tilde{I} = \tilde{I}'_{\rm sub} - \tilde{I}_{\rm sub}, \tag{D.3}$$

from which $\tilde{I}$ may be eliminated using (D.1a), i.e.

$$\tilde{I} = -\tilde{I}_{\rm sub} Z_{\rm in}/Z_0, \tag{D.4}$$

to provide

$$\tilde{I}'_{\rm sub} = \tilde{I}_{\rm sub}(1 - Z_{\rm in}/Z_0). \tag{D.5}$$

Appendix E

Computation of the Radiation Efficiency of a Horizontal Infinitesimal Dipole on a Uniaxially Anisotropic Substrate

It was shown in Sec. 5.2.1 that for the computation of the radiation efficiency of the horizontal infinitesimal dipole on the grounded substrate, the radiated and surface-wave time-averaged Poynting vectors $\mathbf{S}_{\text{rad/sw,av}} = \frac{1}{2}\text{Re}[\mathbf{E}\times\mathbf{H}^*]$ should be computed. In this section, the electric field, $\mathbf{E}$, and magnetic field, $\mathbf{H}$, which are required for the computation of the Poynting vectors are calculated using the spectral-domain Green functions of the structure.

E.1 Spectral Domain Green Functions

The multilayered field Green functions [75] of the uniaxially anisotropic medium, with the tensorial permittivity and permeability expressed in (5.1), are computed from the transmission-line model of each layer with the same procedure as explained in Appendix B. Assuming the time dependence $\exp(+j\omega t)$, the spectral domain electric and magnetic field Green functions for the TM_z modes are computed as follows

$$\tilde{G}_{\text{EJ}}^{xx,\text{TM}_z} = \frac{-{k_x^{\text{TM}_z}}^2}{{k_\rho^{\text{TM}_z}}^2}\tilde{V}^{\text{TM}_z},\ \tilde{G}_{\text{EJ}}^{zx,\text{TM}_z} = \frac{-k_x^{\text{TM}_z}}{\omega\varepsilon_z}\tilde{I}^{\text{TM}_z}, \tag{E.1a}$$

$$\tilde{G}_{\text{HJ}}^{xx,\text{TM}_z} = \frac{k_x^{\text{TM}_z}k_y^{\text{TM}_z}}{{k_\rho^{\text{TM}_z}}^2}\tilde{I}^{\text{TM}_z},\ \tilde{G}_{\text{HJ}}^{zx,\text{TM}_z} = 0, \tag{E.1b}$$

where $\tilde{G}_{\text{EJ}}^{xx,\text{TM}_z}$ and $\tilde{G}_{\text{EJ}}^{zx,\text{TM}_z}$ are the spectral domain electric field Green functions along the x and z axes, respectively, produced by the electric source along the x axis, $k_z^{\text{TM}_z}$ is the longitudinal wave number, ${k_\rho^{\text{TM}_z}}^2 = {k_x^{\text{TM}_z}}^2 + {k_y^{\text{TM}_z}}^2$ is the square of the transverse wave number and ${k_\rho^{\text{TM}_z}}^2 + {k_z^{\text{TM}_z}}^2 = \omega^2\mu_\rho\varepsilon_z = {k^{\text{TM}_z}}^2$, where k^{TM_z} is the TM_z wave number. In addition, from the transmission-line models the characteristic impedance and the phase constant are obtained as $Z_c^{\text{TM}_z} = k_z^{\text{TM}_z}/(\omega\varepsilon_\rho)\sqrt{\varepsilon_\rho/\varepsilon_z}$ and $\beta^{\text{TM}_z} = \sqrt{\varepsilon_\rho/\varepsilon_z}k_z^{\text{TM}_z}$, respectively.

The spectral domain TE_z modes fields Green functions are obtained from the transmission-

line models as follows

$$\tilde{G}_{\mathrm{HJ}}^{xx,\mathrm{TE}_z} = -\frac{k_x^{\mathrm{TE}_z} k_y^{\mathrm{TE}_z}}{{k_\rho^{\mathrm{TE}_z}}^2} \tilde{I}^{\mathrm{TE}_z},\ \tilde{G}_{\mathrm{HJ}}^{zx,\mathrm{TE}_z} = -\frac{k_y^{\mathrm{TE}_z}}{\omega\mu_z} \tilde{V}^{\mathrm{TE}_z}, \tag{E.2a}$$

$$\tilde{G}_{\mathrm{EJ}}^{xx,\mathrm{TE}_z} = -\frac{{k_y^{\mathrm{TE}_z}}^2}{{k_\rho^{\mathrm{TE}_z}}^2} \tilde{V}^{\mathrm{TE}_z},\ \tilde{G}_{\mathrm{EJ}}^{zx,\mathrm{TE}_z} = 0, \tag{E.2b}$$

where $\tilde{G}_{\mathrm{HJ}}^{xx,\mathrm{TE}_z}$ and $\tilde{G}_{\mathrm{HJ}}^{zx,\mathrm{TE}_z}$ are the spectral domain magnetic field Green functions along the x and z axes, respectively, produced by the electric source along the x axis, $k_z^{\mathrm{TE}_z}$ is the longitudinal wave number, ${k_\rho^{\mathrm{TE}_z}}^2 = {k_x^{\mathrm{TE}_z}}^2 + {k_y^{\mathrm{TE}_z}}^2$ is the square of the transverse wave number and ${k_\rho^{\mathrm{TE}_z}}^2 + {k_z^{\mathrm{TE}_z}}^2 = \omega^2\mu_z\varepsilon_\rho = {k^{\mathrm{TE}_z}}^2$, where k^{TE_z} is the TE_z wave number. Moreover, from the transmission-line model, $Z_c^{\mathrm{TE}_z} = \omega\mu_z/k_z^{\mathrm{TE}_z}\sqrt{\mu_\rho/\mu_z}$ and $\beta^{\mathrm{TE}_z} = \sqrt{\mu_\rho/\mu_z}k_z^{\mathrm{TE}_z}$ are computed, which are the TE_z modes characteristic impedance and the phase constant, respectively.

E.1.1 Vector Potentials Green Functions

In the mixed potential integral equations with Sommerfeld choice for the potentials [76], for a source along x, it is assumed that the electric vector potential Green function $\bar{\bar{\mathbf{G}}}_{\mathrm{F}} = 0$, while the magnetic vector potential Green functions $\bar{\bar{\mathbf{G}}}_{\mathrm{A}} = \left(\mathbf{a}_x G_{\mathrm{A}}^{xx} + \mathbf{a}_z G_{\mathrm{A}}^{zx}\right)\mathbf{a}_x$, where G_{A}^{xx} and G_{A}^{zx} are the vector potential Green function produced by $\tilde{J}_x$ along the x and z axes, respectively and we have [110]

$$\bar{\bar{\mathbf{G}}}_{\mathrm{HJ}} = \bar{\bar{\mu}}^{-1}\nabla \times \bar{\bar{\mathbf{G}}}_{\mathrm{A}}, \tag{E.3}$$

where $\bar{\bar{\mathbf{G}}}_{\mathrm{HJ}} = \bar{\bar{\mathbf{G}}}_{\mathrm{HJ}}^{\mathrm{TM}_z} + \bar{\bar{\mathbf{G}}}_{\mathrm{HJ}}^{\mathrm{TE}_z}$ is the total magnetic Green functions with $\bar{\bar{\mathbf{G}}}_{\mathrm{HJ}}^{\mathrm{TM}_z}$ and $\bar{\bar{\mathbf{G}}}_{\mathrm{HJ}}^{\mathrm{TE}_z}$ obtained from (E.1b) and (E.2a), respectively. Substituting $\bar{\bar{\mu}}$ from (5.1) into (E.3) leads to

$$\tilde{\mathbf{G}}_{\mathrm{A}}^{xx} = \frac{1}{j\omega} V^{\mathrm{TE}_z}, \tag{E.4a}$$

$$\tilde{\mathbf{G}}_{\mathrm{A}}^{zx} = \frac{\mu_\rho}{jk_y}\left(\frac{k_x k_y}{k_\rho^2} I^{\mathrm{TM}_z} - \frac{k_x k_y}{k_\rho^2} I^{\mathrm{TE}_z}\right). \tag{E.4b}$$

E.2 Power Computation

To calculate the radiated and surface-wave powers through the Poynting vectors, it is required to compute the spatial domain Green functions. The spectral and spatial domain Green functions are related through the double Fourier transformation as follows

$$G_{\mathrm{A}}(x,y,z) = \frac{1}{2\pi}\int_{-\infty}^{+\infty}\int_{-\infty}^{+\infty} \tilde{G}_{\mathrm{A}}(k_x k_y, z) e^{jk_x x} e^{jk_y y}\, dk_x\, dk_y. \tag{E.5}$$

Next, the far-field electric fields for the x-directed dipole and thus the radiation and surface-wave powers are computed from

$$\mathbf{E}(x,y,z) = -j\omega\overline{\overline{\mathbf{G}}}_{\mathrm{A}}(x,y,z).\mathbf{a}_x. \tag{E.6}$$

E.3 Radiated Power

Assuming that the radiating spectral domain Green function dependence on the z axis is that of a pure spherical wave traveling in the upper semi-infinite free-space, we can define $\tilde{G}_A(k_x,k_y,z) = \tilde{g}_{\mathrm{A}}(k_x,k_y)\exp(-jk_{z0}z)$, where k_{z0} is the propagation constant along z in the free space. Applying the far-field asymptotic approximations ($k_\rho\rho, k_0 r \to \infty$) [75, 101], the far-field Green function associated with the space waves is obtained as follows

$$G_{\mathrm{A}}(x,y,z) = jk_0\cos\theta\tilde{g}_{\mathrm{A}}(k_x,k_y)\frac{\exp(-jk_0 r)}{r}, \tag{E.7}$$

where k_0 is the free-space wave number. Next, the Poynting vector $\mathbf{S}_{\text{rad, av}} = \frac{1}{2}\mathrm{Re}[\mathbf{E}\times\mathbf{H}^*]$ and therefore the radiated power can be calculated by inserting (E.7) into (E.6) and further calculating the magnetic fields from the Maxwell equations, using the following equation

$$P_{\mathrm{rad}} = \int_0^{2\pi}\int_0^{\pi/2} \mathbf{S}_{\text{rad, av}}.\mathbf{a}_r r^2\sin\theta\, d\theta\, d\phi. \tag{E.8}$$

E.4 Surface-wave Power

The surface-wave power P_{sw} is calculated considering cylindrical wave associated to a surface mode as follows

$$P_{sw} = \int_0^{2\pi}\int_{-d}^{\infty} \mathbf{S}_{\text{sw, av}}.\mathbf{a}_\rho\rho\, dz\, d\phi, \tag{E.9}$$

where $\mathbf{S}_{\text{sw, av}}$ is the far-field ($k_\rho\rho \to \infty$) Poynting vector inside the substrate.

In a lossless dielectric, the far-field Sommerfeld transformations are computed from the residues of the spectral Green functions as follows [122]

$$G_{\text{A}}(\rho) = -\pi j \sum_i H_0^{(2)}(k_{\rho_i}\rho) k_{\rho_i}^1 R_i^{xx,zx}, \tag{E.10}$$

where $R_i^{xx,zx}$ is the residue of $\tilde{G}_{\text{A}}^{xx,zx}$ at the poles k_{ρ_i}. As a result, in the substrate

$$E_\phi = (-j\omega)\pi j \sin\phi \sum_i H_0^{(2)}(k_{\rho_i}\rho) k_{\rho_i} R_i^{xx}, \tag{E.11a}$$

$$E_z = (j\omega)\pi j \sum_i H_0^{(2)}(k_{\rho_i}\rho) k_{\rho_i} R_i^{zx}. \tag{E.11b}$$

The magnetic fields are obtained from the electric fields [Eqs. (E.11)] by inserting $\bar{\bar{\mu}}$ from (5.1b) into Maxwell equations

$$\nabla \times \mathbf{H} = j\omega\bar{\bar{\varepsilon}}\mathbf{E}, \tag{E.12a}$$

$$\nabla \times \mathbf{E} = -j\omega\bar{\bar{\mu}}\mathbf{H}, \tag{E.12b}$$

and then applying the far-field approximations ($E_\rho = 0$ and $H_\rho = 0$) as follows

$$H_\phi = \frac{1}{j\omega\mu_\rho}\left[(-j\omega)\pi j \sum_i H_1^{(2)}(k_{\rho_i}\rho) k_{\rho_i}^2 R_i^{zx}\right], \tag{E.13a}$$

$$H_z = \frac{1}{j\omega\mu_z}\sin\phi\left[(-j\omega)\pi j \sum_i H_1^{(2)}(k_{\rho_i}\rho) k_{\rho_i}^2 R_i^{xx}\right]. \tag{E.13b}$$

The surface-wave modes' Poynting vector and therefore the average power are computed by substituting (E.11) and (E.13) into (E.9) and by using the far-field ($k_\rho\rho \to \infty$) asymptotic expression of the Hankel functions $H_p^{(2)}(k_\rho\rho) = \sqrt{2/(\pi k_\rho\rho)}\exp\left[-j\left(k_\rho\rho - p\pi/2 - \pi/4\right)\right]$ [110].

Appendix F

List of Publications and Awards

F.1 Peer-Reviewed Journal Publications

1. *A. Shahvarpour*, A. Alvarez Melcon, and C. Caloz, "Radiation efficiency issues and solutions of planar antennas on electrically thick substrates," accepted for publication in *IEEE Trans. Antennas Propagat.*
2. A. Parsa, *A. Shahvarpour*, and C. Caloz, "Double-band tunable magnetic conductor realized by a grounded ferrite slab covered with metal strip grating," *IEEE Micro. and Wireless Comp. Lett. (MWCL)*, vol. 21, no 5, pp. 231-233, May 2011.
3. *A. Shahvarpour*, C. Caloz, and A. Alvarez Melcon, "Broadband and low-beam squint leaky wave radiation from a uniaxially anisotropic grounded slab," *Radio Sci.*, vol. 46, no. RS4006, pp. 1-13, Aug. 2011. doi:10.1029/2010RS004530.
4. *A. Shahvarpour*, T. Kodera, A. Parsa, and C. Caloz, "Arbitrary electromagnetic conductor boundaries using Faraday rotation in a grounded ferrite slab," *IEEE Trans. Microwave Theory Tech.*, vol. 58, no. 11, pp. 2781-2793, Nov. 2010.
5. *A. Shahvarpour*, S. Gupta, and C. Caloz, "Schrödinger solitons in left-handed SiO_2-Ag-SiO_2 and Ag-SiO_2-Ag plasmonic waveguides using nonlinear transmission line approach," *J. App. Phys.*, vol. 104, pp.124510:1-15, Dec. 2008.

F.2 Conference Publications

1. C. Caloz, *A. Shahvarpour*, D. L Sounas, T. Kodera, B. Gurlek, and N. Chamanara, "Practical realization of perfect electromagnetic conductor (PEMC) boundaries using ferrites, magnet-less non-reciprocal metamaterials (MNMs) and graphene," accepted in *International Symposium on Electromagnetic Theory (EMTS)*, Hiroshima, Japan, 2013. (*Invited*)
2. *A. Shahvarpour*, S. Couture, and C. Caloz, "Bandwidth enhancement of a patch antenna using a wire-ferrite substrate," in *Proc. IEEE AP-S International Symp.*, Chicago, July 2012.
3. *A. Shahvarpour*, A. Alvarez Melcon, and C. Caloz, "Radiation efficiency enhancement of a horizontal dipole on an electrically thick substrate by a PMC ground plane," in

Proc. XXX URSI Assembly and Scientific Symposium of International Union Radio Science, Istanbul, Turkey, August 2011. (*Recipient of Young Scientist Award*)

4. *A. Shahvarpour*, A. Alvarez Melcon, and C. Caloz, "Analysis of the radiation efficiency of a horizontal electric dipole on a grounded dielectric slab," in *Proc. IEEE AP-S International Symp.*, Spokane, Washington, USA, pp. 1293-1296, July 2011.
5. *A. Shahvarpour*, A. Alvarez Melcon, and C. Caloz, "Anisotropic meta-substrate conical-beam leaky-wave antenna," in *Proc. 2010 Asia-Pacific Microwave conference (APMC)*, Yokohama, Japan, pp. 299-302, Dec. 2010. (*Recipient of Best Paper Award*)
6. *A. Shahvarpour*, A. Alvarez Melcon, and C. Caloz, "Analysis of the radiation properties of a point source on a uniaxially anisotropic meta-substrate and application to a high-efficiency antenna," in *Proc. 40th European Microwave Conf. (EuMC)*, Paris, France, pp. 1424-1428, Sept. 2010.
7. *A. Shahvarpour*, A. Alvarez Melcon, and C. Caloz, "Bandwidth enhancement and beam squint reduction of leaky modes in a uniaxially anisotropic meta-substrate," in *Proc. IEEE AP-S International Symp.*, Toronto, Canada, July 2010.
8. *A. Shahvarpour*, A. Alvarez-Melcon, and C. Caloz, "Spectral transmission line analysis of a composite right/left-handed uniaxially anisotropic meta-substrate," in *Proc. 14th International Symp. on Antenna Technology and Applied Electromagnetics (ANTEM)*, Ottawa, Canada, July 2010. (*Finalist of the Student Paper Competition*)
9. *A. Shahvarpour*, T. Kodera, A. Parsa, and C. Caloz, "Realization of an effective free-space perfect electromagnetic conductor (PEMC) boundary by a grounded ferrite slab using Faraday rotation," in *Proc. European Microwave Conf. (EuMC)*, Rome, Italy, pp. 731-734, Sept.-Oct. 2009. (*Recipient of Young Engineers Prize*)
10. *A. Shahvarpour* and C. Caloz, "Ferrite effective perfect magnetic conductor (FE-PMC) and application to waveguide miniaturization," in *Proc. IEEE MTT-S Int. Microwave Symp. Dig.*, Boston, MA, USA, June 2009, pp. 25-28. (*Finalist of the Student Paper Competition*)
11. *A. Shahvarpour*, S. Gupta, and C. Caloz, "Study of left-handed Schrödinger solitons in an Ag film plasmonic waveguide using a nonlinear transmission line approach," in *Proc. XXIXth Assembly of Union Radio Science International (URSI)*, Chicago, IL, Aug. 2008. (*Invited*)

F.3 Non-Refereed Publications

1. *A. Shahvarpour*, C. Caloz, J. S. Gomez Diaz, A. Alvarez Melcon, C. Canyete Rebenaque, P. Vera Castejon, F. Quesada Pereira, and J. L. Gomez Tornero, "Analisis espectral de

metasustratos con anisotropia uni-axial, y aplicación en el ensanchamiento de la banda de ondas leaky-wave," Espacio Teleco. vol. 2, pp. 143-152, 2011.

F.4 Awards and Honors

F.4.1 Awards

1. *IEEE Microwave Theory and Techniques Society (MTT-S) Graduate Fellowship Award*, Montréal, Canada, 2012.
2. *Young Scientist Award*, XXX URSI General Assembly and Scientific Symposium of International Union of Radio Science, Istanbul, Turkey, 2011.
3. *Best Paper Award*, Asia Pacific Microwave Conference (APMC), Yokohama, Japan, 2010.
4. *Young Engineers Prize*, 12th IEEE European Microwave Conference (EuMC), Rome, Italy, 2009.
5. *Student Poster Contest 2nd Prize*, Deuxième Symposium et Assemblée Génerale du Centre de Recherche En Électronique Radiofréquence (CRÉER), École Polytechnique de Montréal, Québec, 2010.
6. *Student Paper Competition Finalist*, International Symposium of Antenna Technology and Applied Electromagnetics (ANTEM), Ottawa, Canada, 2010.
7. *Student Paper Competition Finalist*, International Microwave Symposium (IMS), MA, Boston, USA, 2009.

F.4.2 Travel Grants

1. Travel Grant from IEEE Microwave Theory and Techniques Society (MTT-S) to attend the 2012 International Microwave Symposium (IMS 2012), Montréal, Canada, 2012.
2. Travel Grant from Canadian National Committee of URSI to attend XXX URSI General Assembly and Scientific Symposium of International Union of Radio Science, Istanbul, Turkey, 2011.
3. Travel Grant from the 39th IEEE European Microwave Conference, Rome, Italy, in 2009.
4. Travel Grant from the 2009 International Microwave Symposium (IMS 2009), MA, Boston, USA, 2009.
5. Travel Grant from the XXIXth Assembly of Union Radio Science International (URSI), Chicago, IL, USA, 2008.